

Ministry of Science and Higher Education of the Russian Federation  
ITMO University

ISSN 2220-8054

***NANOSYSTEMS:***  
***PHYSICS, CHEMISTRY, MATHEMATICS***

**2023, volume 14(5)**

**Наносистемы: физика, химия, математика**

**2023, том 14, № 5**



# NANOSYSTEMS:

PHYSICS, CHEMISTRY, MATHEMATICS

## ADVISORY BOARD MEMBERS

**Chairman:** V.N. Vasiliev (*St. Petersburg, Russia*),  
V.M. Buznik (*Moscow, Russia*); V.M. Ievlev (*Voronezh, Russia*), P.S. Kop'ev (*St. Petersburg, Russia*), N.F. Morozov (*St. Petersburg, Russia*), V.N. Parmon (*Novosibirsk, Russia*),  
A.I. Rusanov (*St. Petersburg, Russia*),

## EDITORIAL BOARD

**Editor-in-Chief:** I.Yu. Popov (*St. Petersburg, Russia*)

### Section Co-Editors:

Physics – V.M. Uzdin (*St. Petersburg, Russia*),

Material science – V.V. Gusarov (*St. Petersburg, Russia*); O.V. Al'myasheva (*St. Petersburg, Russia*);

Chemistry – V.K. Ivanov (*Moscow, Russia*),

Mathematics – I.Yu. Popov (*St. Petersburg, Russia*).

### Editorial Board Members:

V.M. Adamyan (*Odessa, Ukraine*); A.P. Alodjants (*St. Petersburg, Russia*); S. Behta (*Stockholm, Sweden*); J. Behrndt (*Graz, Austria*); A. Chatterjee (*Hyderabad, India*); A.V. Chizhov (*Dubna, Russia*); A.N. Enyashin (*Ekaterinburg, Russia*), P.P. Fedorov (*Moscow, Russia*); E.A. Gudilin (*Moscow, Russia*); H. Jónsson (*Reykjavik, Iceland*); A.A. Kiselev (*Durham, USA*); Yu.S. Kivshar (*Canberra, Australia*); S.A. Kozlov (*St. Petersburg, Russia*); P.A. Kurasov (*Stockholm, Sweden*); A.V. Lukashin (*Moscow, Russia*); I.V. Melikhov (*Moscow, Russia*); G.P. Miroshnichenko (*St. Petersburg, Russia*); I.Ya. Mittova (*Voronezh, Russia*); Nguyen Anh Tien (*Ho Chi Minh, Vietnam*); V.V. Pankov (*Minsk, Belarus*); K. Pankrashkin (*Orsay, France*); A.V. Ragulya (*Kiev, Ukraine*); V. Rajendran (*Tamil Nadu, India*); A.A. Rempel (*Ekaterinburg, Russia*); V.Ya. Rudyak (*Novosibirsk, Russia*); H.M. Sedighi (*Ahvaz, Iran*); D Shoikhet (*Karmiel, Israel*); P Stovicek (*Prague, Czech Republic*); V.M. Talanov (*Novocherkassk, Russia*); A.Ya. Vul' (*St. Petersburg, Russia*); A.V. Yakimansky (*St. Petersburg, Russia*), V.A. Zagrebnev (*Marseille, France*).

### Editors:

I.V. Blinova; A.I. Popov; A.I. Trifanov; E.S. Trifanova (*St. Petersburg, Russia*),  
R. Simoneaux (*Philadelphia, Pennsylvania, USA*).

**Address:** ITMO University, Kronverkskiy pr., 49, St. Petersburg 197101, Russia.

**Phone:** +7(812)607-02-54, **Journal site:** <http://nanojournal.ifmo.ru/>,

**E-mail:** [nanojournal.ifmo@gmail.com](mailto:nanojournal.ifmo@gmail.com)

## AIM AND SCOPE

The scope of the journal includes all areas of nano-sciences. Papers devoted to basic problems of physics, chemistry, material science and mathematics inspired by nanosystems investigations are welcomed. Both theoretical and experimental works concerning the properties and behavior of nanosystems, problems of its creation and application, mathematical methods of nanosystem studies are considered.

The journal publishes scientific reviews (up to 30 journal pages), research papers (up to 15 pages) and letters (up to 5 pages). All manuscripts are peer-reviewed. Authors are informed about the referee opinion and the Editorial decision.

# CONTENT

## MATHEMATICS

U.N. Kuljanov

**On the spectrum of the two-particle Schrödinger operator with point potential: one dimensional case** 505

B.Yu. Irgashev

**Boundary value problem for a degenerate equation with a Riemann-Liouville operator** 511

A.M. Khalkhuzhaev, I.A. Khujamiyrov

**On the discrete spectrum of the Schrödinger operator using the 2+1 fermionic trimer on the lattice** 518

## PHYSICS

A.E. Rezvanova, B.S. Kudryashov, A.N. Ponomarev,

A.I. Knyazkova, V.V. Nikolaev, Yu.V. Kistenev

**Composite hydroxyapatite-multi-walled carbon nanotubes: study of porosity by terahertz time domain spectroscopy** 530

K.B. Tsiberkin

**Verification of continuum-based model of carbon materials** 539

I.V. Pleshakov, A.A. Alekseev, E.E. Bibik, V.I. Dudkin,

T.Yu. Kudryashova, E.K. Karseeva, T.A. Kostitsyna, E.A. Medvedeva

**Magnetic nanoparticles in solid matrices: formation and fixation of structures, induced by magnetic field** 544

## CHEMISTRY AND MATERIAL SCIENCE

I.B. Dorosheva, A.A. Rempel, G.O. Kalashnikova, V.N. Yakovenchuk  
**Nanoparticles in titanite ore** 549

A.A. Lobinsky, M.V. Kaneva, A.K. Bachina, M.I. Tenevich

**SILD synthesis of porous manganese oxide nanocoatings as electroactive materials for pseudocapacitors** 554

E.A. Zamyatina, S.Yu. Kottsov, V.A. Anikina, A.L. Popov,

M.P. Shevelyova, N.R. Popova

**Cerium Oxide@Silica core-shell nanocomposite as multimodal platforms for drug release and synergistic anticancer effects** 560

A.A. Ostroushko, I.D. Gagarin, E.V. Kudyukov, T.Yu. Zhulanova, A.E. Permyakova, O.V. Russkikh <b>Synthesis of lanthanum manganite powders via combustion reactions: some aspects of the influence of magnetic field and charge generation in precursors on the formation of properties</b>	<b>571</b>
S.S. Kozlov, A.B. Nikolskaia, O.K. Karyagina, E.K. Kosareva, O.V. Alexeeva, V.I. Petrova, O.V. Almjashaeva, O.I. Shevaleevskiy <b>Planar perovskite solar cells with La<sub>2</sub>NiMnO<sub>6</sub> buffer layer</b>	<b>584</b>
D.S. Dmitriev, M.I. Tenevich <b>Evaluation of the electrochemical active surface area for carbon felt and nanostructured Ni coatings as electrocatalysts for hydrogen evolution reaction</b>	<b>590</b>
A.S. Pashchenko, O.V. Devitsky, L.S. Lunin, M.L. Lunina, O.S. Pashchenko, E.M. Danilina <b>Growth of nanotextured thin films of GaInAsP and GaInAsSbBi solid solutions on GaP substrates by pulsed laser deposition</b>	<b>601</b>
<b>Information for authors</b>	<b>606</b>

## On the spectrum of the two-particle Schrödinger operator with point potential: one dimensional case

Utkir N. Kuljanov<sup>1,2</sup><sup>1</sup>Samarkand State University, Samarkand, Uzbekistan<sup>2</sup>Samarkand branch of Tashkent State University of Economics, Samarkand, Uzbekistan

uquljonov@bk.ru

**ABSTRACT** In the paper, a one-dimensional two-particle quantum system interacted by two identical point interactions is considered. The corresponding Schrödinger operator (energy operator)  $h_\varepsilon$  depending on  $\varepsilon$  is constructed as a self-adjoint extension of the symmetric Laplace operator. The main results of the work are based on the study of the operator  $h_\varepsilon$ . First, the essential spectrum is described. The existence of unique negative eigenvalue of the Schrödinger operator is proved. Further, this eigenvalue and the corresponding eigenfunction are found.

**KEYWORDS** two-particle quantum system, symmetric Laplace operator, eigenvalue, eigenfunction, energy operator

**ACKNOWLEDGEMENTS** Author partially supported by [grant number FZ-20200929224] of Fundamental Science Foundation of Uzbekistan.

**FOR CITATION** Kuljanov U.N. On the spectrum of the two-particle Schrödinger operator with point potential: one dimensional case. *Nanosystems: Phys. Chem. Math.*, 2023, **14** (5), 505–510.

### 1. Introduction

The problems of the point interaction of two and three identical quantum particles interacted by point potentials (also called contact potentials and also, occasionally, singular potentials) have been studied in various physical works. In was the works of F. A. Berezin and L. D. Faddeev [1] and R. A. Minlos and L. D. Faddeev [2,3], where a rigorous mathematical description of the point interaction of two and three particles was proposed.

In [2, 3], the Hamiltonian of the system under consideration was investigated using the theory of self-adjoint extensions of symmetric operators. It was introduced as a self-adjoint extension of the symmetric Laplace operator defined on the domain of functions of three variables  $x_1, x_2, x_3$ ;  $x_j \in \mathbb{R}$ ,  $j = 1, 2, 3$  vanishing if any two arguments  $x_j = x_k$ ,  $j \neq k$ ,  $k = 1, 2, 3$  coincide.

The proposed extension is called the Skornyakov-Ter-Martirosyan extension. In [4], on the background of the results of [1, 2], the Hamiltonian of three particles (two fermions and one particle of a different nature) with the same masses interacting as point potentials was studied and it was shown that the Skornyakov-Ter-Martirosyan extensions are self-adjoint and semi-bounded.

In [5], the results of [1–4] were generalized to the case of three arbitrary particles and it was shown that the corresponding Hamiltonian has the discrete spectrum unbounded below. Note that the advantage of one-dimensional models with point perturbations is clear because they are useful for the study of a variety of qualitative properties. For instance, you can see [6–11] for one body problems with delta potentials.

In the discrete case, there were also found conditions for the existence of the eigenvalues as well as their numbers for the Hamiltonian of the system of two particles depending on parameters. For example, in [12–15], the Hamiltonian  $h$  of the system of two quantum particles moving on a one and three-dimensional lattices interacting via some attractive potential was considered. Conditions for the existence of eigenvalues of the two-particle Schrödinger operator  $h_\mu(k)$ ,  $k \in \mathbb{T}$ ,  $d = 1, 3$ ;  $\mu$ , associated with the Hamiltonian  $h$ , were studied depending on the energy of the particle interaction  $\mu$  and total quasi-momentum  $k \in T^d$ .

In [2, 3], Faddeev and Minlos studied the energy operator of three identical three-dimensional quantum particles (bosons) interacting in a “pointed way”. This operator was defined as a certain self-adjoint extension of the symmetric operator  $H_0 = \Delta_{x_1} - \Delta_{x_2} - \Delta_{x_3}$  on the domain of functions of three variables  $x_1, x_2, x_3 \in \mathbb{R}^3$  that vanish whenever any two arguments coincide  $x_i = x_j$ ,  $i \neq j$ ;  $i, j = 1, 2, 3$ . Minlos and Faddeev found that all nontrivial self-adjoint extensions describing the energy operator have the discrete spectrum unbounded from below and therefore the corresponding quantum system with  $\delta$ -like pair interactions collapses, i.e. we have a phenomenon of “fall to the center”. In recent work [5], Minlos and Melnikov extended these results to the general case of three different particles of different masses. In [2, 5], one can find the mathematical “explanation” for the Thomas effect (unsemiboundedness of the energy operator

from below) and also the interpretation of Danilov’s “experimental” parameter as the one describing the one-parameter family of self-adjoint extensions of the initial symmetric operator (“three-Hamiltonian”).

In this article, following the basic scheme used in [2–5], we study the problem of the point interaction of two arbitrary particles in one-dimensional space. The Laplace operator with domain on variables  $x_1, x_2 \in \mathbb{R}$ , vanishing as  $x_1 = x_2$  is considered. In the momentum representation of the Hamiltonian, after the reduction of the variables, we establish the Skornyakov-Ter-Martirosyan extension  $h_\varepsilon$  as a self-adjoint operator on its domain. The essential spectrum of  $h_\varepsilon$  coincides with the interval  $[0; \infty)$ . It is proved that the operator  $h_\varepsilon$  has no any eigenvalue as  $\varepsilon \leq 0$  and if the parameter of the extension is positive, i.e.  $\varepsilon > 0$ , then  $h_\varepsilon$  has unique negative eigenvalue.

**2. Preliminaries and selection of the extension**

The Hamiltonian (energy operator) of the two-particle system under consideration is defined as an extension  $\tilde{H}$  of the symmetric operator  $\tilde{H}_0$  acting in the Hilbert space  $L_2(\mathbb{R}^2) \equiv L_2$  of the form

$$\left(\tilde{H}_0\phi\right)(x_1, x_2) = \left(-\frac{1}{2m_1}\Delta_{x_1} - \frac{1}{2m_2}\Delta_{x_2}\right)\phi(x_1, x_2),$$

where the domain  $D(\tilde{H}_0)$  of  $\tilde{H}$  is a manifold of functions  $\phi \in L_2$  satisfying condition

$$(\Delta_{x_1} + \Delta_{x_2})\phi \in L_2 \tag{1}$$

with

$$\phi(x, x) = 0. \tag{2}$$

Here  $\Delta_{x_i}$  is the Laplace operator in the  $x_i$  variable  $x_i \in \mathbb{R}$ ,  $m_i$  is the mass of the  $i$ -th particle,  $i = 1, 2$ .

After the action of the corresponding Fourier transform, the operator  $\tilde{H}_0$  transfers to the operator

$$(H_0f)(p_1, p_2) = \left(\frac{1}{2m_1}p_1^2 + \frac{1}{2m_2}p_2^2\right)f(p_1, p_2),$$

defined on the set  $D(H_0) \subset L_2$  of functions  $f(p_1, p_2)$ , satisfying the following conditions:

$$\int_{\mathbb{R}^2} (p_1^4 + p_2^4)|f(p_1, p_2)|^2 dp_1 dp_2 < \infty, \tag{3}$$

with

$$\int_{\Gamma_p} f(p_1, p_2) d\nu_p = 0, \tag{4}$$

where conditions (1) and (2) are equivalent to conditions (3) and (4), respectively. Here  $\Gamma_p = \{(p_1, p_2) \in \mathbb{R}^2 : p_1 + p_2 = p\}$ ,  $p \in \mathbb{R}$  is a family of lines with the natural Lebesgue measure  $d\nu_p$ .

Making the following change of variables

$$P = p_1 + p_2, \quad p = \frac{m_2}{M}p_1 - \frac{m_1}{M}p_2, \quad M = m_1 + m_2$$

we establish the natural isomorphism between the spaces  $L_2(\mathbb{R}) \otimes L_2(\Gamma_p)$  and  $L_2(\mathbb{R}^2)$ .

The last space can be identified with the space  $L_2(\mathbb{R}) \otimes L_2(\mathbb{R})$ , while the operator  $H_0$  is written as the tensor sum of the following operators

$$H_0 = \left(\frac{1}{2M}P^2 + \frac{1}{2m}h_0\right) \otimes I,$$

where  $I$  is the identity operator,  $m = m_1m_2/(m_1 + m_2)$ ,  $(1/2M)P^2$  is the operator of multiplication by the number  $P^2/(2M)$  in the space  $L_2(\mathbb{R})$ , and  $h_0$  is a closed non-negative symmetric operator acting in  $L_2(\mathbb{R})$  as

$$h_0f(p) = p^2f(p).$$

Its domain  $D(h_0)$  consists of functions satisfying the conditions:

$$\int p^4|f(p)|^2 dp < \infty; \quad \int f(p)dp = 0. \tag{5}$$

Further, the integral without indicating limits is understood as integration over  $\mathbb{R}$ .

The symbol  $\mathfrak{R}_z$  denotes the deficiency subspace for the operator  $h_0$ , i.e.

$$\mathfrak{R}_z = \{g \in L_2(\mathbb{R}) : ((h_0 - zI)f, g) = 0, f \in D(h_0)\}.$$

**Lemma 2.1.** For any  $z \in \Pi_0 = \mathbb{C}^1 \setminus [0, \infty)$ , the deficiency subspace  $\mathfrak{R}_z \subset L_2(\mathbb{R})$  of  $h_0$  consists of functions of the form

$$g(p) = \frac{c}{p^2 - \bar{z}}, \quad c \in \mathbb{C}^1.$$

*Proof.* Let  $g \in \mathfrak{R}_z$ . Then for any  $f \in D(h_0)$ , the relation

$$((h_0 - zI)f, g) = \int (p^2 - z)f(p)\overline{g(p)}dp = \int f(p)\overline{(p^2 - \bar{z})g(p)}dp = 0$$

holds.

From the last relation and conditions (5), it follows that

$$(p^2 - \bar{z})g(p) = c$$

or

$$g(p) = \frac{c}{p^2 - \bar{z}}.$$

The lemma is proved. □

It follows from the lemma that for any  $z \in \Pi_0$  the deficiency subspace  $\mathfrak{R}_z$  of the operator  $h_0$  is determined by the formula

$$\mathfrak{R}_z = \{g \in L_2(\mathbb{R}) : ((h_0 - zI)f, g) = 0, f \in D(h_0)\}.$$

Therefore,  $h_0$  is a symmetric operator with deficiency indices (1, 1). Using the general extension theory [4], we find that the operator  $h_0$  has one-parameter family of self-adjoint extensions.

Since the operator  $h_0$  is non-negative, as in [2–5], we use the theory of extensions of semibounded operators. The deficiency subspace  $\mathfrak{R}_{-1}$  of the operator  $h_0$  consists of functions of the form

$$u_{-1}(p) = \frac{c}{p^2 + 1}, \quad c \in \mathbb{C}^1.$$

Using the positivity of  $H_0$  and applying methods of the theory of extensions of semi-bounded operators, as in [2], we prove the following lemma, which allows one to define the adjoint operator  $h_0^*$ .

**Lemma 2.2.** *The domain  $D(h_0^*)$  of  $h_0^*$  consists of functions of the form*

$$g(p) = f(p) + \frac{c_1}{p^2 + 1} + \frac{c_2}{(p^2 + 1)^2}. \quad (6)$$

where  $f \in D(h_0)$ ,  $c_1, c_2 \in \mathbb{C}^1$ . The operator  $h_0^*$  acts on function  $g$  of the form (6) by the following formula

$$(h_0^*g)(p) = p^2g(p) - c_1,$$

where the constant  $c_1$  is taken from the decomposition (6) of the function  $g$ .

Further, we select the extensions of the operator  $h_0$ . We define the set

$$D(h_\varepsilon), D(h_0) \subset D(h_\varepsilon) \subset D(h_0^*)$$

as follows:

$$D(h_\varepsilon) = \left\{ g \in D(h_0^*) : g(p) = f(p) + \frac{c}{p^2 + 1} + \frac{(\varepsilon - 2)c}{(p^2 + 1)^2}, f \in D(h_0) \right\} \quad (7)$$

The restriction of the operator  $h_0$  to the domain  $D(h_\varepsilon)$  is denoted by  $h_\varepsilon$  and it has the form

$$h_\varepsilon g(p) = p^2g(p) - c.$$

By definition of  $h_\varepsilon$ , it is an extension of the operator  $h_0$ .

**Theorem 2.1.** *For any  $\varepsilon \in \mathbb{R}$ , the extension  $h_\varepsilon$  is a self-adjoint operator.*

*Proof.* It is easy to verify that for any  $g_1, g_2 \in D(h_\varepsilon)$ , the relation  $(h_\varepsilon g_1, g_2) = (g_1, h_\varepsilon g_2)$  holds, i.e.  $h_\varepsilon$  is a symmetric operator. Now, we show that the deficiency indices of the operator  $h_\varepsilon$  are equal to (0, 0).

Let  $\psi \in \mathfrak{R}_{-1}(h_\varepsilon)$ . Then the function  $\psi(p)$  has the form

$$\psi(p) = \frac{b}{p^2 + 1}, \quad b \in \mathbb{C}^1.$$

For any  $g \in D(h_\varepsilon)$ , the equality  $((h_\varepsilon + I)g, \psi) = 0$  holds. Correspondingly, the last equality can be written as

$$\begin{aligned} ((h_\varepsilon + I)g, \psi) &= \int ((p^2 + 1)(f(p) + \frac{c}{p^2 + 1} + \frac{(\varepsilon - 2)c}{(p^2 + 1)^2}) - c)\overline{\psi(p)}dp = \\ &= \int ((p^2 + 1)f(p)\overline{\psi(p)}dp + (\varepsilon - 2)c \int \frac{\bar{b}}{(p^2 + 1)^2} dp = 0. \end{aligned} \quad (8)$$

Since

$$\int ((p^2 + 1)f(p)\overline{\psi(p)}dp = 0$$

and  $(\varepsilon - 2)c \neq 0$ , we have  $b = 0$ . Hence  $\psi(p) = 0$ . This proves that the deficiency indices of the operator  $h_\varepsilon$  are equal to (0, 0). □

### 3. Spectral properties of the operator $h_\varepsilon$

The main results of the paper are the following theorems.

**Theorem 3.1.** *For any  $\varepsilon \in \mathbb{R}$ , the essential spectrum of  $h_\varepsilon$  coincides with interval  $[0, \infty)$ . If  $\varepsilon \geq 0$  then  $h_\varepsilon$  has no any negative eigenvalue, and for any  $\varepsilon < 0$ , the operator  $h_\varepsilon$  has unique simple eigenvalue  $z = -\frac{4}{\varepsilon^2}$  and the corresponding eigenfunction has the form  $g_\varepsilon(p) = \frac{1}{p^2 + \frac{4}{\varepsilon^2}}$ .*

*Proof.* First, we show that the essential spectrum of  $h_\varepsilon$  equals to  $[0; \infty)$ . For each  $z \geq 0$ , let us consider the sequence of cut-off layers:

$$G_n(z) = \left\{ p \in \mathbb{R} : \sqrt{z} + \frac{1}{n+1} < |p| < \sqrt{z} + \frac{1}{n} \right\}, \quad n = 1, 2, 3, \dots$$

We split each layer  $G_n(z)$  into two half-layers as

$$G_n^+(z) = \{p \in G_n(z) : p \geq 0\}$$

and

$$G_n^-(z) = \{p \in G_n(z) : p < 0\}.$$

By construction, the volumes of these parts are equal and

$$\mu(G_n^+(z)) = \mu(G_n^-(z)) = \frac{1}{2}\mu(G_n(z))$$

. One can see that

$$V_n = \mu(G_n(z)) = \frac{2}{n(n+1)}.$$

Let  $f_n^{(z)}$ ,  $n = 1, 2, 3, \dots$  be a sequence of the test functions

$$f_n^{(z)}(p) = \begin{cases} \frac{1}{\sqrt{V_n(z)}}, & p \in G_n^+(z); \\ -\frac{1}{\sqrt{V_n(z)}}, & p \in G_n^-(z); \\ 0, & p \in \mathbb{R} \setminus G_n(z). \end{cases}$$

Then, it is easy to verify that  $f_n^{(z)} \in L_2(\mathbb{R})$ ,  $\|f_n^{(z)}\| = 1$  and  $(f_n^{(z)}, f_m^{(z)}) = 0$  as  $n \neq m$ .

One can see that

$$\int f_n^{(z)}(p) dp = 0, \quad n = 1, 2, 3, \dots$$

i.e.  $f_n^{(z)} \in D(h_0)$ . Note that

$$\|(h_\varepsilon - zI)f_n^{(z)}\|^2 = \int_{G_n(z)} \frac{1}{V_n(z)} |(p^2 - z)|^2 dp = \frac{2}{V_n} \int_{\sqrt{z+\frac{1}{n+1}}}^{\sqrt{z+\frac{1}{n}}} (p^2 - z)^2 dp$$

or

$$\|(h_\varepsilon - zI)f_n^{(z)}\|^2 = \frac{2}{V_n} \int_{\sqrt{z+\frac{1}{n+1}}}^{\sqrt{z+\frac{1}{n}}} (p^2 - z)^2 dp. \tag{9}$$

Since

$$|p| < \sqrt{z} + \frac{1}{n}, \quad p^2 - z < \frac{1}{n} \left( 2\sqrt{z} + \frac{1}{n} \right).$$

This gives

$$(p^2 - z)^2 < \left( 2\sqrt{z} + \frac{1}{n} \right)^2 \frac{1}{n^2}.$$

Hence, by (9), we have

$$\|(h_\varepsilon - zI)f_n^{(z)}\|^2 < \left( 2\sqrt{z} + \frac{1}{n} \right)^2 \frac{1}{n^2}.$$

This shows that

$$\lim_{n \rightarrow \infty} \|(h_\varepsilon - zI)f_n^{(z)}\| = 0.$$

This means that if  $z \geq 0$ , then  $z \in \sigma_{ess}(h_\varepsilon)$ , therefore  $[0; \infty) \subset \sigma_{ess}(h_\varepsilon)$ . In order to show the reverse inclusion  $\sigma_{ess}(h_\varepsilon) \subset [0; \infty)$ , we construct the resolvent operator of  $h_\varepsilon$ .

Let

$$(h_\varepsilon - zI)g = \psi.$$

Then

$$(p^2 - z)g(p) - c = \psi(p).$$

If  $z < 0$  then  $p^2 - z \neq 0$ . Hence,

$$g(p) = \frac{\psi(p)}{p^2 - z} + \frac{c}{p^2 - z}. \tag{10}$$

Since  $g \in D(h_\varepsilon)$ , it represents as

$$g(p) = f(p) + \frac{c}{p^2 + 1} + \frac{(\varepsilon - 2)c}{(p^2 + 1)^2} \tag{11}$$

for some  $f \in D(h_\varepsilon)$ . Comparing (10) and (11), we obtain the equation for  $c$ :

$$f(p) + \left( \frac{1}{p^2 + 1} - \frac{1}{p^2 - z} \right) c + \frac{(\varepsilon - 2)c}{(p^2 + 1)^2} = \frac{\psi(p)}{p^2 - z} \tag{12}$$

where  $f \in D(h_0)$ . Integrating both sides of (12), taking into account (5) and the identities

$$\int \frac{dp}{p^2 - z} dp = \frac{\pi}{\sqrt{-z}}, \quad z < 0 \tag{13}$$

and

$$\int \frac{dp}{(p^2 + 1)^2} = \frac{\pi}{2}, \tag{14}$$

we have

$$(\varepsilon\sqrt{-z} - 2)\pi c = 2\sqrt{-z} \int \frac{\psi(p)}{p^2 - z} dp$$

or

$$c = \frac{2\sqrt{-z}}{\pi(\varepsilon\sqrt{-z} - 2)} \int \frac{\psi(p)}{p^2 - z} dp.$$

This gives one

$$g(p) = \frac{\psi(p)}{p^2 - z} + \frac{2\sqrt{-z}}{\pi(\varepsilon\sqrt{-z} - 2)} \cdot \frac{1}{p^2 - z} \int \frac{\psi(q)}{q^2 - z} dq.$$

This, if  $z \in \Pi_0$  and  $\varepsilon\sqrt{-z} - 2 \neq 0$  then the resolvent of the operator  $h_\varepsilon$  acts in  $L_2(\mathbb{R})$  as

$$(R_z(h_\varepsilon)g)(p) = \frac{g(p)}{p^2 - z} + \frac{2\sqrt{-z}}{\pi(\varepsilon\sqrt{-z} - 2)} \cdot \frac{1}{p^2 - z} \int \frac{g(q)}{q^2 - z} dq.$$

This shows that the resolvent of the operator  $h_\varepsilon$  is a bounded operator for  $\varepsilon\sqrt{-z} - 2 \neq 0$  and  $z < 0$ . It means that  $\sigma_{ess}(h_\varepsilon) \subset [0; \infty)$ . It follows directly from here that  $\sigma_{ess}(h_\varepsilon) = [0; \infty)$ . Now, we consider an eigenvalue problem for  $h_\varepsilon$ . From equation  $(h_\varepsilon - zI)g(p) = 0$ , we obtain that if  $\varepsilon \leq 0$  and  $z \in \Pi_0$ , then  $\varepsilon\sqrt{-z} - 2 \neq 0$ . By (12) the resolvent of the operator  $h_\varepsilon$  is defined on  $D(h_\varepsilon)$ . Hence,  $h_\varepsilon$  has no any negative eigenvalue.

Let  $\varepsilon > 0$ . Then from the equality  $\varepsilon\sqrt{-z} - 2 = 0$ , we have  $z = -\frac{4}{\varepsilon^2}$ . The equation

$$(h_\varepsilon - zI)g(p) = 0$$

gives one

$$g(p) = \frac{c}{p^2 - z}. \tag{15}$$

We show that  $g \in D(h_\varepsilon)$ . To obtain this,  $g$  should be represented in the form (11) for some  $f \in D(h_0)$ . Assume that  $g$  is represented as (11). Comparing (11) with (15), we obtain

$$f(p) + \frac{c}{p^2 + 1} + \frac{(\varepsilon - 2)c}{(p^2 + 1)^2} = \frac{c}{p^2 - z},$$

i.e.

$$f(p) = \frac{c(1 - \frac{4}{\varepsilon^2})}{(p^2 + \frac{4}{\varepsilon^2})(p^2 + 1)} - \frac{c(\varepsilon - 2)}{(p^2 + 1)^2}.$$

Taking into account the identities (13) and (14), one can see that  $\int f(p)dp = 0$ . This gives one that  $f \in D(h_0)$ .

Theorem 3.1 is proved.  $\square$

## References

- [1] Berezin F. A., Faddeev L. D. Remark on the Schrödinger equation with singular potential. *Dokl. Akad. Nauk SSSR*, 1961, **137**(5), P. 1011–1014.
- [2] Minlos R. A., Faddeev L. D. Comment on the problem of three particles with point interactions. *Dokl. Akad. Nauk SSSR*, 1961, **141**(6), P. 1335–1338.
- [3] Minlos R. A., Faddeev L. D. Point interaction for a three-particle system in quantum. *Dokl. Akad. Nauk SSSR*, 1962, **14**(1), P. 1315–1316.
- [4] Minlos R. A., Shermatov M. Kh. On point-like interactions of three quantum particles. *Vestnik Moskov Univ. Ser.I Mat. Mekh*, 1989, **6**(1), P. 7–14.
- [5] Melnikov A. M., Minlos R. A. Point interaction of three different particles. *Advances in Soviet Mathematics*, 1991, **6**(1), P. 99–122.
- [6] Akhiezer N. I., Glazman I. M. *Theory of Linear Operators in Hilbert Space*. Publishing Paperback - December 16, USA.: 1993. 377 p.
- [7] Muminov Z. E., Kuljanov U. N., Lakaev SH. S. On the Spectrum of the Two-particle Shrodinger Operator with Point Interaction. *Lobachevskii Journal of Mathematics*, 2021, **42**(3), P. 598–605.
- [8] Fassari S., Rinaldi F. On the Spectrum of the Schrodinger Hamiltonian of the One-Dimensional Harmonic Oscillator Perturbed by Two Identical Attractive Point Interactions. *Rep. Math. Phys.*, 2012, **69**(1), P. 353–370.
- [9] Fassari S., Rinaldi F. On the spectrum of the Schrödinger Hamiltonian with a particular configuration of three one-dimensional point interactions. *Rep. Math. Phys.*, 2009, **64**(3), P. 367–393.
- [10] Albeverio S., Fassari S., Rinaldi F. The discrete spectrum of the spinless one-dimensional Salpeter Hamiltonian perturbed by  $\delta$ -interactions. *J. Phys. A.*, 2015, **48**(3), P. 185–201.
- [11] Albeverio S., Fassari S., Rinaldi F. The Hamiltonian of the harmonic oscillator with an attractive  $\delta'$ - interaction centred at the origin as approximated by the one with a triple of attractive  $\delta$ - interactions. *J. Phys. A.*, 2016, **49**(2), P. 667–688.
- [12] Imomov A.A., Bozorov I.N., Hurrarov A.M., On the number of eigenvalues of a model operator on a one-dimensional lattice. *Vestn. Tomsk. Gos. Univ. Mat. Mekh.*, 2022, **78**, P. 22–37.
- [13] Muminov M.I., Khurramov A.M., Bozorov I.N. On eigenvalues and virtual levels of a two-particle Hamiltonian on a  $d$ -dimensional lattice. *Nanosystems: Phys. Chem. Math.*, 2023, **14**(3), P. 237–244.
- [14] Muminov M.I., Khurramov A.M., Bozorov I.N. Conditions for the existence of bound states of a two-particle Hamiltonian on a three-dimensional lattice. *Nanosystems: Phys. Chem. Math.*, 2022, **13**(3), P. 295–303.
- [15] Bozorov I.N., Khamidov Sh.I., Lakaev S.N. The number and location of eigenvalues of the two particle discrete Schrödinger operators. *Lobachevskii Journal of Mathematics*, 2022, **43**(11), P. 3079–3090.

---

*Submitted 19 August 2022; revised 18 September 2023; accepted 19 September 2023*

*Information about the authors:*

*Utkir Nematovich Kuljanov* – Samarkand State University, 140104, University boulevard. 15, Samarkand, Uzbekistan;  
 Samarkand branch of Tashkent State University of Economics, Professorlar street 51, Samarkand, Uzbekistan;  
 ORCID 0009-0003-4286-4704; uquljonov@bk.ru

## Boundary value problem for a degenerate equation with a Riemann–Liouville operator

Bakhrom Yu. Irgashev<sup>1,2</sup>

<sup>1</sup>Namangan Engineering Construction Institute, Namangan, Uzbekistan

<sup>2</sup>Institute of Mathematics named after V. I. Romanovsky of the Academy of Sciences of the Republic of Uzbekistan, Uzbekistan

bahromirgasev@gmail.com

**ABSTRACT** In the article, the uniqueness and solvability of one boundary value problem for a high-order equation with two lines of degeneracy with a fractional Riemann–Liouville derivative in a rectangular domain is studied by the Fourier method. Sufficient conditions for the well-posedness of the problem posed are obtained.

**KEYWORDS** high order equation, initial-boundary value problem, fractional derivative in the sense of Riemann–Liouville, eigenvalue, eigenfunction, Kilbas–Saigo function, series, convergence, existence, uniqueness

**FOR CITATION** Irgashev B.Yu. Boundary value problem for a degenerate equation with a Riemann–Liouville operator. *Nanosystems: Phys. Chem. Math.*, 2023, **14** (5), 511–517.

### 1. Introduction and problem statement

Fractional partial differential equations underlie the mathematical modeling of various physical processes and environmental phenomena that demonstrate a fractal nature [1, 2]. Model equations with fractional derivatives with constant coefficients are well studied. Recently, specialists have intensively studied equations with variable coefficients. Degenerate equations are among such equations. The number of works on degenerate equations with fractional derivatives is relatively small. Many of these papers deal with ordinary differential equations. In work [2] the following equation was considered:

$$D_{0x}^{\alpha} t^{\beta} u(t) = \lambda u(x), \quad 0 < x < b,$$

where  $0 < \alpha < 1$ ,  $\lambda$  is the spectral parameter,  $\beta = \text{const} \geq 0$ . In the same work, it was noted that the equation

$$D_{0x}^{\alpha} t^{\beta} u(t) + \sum_{j=1}^n a_j(x) D_{0x}^{\alpha_j} u(t) + b(x) u = c(x), \quad 0 \neq \alpha_j < \alpha,$$

plays an important role in the theory of inverse problems for degenerate equations of hyperbolic type. In article [3], the following problem was investigated for solvability

$$\begin{cases} \partial_0^{\nu} (k(t) y(t)) + c(y(t)) = f(t), \\ k(0) y(0) = 0. \end{cases}$$

Here  $\partial_0^{\nu}$  is the fractional differentiation operator in the Caputo sense,  $0 < \nu < 1$ ,  $k(t) \in C^1[0, T]$ ,  $k(t) \geq 0$ , for  $t \in [0, T]$ ,  $c(\eta) \in C(\mathbb{R})$ ,  $c(0) = 0$ . In paper [4], solutions in the closed form to the fractional order equations were found

$$(D_{0+}^{\alpha} y)(x) = ax^{\beta} y(x) + f(x) \quad (0 < x < d \leq \infty, \alpha > 0, \beta \in \mathbb{R}, a \neq 0),$$

$$(D_{-}^{\alpha} y)(x) = ax^{\beta} y(x) + f(x) \quad (0 \leq d < x < \infty, \alpha > 0, \beta \in \mathbb{R}, a \neq 0),$$

with the fractional Riemann–Liouville derivatives on the semiaxis  $(0, \infty)$  [5]:

$$(D_{0+}^{\alpha} y)(x) = \left(\frac{d}{dx}\right)^{[\alpha]+1} \frac{1}{\Gamma(1-\{\alpha\})} \int_0^x \frac{y(t) dt}{(x-t)^{\{\alpha\}}}, \quad (x > 0; \alpha > 0),$$

$$(D_{-}^{\alpha} y)(x) = \left(-\frac{d}{dx}\right)^{[\alpha]+1} \frac{1}{\Gamma(1-\{\alpha\})} \int_x^{\infty} \frac{y(t) dt}{(t-x)^{\{\alpha\}}}, \quad (x > 0; \alpha > 0),$$

( $[\alpha]$  and  $\{\alpha\}$  mean the integer and fractional parts of the real number  $\alpha$ , respectively). Applied problems lead to such equations [6]. One can find an example of such equation in the theory of polarography [7]:

$$(D_{0+}^{1/2} y)(x) = ax^{\beta} y(x) + x^{-1/2}, \quad (0 < x, -1/2 < \beta \leq 0),$$

which arises for  $a = -1$  from diffusion problems [7]. As for the degenerate partial differential equations involving fractional derivatives, it should be noted that the researches in this area are quite new. We mention here papers [8–15], in which various boundary value problems for degenerate equations involving fractional derivatives were studied.

It should also be noted that fractional-order integro-differential operators have been recently actively used in nanosystem studies. We note in this field, for example, works [16–18].

In this paper, we study a boundary value problem in a rectangular domain for an equation of high even order involving a fractional derivative, which has degeneracy in both variables.

In the region  $\Omega = \Omega_x \times \Omega_y$ ,  $\Omega_x = \{x : 0 < x < 1\}$ ,  $\Omega_y = \{y : 0 < y < 1\}$ , let us consider the equation

$$D_{0x}^\alpha u(x, y) + x^\beta K(y) l(u(x, y)) = 0, \tag{1}$$

where

$$l(u(x, y)) = (-1)^s \frac{\partial^{2s} u(x, y)}{\partial y^{2s}} + \frac{\partial^{s-1}}{\partial y^{s-1}} \left( (-1)^{s-1} p_{s-1}(y) \frac{\partial^{s-1} u(x, y)}{\partial y^{s-1}} \right) + \dots + \frac{\partial}{\partial y} \left( -p_1(y) \frac{\partial u(x, y)}{\partial y} \right) + p_0(y) u(x, y),$$

$$p_j(y) \in C^j(\bar{\Omega}_y), \quad j = 0, 1, \dots, s-1, \quad s \in \mathbb{N},$$

$K(y) \in C[0; 1]$ ;  $K(y) \in C^{(2s)}$  for  $y \in (0, 1]$ ;

$$K(y) > 0, \quad y \in (0, 1], \quad K(0) = 0, \quad K^{(i)}(y) = O(y^{m-i}), \quad y \rightarrow +0, \quad 0 \leq m < s, \quad i = 0, 1, \dots, 2s,$$

$0 < \alpha < 1, -\alpha < \beta \in \mathbb{R}$ ,  $D_{0x}^\alpha$  is the Riemann–Liouville fractional differentiation operator of order  $\alpha$

$$D_{0x}^\alpha u(x, y) = \frac{1}{\Gamma(1-\alpha)} \frac{\partial}{\partial x} \int_0^x \frac{u(\tau, y) d\tau}{(x-\tau)^\alpha}.$$

Let us consider the following problem for equation (1).

**Problem A.** Find a solution to equation (1) belonging to the class

$$D_{0x}^\alpha u(x, y) \in C(\Omega), \quad x^{1-\alpha} u(x, y) \in C(\bar{\Omega}),$$

$$\frac{\partial^{2s-1} u(x, y)}{\partial y^{2s-1}} \in C(\Omega_x \times \bar{\Omega}_y), \quad \frac{\partial^{2s} u(x, y)}{\partial y^{2k}} \in C(\Omega_x \times \Omega_y),$$

satisfying the conditions

$$\frac{\partial^j u(x, 0)}{\partial y^j} = \frac{\partial^j u(x, 1)}{\partial y^j} = 0, \quad 0 < x \leq 1, \quad j = 0, 1, \dots, s-1, \tag{2}$$

$$\lim_{x \rightarrow 0} x^{1-\alpha} u(x, y) = \frac{\varphi(y)}{\Gamma(\alpha)}, \tag{3}$$

where  $\varphi(y) \in C^{(2s)}$ ,  $y \in [0, 1]$ .

## 2. Searching a solution

We are looking for a solution in the form

$$u(x, y) = X(x) Y(y).$$

Then, with respect to the variable  $y$ , taking into account condition (2), we obtain the following spectral problem:

$$\begin{cases} l(Y(y)) = \lambda \frac{Y(y)}{K(y)}, \\ Y^{(j)}(0) = Y^{(j)}(1) = 0, \quad j = 0, 1, \dots, s-1. \end{cases} \tag{4}$$

We reduce problem (4) to an integral equation using Green’s function and obtain the necessary estimates for the eigenfunctions. Further, we will assume that  $\lambda > 0$ , this condition is valid, for example, in the case when  $0 \leq p_j(y)$ ,  $j = 0, 1, \dots, s-1$ . This implies the existence of continuous symmetric Green’s function, which will be denoted by  $G(y, \xi)$ . Taking into account the boundary conditions at the point  $y = 0$  and applying the Lagrange theorem on finite increments (the mean-value theorem (for derivatives)), we have

$$Y(y) = O(y^s), \quad y \rightarrow +0.$$

This relation is also valid for Green’s function. It remains to show the existence of eigenvalues and eigenfunctions of problem (4). The integral equation equivalent to the problem (4) has the following form

$$Y(y) = \lambda \int_0^1 \frac{G(y, \xi) Y(\xi) d\xi}{K(\xi)}, \tag{5}$$

we rewrite (5) in the form

$$\frac{Y(y)}{\sqrt{K(y)}} = \lambda \int_0^1 \frac{G(y, \xi)}{\sqrt{K(\xi)}\sqrt{K(y)}} \frac{Y(\xi)}{\sqrt{K(\xi)}} d\xi.$$

Let us introduce the notation

$$\bar{Y}(y) = \frac{Y(y)}{\sqrt{K(y)}}, \quad \bar{G}(y, \xi) = \frac{G(y, \xi)}{\sqrt{K(\xi)}\sqrt{K(y)}}.$$

From this, we have

$$\bar{Y}(y) = \lambda \int_0^1 \bar{G}(y, \xi) \bar{Y}(\xi) d\xi. \quad (6)$$

Relation (6) is an integral equation with symmetric and continuous, in both variables, kernel. According to the theory of equations with symmetric kernels, equation (6) has at most a countable number of eigenvalues and eigenfunctions. Thus, problem (4) has eigenvalues  $\lambda_n > 0$ ,  $n = 1, 2, \dots$ , and the corresponding eigenfunctions are  $Y_n(y)$ . Let's order the eigenvalues increasingly:  $0 < \lambda_1 \leq \lambda_2 \leq \dots$ . Further, we assume that

$$\|Y_n(y)\|^2 = \int_0^1 \frac{Y_n^2(y) dy}{K(y)} = 1.$$

From here, using (5), we come to the Bessel inequality

$$\sum_{n=1}^{\infty} \left( \frac{Y_n(y)}{\lambda_n} \right)^2 \leq \int_0^1 \frac{G^2(y, \xi) d\xi}{K(\xi)} < \infty. \quad (7)$$

Let us find the conditions ensuring that given function is expanded into a Fourier series in terms of the system of eigenfunctions of problem (4). The following theorem holds.

**Theorem 1.** If the function  $\varphi(y)$  satisfies the following conditions:

- 1).  $\varphi^{(j)}(0) = \varphi^{(j)}(1) = 0$ ,  $j = \bar{0}, s-1$ ;
- 2).  $\varphi^{(2s)}(y)$  is continuous on  $[0, 1]$ ,

then it can be expanded in terms of the eigenfunctions of the problem (4), which converges uniformly and absolutely.

**Proof.** Let  $l(\varphi(y)) = g(y)$ , then

$$\varphi(y) = \int_0^1 G(y, \xi) g(\xi) d\xi.$$

Correspondingly,

$$\frac{\varphi(y)}{\sqrt{K(y)}} = \int_0^1 \frac{G(y, \xi)}{\sqrt{K(y)}\sqrt{K(\xi)}} \sqrt{K(\xi)} g(\xi) d\xi,$$

or

$$\frac{\varphi(y)}{\sqrt{K(y)}} = \int_0^1 \bar{G}(y, \xi) \sqrt{K(\xi)} g(\xi) d\xi.$$

Let us use the Hilbert-Schmidt theorem, then one has

$$\frac{\varphi(y)}{\sqrt{K(y)}} = \sum_{n=1}^{\infty} c_n \frac{Y_n(y)}{\sqrt{K(y)}},$$

where

$$c_n = \int_0^1 \frac{\varphi(y) Y_n(y)}{K(y)} dy.$$

Further, after reduction by  $\frac{1}{\sqrt{K(y)}}$ , we obtain

$$\varphi(y) = \sum_{n=1}^{\infty} c_n Y_n(y).$$

Theorem 1 is proved.

Let us fix  $n$  and start solving the problem of searching the function  $X_n(x)$ . We assume that the initial function  $\varphi(y)$  satisfies the conditions of Theorem 1. Taking into account condition (3), we obtain the following initial problem:

$$\begin{cases} D_{0x}^\alpha X_n(x) = -\lambda_n x^\beta X_n(x), \\ \lim_{x \rightarrow 0} x^{1-\alpha} X_n(x) = \frac{\varphi_n}{\Gamma(\alpha)}, \end{cases} \tag{8}$$

where

$$\varphi_n = \int_0^1 \frac{\varphi(y) Y_n(y) dy}{K(y)}, \quad n = 1, 2, \dots$$

Using the results of [14], the solution to problem (8) is written as

$$X_n(x) = \frac{x^{\alpha-1}}{\Gamma(\alpha)} \varphi_n E_{\alpha, 1+\frac{\beta}{\alpha}, 1+\frac{\beta-1}{\alpha}}(-\lambda_n x^{\alpha+\beta}),$$

where

$$E_{\alpha, m, l}(z) = \sum_{i=0}^{\infty} c_i z^i, \quad c_0 = 1, \quad c_i = \prod_{j=0}^{i-1} \frac{\Gamma(\alpha(jm+l)+1)}{\Gamma(\alpha(jm+l+1)+1)}, \quad i \geq 1$$

is the Kilbas–Saigo function [14].

It follows from the results of [16] that the following estimate holds:

$$|X_n(x)| \leq M x^{\alpha-1} |\varphi_n|, \quad 0 < M = \text{const}. \tag{9}$$

Now, we will seek the solution of the problem in the form

$$u(x, y) = \sum_{n=1}^{\infty} X_n(x) Y_n(y). \tag{10}$$

Let us find the conditions under which (10) is a regular solution to Problem A. The following theorem is true.

**Theorem 2.** Let the function  $\varphi(y)$ , satisfy the following conditions:

- 1).  $\varphi(y) \in C^{2s}[0, 1]$ ,  $\varphi^{(j)}(0) = \varphi^{(j)}(1) = 0, j = 0, 1, \dots, s-1$ ,
  - 2).  $(K(y)l(\varphi(y)))^{(j)}(0) = (K(y)l(\varphi(y)))^{(j)}(1) = 0, K(y)l(\varphi(y)) \in C^{2s}[0, 1], j = 0, 1, \dots, s-1$ ,
- then a solution to problem A exists.

**Proof.** Series (10) formally satisfies equation (1). Let us show that one can differentiate the series. Considering (9), we have

$$|x^{1-\alpha} u(x, y)| \leq M \sum_{n=1}^{\infty} |\varphi_n| |Y_n(y)|.$$

Using the Cauchy–Bunyakovsky inequality, one obtains

$$\sum_{n=1}^{\infty} |\varphi_n| |Y_n(y)| \leq \sqrt{\sum_{n=1}^{\infty} \left(\frac{Y_n(y)}{\lambda_n}\right)^2} \sqrt{\sum_{n=1}^{\infty} (\lambda_n \varphi_n)^2}.$$

The convergence of the first factor in the last inequality follows from (7). Consider the second multiplier. We have

$$\varphi_n = \int_0^1 \frac{\varphi(y) Y_n(y) dy}{K(y)} = \frac{1}{\lambda_n} \int_0^1 \varphi(y) l(Y_n(y)) dy.$$

Integrating by parts, we obtain

$$\varphi_n = \frac{1}{\lambda_n} \int_0^1 l(\varphi(y)) Y_n(y) dy. \tag{11}$$

Hence,

$$\lambda_n \varphi_n = \int_0^1 K(y) l(\varphi) \frac{Y_n(y)}{K(y)} dy.$$

Consequently,  $\lambda_n \varphi_n$  are the Fourier coefficients of the function  $K(y)l(\varphi)$ . Then, from the Bessel inequality, one obtains

$$\sum_{n=1}^{\infty} \lambda_n^2 |\varphi_n|^2 \leq \int_0^1 K(y) \{l(\varphi)\}^2 dy < \infty. \tag{12}$$

From (7) and (12), the convergence of the series (10) and the fulfillment of condition (3) follows. Let us pass to the derivatives. In view of equation (8), we formally have

$$\begin{aligned}
 |D_{0x}^\alpha u(x, y)| &\leq \sum_{n=1}^\infty |D_{0x}^\alpha X_n(x)| |Y_n(y)| \leq Mx^{\alpha+\beta-1} \sum_{n=1}^\infty |\lambda_n \varphi_n| |Y_n(y)| \leq \\
 &\leq Mx^{\alpha+\beta-1} \sqrt{\sum_{n=1}^\infty (\lambda_n^2 \varphi_n)^2} \sqrt{\sum_{n=1}^\infty \left(\frac{Y_n(y)}{\lambda_n}\right)^2}, \quad x > 0.
 \end{aligned}
 \tag{13}$$

Further, keeping in mind (11), one has

$$\varphi_n = \left(\frac{1}{\lambda_n}\right)^2 \int_0^1 K(y) l(\varphi(y)) l(Y_n(y)) dy = \left(\frac{1}{\lambda_n}\right)^2 \int_0^1 l(K(y) l(\varphi(y))) Y_n(y) dy.$$

Now, we apply the Bessel inequality

$$\sum_{n=1}^\infty (\lambda_n^2 \varphi_n)^2 \leq \int_0^1 K(y) \{l(K(y) l(\varphi(y)))\}^2 dy < \infty.
 \tag{14}$$

The convergence (13) follows from (7) and (14). So the following functional series

$$D_{0x}^\alpha u(x, y) = \sum_{n=1}^\infty D_{0x}^\alpha X_n(x) Y_n(y),$$

converges evenly. Uniform convergence of the next series,

$$l(u(x, y)) = \sum_{n=1}^\infty X_n(x) l(Y_n(y)) = \frac{1}{K(y)} \sum_{n=1}^\infty \lambda_n X_n(x) Y_n(y),$$

is shown by the same way.

Theorem 2 is proved.

### 3. Uniqueness of the solution

Let us proceed to the proof of the uniqueness of the solution. The following theorem holds.

**Theorem 3.** If there is a solution to Problem A, then it is unique.

**Proof.** Let the function  $u(x, y)$  be a solution to Problem A with zero initial and boundary conditions. Consider its Fourier coefficients in terms of the system of eigenfunctions of problem (4):

$$u_n(x) = \int_0^1 \frac{u(x, y) Y_n(y) dy}{K(y)}, \quad n = 1, 2, \dots$$

It is rather simple to show that  $u_n(x)$  is a solution to the problem

$$\begin{cases} D_{0x}^\alpha u_n(x) = -\lambda_n x^\beta u_n(x), \\ \lim_{x \rightarrow 0} x^{1-\alpha} u_n(x) = 0. \end{cases}$$

This problem has a trivial solution only [14], i.e.,

$$\int_0^1 \frac{u(x, y) Y_n(y) dy}{K(y)} = 0, \quad n = 1, 2, \dots$$

Because  $\bar{G}(y, \xi)$  is symmetric continuous function and the following integrals converge:

$$\int_0^1 \bar{G}^2(y, \xi) d\xi < \infty, \quad \int_0^1 \bar{G}^2(y, \xi) dy < \infty, \quad \int_0^1 \int_0^1 \bar{G}^2(y, \xi) dy d\xi < \infty, \quad \lambda_n > 0, \quad \forall n,$$

it follows from Mercer’s theorem that

$$\bar{G}(y, \xi) = \sum_{n=1}^\infty \frac{\bar{Y}_n(y) \bar{Y}_n(\xi)}{\lambda_n}.$$

Then, we have

$$\frac{u(x, y)}{\sqrt{K(y)}} = \int_0^1 \bar{G}(y, \xi) \left(\sqrt{K(\xi)} l(u(x, \xi))\right) d\xi =$$

$$\int_0^1 \sum_{n=1}^{\infty} \frac{\overline{Y}_n(y) \overline{Y}_n(\xi)}{\lambda_n} \left( \sqrt{K(\xi)} l(u(x, \xi)) \right) d\xi =$$

$$\sum_{n=1}^{\infty} \frac{Y_n(y)}{\lambda_n \sqrt{K(y)}} \int_0^1 \frac{Y_n(\xi) \sqrt{K(\xi)}}{\sqrt{K(\xi)}} l(u(x, \xi)) d\xi.$$

Since the series converges uniformly, the integrating and the summation can be rearranged. Correspondingly, the last expression transforms to the following one

$$\sum_{n=1}^{\infty} \frac{Y_n(y)}{\lambda_n \sqrt{K(y)}} \int_0^1 Y_n(\xi) l(u(x, \xi)) d\xi =$$

$$\sum_{n=1}^{\infty} \frac{Y_n(y)}{\lambda_n \sqrt{K(y)}} \int_0^1 l(Y_n(\xi)) u(x, \xi) d\xi =$$

$$\sum_{n=1}^{\infty} \frac{Y_n(y)}{\sqrt{K(y)}} \int_0^1 \frac{Y_n(\xi) u(x, \xi)}{K(\xi)} d\xi = 0.$$

Hence,

$$u(x, y) \equiv 0.$$

Theorem 3 is proved.

#### 4. Conclusion

In this paper, we study the initial boundary value problem for a high-order equation involving fractional derivative in the sense of Riemann–Liouville. The equation has two lines of degeneration  $x = 0$  and  $y = 0$ . The solution is constructed as a series in terms of eigenfunctions of the one-dimensional spectral problem. Sufficient conditions for the expansion of this function in terms of the system of eigenfunctions of the spectral problem were found. The convergence theorems for the series and the uniqueness of the constructed solution of the problem were proved. In this case, various theorems from the theory of differential and integral equations were used. In the future, one can study boundary value problems for inhomogeneous equations, inverse problems with unknown right hand side, problems with nonlocal conditions that have various applications in nanosystems (see [18]). Note that the studied problem has not only theoretical but also applied importance since fractional integro-differential operators are widely used in mathematical models of nanosystem dynamics. In particular, among the mathematical models of transport-diffusion transfer, fractional differential calculus is singled out as a tool for describing transfer processes in complex-structured media [20].

It was noted in [21], that fractional differential equations are convenient for the analysis of frequency characteristics of semiconductor devices in which dispersive transport occurs, because their Fourier transforms give rise to algebraic equations that are much simpler to solve than integral equations derived from equations with variable diffusion coefficient and mobility.

A number of experimental facts testify to the anomalous diffusion of impurities and defects in various materials (see the literature review on this topic in [22]). Equations containing fractional derivatives form the mathematical basis of anomalous self-similarity diffusion [23].

#### References

- [1] Bogolyubov A.N., Koblikov A.A., Smirnova D.D. and Shapkina N.E. Mathematical modelling of media with time dispersion using fractional derivatives. *Matem. Mod.*, 2013, **25**(12), P. 50–64.
- [2] Nakhushiev A.M. *Fractional Calculus and Its Application*. Fizmatlit, Moscow, 2003 [in Russian].
- [3] Artyushin A.N. Fractional integral inequalities and their applications to degenerate differential equations with the Caputo fractional derivative. *Siberian Mathematical Journal*, 2020, **62**(2), P. 208–221.
- [4] Kilbas A.A., Saigo Megumi. Solution in closed form of a class of linear differential equations of fractional order. *Different. Equat.*, 1997, **33**(2), P. 194–204.
- [5] Samko S.G., Kilbas A.A., Marichev O.I. *Fractional integrals and derivatives and some of their applications*. Minsk, Science and technology, 1987, p. 688 [in Russian].
- [6] Oldham, K.B., Spanier, J. *The Fractional Calculus*. Academic Press, New York, London, 1974.
- [7] Wiener K. On solutions of a differential equation of nonintegral order that occurs in the theory of polarography, *Wiss. Z. Martin-Luther-Univ. Halle-Wittenberg Math.-Natur. Reihe*, 1983, **32**(1), P. 41–46 (in German).
- [8] Karimov E., Ruzhansky M., Toshemirov B. Solvability of the boundary-value problem for a mixed equation involving hyper-Bessel fractional differential operator and bi-ordinal Hilfer fractional derivative. *Mathematical Methods in the Applied Sciences*, 2023, **41**(1), P.54–77.
- [9] Ruzhansky M., Torebek B. T., Turmetov B. Well-posedness of Tricomi-Gellerstedt-Keldysh-type fractional elliptic problems. *Journal of Integral Equations and Applications*. 2022, **34**(3), P. 373–387.
- [10] Smadiyeva A.G. Degenerate time-fractional diffusion equation with initial and initial-boundary conditions. *Georgian Mathematical Journal*, 2023, **30**(3), P.435–443.

- [11] Smadiyeva A.G. Well-posedness of the initial-boundary value problems for the time-fractional degenerate diffusion equations. Bulletin of the Karaganda University. *Mathematics series*, 2022, **107**(3), P.145–151.
- [12] Urinov A.K., Usmonov D.A. Non-local initial-boundary value problem for a degenerate fourth-order equation with a fractional Gerasimov-Caputo derivative. *Vestnik KRAUNC. Fiz.-mat. nauki*. 2023, **42**(1), P. 123–139.
- [13] Irgashev B.Yu. A boundary value problem with conjugation conditions for a degenerate equation with the Caputo fractional derivative. *Russian Mathematics*, 2022, **66**(4), P. 24–31.
- [14] Kilbas Anatoly A., Srivastava Hari M., Trujillo Juan J. *Theory and applications of fractional differential equations*. North-Holland Mathematics Studies, 204. Elsevier Science B.V., Amsterdam, 2006.
- [15] Irgashev B.Y. Initial-boundary problem for degenerate high order equation with fractional derivative. *Indian J. Pure Appl. Math.*, 2022, **53**, P. 170–180.
- [16] Hilfer R. (Ed.). *Applications of fractional calculus in physics* / World Scientific Publishing Co, Singapore. 1999.
- [17] Baleanu D., Guevenc Z.B., Machado J.A.T. (Eds.). *New Trends in Nanotechnology and Fractional Calculus Applications*. Springer, Berlin, 2010.
- [18] Baltaeva U., Alikulov Y., Baltaeva I.I., Ashirova A. Analog of the Darboux problem for a loaded integro-differential equation involving the Caputo fractional derivative. *Nanosystems: Phys. Chem. Math.* 2021, **12**(4), P. 418–424.
- [19] Lotfi Boudabsa, Thomas Simon. Some Properties of the Kilbas-Saigo Function. *Mathematics*, 217(9), 2021, P. 1–24.
- [20] Zvonarev S.V., Kortov V.S., Shtang T.V. *Modeling the structure and properties of nanosystems*. Educational methodical manual. Yekaterinburg, Publishing House of the Ural University, 2014, p. 120 (in Russian).
- [21] Sibatov R.T., Uchaikin V.V. Fractional differential approach to dispersive transport in semiconductors. *Physics-Uspexhi*, 2009, **52**(10), P. 1019–1043.
- [22] Sibatov R.T., Svetukhin V.V. Subdiffusion kinetics of nanoprecipitate growth and destruction in solid solutions. *Theor. Math. Phys.*, 2015, **183**, P. 846–859.
- [23] Uchaikin V.V., Sibatov R.T. *Fractional Kinetics in Solids: Anomalous Charge Transport in Semiconductors, Dielectrics and Nanosystems*. CRC Press, Boca Raton, FL, 2013.

---

*Submitted 21 June 2023; revised 8 September 2023; accepted 9 September 2023*

*Information about the authors:*

*Bakhrom Yu. Irgashev* – Namangan Engineering Construction Institute, Namangan, Uzbekistan; Institute of Mathematics named after V.I.Romanovsky of the Academy of Sciences of the Republic of Uzbekistan, Uzbekistan; ORCID 0000-0001-7204-9127; bahromirgasev@gmail.com

## On the discrete spectrum of the Schrödinger operator using the 2+1 fermionic trimer on the lattice

Ahmad M. Khalkhuzhaev<sup>1</sup>, Islom A. Khujamiyrov<sup>2</sup>

<sup>1</sup>V. I. Romanovsky Institute of Mathematics of the Academy of Sciences of the Republic of Uzbekistan, Tashkent, Uzbekistan

<sup>2</sup>Samarkand State University, Samarkand, Uzbekistan

Corresponding author: Ahmad M. Khalkhuzhaev, [ahmad\\_x@mail.ru](mailto:ahmad_x@mail.ru)

PACS 02.30.Tb

**ABSTRACT** We consider the three-particle discrete Schrödinger operator  $H_{\mu,\gamma}(\mathbf{K})$ ,  $\mathbf{K} \in \mathbb{T}^3$ , associated with the three-particle Hamiltonian (two of them are fermions with mass 1 and one of them is arbitrary with mass  $m = 1/\gamma < 1$ ), interacting via pair of repulsive contact potentials  $\mu > 0$  on a three-dimensional lattice  $\mathbb{Z}^3$ . It is proved that there are critical values of mass ratios  $\gamma = \gamma_1$  and  $\gamma = \gamma_2$  such that if  $\gamma \in (0, \gamma_1)$ , then the operator  $H_{\mu,\gamma}(\mathbf{0})$  has no eigenvalues. If  $\gamma \in (\gamma_1, \gamma_2)$ , then the operator  $H_{\mu,\gamma}(\mathbf{0})$  has a unique eigenvalue; if  $\gamma > \gamma_2$ , then the operator  $H_{\mu,\gamma}(\mathbf{0})$  has three eigenvalues lying to the right of the essential spectrum for all sufficiently large values of the interaction energy  $\mu$ .

**KEYWORDS** Schrödinger operator, Hamiltonian, contact potential, fermion, eigenvalue, quasi-momentum, invariant subspace, Faddeev operator.

**ACKNOWLEDGEMENTS** We thank unknown referee for careful reading of the manuscript and useful comments.

**FOR CITATION** Khalkhuzhaev A.M., Khujamiyrov I.A. On the discrete spectrum of the Schrödinger operator using the 2+1 fermionic trimer on the lattice. *Nanosystems: Phys. Chem. Math.*, 2023, **14** (5), 518–529.

### 1. Introduction

The study of few-body systems with contact interaction has a long history and a wide literature throughout the last eight decades, a concise retrospective may be found in [1]. The 2+1 fermionic system is an actual building block for the heteronuclear mixtures with inter-species contact interaction, see [2] for an outlook. For the 2+1 fermionic model, the rigorous construction of the Hamiltonian  $H_\alpha$  for  $m > m^*$ , together with the precise determination of  $m^*$  and the proof of the self-adjointness and the semi-boundedness from below of  $H_\alpha$ , was done in the work [3] by Correggi, Dell’Antonio, Finco, Michelangeli, and Teta, by means of quadratic form techniques for contact interactions [4]. In [5] the authors had qualified the main features of the spectrum of the Hamiltonian of point interaction for a three-dimensional quantum system consisting of three point-like particles, two identical fermions, plus a third particle of different species, with two-body interaction of zero range. For arbitrary magnitude of the interaction and arbitrary value of the mass parameter (the ratio between the mass of the third particle and that of each fermion) above the stability threshold, the essential spectrum is identified, the discrete spectrum is localized and its finiteness is proved. The existence or absence of bound states is proved in physically relevant regimes of masses.

Throughout physics, stable composite objects are usually formed by way of attractive forces, which allow the constituents to lower their energy by binding together. Repulsive forces separate particles in free space. However, in structured environment such as a periodic potential and in the absence of dissipation, stable composite objects can exist even for repulsive interactions that arise from the lattice band structure [6]. The Bose–Hubbard model which is used to describe the repulsive pairs is the theoretical basis for applications. The work [6] exemplifies the important correspondence between the Bose–Hubbard model [7], [8] and atoms in optical lattices, and helps pave the way for many more interesting developments and applications [9]. Stable repulsively bound objects should be viewed as a general phenomenon and their existence will be ubiquitous in cold atoms lattice physics. They give rise also to new potential composites with fermions [10] or Bose–Fermi mixtures [11], and can be formed in an analogous manner with more than two particles [12].

Systems of particles, with zero-range interactions between the pairs of particles, are investigated not only theoretically but also experimentally. Delta-like character of the interaction turns out to be realistic. This is a special case of the *unitary regime*, i.e. the case of negligible interaction range and huge, virtually infinite, scattering length. In this case, unitary gases possess a property of superfluidity [13], and they were intensively studied both experimentally and theoretically [14].

In this paper, we consider the Hamiltonian  $H_{\mu,\gamma}$  for systems of three quantum particles (two of them are fermions with mass 1 and one of them is arbitrary with mass  $m = 1/\gamma < 1$ ) with paired contact repulsive potentials  $\mu > 0$  on a

three-dimensional lattice  $\mathbb{Z}^3$ . In the momentum representation, the total three-particle Hamiltonian expands into a direct operator integral (see. [15])

$$H_{\mu,\gamma} = \int_{\mathbb{T}^3} \oplus H_{\mu,\gamma}(\mathbf{K}) d\mathbf{K}.$$

The fiber operator  $H_{\mu,\gamma}(\mathbf{K}) = H_{0,\gamma}(\mathbf{K}) + \mu(V_1 + V_2)$  parametrically depends on the *total quasimomentum*  $\mathbf{K} \in \mathbb{T}^3 \equiv \mathbb{R}^3/(2\pi\mathbb{Z}^3)$ . It is shown that the essential spectrum of the self-adjoint operator  $H_{\mu,\gamma}(\mathbf{K})$  consists of one or two segments, depending on the three-particle quasimomentum  $\mathbf{K} \in \mathbb{T}^3$  and the interaction energy  $\mu > 0$ . Unlike the continuous case, the Schrödinger operator on a lattice can have eigenvalues at the right part of the essential spectrum as well.

The principal results of this paper are given for sufficiently big values of interaction energy  $\mu > 0$ , i.e., when the two-particle subsystems have bound states with positive energies: there are threshold values of the particle mass ratio  $\gamma_1, \gamma_2$  such that if  $\gamma \in (0, \gamma_1)$ , then the operator  $H_{\mu,\gamma}(\mathbf{0})$  has no eigenvalues; if  $\gamma \in (\gamma_1, \gamma_2)$ , then the operator  $H_{\mu,\gamma}(\mathbf{0})$  has a unique eigenvalue; if  $\gamma > \gamma_2$ , then the operator  $H_{\mu,\gamma}(\mathbf{0})$  has three eigenvalues lying to the right of the essential spectrum. Existence of at least one eigenvalue of the three-particle discrete Schrödinger operator  $H_\mu(\mathbf{K}) = H_0(\mathbf{K}) - \mu V$  ( $\mu \in \mathbb{R}$ ) for dimensions  $d = 1, 2$  was shown in [15] and [12], whose proofs are based on the unboundedness of the norm of the Faddeev operator  $\mathbf{T}(\mathbf{K}, z)$  at the lower bound of the essential spectrum  $z = \inf(\sigma_{ess}(H_\mu(\mathbf{K})))$ . If  $d \geq 3$ , then the operator  $\mathbf{T}(\mathbf{K}, z)$  is also bounded at the edges of the essential spectrum, i.e. in this case, methods for  $d = 1, 2$  is not applicable.

In [16], the model operator  $H_\gamma^{as}$  (see (2.6) paper in [16]), associated with three-particle discrete Schrödinger operator on a three-dimensional cubic lattice with pairwise zero-range attractive potentials, is studied, where the family of Friedrichs models with parameters  $h_\alpha(\mathbf{k}), \alpha = 1, 2, \mathbf{k} \in \mathbb{T}^3$  is used. The existence of the critical value  $\gamma^*$  of the parameter  $\gamma$  is proved so that if two-particle subsystems have a resonance with zero energy and do not have bound states with negative energy, then  $H_\gamma^{as}$  has an infinite number of eigenvalues, lying to the left of the essential spectrum for  $\gamma > \gamma^* \approx 13.607$ , and there is no Efimov's effect for  $\gamma < \gamma^*$ . The similar result holds for the operator we are considering  $H_{\mu,\gamma}(\boldsymbol{\pi})$ , i.e., at  $\gamma > \gamma^*$  and fixed  $\mu = \mu_0(\gamma)$ , the operator  $H_{\mu,\gamma}(\boldsymbol{\pi})$  has an infinite number of eigenvalues to the right of the essential spectrum. "The two-particle branch" of the essential operator spectrum of  $H_{\mu,\gamma}(\mathbf{K})$  is shifted to  $+\infty$  with the order  $\mu$  if  $\mu \rightarrow +\infty$ , as a result of which an infinite number of eigenvalues of the operator are "absorbed" by the essential spectrum. Therefore, a natural question arises: whether there are eigenvalues of the operator  $H_{\mu,\gamma}(\mathbf{0})$ , lying to the right of the essential spectrum for sufficiently large  $\mu$ , and if so, how many?

In this paper, we prove that the operator  $H_{\mu,\gamma}(\mathbf{0}), \mathbf{0} = (0, 0, 0)$ , for  $\gamma \in (0, \gamma_1)$  ( $\gamma_1 \approx 2, 937$ ) has no eigenvalues, but for  $\gamma_1 < \gamma < \gamma_2$  ( $\gamma_2 \approx 5, 396$ ) has a unique eigenvalue, and for  $\gamma > \gamma_2$  has exactly three eigenvalues to the right of the essential spectrum for sufficiently large  $\mu$ . Physically, this shows the conditions for the system of two fermions (of mass 1), and an arbitrary particle (of mass  $m, m < 1$ ) with pairwise repulsive interaction  $\mu$ , which is sufficiently large, to have no bound states, one bound state and three bound states, respectively.

Applying the perturbation theory, one can show that the results obtained are preserved for small values  $\mathbf{K}$ . Note that the problem of finding the number of eigenvalues of the operator  $H_{\mu,\gamma}(\mathbf{K})$ , which are more  $z$  ( $z > \tau_{\max,\gamma}(\mu, \mathbf{K})$ ) reduces to the problem of finding the number of eigenvalues of the Faddeev-type operator  $A_{\mu,\gamma}(\mathbf{K}, z)$ , which are more 1 (see. (4.2)). Sensitivity of the kernel of the integral operator  $A_{\mu,\gamma}(\mathbf{K}, z)$  regarding change  $\mathbf{K}$  leads to a change in the number of eigenvalues of the operator  $H_{\mu,\gamma}(\mathbf{K})$ . Therefore, set the number of eigenvalues for all  $\mathbf{K} \in \mathbb{T}^3$  is very difficult.

## 2. Statement of the problem and formulation of the main result

Let  $\mathbb{Z}^3$  is a three-dimensional lattice,  $\ell^2[(\mathbb{Z}^3)^d], d = 2, 3$  is a Hilbert space of square integrable functions given on  $(\mathbb{Z}^3)^d$  and  $\ell^{2,as}[(\mathbb{Z}^3)^d] \subset \ell^2[(\mathbb{Z}^3)^d]$  is a subspace of antisymmetric functions with respect to permutation of the first two coordinates.

We consider a Hamiltonian of a system of three quantum particles (two of them are fermions with mass 1 and one of them is arbitrary with mass  $m = 1/\gamma < 1$ ) that interact through pairwise zero-range repulsive potentials on  $\mathbb{Z}^3$ . Without a loss of generality, we assume that the first two particles are fermions while the third one is a particle of a different nature.

The Hamiltonian of the system of two arbitrary particles (a fermion and another particle) on  $\mathbb{Z}^3$  in the coordinate representation is associated with the bounded self-adjoint operator  $\hat{h}_{0,\gamma}$  in  $\ell^2[(\mathbb{Z}^3)^2]$ :

$$\hat{h}_{0,\gamma} = -\frac{1}{2}\Delta \otimes I - \frac{\gamma}{2}I \otimes \Delta,$$

where  $\Delta$  is the lattice Laplacian,  $I$  is the unity operator in  $\ell^2(\mathbb{Z}^3)$ , and  $\gamma = \frac{1}{m}$ .

The total Hamiltonian  $\hat{h}_{\mu,\gamma}$  of the system of two arbitrary particles with the zero-range repulsive potential acts in  $\ell^2[(\mathbb{Z}^3)^2]$  and is a bounded perturbation of the free Hamiltonian  $\hat{h}_{0,\gamma}$  :

$$\hat{h}_{\mu,\gamma} = \hat{h}_{0,\gamma} + \mu\hat{v},$$

where  $\mu, \mu > 0$ , is the interaction energy of two repelling particles (a fermion and another particle), operator  $\hat{v}$  describes the zero-range interaction of these particles

$$(\hat{v}\hat{\psi})(\mathbf{x}_2, \mathbf{x}_3) = \delta_{\mathbf{x}_2\mathbf{x}_3}\hat{\psi}(\mathbf{x}_2, \mathbf{x}_3)$$

and  $\delta_{\mathbf{x}_2\mathbf{x}_3}$  is the Kronecker symbol. In the space  $\ell^{2,as}[(\mathbb{Z}^3)^2]$ , there is no two-particle zero-range interaction of fermions (see [15], [17]).

Similarly, the free Hamiltonian  $\hat{H}_{0,\gamma}$  of the system of three particles (two fermions and another particle) on lattice  $\mathbb{Z}^3$  is specified in  $\ell^{2,as}[(\mathbb{Z}^3)^3]$  by the formula

$$\hat{H}_{0,\gamma} = -\frac{1}{2}\Delta \otimes I \otimes I - \frac{1}{2}I \otimes \Delta \otimes I - \frac{\gamma}{2}I \otimes I \otimes \Delta.$$

The total Hamiltonian  $\hat{H}_{\mu,\gamma}$  of the system of three particles with pairwise zero-range interactions is a bounded perturbation of the free Hamiltonian  $\hat{H}_{0,\gamma}$ :

$$\hat{H}_{\mu,\gamma} = \hat{H}_{0,\gamma} + \mu(\hat{V}_1 + \hat{V}_2),$$

where

$$(\hat{V}_1\hat{\psi})(\mathbf{x}_1, \mathbf{x}_2, \mathbf{x}_3) = \delta_{\mathbf{x}_2\mathbf{x}_3}\hat{\psi}(\mathbf{x}_1, \mathbf{x}_2, \mathbf{x}_3)$$

and

$$(\hat{V}_2\hat{\psi})(\mathbf{x}_1, \mathbf{x}_2, \mathbf{x}_3) = \delta_{\mathbf{x}_3\mathbf{x}_1}\hat{\psi}(\mathbf{x}_1, \mathbf{x}_2, \mathbf{x}_3).$$

Let  $\mathbb{T}^3$  is a three-dimensional torus and  $L_2^{as}[(\mathbb{T}^3)^2] \subset L_2[(\mathbb{T}^3)^3]$  be the Hilbert space of square integrable functions, defined on  $(\mathbb{T}^3)^3$  and antisymmetric with respect to permutation of the first two coordinates. Assume that  $d\mathbf{p}$  is a unit measure in the torus  $\mathbb{T}^3$ , that is

$$\int_{\mathbb{T}^3} d\mathbf{p} = 1.$$

The study of spectra of the Hamiltonians  $h_{\mu,\gamma}$  and  $H_{\mu,\gamma}$  is reduced to studying the spectra of the family of operators  $h_{\mu,\gamma}(\mathbf{k}), \mathbf{k} \in \mathbb{T}^3$  and  $H_{\mu,\gamma}(\mathbf{K}), \mathbf{K} \in \mathbb{T}^3$ , respectively (see [15], [18]).

The two-particle discrete Schrödinger operator  $h_{\mu,\gamma}(\mathbf{k}), \mathbf{k} \in \mathbb{T}^3$  acts in  $L_2(\mathbb{T}^3)$  by the formula

$$h_{\mu,\gamma}(\mathbf{k}) = h_{0,\gamma}(\mathbf{k}) + \mu v,$$

where

$$\begin{aligned} (h_{0,\gamma}(\mathbf{k})f)(\mathbf{p}) &= \mathcal{E}_{\mathbf{k},\gamma}(\mathbf{p})f(\mathbf{p}), \quad \mathcal{E}_{\mathbf{k},\gamma}(\mathbf{p}) = \varepsilon(\mathbf{p}) + \gamma\varepsilon(\mathbf{k} - \mathbf{p}), \\ \varepsilon(\mathbf{p}) &= 3 - \xi(\mathbf{p}), \quad \xi(\mathbf{p}) = \sum_{i=1}^3 \cos p_i, \quad \mathbf{p} = (p_1, p_2, p_3) \in \mathbb{T}^3, \\ (vf)(\mathbf{p}) &= \int_{\mathbb{T}^3} f(\mathbf{s})d\mathbf{s}. \end{aligned} \tag{2.1}$$

The respective three-particle discrete Schrödinger operator  $H_{\mu,\gamma}(\mathbf{K})$  acts in  $L_2^{as}[(\mathbb{T}^3)^2]$  by the formula

$$H_{\mu,\gamma}(\mathbf{K}) = H_{0,\gamma}(\mathbf{K}) + \mu(V_1 + V_2),$$

where

$$\begin{aligned} (H_{0,\gamma}(\mathbf{K})f)(\mathbf{p}, \mathbf{q}) &= E_{\mathbf{K},\gamma}(\mathbf{p}, \mathbf{q})f(\mathbf{p}, \mathbf{q}), \quad E_{\mathbf{K},\gamma}(\mathbf{p}, \mathbf{q}) = \varepsilon(\mathbf{p}) + \varepsilon(\mathbf{q}) + \gamma\varepsilon(\mathbf{K} - \mathbf{p} - \mathbf{q}), \\ (V_1f)(\mathbf{p}, \mathbf{q}) &= \int_{\mathbb{T}^3} f(\mathbf{p}, \mathbf{s})d\mathbf{s}, \quad (V_2f)(\mathbf{p}, \mathbf{q}) = \int_{\mathbb{T}^3} f(\mathbf{s}, \mathbf{q})d\mathbf{s}. \end{aligned}$$

Let us first introduce the following notation:

$$W = \int_{\mathbb{T}^3} \frac{d\mathbf{s}}{\varepsilon(\mathbf{s})}, \quad W_1 = \int_{\mathbb{T}^3} \frac{\cos s_1 d\mathbf{s}}{\varepsilon(\mathbf{s})}, \quad W_{11} = \int_{\mathbb{T}^3} \frac{\cos^2 s_1 d\mathbf{s}}{\varepsilon(\mathbf{s})}, \quad W_{12} = \int_{\mathbb{T}^3} \frac{\cos s_1 \cos s_2 d\mathbf{s}}{\varepsilon(\mathbf{s})}.$$

The integral  $W$  is called the Watson integral and the other integrals  $W_1, W_{11}$  and  $W_{12}$ — Watson-type integrals (see, for example [20]).

The main result of the paper is the following theorem:

**Theorem 2.1.** *Let*

$$\gamma_1 = \frac{W}{W_{11}W + 2WW_{12} - 3W_1^2} \approx 2,9368, \quad \gamma_2 = \frac{1}{W_{11} - W_{12}} \approx 5,3985. \tag{2.2}$$

(i) *Assume that  $\gamma \in (0, \gamma_1)$ . Then, there exists  $\mu_\gamma > 0$  such that for any  $\mu > \mu_\gamma$  the operator  $H_{\mu,\gamma}(\mathbf{0})$  has no eigenvalues lying to the above of the essential spectrum.*

- (ii) Assume that  $\gamma \in (\gamma_1, \gamma_2)$ . Then, there exists  $\mu_\gamma > 0$  such that for any  $\mu > \mu_\gamma$  the operator  $H_{\mu,\gamma}(\mathbf{0})$  has a unique eigenvalue lying to the above of the essential spectrum.
- (iii) Assume that  $\gamma \in (\gamma_2, +\infty)$ . Then, there exists  $\mu_\gamma > 0$  such that for any  $\mu > \mu_\gamma$  the operator  $H_{\mu,\gamma}(\mathbf{0})$  have three eigenvalues to the above of the essential spectrum.

**Remark 2.2.** The number  $\mu_\gamma$  takes on different values in the three cases of the Theorem 2.1.

### 3. On the spectrum of the two-particle operator $h_{\mu,\gamma}(\mathbf{k})$

In this section, we study some facts related to the spectrum of the operator  $h_{\mu,\gamma}(\mathbf{k})$ .

Since  $v$  is compact, by Weyl's Theorem [19] for any  $\mathbf{k} \in \mathbb{T}^3$ , the essential spectrum  $\sigma_{ess}(h_{\mu,\gamma}(\mathbf{k}))$  of  $h_{\mu,\gamma}(\mathbf{k})$  coincides with the spectrum of  $h_{0,\gamma}(\mathbf{k})$ , i.e.,

$$\sigma_{ess}(h_{\mu,\gamma}(\mathbf{k})) = [\mathcal{E}_{\min,\gamma}(\mathbf{k}), \mathcal{E}_{\max,\gamma}(\mathbf{k})],$$

where

$$\mathcal{E}_{\min,\gamma}(\mathbf{k}) = \min_{\mathbf{q} \in \mathbb{T}^3} \mathcal{E}_{\mathbf{k},\gamma}(\mathbf{q}) = 3(1 + \gamma) - \sum_{i=1}^3 \sqrt{1 + 2\gamma \cos k_i + \gamma^2},$$

$$\mathcal{E}_{\max,\gamma}(\mathbf{k}) = \max_{\mathbf{q} \in \mathbb{T}^3} \mathcal{E}_{\mathbf{k},\gamma}(\mathbf{q}) = 3(1 + \gamma) + \sum_{i=1}^3 \sqrt{1 + 2\gamma \cos k_i + \gamma^2}.$$

The following Lemma provides an implicit equation for eigenvalues of  $h_{\mu,\gamma}(\mathbf{k})$  which is a simple application of the Fredholm determinants theory.

**Lemma 3.1.** The number  $z \in \mathbb{C} \setminus [\mathcal{E}_{\min,\gamma}(\mathbf{k}), \mathcal{E}_{\max,\gamma}(\mathbf{k})]$  is an eigenvalue of  $h_{\mu,\gamma}(\mathbf{k})$  with multiplicity  $m$  if and only if  $z$  is a zero of the function

$$\Delta_{\mu,\gamma}(\mathbf{k}, z) = 1 - \mu \int_{\mathbb{T}^3} \frac{d\mathbf{q}}{z - \mathcal{E}_{\mathbf{k},\gamma}(\mathbf{q})} \tag{3.1}$$

with the multiplicity  $m$ .

The function  $\Delta_{\mu,\gamma}(\mathbf{k}, z)$  is called the *Fredholm determinant* associated to  $h_{\mu,\gamma}(\mathbf{k})$ .

Note that, the function  $\Delta_{\mu,\gamma}(\mathbf{k}, z)$  is the Fredholm determinant of the operator  $I - \mu v r_{0,\gamma}(\mathbf{k}, z)$ , where  $r_{0,\gamma}(\mathbf{k}, z)$  is the resolvent of the operator  $h_{0,\gamma}(\mathbf{k})$  and  $v$  is the integral operator with the kernel  $v(\mathbf{q}, \mathbf{q}') = 1$ .

Let us introduce first the following real number:

$$\mu_0(\gamma) = (1 + \gamma) \frac{1}{W}.$$

Note that this number means harmonic values of the kinetic energies of a fermion and another particle.

**Lemma 3.2.** Assume that  $\mu > \mu_0(\gamma)$ . Then for each  $\mathbf{k} \in \mathbb{T}^3$  the operator  $h_{\mu,\gamma}(\mathbf{k})$  has a unique simple eigenvalue  $z_{\mu,\gamma}(\mathbf{k})$  above the essential spectrum.

**Lemma 3.3.** The eigenvalue  $z_{\mu,\gamma}(\mathbf{k}) = z_{\mu,\gamma}(k_1, k_2, k_3)$  is symmetric function with respect to permutation of the variables  $k_i, k_j$ , even with respect to  $k_i \in [-\pi, \pi]$ , and decreasing with respect to  $k_i \in [0, \pi]$ ,  $i = 1, 2, 3$ .

*Proof.* The proof of the lemma follows directly from the properties of the function  $\Delta_{\mu,\gamma}(\mathbf{k}, z)$  and assertions of Lemma 3.1. □

**Lemma 3.4.** For any  $\gamma > 0$  and  $\mu > 3(1 + \gamma)$ , we have the following relations

$$\mu + 3(1 + \gamma) < z_{\mu,\gamma}(\boldsymbol{\pi}) \leq z_{\mu,\gamma}(\mathbf{k}) \leq z_{\mu,\gamma}(\mathbf{0}) < \mu + 3(1 + \gamma) + \frac{9(1 + \gamma)^2}{\mu}.$$

*Proof.* The proof of the Lemma follows from Lemma (3.3) and properties of the function  $\Delta_{\mu,\gamma}(\mathbf{k}, z)$ . □

**Corollary 3.5.** For any  $\gamma > 0$ , the function  $z_{\mu,\gamma}(\mathbf{k})$  has the following asymptotic expansions:

$$z_{\mu,\gamma}(\mathbf{k}) = \mu + 3(1 + \gamma) + O\left(\frac{1}{\mu}\right) \tag{3.2}$$

as  $\mu \rightarrow \infty$ , uniformly  $\mathbf{k} \in \mathbb{T}^3$ .

**4. Essential spectrum of a three-particle operator  $H_{\mu,\gamma}(\mathbf{K})$ .**

For any  $\mathbf{K} \in \mathbb{T}^3$ , recalling that

$$E_{\min,\gamma}(\mathbf{K}) = \min_{\mathbf{p},\mathbf{q} \in \mathbb{T}^3} E_{\mathbf{K},\gamma}(\mathbf{p}, \mathbf{q}), \quad E_{\max,\gamma}(\mathbf{K}) = \max_{\mathbf{p},\mathbf{q} \in \mathbb{T}^3} E_{\mathbf{K},\gamma}(\mathbf{p}, \mathbf{q}),$$

$$\tau_{\min,\gamma}(\mu, \mathbf{K}) = \min_{\mathbf{p} \in \mathbb{T}^3} \{z_{\mu,\gamma}(\mathbf{K} - \mathbf{p}) + \varepsilon(\mathbf{p})\}, \quad \tau_{\max,\gamma}(\mu, \mathbf{K}) = \max_{\mathbf{p} \in \mathbb{T}^3} \{z_{\mu,\gamma}(\mathbf{K} - \mathbf{p}) + \varepsilon(\mathbf{p})\},$$

where  $z_{\mu,\gamma}(\mathbf{p})$  is an eigenvalue of the operator  $h_{\mu,\gamma}(\mathbf{p})$  and the essential spectrum of  $H_{\mu,\gamma}(\mathbf{K})$  coincides with the union of two segment:

$$\sigma_{ess}(H_{\mu,\gamma}(\mathbf{K})) = [E_{\min,\gamma}(\mathbf{K}), E_{\max,\gamma}(\mathbf{K})] \cup [\tau_{\min,\gamma}(\mu, \mathbf{K}), \tau_{\max,\gamma}(\mu, \mathbf{K})]. \tag{4.1}$$

The proof of a similar assertion is given in the paper [18]. Note that  $[\tau_{\min,\gamma}(\mu, \mathbf{K}), \tau_{\max,\gamma}(\mu, \mathbf{K})]$  and  $[E_{\min,\gamma}(\mathbf{K}), E_{\max,\gamma}(\mathbf{K})]$  are called the ‘‘two-particle branch’’ and the ‘‘three-particle branch’’ of the essential spectrum of  $H_{\mu,\gamma}(\mathbf{K})$ , respectively.

For fixed  $\gamma, \gamma > 0$ , we study the discrete spectrum of the operator  $H_{\mu,\gamma}(\mathbf{0})$ ,  $\mathbf{0} = (0, 0, 0)$  for sufficiently large  $\mu > 0$ . It follows from Lemma 2.4 and the structure of the essential spectrum that (see (4.1)), that the two-particle branch  $[\tau_{\min,\gamma}(\mu, \mathbf{0}), \tau_{\max,\gamma}(\mu, \mathbf{0})]$  of the essential spectrum shifts  $+\infty$  with order  $\mu$  at  $\mu \rightarrow +\infty$ .

In what follows we always assume  $z \geq \inf \sigma_{ess}(H_{\mu,\gamma}(\mathbf{0})) = \tau_{\max,\gamma}(\mu, \mathbf{0})$ .

**Discrete spectrum of a three-particle operator  $H_{\mu,\gamma}(\mathbf{0})$ .**

First, we show that the operator  $H_{\mu,\gamma}(\mathbf{K})$  has no eigenvalues below the essential spectrum.

**Lemma 4.1.** *Assume that  $\mathbf{K} \in \mathbb{T}^3$ . Then for any  $\mu > 0$  and  $\gamma > 0$  the operator  $H_{\mu,\gamma}(\mathbf{K})$  has no eigenvalues below the essential spectrum.*

*Proof.* Since the operator  $V = V_1 + V_2$  is positive by the minimax principle we can conclude that

$$\inf_{\|f\|=1} (H_{\mu,\gamma}(\mathbf{K})f, f) = \inf_{\|f\|=1} [(H_{0,\gamma}(\mathbf{K})f, f) + \mu(Vf, f)] \geq \inf_{\|f\|=1} (H_{0,\gamma}(\mathbf{K})f, f) = E_{\min,\gamma}(\mathbf{K}),$$

leading to  $\sigma(H_{\mu,\gamma}(\mathbf{K})) \cap (-\infty, E_{\min,\gamma}(\mathbf{K})) = \emptyset$ . □

For any  $z > \tau_{\max,\gamma}(\mu, \mathbf{0})$ , we define the self-adjoint compact operator of the form

$$(A_{\mu,\gamma}(z)\psi)(\mathbf{p}) = \frac{-\mu}{\sqrt{\Lambda_{\mu,\gamma}(\mathbf{p}, z)}} \int_{\mathbb{T}^3} \frac{\psi(\mathbf{s})ds}{(z - E_{0,\gamma}(\mathbf{p}, \mathbf{s}))\sqrt{\Lambda_{\mu,\gamma}(\mathbf{s}, z)}} \tag{4.2}$$

defined in

$$D(A_{\mu,\gamma}(z)) = \left\{ \psi \in L_2(\mathbb{T}^3) : \int_{\mathbb{T}^3} \frac{\psi(\mathbf{s})ds}{\sqrt{\Lambda_{\mu,\gamma}(\mathbf{s}, z)}} = 0 \right\},$$

where

$$\Lambda_{\mu,\gamma}(\mathbf{p}, z) := \Delta_{\mu,\gamma}(-\mathbf{p}, z - \varepsilon(\mathbf{p})), \tag{4.3}$$

and the function  $\Delta_{\mu,\gamma}(\cdot, \cdot)$  is given by formula (3.1).

The operator  $A_{\mu,\gamma}(z)$  is called the Faddeev-type operator corresponding to the operator  $H_{\mu,\gamma}(\mathbf{0})$  (see Remark 4.3 and [21], [22]).

Hence, we found the equivalent equation for the eigenfunctions of the three-particle operator  $H_{\mu,\gamma}(\mathbf{0})$ .

**Lemma 4.2.** *The number  $z > \tau_{\max,\gamma}(\mu, \mathbf{0})$  is an eigenvalue of the operator  $H_{\mu,\gamma}(\mathbf{0})$  if and only if the number 1 is an eigenvalue of the operator  $A_{\mu,\gamma}(z)$ .*

*Proof.* Let  $z > \tau_{\max,\gamma}(\mu, \mathbf{0})$  is the eigenvalue of the operator  $H_{\mu,\gamma}(\mathbf{0})$  and  $f$  is the respective eigenfunction, i.e., the equation

$$E_{0,\gamma}(\mathbf{p}, \mathbf{q})f(\mathbf{p}, \mathbf{q}) + \mu \int_{\mathbb{T}^3} f(\mathbf{p}, \mathbf{s})ds + \mu \int_{\mathbb{T}^3} f(\mathbf{s}, \mathbf{q})ds = zf(\mathbf{p}, \mathbf{q}) \tag{4.4}$$

has a nonzero solution  $f \in L_2^{as}[(\mathbb{T}^3)^2]$ . Introducing the notation

$$\varphi(\mathbf{p}) = (V_1 f)(\mathbf{p}, \mathbf{q}) = \int_{\mathbb{T}^3} f(\mathbf{p}, \mathbf{s})ds, \tag{4.5}$$

from (4.4) for  $z > \tau_{\max,\gamma}(\mu, \mathbf{0})$ , we have

$$f(\mathbf{p}, \mathbf{q}) = \mu \frac{\varphi(\mathbf{p}) - \varphi(\mathbf{q})}{z - E_{0,\gamma}(\mathbf{p}, \mathbf{q})}. \tag{4.6}$$

Since the function  $f$  is antisymmetric, the function  $\varphi$  given by formula (4.5), belongs to the space  $L_2(\mathbb{T}^3)$  and satisfies the condition

$$\int_{\mathbb{T}^3} \varphi(\mathbf{p}) \, d\mathbf{p} = 0.$$

Substituting the expression (4.6) into (4.5), we obtain that the equation

$$\varphi(\mathbf{p}) \left( 1 - \mu \int_{\mathbb{T}^3} \frac{ds}{z - E_{\mathbf{0},\gamma}(\mathbf{p}, \mathbf{s})} \right) = -\mu \int_{\mathbb{T}^3} \frac{\varphi(\mathbf{s}) ds}{z - E_{\mathbf{0},\gamma}(\mathbf{p}, \mathbf{s})}$$

has a nonzero solution  $\varphi \in L_2(\mathbb{T}^3)$ . Hence, using notation (3.1) and (4.3), we make sure that  $\varphi \in L_2(\mathbb{T}^3)$  is the solution of the equation

$$\varphi(\mathbf{p}) = \frac{-\mu}{\Lambda_{\mu,\gamma}(\mathbf{p}, z)} \int_{\mathbb{T}^3} \frac{\varphi(\mathbf{s}) ds}{z - E_{\mathbf{0},\gamma}(\mathbf{p}, \mathbf{s})}. \tag{4.7}$$

If we set  $\psi(\mathbf{p}) = \sqrt{\Lambda_{\mu,\gamma}(\mathbf{p}, z)} \varphi(\mathbf{p})$ , from (4.7) we have

$$\psi(\mathbf{p}) = \frac{-\mu}{\sqrt{\Lambda_{\mu,\gamma}(\mathbf{p}, z)}} \int_{\mathbb{T}^3} \frac{\psi(\mathbf{s}) ds}{(z - E_{\mathbf{0},\gamma}(\mathbf{p}, \mathbf{s})) \sqrt{\Lambda_{\mu,\gamma}(\mathbf{s}, z)}},$$

i.e.,  $\lambda = 1$  is the eigenvalue of the operator  $A_{\mu,\gamma}(z)$  and

$$\int_{\mathbb{T}^3} \frac{\psi(\mathbf{s}) ds}{\sqrt{\Lambda_{\mu,\gamma}(\mathbf{s}, z)}} = 0.$$

Suppose that, for some  $z > \tau_{\max,\gamma}(\mu, \mathbf{0})$  the number 1 is the eigenvalue of the operator  $A_{\mu,\gamma}(z)$ , and  $\psi \in D(A_{\mu,\gamma}(z))$  is the corresponding eigenfunction. Then, the function  $f$  is given by formula (4.6), where  $\varphi(\mathbf{p}) = \psi(\mathbf{p}) \sqrt{\Lambda_{\mu,\gamma}(\mathbf{p}, z)}$ , belongs to the space  $L_2^{as}[(\mathbb{T}^3)^2]$  and satisfies the equality (4.4).  $\square$

**Remark 4.3.** a) Note that the relation between eigenfunctions  $f$  and  $\psi$ , respectively, of  $H_{\mu,\gamma}(\mathbf{0})$  and  $A_{\mu,\gamma}(z)$  corresponding to the eigenvalues  $z$  and 1 is

$$f(\mathbf{p}, \mathbf{q}) = \mu \frac{(\Lambda_{\mu,\gamma}(\mathbf{p}, z))^{-1/2} \psi(\mathbf{p}) - (\Lambda_{\mu,\gamma}(\mathbf{q}, z))^{-1/2} \psi(\mathbf{q})}{z - E_{\mathbf{0},\gamma}(\mathbf{p}, \mathbf{q})}.$$

Therefore, we can say that the operator  $A_{\mu,\gamma}(z)$  is the Faddeev-type operator.

b) A limit operator

$$\lim_{z \rightarrow \tau_{\max,\gamma}(\mu, \mathbf{0})} A_{\mu,\gamma}(z) = A_{\mu,\gamma}(\tau_{\max,\gamma}(\mu, \mathbf{0}))$$

is a compact self-adjoint operator in  $L_2(\mathbb{T}^3)$ .

For the bounded self-adjoint operator  $B$ , acting in the Hilbert space  $\mathcal{H}$  and for some  $\lambda \in \mathbb{R}$  define a number  $n[\lambda, B]$  by

$$n[\lambda, B] := \max\{\dim \mathcal{H}_B(\lambda) : \mathcal{H}_B(\lambda) \subset \mathcal{H}; (B\varphi, \varphi) > \lambda, \varphi \in \mathcal{H}_B(\lambda), \|\varphi\| = 1\}.$$

If some point of the essential spectrum of the operator  $B$  is greater than  $\lambda$  then  $n[\lambda, B]$  equals infinity, if  $n[\lambda, B]$  is finite, it equals to the number of eigenvalues of the operator  $B$ , that are greater than  $\lambda$  (see. example Lemma Glazman [23]).

The known Birman–Schwinger principle (see. [15]) leads to the following lemma.

**Lemma 4.4.** Let  $\mu > \mu_0(\gamma)$ . Then, for any  $z \geq \tau_{\max,\gamma}(\mu, \mathbf{0})$  the equality holds

$$n[z, H_{\mu,\gamma}(\mathbf{0})] = n[1, A_{\mu,\gamma}(z)].$$

### 5. On the spectrum of the operator $A_{\mu,\gamma}(z)$ .

It is well-known that the three-particle branch  $[E_{\min,\gamma}(\mathbf{0}), E_{\max,\gamma}(\mathbf{0})]$  of the essential spectrum of the operator  $H_{\mu,\gamma}(\mathbf{0})$  is independent of the parameter  $\mu > 0$ , and the two-particle branch  $[\tau_{\min,\gamma}(\mu, \mathbf{0}), \tau_{\max,\gamma}(\mu, \mathbf{0})]$  of the essential spectrum shifts to  $+\infty$ , when  $\mu \rightarrow +\infty$ . Therefore, in what follows, we assume that  $\mu$  is large enough and  $z \geq \tau_{\max,\gamma}(\mu, \mathbf{0})$ .

Using the equality  $\frac{1}{1+x} = 1 - x + \frac{x^2}{1+x}$ , ( $x \neq -1$ ), and given notation (2.1), we have

$$\frac{1}{z - E_{\mathbf{0},\gamma}(\mathbf{p}, \mathbf{s})} = \frac{1}{a(\gamma, z)} \left( 1 - \frac{(\xi(\mathbf{p}) + \xi(\mathbf{s}) + \gamma\xi(\mathbf{p} + \mathbf{s}))}{a(\gamma, z)} + \frac{\zeta(\gamma; \mathbf{p}, \mathbf{s})}{a(\gamma, z)} \right), \tag{5.1}$$

where

$$a(\gamma, z) = z - 6 - 3\gamma \text{ and } \zeta(\gamma; \mathbf{p}, \mathbf{s}) = \frac{(\xi(\mathbf{p}) + \xi(\mathbf{s}) + \gamma\xi(\mathbf{p} + \mathbf{s}))^2}{z - E_{0,\gamma}(\mathbf{p}, \mathbf{s})}.$$

Taking into account the equality (5.1), we represent the operator  $A_{\mu,\gamma}(z)$  as a sum

$$A_{\mu,\gamma}(z) = A_{\mu,\gamma}^{(1)}(z) + A_{\mu,\gamma}^{(2)}(z), \tag{5.2}$$

where

$$(A_{\mu,\gamma}^{(1)}(z)\psi)(\mathbf{p}) = \frac{\mu}{a^2(\gamma, z)} \int_{\mathbb{T}^3} \frac{(\xi(\mathbf{p}) + \xi(\mathbf{s}) + \gamma\xi(\mathbf{p} + \mathbf{s}) - a(\gamma, z))\psi(\mathbf{s})d\mathbf{s}}{\sqrt{\Lambda_{\mu,\gamma}(\mathbf{p}, z)}\sqrt{\Lambda_{\mu,\gamma}(\mathbf{s}, z)}},$$

$$(A_{\mu,\gamma}^{(2)}(z)\psi)(\mathbf{p}) = -\frac{\mu}{a^2(\gamma, z)} \int_{\mathbb{T}^3} \frac{\zeta(\gamma; \mathbf{p}, \mathbf{s})\psi(\mathbf{s})d\mathbf{s}}{\sqrt{\Lambda_{\mu,\gamma}(\mathbf{p}, z)}\sqrt{\Lambda_{\mu,\gamma}(\mathbf{s}, z)}}.$$

In what follows, it is shown that the norm of the operator  $A_{\mu,\gamma}^{(2)}(z)$  tends to zero as  $\mu \rightarrow +\infty$  (see Lemma 5.5). Therefore, let us establish the existence of eigenvalues of the operator  $A_{\mu,\gamma}^{(1)}(z)$  which are greater 1 for large enough  $\mu > 0$ .

Let us find the invariant subspaces with respect to  $A_{\mu,\gamma}^{(1)}(z)$ .

The Hilbert space  $L_2(\mathbb{T}^3)$  can be represented as a direct sum

$$L_2(\mathbb{T}^3) = L_2^o(\mathbb{T}^3) \oplus L_2^e(\mathbb{T}^3),$$

where

$$L_2^o(\mathbb{T}^3) = \{\psi \in L_2(\mathbb{T}^3) : \psi(-\mathbf{p}) = -\psi(\mathbf{p})\}, \quad L_2^e(\mathbb{T}^3) = \{\psi \in L_2(\mathbb{T}^3) : \psi(-\mathbf{p}) = \psi(\mathbf{p})\}.$$

**Lemma 5.1.** *The subspaces  $L_2^e(\mathbb{T}^3)$  and  $L_2^o(\mathbb{T}^3)$  are invariant under the operators  $A_{\mu,\gamma}(z)$ ,  $A_{\mu,\gamma}^{(1)}(z)$  and  $A_{\mu,\gamma}^{(2)}(z)$ .*

*Proof.* From the definitions  $\Lambda_{\mu,\gamma}(\mathbf{p}, z)$  and  $\varepsilon(\mathbf{p})$  it follows that

$$\Lambda_{\mu,\gamma}(-\mathbf{p}, z) = \Delta_{\mu,\gamma}(\mathbf{p}, z - \varepsilon(-\mathbf{p})) = \Delta_{\mu,\gamma}(-\mathbf{p}, z - \varepsilon(\mathbf{p})) = \Lambda_{\mu,\gamma}(\mathbf{p}, z). \tag{5.3}$$

If  $\psi \in L_2^e(\mathbb{T}^3)$ , then making the change of variable  $\mathbf{s} = -\mathbf{q}$ , given equalities  $E_{0,\gamma}(-\mathbf{p}, -\mathbf{q}) = E_{0,\gamma}(\mathbf{p}, \mathbf{q})$  and (5.3), we get

$$\begin{aligned} \tilde{\psi}(-\mathbf{p}) &= (A_{\mu,\gamma}(z)\psi)(-\mathbf{p}) = -\frac{\mu}{\sqrt{\Lambda_{\mu,\gamma}(-\mathbf{p}, z)}} \int_{\mathbb{T}^3} \frac{\psi(\mathbf{s})d\mathbf{s}}{(z - E_{0,\gamma}(-\mathbf{p}, \mathbf{s}))\sqrt{\Lambda_{\mu,\gamma}(\mathbf{s}, z)}} = \\ &= -\frac{\mu}{\sqrt{\Lambda_{\mu,\gamma}(\mathbf{p}, z)}} \int_{\mathbb{T}^3} \frac{\psi(\mathbf{q})d\mathbf{q}}{(z - E_{0,\gamma}(-\mathbf{p}, -\mathbf{q}))\sqrt{\Lambda_{\mu,\gamma}(\mathbf{q}, z)}} = \tilde{\psi}(\mathbf{p}). \end{aligned}$$

Therefore, the subspace  $L_2^e(\mathbb{T}^3)$  is invariant under  $A_{\mu,\gamma}(z)$ . Since the operator  $A_{\mu,\gamma}(z)$  is self-adjoint, orthogonal complement  $L_2^o(\mathbb{T}^3)$  of subspaces  $L_2^e(\mathbb{T}^3)$  is also invariant under the operator  $A_{\mu,\gamma}(z)$ . The other statements are proved similarly.  $\square$

Denote by  $P^o$  and  $P^e$  the space projection operators in  $L_2(\mathbb{T}^3)$  into subspaces  $L_2^o(\mathbb{T}^3)$  and  $L_2^e(\mathbb{T}^3)$ , respectively. For  $\psi \in L_2(\mathbb{T}^3)$ , the following equalities are true

$$(P^o\psi)(\mathbf{p}) = \frac{1}{2}[\psi(\mathbf{p}) - \psi(-\mathbf{p})], \quad (P^e\psi)(\mathbf{p}) = \frac{1}{2}[\psi(\mathbf{p}) + \psi(-\mathbf{p})].$$

From the invariance of subspaces  $L_2^o(\mathbb{T}^3)$  and  $L_2^e(\mathbb{T}^3)$  with respect to the operator  $A_{\mu,\gamma}^{(1)}(z)$ , it follows that the projectors  $P^o$  and  $P^e$  are permutable with operator  $A_{\mu,\gamma}^{(1)}(z)$ , i.e.,

$$P^o A_{\mu,\gamma}^{(1)}(z) = A_{\mu,\gamma}^{(1)}(z)P^o, \quad P^e A_{\mu,\gamma}^{(1)}(z) = A_{\mu,\gamma}^{(1)}(z)P^e.$$

Denote by  $A_{\mu,\gamma}^{(1,o)}(z)$  the operator restriction  $A_{\mu,\gamma}^{(1)}(z)$  to subspace  $L_2^o(\mathbb{T}^3)$ . Then by definition of the operator  $A_{\mu,\gamma}^{(1,o)}(z) = P^o A_{\mu,\gamma}^{(1)}(z)P^o = A_{\mu,\gamma}^{(1)}(z)P^o$  it follows that for any  $\psi \in L_2(\mathbb{T}^3)$ , it occurs that

$$(A_{\mu,\gamma}^{(1,o)}(z)\psi)(\mathbf{p}) = -\frac{\mu\gamma}{a^2(\gamma, z)\sqrt{\Lambda_{\mu,\gamma}(\mathbf{p}, z)}} \sum_{i=1}^3 \int_{\mathbb{T}^3} \frac{\sin p_i \sin s_i \psi(\mathbf{s})d\mathbf{s}}{\sqrt{\Lambda_{\mu,\gamma}(\mathbf{s}, z)}}.$$

By analogous reasoning, one can verify that the restriction  $A_{\mu,\gamma}^{(1,e)}(z) = A_{\mu,\gamma}^{(1)}(z) - A_{\mu,\gamma}^{(1,o)}(z)$  of the operator  $A_{\mu,\gamma}^{(1)}(z)$  to the subspace  $L_2^e(\mathbb{T}^3)$  has the form:

$$(A_{\mu,\gamma}^{(1,e)}(z)\psi)(\mathbf{p}) = \frac{\mu}{a^2(\gamma, z)\sqrt{\Lambda_{\mu,\gamma}(\mathbf{p}, z)}} \int_{\mathbb{T}^3} \left( \sum_{i=1}^3 (\cos p_i + \cos s_i + \right.$$

$$+\gamma \cos p_i \cos s_i - a(\gamma, z)) \frac{\psi(\mathbf{s}) ds}{\sqrt{\Lambda_{\mu, \gamma}(\mathbf{s}, z)}}.$$

**Lemma 5.2.** For any  $z > \tau_{\max, \gamma}(\mu, \mathbf{0})$ , the operator  $A_{\mu, \gamma}^{(1, o)}(z)$  is negative, that is

$$\left( A_{\mu, \gamma}^{(1, o)}(z) \psi, \psi \right) \leq 0 \quad \text{for all } \psi \in L_2^o(\mathbb{T}^3).$$

*Proof.* Indeed, for any  $\psi \in L_2^o(\mathbb{T}^3)$ , we have

$$\begin{aligned} \left( A_{\mu, \gamma}^{(1, o)}(z) \psi, \psi \right) &= -\frac{\mu\gamma}{a^2(\gamma, z)} \int_{(\mathbb{T}^3)^2} \frac{\left( \sum_{i=1}^3 \sin p_i \sin s_i \right) \psi(\mathbf{s}) \overline{\psi(\mathbf{p})} ds dp}{\sqrt{\Lambda_{\mu, \gamma}(\mathbf{p}, z)} \sqrt{\Lambda_{\mu, \gamma}(\mathbf{s}, z)}} = \\ &= -\frac{\mu\gamma}{a^2(\gamma, z)} \sum_{i=1}^3 \int_{\mathbb{T}^3} \frac{\sin s_i \psi(\mathbf{s}) ds}{\sqrt{\Lambda_{\mu, \gamma}(\mathbf{s}, z)}} \int_{\mathbb{T}^3} \frac{\sin p_i \overline{\psi(\mathbf{p})} dp}{\sqrt{\Lambda_{\mu, \gamma}(\mathbf{p}, z)}} = \\ &= -\frac{\mu\gamma}{a^2(\gamma, z)} \sum_{i=1}^3 \left| \int_{\mathbb{T}^3} \frac{\sin p_i \psi(\mathbf{p}) dp}{\sqrt{\Lambda_{\mu, \gamma}(\mathbf{p}, z)}} \right|^2 \leq 0. \end{aligned}$$

□

Let  $\Phi$  be the one-dimensional subspace spanned by a function

$$\varphi_0(\mathbf{p}) = \frac{c(z)}{\sqrt{\Lambda_{\mu, \gamma}(\mathbf{p}, z)}},$$

where  $c(z)$  is the normalizing factor, that is

$$\frac{1}{c^2(z)} = \int_{\mathbb{T}^3} \frac{ds}{\Lambda_{\mu, \gamma}(\mathbf{s}, z)}.$$

Denote by  $Q$  the subspace projection operator  $L_2^e(\mathbb{T}^3) \ominus \Phi$ .

Let  $B_{\mu, \gamma}(z)$  be the operator restriction  $A_{\mu, \gamma}^{(1, e)}(z)$  to the subspace  $L_2^e(\mathbb{T}^3) \ominus \Phi$ , that is

$$(Q\varphi)(\mathbf{p}) = \varphi(\mathbf{p}) - (\varphi, \varphi_0)\varphi_0(\mathbf{p}), \quad \varphi \in L_2^e(\mathbb{T}^3).$$

Now, using some calculations, we have

$$(B_{\mu, \gamma}(z)\psi)(\mathbf{p}) = (QA_{\mu, \gamma}^{(1, e)}Q\psi)(\mathbf{p}) = \frac{\mu\gamma}{a^2(\gamma, z)\sqrt{\Lambda_{\mu, \gamma}(\mathbf{p}, z)}} \sum_{i=1}^3 \int_{\mathbb{T}^3} \varphi_i(\mathbf{p})\varphi_i(\mathbf{s}) \frac{\psi(\mathbf{s}) ds}{\sqrt{\Lambda_{\mu, \gamma}(\mathbf{s}, z)}},$$

where

$$\varphi_i(p) = c^2(z)b_i(z) - \cos p_i \tag{5.4}$$

and

$$b_i(z) := b_i(\mu, \gamma, z) = \int_{\mathbb{T}^3} \frac{\cos s_i ds}{\Lambda_{\mu, \gamma}(\mathbf{s}, z)}, \quad i = 1, 2, 3.$$

Let

$$b_{ij}(z) := b_{ij}(\mu, \gamma, z) = \int_{\mathbb{T}^3} \frac{\varphi_i(\mathbf{s})\varphi_j(\mathbf{s}) ds}{\Lambda_{\mu, \gamma}(\mathbf{s}, z)}, \quad i, j = 1, 2, 3, \tag{5.5}$$

where by functional invariance of  $\Lambda_{\mu, \gamma}(\mathbf{p}, z)$  regarding the permutation of variables  $p_i$  and  $p_j$  it follows that

$$b_{11}(z) = b_{22}(z) = b_{33}(z), \quad b_{12}(z) = b_{21}(z) = b_{23}(z) = b_{32}(z) = b_{13}(z) = b_{31}(z).$$

**Lemma 5.3.** Let

$$d(z) := d(\mu, \gamma, z) = \frac{\mu\gamma}{a^2(\gamma, z)}.$$

Then for sufficiently large and positive  $\mu$  the number

$$\lambda_1(z) = d(z)(b_{11}(z) + 2b_{12}(z)) \tag{5.6}$$

is simple and

$$\lambda_{2,3}(z) = d(z)(b_{11}(z) - b_{12}(z)) \tag{5.7}$$

is an eigenvalue with the multiplicity two of the operator  $B_{\mu, \gamma}(z)$ .

*Proof.* Suppose the equation

$$(B_{\mu,\gamma}(z)\psi)(\mathbf{p}) = \lambda\psi(\mathbf{p})$$

has a nonzero solution  $\psi \in L_2^e(\mathbb{T}^3)$ . From here,

$$\psi(\mathbf{p}) = \frac{d(z)}{\lambda\sqrt{\Lambda_{\mu,\gamma}(\mathbf{p}, z)}} \sum_{i=1}^3 C_i \varphi_i(\mathbf{p}), \tag{5.8}$$

where

$$C_i = \int_{\mathbb{T}^3} \frac{\varphi_i(\mathbf{s})\psi(\mathbf{s})d\mathbf{s}}{\sqrt{\Lambda_{\mu,\gamma}(\mathbf{s}, z)}}, \quad i = 1, 2, 3. \tag{5.9}$$

Substituting the right hand side of the equality (5.8) in (5.9), we obtain a system of equations for  $C_1, C_2$  and  $C_3$ :

$$\begin{cases} (d(z)b_{11}(z) - \lambda) C_1 + d(z)b_{12}(z)C_2 + d(z)b_{12}(z)C_3 = 0 \\ d(z)b_{12}(z)C_1 + (d(z)b_{11}(z) - \lambda) C_2 + d(z)b_{12}(z)C_3 = 0 \\ d(z)b_{12}(z)C_1 + d(z)b_{12}(z)C_2 + (d(z)b_{11}(z) - \lambda) C_3 = 0 \end{cases}$$

Determinant  $D(\lambda)$  of this system is a third degree polynomial with respect to  $\lambda$ .

Solving the equation  $D(\lambda) = 0$ , it makes sure that  $\lambda_1(z)$  and  $\lambda_2(z)$ , defined by formulas (5.6) and (5.7), are simple and double zeros, respectively. After elementary calculations, we verify that

$$\psi_1(\mathbf{p}) = \frac{(\varphi_1(\mathbf{p}) + \varphi_2(\mathbf{p}) + \varphi_3(\mathbf{p}))C}{\sqrt{\Lambda_{\mu,\gamma}(\mathbf{p}, z)}},$$

is an eigenfunction corresponding to the eigenvalue  $\lambda_1(z)$ . General view of an element from the subspace of its own functions, corresponding to the double eigenvalue  $\lambda_{2,3}(z)$ , looks like

$$\psi_2(\mathbf{p}) = \frac{(\varphi_1(\mathbf{p}) - \varphi_3(\mathbf{p}))}{\sqrt{\Lambda_{\mu,\gamma}(\mathbf{p}, z)}} C_1 + \frac{(\varphi_2(\mathbf{p}) - \varphi_3(\mathbf{p}))}{\sqrt{\Lambda_{\mu,\gamma}(\mathbf{p}, z)}} C_2.$$

□

**Lemma 5.4.** Assume that  $\mu > 6(1 + \gamma)$  and  $z \geq \tau_{\max,\gamma}(\mu, \mathbf{0})$ . Then the inequalities

$$\frac{(z_{\mu,\gamma}(\mathbf{p}) - 6 - 6\gamma)(z - 12 - 6\gamma)}{\mu(z - z_{\mu,\gamma}(\mathbf{p}) - \varepsilon(\mathbf{p}))} \leq \frac{1}{\Lambda_{\mu,\gamma}(\mathbf{p}, z)} \leq \frac{z \cdot z_{\mu,\gamma}(\mathbf{p})}{\mu(z - z_{\mu,\gamma}(\mathbf{p}) - \varepsilon(\mathbf{p}))} \tag{5.10}$$

hold, where  $z_{\mu,\gamma}(\mathbf{p})$  is an eigenvalue of the two-particle operator  $h_{\mu,\gamma}(\mathbf{p})$ .

Moreover, we obtain the following asymptotics

$$\frac{1}{\Lambda_{\mu,\gamma}(\mathbf{p}, \tau_{\max,\gamma}(\mu, \mathbf{0}))} = \frac{\mu}{\varepsilon(\mathbf{p})} \left( 1 + O\left(\frac{1}{\mu}\right) \right) \tag{5.11}$$

as  $\mu \rightarrow +\infty$ .

*Proof.* For all  $\mathbf{p} \in \mathbb{T}^3$ , by Lemma (3.1), we establish

$$\mu \int_{\mathbb{T}^3} \frac{d\mathbf{s}}{z_{\mu,\gamma}(\mathbf{p}) - \varepsilon(\mathbf{s}) - \gamma\varepsilon(\mathbf{p} - \mathbf{s})} = \mu \int_{\mathbb{T}^3} \frac{d\mathbf{s}}{z_{\mu,\gamma}(\mathbf{p}) - \varepsilon(\mathbf{s}) - \gamma\varepsilon(\mathbf{p} + \mathbf{s})} \equiv 1.$$

Observe that

$$\begin{aligned} \Lambda_{\mu,\gamma}(\mathbf{p}, z) &= 1 - \mu \int_{\mathbb{T}^3} \frac{d\mathbf{s}}{z - E_{\mathbf{0},\gamma}(\mathbf{p}, \mathbf{s})} = \\ &= \mu \int_{\mathbb{T}^3} \frac{d\mathbf{s}}{z_{\mu,\gamma}(\mathbf{p}) - \varepsilon(\mathbf{s}) - \gamma\varepsilon(\mathbf{p} + \mathbf{s})} - \mu \int_{\mathbb{T}^3} \frac{d\mathbf{s}}{z - \varepsilon(\mathbf{p}) - \varepsilon(\mathbf{s}) - \gamma\varepsilon(\mathbf{p} + \mathbf{s})} = \\ &= \mu(z - z_{\mu,\gamma}(\mathbf{p}) - \varepsilon(\mathbf{p})) \int_{\mathbb{T}^3} \frac{d\mathbf{s}}{[z_{\mu,\gamma}(\mathbf{p}) - \varepsilon(\mathbf{s}) - \gamma\varepsilon(\mathbf{p} + \mathbf{s})][z - E_{\mathbf{0},\gamma}(\mathbf{p}, \mathbf{s})]}. \end{aligned} \tag{5.12}$$

Then, using the assertion  $0 \leq \varepsilon(\mathbf{s}) \leq 6$ , we get

$$\frac{1}{z_{\mu,\gamma}(\mathbf{p})} \leq \frac{1}{z_{\mu,\gamma}(\mathbf{p}) - \varepsilon(\mathbf{s}) - \gamma\varepsilon(\mathbf{p} + \mathbf{s})} \leq \frac{1}{z_{\mu,\gamma}(\mathbf{p}) - 6 - 6\gamma}, \tag{5.13}$$

$$\frac{1}{z} \leq \frac{1}{z - E_{\mathbf{0},\gamma}(\mathbf{p}, \mathbf{s})} \leq \frac{1}{z - 12 - 6\gamma}. \quad (5.14)$$

(5.10) follows directly from relations (5.13), (5.14) and (5.12).

Now, (5.11) can be obtained as in

$$\begin{aligned} \frac{1}{z_{\mu,\gamma}(\mathbf{p}) - \varepsilon(\mathbf{s}) - \gamma\varepsilon(\mathbf{p} + \mathbf{s})} &= \frac{1}{z_{\mu,\gamma}(\mathbf{p}) - 3 - 3\gamma} \left( 1 - \frac{\xi(\mathbf{s}) + \gamma\xi(\mathbf{p} + \mathbf{s})}{z_{\mu,\gamma}(\mathbf{p}) - \varepsilon(\mathbf{s}) - \gamma\varepsilon(\mathbf{p} + \mathbf{s})} \right), \\ \frac{1}{z - \varepsilon(\mathbf{s}) - \gamma\varepsilon(\mathbf{p} + \mathbf{s}) - \varepsilon(\mathbf{p})} &= \frac{1}{z - 6 - 3\gamma} \left( 1 - \frac{\xi(\mathbf{s}) + \gamma\xi(\mathbf{p} + \mathbf{s}) + \xi(\mathbf{p})}{z - \varepsilon(\mathbf{s}) - \gamma\varepsilon(\mathbf{p} + \mathbf{s}) - \varepsilon(\mathbf{p})} \right). \end{aligned}$$

If we take into account the inequalities

$$\mu + 3(1 + \gamma) < z_{\mu,\gamma}(\boldsymbol{\pi}) \leq z_{\mu,\gamma}(\mathbf{k}) \leq z_{\mu,\gamma}(\mathbf{0}) < \mu + 3(1 + \gamma) + \frac{9(1 + \gamma)^2}{\mu} \leq z \quad (5.15)$$

for sufficiently large  $\mu > 0$ , from (5.12), we have

$$\Lambda_{\mu,\gamma}(\mathbf{p}, \tau_{\max,\gamma}(\mu, \mathbf{0})) = \frac{\mu(z - z_{\mu,\gamma}(\mathbf{p}) - \varepsilon(\mathbf{p}))}{[z_{\mu,\gamma}(\mathbf{p}) - 3 - 3\gamma][z - 6 - 3\gamma]} \left[ 1 + O\left(\frac{1}{\mu}\right) \right], \mu \rightarrow \infty.$$

Hence, again using the relations (5.15), one can make sure it's true (5.11).  $\square$

**Lemma 5.5.** Assume that  $\gamma > 0$ . Then there exists  $\mu_\gamma > 0$  such that for any  $\mu > \mu_\gamma$  satisfying

$$\|A_{\mu,\gamma}^{(2)}(z)\| \leq \frac{C}{\mu},$$

which is carried out uniformly  $z \geq \tau_{\max,\gamma}(\mu, \mathbf{0})$ ,  $C$  is positive real number depending only on  $\gamma$ .

*Proof.* Let  $\psi \in L_2(\mathbb{T}^3)$  and  $\|\psi\| = 1$ . Using the inequalities  $\xi(\mathbf{p}) \leq 3$  and  $E_{\mathbf{0},\gamma}(\mathbf{p}, \mathbf{s}) \geq 0$ , we get

$$\begin{aligned} \left| \left( A_{\mu,\gamma}^{(2)}(z)\psi, \psi \right) \right| &\leq \frac{\mu}{(z - 6 - 3\gamma)^2} \int_{\mathbb{T}^3} \int_{\mathbb{T}^3} \frac{(\xi(\mathbf{p}) + \xi(\mathbf{s}) + \gamma\xi(\mathbf{p} + \mathbf{s}))^2 |\psi(\mathbf{s})| |\overline{\psi(\mathbf{p})}| d\mathbf{s} d\mathbf{p}}{(z - E_{\mathbf{0},\gamma}(\mathbf{p}, \mathbf{s})) \sqrt{\Lambda_{\mu,\gamma}(\mathbf{s}, z)} \sqrt{\Lambda_{\mu,\gamma}(\mathbf{p}, z)}} \leq \\ &\leq \frac{\mu(6 + 3\gamma)^2}{(z - 6 - 3\gamma)^3} \int_{\mathbb{T}^3} \int_{\mathbb{T}^3} \frac{|\psi(\mathbf{s})| |\overline{\psi(\mathbf{p})}| d\mathbf{s} d\mathbf{p}}{\sqrt{\Lambda_{\mu,\gamma}(\mathbf{s}, z)} \sqrt{\Lambda_{\mu,\gamma}(\mathbf{p}, z)}} = \\ &= \frac{\mu(6 + 3\gamma)^2}{(z - 6 - 3\gamma)^3} \left( \int_{\mathbb{T}^3} \frac{|\psi(\mathbf{s})| d\mathbf{s}}{\sqrt{\Lambda_{\mu,\gamma}(\mathbf{s}, z)}} \right)^2. \end{aligned} \quad (5.16)$$

Since  $z > z_{\mu,\gamma}(\mathbf{p}) + 6 \geq \tau_{\max,\gamma}(\mu, \mathbf{0})$ , considering (5.10), if  $\mu > 6(1 + \gamma)$ , we get

$$\begin{aligned} \left( \int_{\mathbb{T}^3} \frac{|\psi(\mathbf{s})| d\mathbf{s}}{\sqrt{\Lambda_{\mu,\gamma}(\mathbf{s}, z)}} \right)^2 &\leq \left( \int_{\mathbb{T}^3} \sqrt{\frac{z_{\mu,\gamma}(\mathbf{s})z}{\mu(z - z_{\mu,\gamma}(\mathbf{s}) - \varepsilon(\mathbf{s}))}} |\psi(\mathbf{s})| d\mathbf{s} \right)^2 \leq \\ &\leq \frac{z^2}{\mu} \int_{\mathbb{T}^3} |\psi(\mathbf{s})|^2 d\mathbf{s} \int_{\mathbb{T}^3} \frac{d\mathbf{s}}{\varepsilon(\mathbf{s})}. \end{aligned} \quad (5.17)$$

Since

$$\frac{z}{z - 6 - 3\gamma} \leq 2, \quad z \geq \mu + 3(1 + \gamma),$$

from (5.16) and (5.17) at  $\mu > 6(1 + \gamma)$ , we have

$$\left| \left( A_{\mu,\gamma}^{(2)}(z)\psi, \psi \right) \right| \leq \frac{4(6 + 3\gamma)^2 W}{\mu \left( 1 - \frac{3}{\mu} \right)} \leq \frac{C_\gamma}{\mu},$$

where  $C_\gamma = 8(6 + 3\gamma)^2 W$ .  $\square$

## 6. Proofs of the main results

The following Lemma plays an important role in the proof of the main results.

**Lemma 6.1.** Assume that  $\gamma > 0$ . Then we obtain the following asymptotics:

$$\lambda_1(\tau_{\max,\gamma}(\mu, \mathbf{0})) = \frac{\gamma}{\gamma_1} + O\left(\frac{1}{\mu}\right), \quad (6.1)$$

$$\lambda_{2,3}(\tau_{\max,\gamma}(\mu, \mathbf{0})) = \frac{\gamma}{\gamma_2} + O\left(\frac{1}{\mu}\right), \quad (6.2)$$

where  $\gamma_1$  and  $\gamma_2$  are defined by formula (2.2).

*Proof.* Let us prove equality (6.2). Taking into account equalities (5.4), (5.5), (5.11) and (5.15), we have

$$\begin{aligned} \lambda_{2,3}(\tau_{\max,\gamma}(\mu, \mathbf{0})) &= \gamma \left( \frac{\mu}{(z_{\mu,\gamma}(\mathbf{0}) - 6 - 3\gamma)^2} \int_{\mathbb{T}^3} \frac{(\cos^2 s_1 - \cos s_1 \cos s_2) ds}{\Lambda_{\mu,\gamma}(\mathbf{s}, z_{\mu,\gamma}(\mathbf{0}))} \right) + O\left(\frac{1}{\mu}\right) = \\ &= \gamma \int_{\mathbb{T}^3} \frac{(\cos^2 s_1 - \cos s_1 \cos s_2) ds}{z_{\mu,\gamma}(\mathbf{0}) - \varepsilon(\mathbf{s}) - z_{\mu,\gamma}(\mathbf{s})} \left( 1 + O\left(\frac{1}{\mu}\right) \right) + O\left(\frac{1}{\mu}\right) = \\ &= \gamma \int_{\mathbb{T}^3} \frac{(\cos^2 s_1 - \cos s_1 \cos s_2) ds}{\varepsilon(\mathbf{s})} + O\left(\frac{1}{\mu}\right) = \frac{\gamma}{\gamma_2} + O\left(\frac{1}{\mu}\right). \end{aligned}$$

□

**Proof of Theorem 2.1 1.** *i)* Assume that  $\gamma \in (0, \gamma_1)$ . Then applying Lemma 5.5 and using (5.2), we obtain that there exists  $\mu_\gamma > 0$  such that for any  $\mu > \mu_\gamma$ , the operators  $A_{\mu,\gamma}(z)$  and  $A_{\mu,\gamma}^{(0)}(z)$  have the same number of eigenvalues greater than 1. From Lemma 5.1 and Lemma 5.2, we obtain

$$n \left[ 1, A_{\mu,\gamma}^{(1)}(z) \right] = n \left[ 1, A_{\mu,\gamma}^{(1,o)}(z) \right] + n \left[ 1, A_{\mu,\gamma}^{(1,e)}(z) \right] = n \left[ 1, A_{\mu,\gamma}^{(0,e)}(z) \right].$$

From the statement of Lemma 5.3, one can conclude that the operator  $A_{\mu,\gamma}^{(1,e)}(\tau_{\max,\gamma}(\mu, \mathbf{0}))$  have three eigenvalues  $\lambda_1(z), \lambda_{2,3}(z)$  taking into account the multiplicity. Since  $0 < \gamma < \gamma_1$ , the inequalities  $\lambda_1(\tau_{\max,\gamma}(\mu, \mathbf{0})) < 1$ ,  $\lambda_{2,3}(\tau_{\max,\gamma}(\mu, \mathbf{0})) < 1$  are valid for sufficiently large  $\mu > 0$ . By the Birman–Schwinger principle (see Lemma 4.3) the operator  $H_{\mu,\gamma}(\mathbf{0})$  has no eigenvalues  $z > \tau_{\max,\gamma}(\mu, \mathbf{0})$ .

The statements *ii)* and *iii)* can be proven similarly.

## References

- [1] Michelangeli A., Ottolini A. On point interactions realised as Ter-Martirosyan-Skorniyakov hamiltonians. *Rep. Math. Phys.*, 2017, **79**(2), P. 215–260.
- [2] Michelangeli A., Pfeiffer P. Stability of the (2+2)-fermionic system with zero-range interaction. *J. Phys. A Math. Theor.*, 2016, **49**, P. 105301.
- [3] Correggi M., Dell’Antonio G., Finco D., Michelangeli A., Teta A. Stability for a system of N fermions plus a different particle with zero-range interactions. *Rev. Math. Phys.*, 2012, **24**(7), P. 1250017.
- [4] Finco D., Teta A. Quadratic forms for the fermionic unitary gas model. *Rep. Math. Phys.*, 2012, **69**(2), P. 131–159.
- [5] Becker S., Michelangeli A., Ottolini A. Spectral Analysis of the 2+1 Fermionic Trimer with Contact Interactions. *Math. Phys. Anal. Geom.*, 2018, **21**, P. 35.
- [6] Winkler K., Thalhammer G., Lang F., Grimm R., Hecker Denschlag J., Daley A.J., Kantian A., Büchler H.P., Zoller P. Repulsively bound atom pairs in an optical lattice. *Nature*, 2006, **441**, P. 853–856.
- [7] Bloch I. Ultracold quantum gases in optical lattices. *Nat. Phys.*, 2005, **1**, P. 23–30.
- [8] Jaksch D., Zoller P. The cold atom Hubbard toolbox. *Ann. Phys.*, 2005, **315**(1), P. 52–79.
- [9] Thalhammer G., Theis M., Winkler K., Grimm R., Hecker Denschlag J. Inducing an optical Feshbach resonance via stimulated Raman coupling. *Phys. Rev. A*, 2005, **71**, P. 033403
- [10] Heo M.S., Wang T.T., Christensen C.A., Rvachov T.M., Cotta D.A., Choi J.H., Lee Y.R., Ketterle W. Formation of ultracold fermionic NaLi Feshbach molecules. *Phys. Rev. A*, 2012, **86**(2), P. 021602.
- [11] M. Lewenstein et al., Atomic Bose-Fermi mixtures in an optical lattice. *Phys. Rev. Lett.*, 2004, **92**, P. 050401.
- [12] Lakaev S.N., Dell’Antonio G.F., Khalkhuzhaev A.M. Existence of an isolated band of a system of three particles in an optical lattice. *J. Phys. A: Math. Theor.*, 2016, **49**(14), 145204/15.
- [13] Braaten E., Hammer H.W. Universality in few-body systems with large scattering length. *Phys. Rep.*, 2006, **428**, P. 259–390.
- [14] Giorgini S., Pitaevskii L.P., Stringari S. Theory of ultracold atomic Fermi gases. *Rev. Mod. Phys.*, 2008, **80**, P. 1215–74.
- [15] Lakaev S.N., Lakaev Sh. S. The existence of bound states in a system of three particles in an optical lattice. *J. Phys. A: Math. Theor.*, 2017, **50**(33), 335202/17.
- [16] Dell’Antonio G.F., Muminov Z.I. and Shermatova Y. M. On the number of eigenvalues of a model operator related to a system of three particles on lattices. *J. Phys. A: Math. Theor.*, 2011, **44**(31), P. 315302/27.
- [17] Lakaev S.N., Khalkhuzhaev A.M. On the number of eigenvalues of the two-particle discrete Schrodinger operator. (*Russian*) *Theoret. and Math. Phys.* 2009, **158**(2), P. 221–232.
- [18] Khalkhuzhaev A.M. The essential spectrum of the three-particle discrete operator corresponding to a system of three fermions on a lattice. *Russian Mathematics*, 2017, **61**(9), P. 67–78.

- [19] Reed M. and Simon B. *Methods of Modern Mathematical Physics VI: Analysis of Operators* New York, Academic Press, 1979.
- [20] Zucker I.J. 70+ Years of the Watson Integrals. *J. Stat. Phys.*, 2011, **145**(3), P. 591–612.
- [21] Faddeev L.D. Mathematical questions in the quantum theory of scattering for a system of three particles. *Trudy Mat. Inst. Steklov*, 1963, **69**, P. 3–122.
- [22] Lakaev S.N. On Efimov's effect in a system of three identical quantum particles. *Functional Analysis and Its Applications*, 1993, **27**, P. 166–175.
- [23] Pankov A.A. *Lecture Notes on Schrödinger equations*. Nova Science Publishers, New York. 2007.

---

*Submitted 3 July 2023; revised 13 September 2023; accepted 14 September 2023*

*Information about the authors:*

*Ahmad M. Khalkhuzhaev* – V.I. Romanovsky Institute of Mathematics of the Academy of Sciences of the Republic of Uzbekistan, Tashkent, Mirzo Ulugbek 81, 100170; ORCID 0009-0003-0569-6780; ahmad.x@mail.ru

*Islom A. Khujamiyrov* – Samarkand State University, University Boulevard 15, Samarkand 140104, Uzbekistan; ORCID 0000-0001-5439-8729; xujamiyrov1990@mail.ru

*Conflict of interest:* the authors declare no conflict of interest.

## Composite hydroxyapatite-multi-walled carbon nanotubes: study of porosity by terahertz time domain spectroscopy

Anastasiya E. Rezvanova<sup>1,a</sup>, Boris S. Kudryashov<sup>1,b</sup>, Alexander N. Ponomarev<sup>1,c</sup>,  
Anastasiya I. Knyazkova<sup>2,d</sup>, Victor V. Nikolaev<sup>2,e</sup>, Yuri V. Kistenev<sup>2,f</sup>

<sup>1</sup>Institute of Strength Physics and Materials Science of the Siberian Branch of the Russian Academy of Sciences, Tomsk, Russia

<sup>2</sup>Tomsk State University, the Faculty of Physics, Tomsk, Russia

<sup>a</sup>ranast@ispms.ru, <sup>b</sup>bsk3@ispms.ru, <sup>c</sup>alex@ispms.ru, <sup>d</sup>a.knyazkova@bk.ru, <sup>e</sup>vik-nikol@bk.ru, <sup>f</sup>yuk@iao.ru

Corresponding author: A.E. Rezvanova, ranast@ispms.ru; B.S. Kudryashov, bsk3@ispms.ru

PACS 42.25.Gy, 42.25.-p, 33.60.Fy, 07.79.Fc

**ABSTRACT** Optical properties of a ceramic biocomposite material based on hydroxyapatite (HA) with the additives up to 0.5 wt.% of multi-walled carbon nanotubes (MWCNTs) have been studied by terahertz time-domain spectroscopy in the frequency range 0.25 – 1.1 THz. It was found that the refractive index of the composite varies between 2.6 and 2.8 depending on the porosity of the material. The absorption coefficient decreases with increasing of MWCNTs concentration in the ceramic biocomposite. The values of the refractive index and the absorption coefficient of our ceramics close to those for cortical bone, dentine and enamel. The absorption curves show frequency peaks whose positions correspond to the macrocrystallite sizes. The size of macrocrystallites decreases with increasing concentration of MWCNTs, which leads to an increase in microhardness according to the Hall–Petch equation. The time delay of the terahertz signal through the sample increases for higher concentration of MWCNTs. This indicates that nanotubes embedded into the HA matrix fill the pores and decrease the area of the pore space, which increases the density of the ceramic composite and decreases its porosity.

**KEYWORDS** ceramic composite, hydroxyapatite, multi-walled carbon nanotubes, terahertz spectroscopy, porosity

**ACKNOWLEDGEMENTS** The work by Rezvanova, Ponomarev, and Kudryashov was performed within the Government Statement of Work for the ISPMS SB RAS, project FWRW-2022-0002 and FWRW-2021-0007. The research by Knyazkova, Nikolaev, and Kistenev was supported by the grant under RF Government Decree No. 220 dated 09 April 2010 (Agreement No. 075-15-2021-615 of 04 June 2021). The authors are grateful to A. A. Neiman from the Nanotekh Regional Core Facility Centre of the Institute of Strength Physics and Materials Science SB RAS for his help with SEM images.

**FOR CITATION** Rezvanova A.E., Kudryashov B.S., Ponomarev A.N., Knyazkova A.I., Nikolaev V.V., Kistenev Yu.V. Composite hydroxyapatite-multi-walled carbon nanotubes: study of porosity by terahertz time domain spectroscopy. *Nanosystems: Phys. Chem. Math.*, 2023, **14** (5), 530–538.

### 1. Introduction

Calcium phosphate biomaterials, such as hydroxyapatite (HA), have excellent biocompatibility, bioactivity, osteoconductivity, and long degradation time. It makes them applicable in producing bone implants for orthopedic and dental medicine [1, 2]. Porosity is one of the important properties of biomedical materials, which is defined as the ratio of the void volume to the total volume of a porous material. The influence of porosity on the mechanical properties from one side and degradation, biocompatibility, and osteogenesis of the bioceramic scaffold, from the other side, should be taken into account in the design of such implants [3]. Porosity plays a significant role in bone tissue regeneration [4], crack propagation and fracture toughness of HA ceramics [5]. The porosity of HA ceramics depends on the amount of the multi-walled carbon nanotubes (MWCNTs) additives [5, 6]. MWCNTs additives increase the density of HA-MWCNTs composites by activating the sintering process in ceramics [2, 6].

The porosity of ceramic materials, the total porosity of open and closed pores can be measured by destructive and non-destructive methods [7–11]. Destructive methods include liquid pycnometry [7] and mercury porosimetry [8] that based on invasive analysis. These methods have several disadvantages including the destruction of a sample, losing mechanical and other properties.

The most common nondestructive methods are small-angle neutron scattering [9], transmission electron microscopy [10], the nuclear magnetic resonance method [11], etc. These methods allow one to carry out a noncontact,

noninvasive and fast analysis of the material porosity. The method of terahertz time-domain spectroscopy (THz-TDS) can be also used for this purpose. It holds certain advantages. The THz method [12] consists in recording the temporal shape of a terahertz electric field pulse after passing through the material matrix and analyzing it using the fast Fourier transform. Terahertz electromagnetic waves can penetrate through various materials, such as biomaterials, including polymers and ceramic materials, thereby providing their spectroscopic data [13]. The photon energy of THz waves is several orders of magnitude lower than the quantum energy of the X-ray wave. That is why the THz wave is a more efficient tool for nondestructive noncontact investigation [14, 15].

The analysis of the behavior of a THz pulse propagating through a sample makes it possible to determine such optical properties as absorption coefficient, refractive index, and THz pulse propagation time delay, which are used to estimate the material porosity [13]. The nonionizing radiation between 0.5 and 1.5 THz enables safe investigation of optical properties of human tissues and tissue replacement materials [16]. THz-TDS was used for *in vitro* studies of refractive indices and absorption coefficients of the jawbone [12], tooth enamel [17], dentin [17], cortical bone [18] and femoral bone [19]. The refractive index of enamel is bigger than that of dentin, while absorption has a similar frequency dependence [17]. In [20] the possibility of using THz spectroscopy for diagnosing dental caries is observed. It was shown, that the attenuation of the THz signal during caries is significantly higher than the one for healthy teeth.

The aim of this work is to study the optical properties of a porous ceramic biocomposite material by noninvasive THz time-domain spectroscopy in the frequency range 0.25 – 1.1 THz. The studies were performed on HA-based ceramic samples with different concentrations of MWCNTs (up to 0.5 wt.%). Refractive index, absorption coefficient and time delay of the terahertz pulse propagation through the HA-MWCNTs ceramic composite material were determined.

## 2. Materials and methods

### 2.1. HA-MWCNTs composites

The object of terahertz (THz) studies is a ceramic composite material with the hydroxyapatite (HA) matrix. The additives of multi-walled carbon nanotubes (MWCNTs) are used for reinforcement and control of porosity of the HA material structure. The studies were carried out on three sample sets: the HA and HA with 0.1 and 0.5 wt.% MWCNTs additives.

Hydroxyapatite was synthesized from calcium carbonate and orthophosphoric acid:  $5\text{CaCO}_3 + 3\text{H}_3\text{PO}_4 + \text{Ca}_5(\text{PO}_4)_3\text{OH} + 4\text{H}_2\text{O} + 5\text{CO}_2$ . The HA powder was calcinated at the temperature 850 °C for 1 h in wet atmosphere and then mixed with the MWCNTs powder [6, 21, 22]. MWCNTs with the mean diameter 18 nm were prepared using the chemical vapor deposition (CVD) method [23, 24] and characterized by the calorimetric, scanning electron microscopy (SEM), Energy Dispersive X-ray microanalysis (EDX), X-ray photoelectron spectroscopy (XPS), transmission electron microscope (TEM) and near edge X-ray absorption fine structure (NEXAFS) spectroscopy [25–27]. The MWCNTs powder contains a small amount of the Co/Fe catalyst (less than 0.3 wt.%) and has a high-quality surface with a small number of defects and other impurities.

Cylindrical samples were prepared under the pressure 120 MPa and subsequent annealing at the temperature 1100 °C in argon atmosphere for 1 hour [2, 5]. The thickness and diameter of the ceramic samples are  $3 \pm 0.1$  mm and  $8 \pm 0.05$  mm, respectively. The porosity was calculated using the theoretical density  $3.167 \text{ g/cm}^3$  of stoichiometric HA [5]. The density of samples is varied from 8 to 27.5 % by changing the concentration of nanotubes.

This is consistent with a decrease in porosity near 3 times for HA+0.5 wt.% MWCNTs in comparison to HA without MWCNTs additives, that was found by the Brunauer–Emmett–Teller (BET)-method [28]. MWCNTs in the composite fill the pores between the HA grains, according for SEM characterization [2, 28].

### 2.2. Sample characterization

NEXAFS spectra of HA and HA with the additives of the MWCNTs were measured at the RGL-PES station of the 3rd generation synchrotron radiation source BESSY II (Berlin, Germany) in high-vacuum conditions ( $\sim 10^{-10}$  Torr). The samples were degassed in dynamic high-vacuum conditions for more than 12 hours. Leakage current mode of the Keithley picoammeter was used for obtaining the NEXAFS spectra. The depth of the NEXAFS analysis was 15 – 20 nm. The spectra were used to analyze the chemical state and the local atomic structure of carbon in the MWCNTs. The NEXAFS spectra were normalized to the recorded contemporaneously of primary flux from a gold covered grid. The energy resolution of the monochromator in the ranges of the carbon K-edge ( $h\nu \sim 285 \text{ eV}$ ) was equal to  $\sim 70 \text{ meV}$ .

The SEM images of the samples were obtained and characterized by using Zeiss EVO-50 field emission SEM (Carl Zeiss SMT Ltd.) at the accelerating voltage of 15.0 kV.

Optical characteristics of HA-MWCNTs were analyzed using a T-SPEC spectrometer (EKSPLA, Estonia). It operates in the frequency range 0.25 – 1.3 THz in the transmission mode. Sketch of T-SPEC spectrometer [29] is shown in Fig. 1(a). It has 4 main components:

- femtosecond pulse laser in the near-infrared range;
- terahertz emitter (photoconductive antenna, i.e. an optically activated fast switch built into the antenna structure);
- delay mechanism between the pumping and probing beams;

— THz detector with time synchronization.

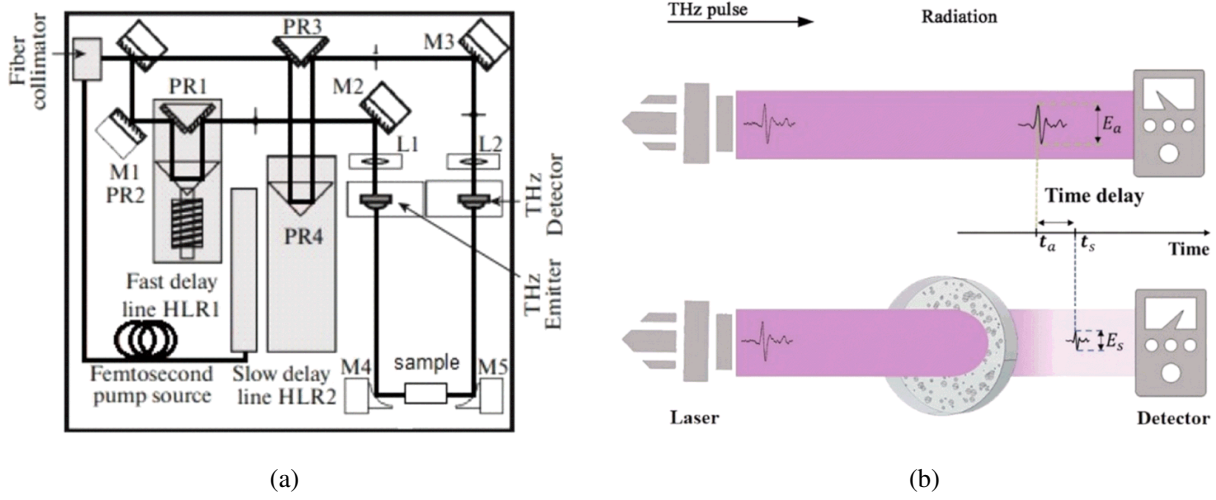


FIG. 1. (a) T-SPEC Real-Time Terahertz Spectrometer: M1, M2, M3, M4, M5 – mirrors, L1, L2 – lenses, PR1, PR2, PR3, PR4 – prisms, HLR1 – fast delay line, HLR2 – slow delay line; (b) sketch of the terahertz pulse propagations through air and a sample

The femtosecond fiber laser is used at the pulse duration 10 – 150 fs, central wavelength  $1050 \pm 40$  nm, pulse repetition rate 30 – 100 MHz, and power 100 mW. The laser output radiation is divided into two optical paths – the pumping and probing beams – by using the polarizing beam splitter (BS1). After the HLR1 delay line, the pumping beam is focused on the source of subpicosecond pulses of THz radiation (photoconductive antenna). The terahertz beam is focused on a sample spot using parabolic mirrors. The photoconductive output of the THz detector is proportional to the strength of the instantaneous electric field of the THz pulse generated during the ultrashort pumping pulse. Scanning with a fast delay line at the frequency 10 Hz forms the wave front of the electric field of THz radiation.

Sample response and a reference measurement are used to calculate the refractive index and absorption coefficient. The collected data then processed using the Fourier transform [30, 31]. In the transmission mode, the temporal response of the detector (time domain) is converted into the frequency characteristic of detector (frequency domain). If electric field strengths of the reference (in air medium without sample) and sample signals are denoted by  $E_a(\omega)$  and  $E_s(\omega)$ , respectively, the ratio between the sample and reference pulses can be written as (1):

$$\frac{E_a(\omega)}{E_s(\omega)} = A e^{i\Delta\varphi}, \quad (1)$$

where  $A$  is the magnitude of the ratio and  $\Delta\varphi$  is the phase difference. It can also be written as (2):

$$\frac{E_s(\omega)}{E_a(\omega)} = T(\omega) e^{i\frac{\omega}{c}(\widehat{n}_s - 1)d}, \quad (2)$$

where  $\omega$  is the angular frequency,  $c$  is the speed of light,  $T(\omega)$  is the Fresnel transmission coefficient,  $d$  is the sample thickness, and  $\widehat{n}_s$  is the frequency-dependent complex refractive index of the sample. The value of  $\widehat{n}_s$  is the sum of the two components: the refractive index  $n_s(\omega)$  and the absorption (extinction) coefficient  $k_s(\omega)$  (3):

$$\widehat{n}_s(\omega) = n_s(\omega) + k_s(\omega). \quad (3)$$

A sketch of the terahertz pulse propagations through the air and the ceramic sample during measurements is shown in Fig. 1(b).

The signal  $E_a(\omega)$  propagates for time  $t_a$  during the measurements of a reference pulse in the absence of a sample. In the second measurement during the THz pulse propagates through the sample, the signal intensity decreases  $E_s(\omega) < E_a(\omega)$  and the signal propagation time increases  $t_s < t_a$ , that lead to the time delay  $\Delta t = t_a - t_s$  of the THz pulse propagation through a denser medium.

The refractive index  $n_s$  of the sample is obtained using the phase delay, according to Eq. (4):

$$n_s = 1 + \frac{c}{\omega d} \Delta\varphi. \quad (4)$$

The Fresnel transmission coefficient  $T(\omega)$  is evaluated by using the calculated refractive index  $n_s$ . The absorption coefficient  $a_s$  is calculated by Eq. (5):

$$a_s = \frac{2\omega k_s}{c} = -\frac{2}{d} \ln \left( \frac{A}{T(\omega)} \right). \quad (5)$$

The sample is placed in the path of propagation of THz radiation in a special metal cell-holder. First, rough 2D scanning is performed over the entire surface of the sample (the scan area  $3.6 \times 3.6$  mm and the vertical and horizontal scan step 0.25 mm). Then, the THz signal propagating through the center of the cell (the scan area  $1.5 \times 1.5$  mm and the vertical and horizontal scan step 0.5 mm) is recorded, which makes it possible to avoid artifacts due to the metal cell-holder. Nine measurements were performed on each sample. The spectrum was averaged over 256-ps intervals to obtain a better signal-to-noise ratio.

Data are visualized using the TeraVil program for the T-SPEC spectrometer. Statistical analysis and data processing are carried out in Python 3.6 using libraries (numpy, scipy, matplotlib) and GNU Octave 6.4.0. free software.

### 3. Results and discussion

The density of the unoccupied states of carbon and the local atomic structure of HA-MWCNTs were investigated by the XANES method (see Fig. 2). The atomic and electronic structures of HA-MWCNTs depend on the concentration of MWCNTs. NEXAFS absorption spectra for the initial MWCNTs that used as the additives in the composite ceramics is shown in Fig. 2 for comparison [25]. For MWCNTs the structure of the  $\pi^*$ (C=C) resonance at the photon energy  $\sim 285$  eV,  $\sigma^*$ (C=C) resonance at  $\sim 291$  eV is observed [25]. For composites HA with MWCNTs observed the presence of the  $\pi^*$ (C=O) and  $\sigma^*$ (C-O) states that can indicate the possible oxidation of the MWCNTs from water produced during the dehydroxylation of HA. It is seen that with the increasing of the concentration of MWCNTs additives the intensity of  $\pi^*$ (C=C) and  $\sigma^*$ (C=C) chemical bonds decreases and at the same time the intensity with energy near 284 eV increase, that apparently related to the decomposition of MWCNTs and increasing the amount of amorphous carbon. Therefore, it is possible to assume that the presence of the MWCNTs leads to the activation of sintering processes of HA ceramics and increase of density. The partial carbonization of HA ceramics with the MWCNTs additives was indicated by the results of FT-IR studies [2]. With increasing of the amount of nanotubes in composite ceramics, the intensity of the carbonate stretching band of FT-IR spectra increases due to partial oxidation of the nanotubes and as a result more intensive carbonization of the A-type HA [2].

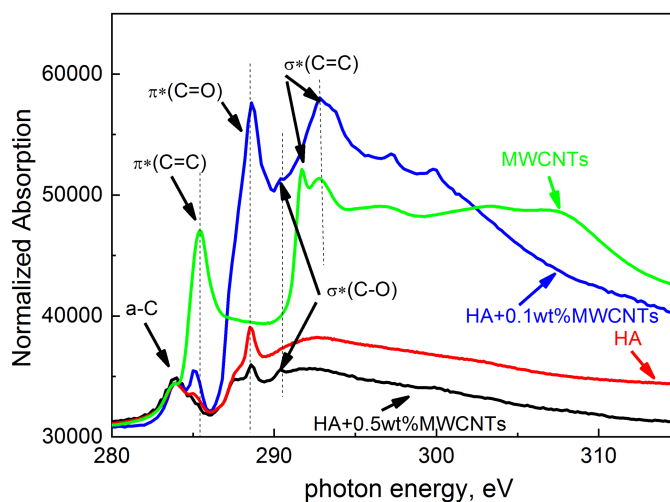


FIG. 2. XANES spectra of initial MWCNTs (green curve), HA (red curve), HA with 0.1 wt.% MWCNTs (blue curve) and HA with 0.5 wt.% MWCNTs (black curve)

The temporal wave forms of the field of the THz pulses transmitted through the air (reference) and composite HA ceramics and HA with the MWCNTs concentrations 0.1 and 0.5 wt.% were obtained by measurements of electric field strengths. The total number of such wave forms was 54. The dependencies for the electric field strength on the time of THz pulse propagation through the air and ceramics HA, HA+0.1 wt.% MWCNTs and HA+0.5 wt.% MWCNTs are shown in Fig. 3(a).

As it is seen in Fig. 3(a), the time delay appears between the THz pulse through the air (reference) and ceramic sample. The THz signal propagation time for the reference and the sample were measured by the THz detector with time synchronization, and the time delay of the pulse was determined as the difference between the main time peaks of the reference and the sample.

Figure 3(b) shows the linear dependence of the THz pulse time delay vs. the MWCNTs concentration and the porosity of the ceramic biocomposite. The time delay increases with a decreasing of the porosity [32,33]. It is seen in the Fig. 3(b) that the time delay increases with increasing of the amount of MWCNTs in the HA bioceramic composite. This indicates that the additives of MWCNTs lead to denser HA ceramics, decreasing its porosity [2, 6]. It is shown that the porosity of HA ceramic composite linearly depends on the time delay.

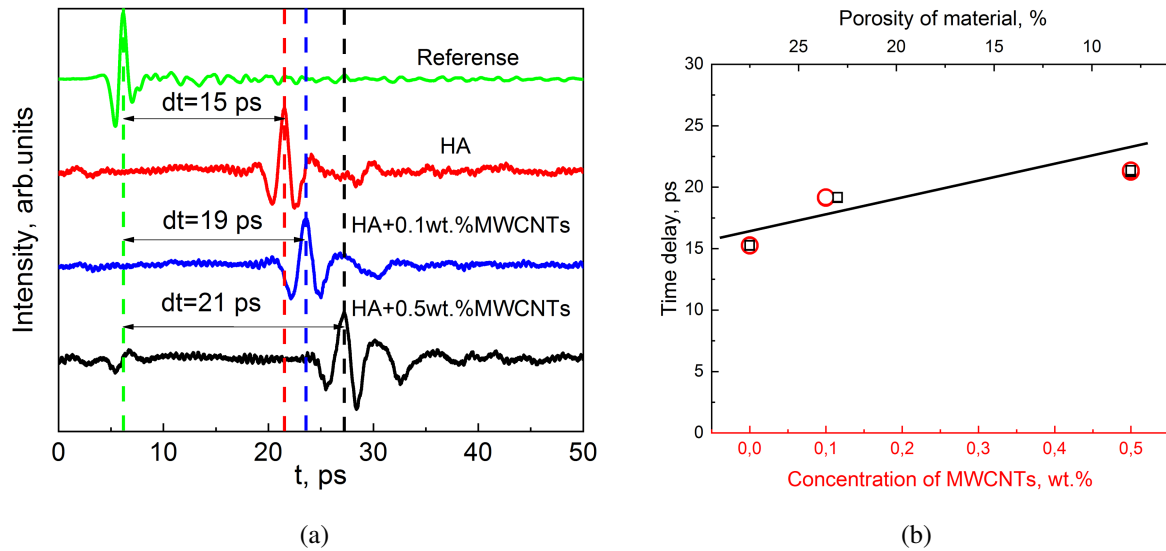


FIG. 3. (a) Dependencies of the electric field strength on the time of THz pulse propagation through the air (green curve), HA ceramics (red curve), HA+0.1 wt.% MWCNTs ceramics (blue curve), HA+0.5 wt.% MWCNTs ceramics (black curve); (b) the THz pulse propagation time delay dependence on the MWCNTs concentration (open circles) and the porosity of the composite (open square). The line is mean values of the time delay.

In addition, the frequency dependencies of the refractive index (Fig. 4(a)) and absorption coefficient (Fig. 4(b)) for the studied samples are obtained. Error bars are presented standard deviation obtained from 6 measurements for each sample. The refractive index  $n_s$  and the absorption coefficient  $a_s$  in the frequency range 0.25 – 1.1 THz are obtained by using Eqs. (4) and (5), respectively. It is seen that, the absorption coefficient  $a_s$  decreases with increasing of the MWCNTs concentration up to 0.5 wt.% (Fig. 4(b)). The HA sample without nanotubes has the highest absorption coefficient, which indicates the largest porosity of the sample.

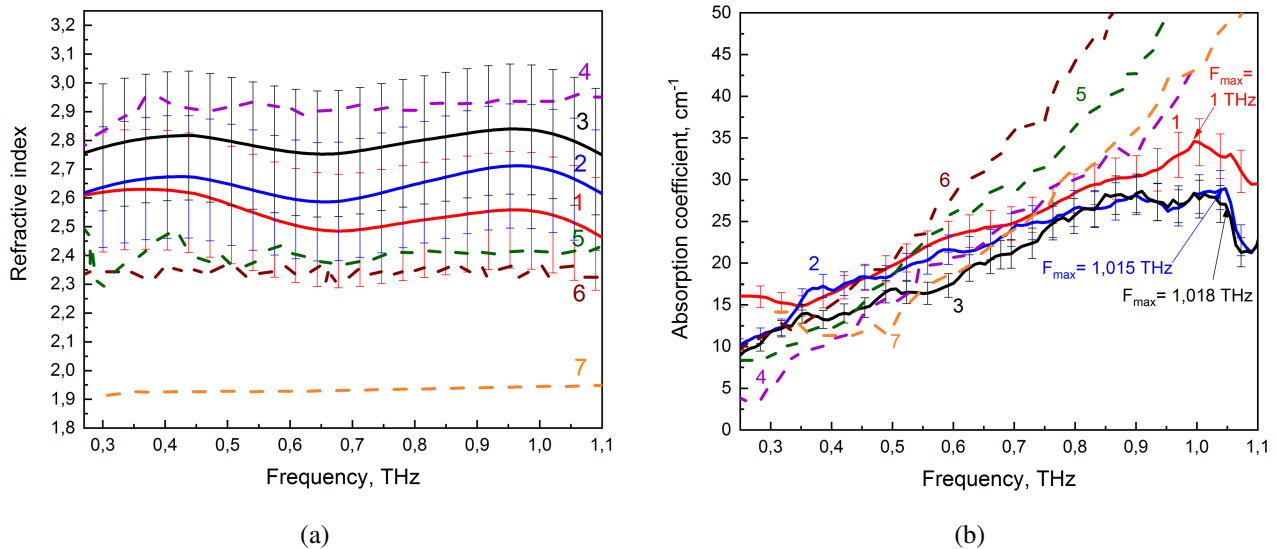


FIG. 4. (a) Frequency dependence of the refractive index  $n$ : HA (solid red curve – 1), HA+0.1 wt.% MWCNTs (solid blue curve – 2), HA+0.5 wt.% MWCNTs (solid black curve – 3). Refractive indices of enamel (pink dash curve – 4), dentin [20] (green dash curve – 5), cortical human bone [14, 19] (dash brown curve – 6, dash orange curve – 7) are added for comparison; (b) Frequency dependence of the absorption coefficient  $a$ : HA (solid red curve – 1), HA+0.1 wt.% MWCNTs (solid blue curve – 2), HA+0.5 wt.% MWCNTs (solid black curve – 3). Absorption coefficients of enamel [17] (dash purple curve – 4), dentin [17] (dash green curve – 5), cortical human bone [14, 19] (dash brown curve – 6, dash orange curve – 7) were added for comparison.

The opposite effect was observed for rubber with MWCNTs additives. The absorption coefficient of rubber was increased with increasing concentration of MWCNTs, since MWCNTs are electrically conductive materials, while density and porosity of rubber were slightly changed [34, 35]. For HA composites the MWCNTs additives lead to the sintering activation and as the result, for the increase of the density and decrease of the porosity [6]. The HA ceramic sample without nanotubes additives has the highest absorption coefficient, which indicates the largest porosity of the sample. The HA sample without nanotubes has porosity  $\sim 27.5\%$ , which is  $\sim 3$  times higher than that of the HA sample with 0.5 wt.% MWCNTs [5]. It is seen from these comparisons that the influence of MWCNTs additives to the absorption coefficient of HA and rubber are different due to the larger structural inhomogeneity of the HA composite in comparison to the rubber.

It is seen in Fig. 4(a) that the refractive indices of our ceramic samples (curves 1 – 3) indicate the same dependence in the frequency range 0.25 – 1.1 THz. It was shown that average refractive index increases from 2.6 to 2.8 with increasing of concentration of nanotubes in the HA ceramics. In different literature data of THz refractive indices for human cortical bones are as follows:  $n_s \sim 1.9$  (curve 6) and 2.5 (curves 7) [14, 19]. In addition, the refractive values for enamel tissue are  $\sim 3.1$  [17, 20, 36] and for dentin  $\sim 2.3$  (curves 4, 5) [17, 20, 37]. The obtained results allow us to conclude that the HA with the additives of MWCNTs have the proximity of the physical properties of the ceramic material to the enamel and dentin.

In Fig. 4(b), the absorption coefficients of ceramic samples HA (curve 1) and HA-MWCNTs (curve 2 and 3) are shown. The absorption coefficients,  $a$ , obtained in our experiment (curves 1 – 3) are lower than that for cortical human bones [14, 19] (curves 6 and 7), but are close to values of absorption for enamel and dentin (curves 4 and 5) [17, 36, 37].

As for the frequency dependence of  $a$  for the HA without additives (curve 1), it shows a maximum peak at frequency  $\sim 1$  THz. For the HA with 0.1 wt.% MWCNTs (curve 2) and 0.5 wt.% MWCNTs additives (curve 3), the values of the maximum peaks are slightly shifted to higher frequency. A possible reason for this phenomenon may be an increase of noise intensity with increasing in frequency or other reasons. Plazanet et al. [38] found that the maximum peaks for pure non-stoichiometric HA is not observed in the frequency range from 0 to 2.25 THz. However, the absorption coefficient peak for the same HA heated to 1000 °C was found at frequency of 2 THz.  $\alpha$ -TCP,  $\beta$ -TCP and stoichiometric (s-HA) were also observed at frequency 2.1 THz. The vibrational band is intense and narrow for s-HA [38].

It can be assumed that the position of the frequency maximum corresponds to the grain size (macrocrystallites), which increase due to recrystallization of HA ceramics during heating [38]. The diameters of macrocrystallites ( $D \sim 100 \mu\text{m}$ ) were estimated by Eq. (6):

$$D = \frac{c}{fn}, \quad (6)$$

where  $c$  is the speed of light,  $f$  is the frequency,  $n$  is the refractive index.

The addition of MWCNTs leads to a small (about 10  $\mu\text{m}$ ) decreasing of  $D$ . In Fig. 5, the dependence of the Vickers hardness as a function of  $D^{-0.5}$  was plotted by using the previous experimental the Vickers hardness values [5] and the estimated macrocrystallite sizes.

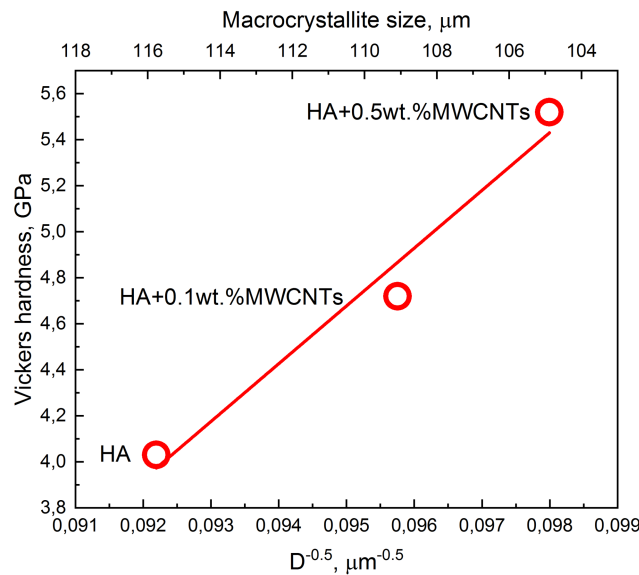


FIG. 5. Dependence the macrocrystallites sizes on the Vickers microhardness

It is seen in Fig. 5 that the hardness linearly increases with increasing concentration of nanotubes. It may be due to a decreasing in the size of macrocrystallites according to the Hall–Petch [39, 40], Eq. (7):

$$H = H_0 + k_h D^{-0.5}, \quad (7)$$

where  $H$  is the hardness, a  $H_0$  and  $k_h$  are the material-specific constants related to hardness measurements.

We also estimate dimensionless size-parameter [41]  $x \sim \pi$  by Eq. (8):

$$x = \frac{\pi D}{\lambda} = \frac{\pi D n f}{c}, \quad (8)$$

where  $D$  is the diameter of the macrocrystallites.

Previously, it was found that the X-ray diffraction peaks are slightly shifted for our samples in comparison with HA standard (JCPDS-09-0432/1996). This shift indicates the homogeneous internal macrostresses in the HA ceramics [6]. Such macrostresses can arise from the result of the low thermal diffusivity due to heterogeneous heating/cooling of the ceramics during sintering. Fig. 6 shows SEM image of agglomerates of HA powder with sizes distribution histogram. It is seen, that the average size of such macrocrystallites takes the value  $D \sim 113.2 \mu\text{m}$ . The experimental study of particles sizes corresponds to analytical calculation of the macrocrystallites sizes of HA ceramics with MWCNTs additives by using Eq. (6). A decrease in the diameters of microcrystallites in Fig. 5 is arising from the activation of the sintering process as a result of adding MWCNTs. It leads to the decrease of macrostresses between the crystallites and an increase of microhardness of the composite materials [2, 6].

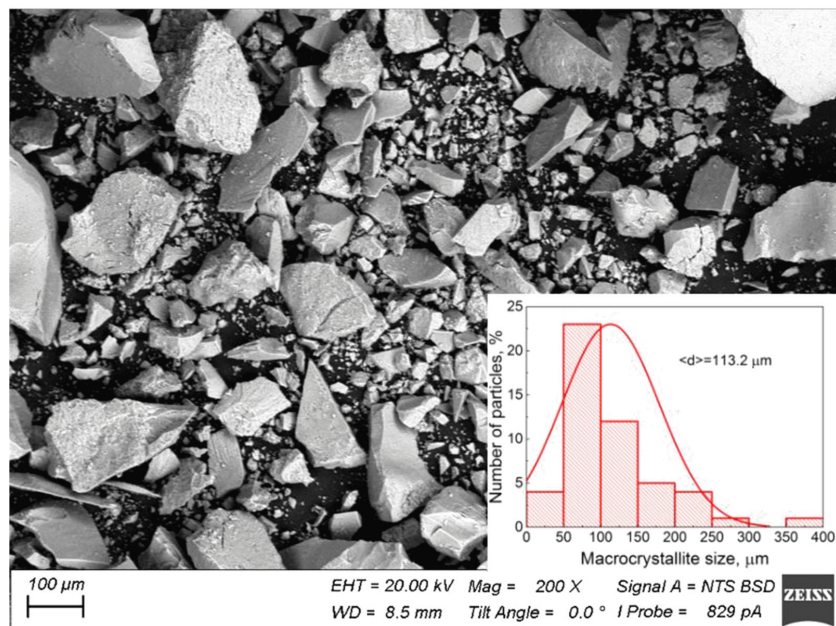


FIG. 6. SEM image of HA macrocrystallites

#### 4. Conclusions

In this work, we used terahertz time-domain spectroscopy and optical parameters in the frequency range 0.25 – 1.1 THz to study the porous structure of a hydroxyapatite (HA) ceramics and HA ceramics reinforced with 0.1 and 0.5 wt.% multi-walled carbon nanotubes (MWCNTs). This method, based on the detection of the terahertz pulse time delay, provides information about porosity of the composites.

With an increasing in the MWCNTs concentration in the material, the time delay of the terahertz pulse propagation through the sample matrix increases. This indicates that nanotubes embedded into the HA matrix fill the pores and decrease the area of the pore space, which increases the density of the ceramic composite and decreases its porosity.

Frequency dependencies of the absorption coefficient and refractive index of HA and HA-MWCNTs ceramics were obtained for the studied samples. The obtained values show that the optical properties of the composite can be controlled by the addition of nanotubes to HA ceramics. It is shown, that with increasing concentration of nanotubes (up to 0.5 wt.%), the absorption coefficient decreases. The HA sample without MWCNTs has the highest absorption coefficient. With increasing of the MWCNTs concentration, the refractive index increases from 2.6 to 2.8, which correlates with a decrease in porosity. The values of the refractive index and the absorption coefficient of our ceramics are close to those for cortical bone, dentine and enamel. The obtained results allow us to conclude that the HA composites with additives of MWCNTs up to 0.5 wt.% have the proximity of the optical properties to the natural bone matrix.

In addition, the absorption curves show frequency peaks whose positions correspond to the grain (macrocrystallite) sizes. The size of macrocrystallites  $D$  decreases with increasing concentration of MWCNTs. This leads to an increase in the microhardness according to the Hall–Petch equation.

Thus, it was found that addition of nanotubes to ceramics makes it possible to control porosity, which affects the optical properties of the ceramic materials. This bears witness to the relation between the optical properties and porosity of the HA-MWCNTs ceramic biocomposite.

## References

- [1] Fiume E., Magnaterra G., Rahdar A., Verné E., Baino F. Hydroxyapatite for biomedical applications: A short overview. *Ceramics*, 2021, **4** (4), P. 542–563.
- [2] Barabashko M.S., Tkachenko M.V., Neiman A.A., Ponomarev A.N., Rezvanova A.E. Variation of Vickers microhardness and compression strength of the bioceramics based on hydroxyapatite by adding the multi-walled carbon nanotubes. *Appl. Nanosci.*, 2019, **10** (8), P. 2601–2608.
- [3] Han Y., Wei Q., Chang P., Hu K., Okoro O.V., Shavandi A., Nie L. Three-dimensional printing of hydroxyapatite composites for biomedical application. *Crystals*, 2021, **11** (4), 353.
- [4] Ebrahimi M. Porosity parameters in biomaterial science: Definition, impact, and challenges in tissue engineering. *Front. Mater. Sci.*, 2021, **11** (4), 353.
- [5] Ponomarev A.N., Barabashko M.S., Rezvanova A.E., Evtushenko E.P. Influence of Porosity on Fracture Toughness of Hydroxyapatite/Multi-Walled Carbon Nanotubes Biocomposite Materials. *Russ. Phys. J.*, 2021, **63** (11), P. 1885–1890.
- [6] Barabashko M.S., Tkachenko M.V., Rezvanova A.E., Ponomarev A.N. Analysis of temperature gradients in the hydroxyapatite ceramics with the additives of multi-walled carbon nanotubes. *Russ. J. Phys. Chem.*, 2021, **95** (5), P. 1017–1022.
- [7] Sreedhara S.S., Tata N.R. A novel method for measurement of porosity in nanofiber mat using pycnometer in filtration. *J. Eng. Fiber. Fabr.*, 2013, **8** (4), 155892501300800.
- [8] Giesche H. Mercury porosimetry: A general (practical) overview. *Part. Part. Syst. Charact.*, 2006, **23** (1), P. 9–19.
- [9] Hollamby M.J. Practical applications of small-angle neutron scattering. *Phys. Chem. Chem. Phys.*, 2013, **15** (26), P. 10566–10579.
- [10] Chalmers G.R., Bustin R.M., Power I.M. Characterization of gas shale pore systems by porosimetry, pycnometry, surface area, and field emission scanning electron microscopy/transmission electron microscopy image analyses: Examples from the Barnett, Woodford, Haynesville, Marcellus, and Doig units. *Am. Assoc. Pet. Geol. Bull.*, 2012, **96** (6), P. 1099–1119.
- [11] Mitchell J., Webber J., Strange J. Nuclear magnetic resonance cryoporometry. *Phys. Rep.*, 2008, **461** (1), P. 1–36.
- [12] Nikoghosyan A.S., Ting H., Shen J., Martirosyan R.M., Tunyan M.Y., Papikyan A.V., Papikyan A.A. Optical properties of human jawbone and human bone substitute Cerabone® in the terahertz range. *J. Contemp. Phys.*, 2016, **51** (3), P. 256–264.
- [13] Bawuah P., Markl D., Farrell D., Evans M., Portieri A., Anderson A., Goodwin D., Lucas R., Zeitler J.A. Terahertz-based porosity measurement of pharmaceutical tablets: A tutorial. *J. Infrared, Millimeter, Terahertz Waves*, 2020, **41** (4), P. 450–469.
- [14] Stringer M.R., Lund D.N., Foulds A.P., Uddin A., Berry E., Miles R.E., Davies A.G. The analysis of human cortical bone by terahertz time-domain spectroscopy. *Phys. Med. Biol.*, 2005, **50** (14), P. 3211–3219.
- [15] Kistenev Y.V., Nikolaev V.V., Kurochkina O.S., Borisov A.V., Sandykova E.A., Krivova N.A., Tuchina D.K., Timoshona P.A. Use of terahertz spectroscopy for in vivo studies of lymphedema development dynamics. *Opt. Spectrosc.*, 2019, **126** (5), P. 523–529.
- [16] Sudworth C.D., Fitzgerald A.J., Berry E., Zinov'ev N.N., Homer-Vanniasinkam S., Miles R.E., Chamberlain M., Smith M.A. The optical properties of human tissue at terahertz frequencies. *European Conference on Biomedical Optics*, 2003, **5143**, P. 59–68.
- [17] Sim Y.C., Maeng I., Son J.-H. Frequency-dependent characteristics of terahertz radiation on the enamel and dentin of human tooth. *Curr. Appl. Phys.*, 2009, **9** (5), P. 946–949.
- [18] Berry E., Fitzgerald A.J., Zinov'ev N.N., Walker G.C., Homer-Vanniasinkam S., Sudworth C.D., Miles R.E., Chamberlain J.M., Smith M.A. Optical properties of tissue measured using terahertz-pulsed imaging. *Proceedings of SPIE*, 2003, **5030**, P. 459–470.
- [19] Bessou M., Chassagne B., Caumes J.-P., Pradère C., Maire P., Tondusson M., Abraham E. Three-dimensional terahertz computed tomography of human bones. *Appl. Opt.*, 2012, **51** (28), P. 6738–6744.
- [20] Cai J., Guang M., Zhou J. et al. Dental caries diagnosis using terahertz spectroscopy and birefringence. *Optics Express*, 2022, **30** (8), P. 13134–13147.
- [21] Zyman Z., Ivanov I., Rochmistrov D., Glushko V., Tkachenko N., Kijko S. Sintering peculiarities for hydroxyapatite with different degrees of crystallinity. *J. Biomed. Mater. Res.*, 2001, **54** (2), P. 256–263.
- [22] Zyman Z.Z., Tkachenko M.V., Polevodin D.V. Preparation and characterization of biphasic calcium phosphate ceramics of desired composition. *J. Mater. Sci. Mater. Med.*, 2008, **19** (8), P. 2819–2825.
- [23] Usoltseva A., Kuznetsov V., Rudina N., Moroz E., Haluska M., Roth S. Influence of catalysts' activation on their activity and selectivity in carbon nanotubes synthesis. *Phys. Stat. Sol.*, 2007, **244** (11), P. 3920–3924.
- [24] Kuznetsov V.L., Krasnikov D.V., Schmakov A.N., Elumeeva K.V. In situ and ex situ time resolved study of multi-component Fe-Co oxide catalyst activation during MWNT synthesis. *Phys. Stat. Sol.*, 2012, **249** (12), P. 2390–2394.
- [25] Barabashko M.S., Drozd M., Szewczyk D., Jeżowski A., Bagatskii M.I., Sumarokov V.V., Doblin A.V., Nesov S.N., Korusenko P.M., Ponomarev A.N., Geidarov V.G., Kuznetsov V.L., Moseenkov S.I., Sokolov D.V., Smirnov D.A. Calorimetric, NEXAFS and XPS studies of MWCNTs with low defectiveness. *Fullerenes, Nanotubes Carbon Nanostruct.*, 2021, **29** (5), P. 331–336.
- [26] Ponomarev A., Egorushkin V., Bobenko N., Barabashko M., Rezvanova A., Belosludtseva A. On the possible nature of armchair-zigzag structure formation and heat capacity decrease in MWCNTs. *Materials*, 2022, **15** (2), 518.
- [27] Kudryashov B.S., Rezvanova A.E., Ponomarev A.N., Belosludtseva A.A., Barabashko M.S. Analysis of electron microscopic images of multi-walled carbon nanotubes: Determination of the average diameter. *AIP Conference Proceedings*, 2022, **2509** (1), 020118.
- [28] Barabashko M., Ponomarev A., Rezvanova A., Kuznetsov V., Moseenkov S. Young's modulus and vickers hardness of the hydroxyapatite bioceramics with a small amount of the multi-walled carbon nanotubes. *Materials*, 2022, **15** (15), 5304.
- [29] TeraVil Ltd. URL: <https://www.teravil.lt/t-spec.php>. Accessed 27 July 2022.
- [30] Nishizawa S., Sakai K., Hangyo M., Nagashima T., Takeda M.W., Tominaga K., Oka A., Tanaka K., Morikawa O. Terahertz time-domain spectroscopy. *Top. Appl. Phys.*, 2005, **97**, P. 203–270.
- [31] Sakai K., Tani M. Introduction to Terahertz Pulses. *Top. Appl. Phys.*, 2006, **97**, P. 1–31.
- [32] Bawuah P., Ervasti T., Tan N., Zeitler J.A., Ketolainen J., Peiponen K.-E. Noninvasive porosity measurement of biconvex tablets using terahertz pulses. *Int. J. Pharm.*, 2016, **509** (1–2), P. 439–443.
- [33] Naftaly M., Tikhomirov I., Hou P., Markl D. Measuring open porosity of porous materials using THz-TDS and an index-matching medium. *Sensors*, 2020, **20** (11), 3120.
- [34] Rungasawang R., Geethamma V. G., Parrott E.P.J., Ritchie D.A., Terentjev E.M. Terahertz spectroscopy of carbon nanotubes embedded in a deformable rubber. *J. Appl. Phys.*, 2008, **103** (12).

- [35] Parrott E.P.J., Zeitler J.A., McGregor J., Oei Shu-Pei, Unalan H.E., Milne W.I., Tessonier J.-P., Su Dang Sheng, Schlogl R., Gladden L.F. The use of terahertz spectroscopy as a sensitive probe in discriminating the electronic properties of structurally similar multi-walled carbon nanotubes. *Advanced Materials*, 2009, **21** (38–39), P. 3953–3957.
- [36] Crawley D., Longbottom C., Wallace V.P., Cole B., Arnone D., Pepper M. Three-dimensional terahertz pulse imaging of dental tissue. *J. Biomed. Opt.*, 2003, **8** (2), P. 303–307.
- [37] Nazarov M.M., Shkurinov A.P., Kuleshov E.A., Tuchin V.V. Terahertz time-domain spectroscopy of biological tissues. *Quantum Electron*, 2008, **38** (7), P. 647–654.
- [38] Plazenet M., Tasseva J., Bartolini P., Taschin A., Torre R., Combes C., Rey C., Michele A.Di., Verezhak M., Gourrier A. Time-domain THz spectroscopy of the characteristics of hydroxyapatite provides a signature of heating in bone tissue. *PLoS One*, 2018, **13** (8), e0201745.
- [39] Lee H.-J., Han J.-K., Janakiraman S., Ahn B., Kawasaki M., Langdon T.G. Significance of grain refinement on microstructure and mechanical properties of an Al-3% Mg alloy processed by high-pressure torsion. *J. Alloys Compd.*, 2016, **686**, P. 998–1007.
- [40] Sotelo Martin L. E., Castro R. H. R. Al excess extends Hall-Petch relation in nanocrystalline zinc aluminate. *J. Am. Ceram. Soc.*, 2022, **105** (2), P. 1417–1427.
- [41] Garet F., Hofman M., Meilhan J., Simoens F., Coutaz J.-L. Evidence of Mie scattering at terahertz frequencies in powder materials. *Appl. Phys. Lett.*, 2014, **105** (3), 031106.

---

Submitted 15 July 2023; revised 22 September 2023; accepted 23 September 2023

*Information about the authors:*

*Anastasiya E. Rezvanova* – Institute of Strength Physics and Materials Science of the Siberian Branch of the Russian Academy of Sciences, 2/4 Akademicheskii ave., Tomsk, Russia, 634055; ORCID 0000-0002-7067-7979; ranast@ispms.ru

*Boris S. Kudryashov* – Institute of Strength Physics and Materials Science of the Siberian Branch of the Russian Academy of Sciences, 2/4 Akademicheskii ave., Tomsk, Russia, 634055; ORCID 0009-0000-5133-4893; bsk3@ispms.ru

*Alexander N. Ponomarev* – Institute of Strength Physics and Materials Science of the Siberian Branch of the Russian Academy of Sciences, 2/4 Akademicheskii ave., Tomsk, Russia, 634055; ORCID 0000-0003-1524-7842; alex@ispms.ru

*Anastasiya I. Knyazkova* – Tomsk State University, the Faculty of Physics, 36 Lenin ave., Tomsk, Russia, 634050; ORCID 0000-0002-1454-299X; a\_knyazkova@bk.ru

*Victor V. Nikolaev* – Tomsk State University, the Faculty of Physics, 36 Lenin ave., Tomsk, Russia, 634050; ORCID 0000-0001-8189-0188; vik-nikol@bk.ru

*Yuri .V. Kistenev* – Tomsk State University, the Faculty of Physics, 36 Lenin ave., Tomsk, Russia, 634050; ORCID 0000-0001-5760-1462; yuk@iao.ru

*Conflict of interest:* the authors declare no conflict of interest.

*Authors contributions:* A.E. Rezvanova, B.S. Kudryashov and A.N. Ponomarev produced ceramic porous material based on hydroxyapatite with multi-walled carbon nanotubes additives, wrote the main manuscript text and prepared all figures. A.I. Knyazkova, V.V. Nikolaev and Yu.V. Kistenev carried out THz measurements and the interpretation of the results. All authors reviewed the manuscript.

*Availability of data and materials:* Data underlying the results presented in this paper are not publicly available at this time but may be obtained from the authors upon reasonable request.

## Verification of continuum-based model of carbon materials

Kirill B. Tsiberkin

Perm State University, Perm, Russia

kbsiberkin@psu.ru

PACS 73.22.-f, 71.10.-w

**ABSTRACT** The continuous medium approximation to the description of a carbon material previously used to model the properties of spherical carbon shells of nanometer diameter. This approach is based on the transition from lattice operators to field operators. The present study verifies the given model evaluating the energy spectrum of electrons in a perfect flat carbon monolayer. An implementation of the Dirac cones within the continuous medium framework is demonstrated. Its are close to the positions of the vertices of the Brillouin zone for graphene. Increase of the Taylor series expansion order of field operators makes the result precise, and the approximate positions of the Dirac cones match the exact data for graphene.

**KEYWORDS** carbon lattice, continuum model, Dirac cone

**FOR CITATION** Tsiberkin K.B. Verification of continuum-based model of carbon materials. *Nanosystems: Phys. Chem. Math.*, 2023, **14** (5), 539–543.

### 1. Introduction

It is necessary to know the key features of the energy spectrum of conduction electrons in the carbon layer to build a complete picture of the observed characteristics of carbon materials and the possibility of reliable prediction the properties of composites of various structures synthesized on their basis [1–3]. However, the known variety of carbon structures restricts the calculations effectiveness, since it requires an individual approach to each specific geometry. For example, it is implemented for carbon nanotubes and spherical shells [4–6].

A number of papers, e.g., [7–9], present a detailed analysis for carbon clusters, namely, fullerenes of a fixed dimension  $C_{24}$ ,  $C_{60}$ ,  $C_{70}$ . Such structures include relatively small number of atoms. Therefore, one can formulate a complete system of lattice equations based on the Hubbard model and analyze it. On the other hand, when synthesizing of larger size carbon structures like spherical shells, one can only control its characteristic average size. The specific diameter of a particular shell remains random. In addition, the amount of lattice sites reaches tens of thousands [10, 11]. Thus, it remains relevant to develop an efficient simplified model for description the energy spectrum of carbon structures of arbitrary dimensions.

Paper [12] presents the transformation from the lattice operators for electrons to the field operators and continuous medium limit. It potentially allows one to model the systems of complex geometry, including those with an irregular arrangement of atoms. The model was built in relation with high-dimensional spherical carbon shells, the synthesis technology, analysis of the growth kinetics and geometric parameters of which are described in papers [10, 11]. The optical and magnetic characteristics of a composite based on such shells are calculated, and theoretical results have a good agreement with the experimental data.

However, there is a question about the Dirac point implementation within the averaged framework. The present paper shows that it occurs at first when the terms of the third order are taken into account in the expansion of the electron field operators. The even terms in the Taylor series expansion determine the modulus of the wave number corresponding to the Dirac points, and the odd terms determine the structure and asymmetry of the Dirac cones, which, in contrast to the exact solution, turn out to be somewhat deformed within the approximations.

### 2. Continuum-based model of carbon lattice

The basic Hamiltonian for the considered model is the graphene monolayer in the tight-binding approximation [2, 3]:

$$H = -\theta \sum_{j,\delta,\sigma} \left( a_{j\sigma}^\dagger b_{j+\delta,\sigma} + b_{j\sigma}^\dagger a_{j-\delta,\sigma} \right), \quad (1)$$

where  $a$ ,  $b$  are the creation–annihilation fermionic operators of an electron with given spin  $\sigma$  at lattice site with number  $j$ . It is related to the carbon sublattice  $A$  and  $B$ , respectively.  $\delta$  are radius-vectors from the node  $j$  to the nearest neighbours. In a flat lattice, these vectors are well-known (Fig. 1):

$$\delta_1 = (-1; 0)a_0, \quad \delta_{2,3} = \left( \frac{1}{2}; \pm \frac{\sqrt{3}}{2} \right) a_0,$$

where  $a_0$  is the interatomic bond length. The parameter  $\theta$  is the hopping integral of transition between two lattice sites. The Coulomb repulsion of the electrons and impurities are not considered in the present study.

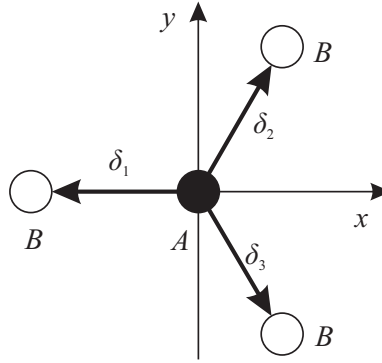


FIG. 1. The carbon–carbon bond vectors in a flat layer

The time-dependent Heisenberg equation

$$i \frac{dX}{dt} = [X, H]$$

allows one to build the evolution equations for the amplitudes of the electron wave functions at the lattice sites:

$$\begin{aligned} i \frac{da_{j\sigma}}{dt} &= -\theta \sum_{\delta} b_{j+\delta, \sigma}, \\ i \frac{db_{j\sigma}}{dt} &= -\theta \sum_{\delta} a_{j-\delta, \sigma}. \end{aligned} \quad (2)$$

In this system of equations, the geometry of a particular lattice is determined only by the  $\delta$  vectors.

To pass to the continuous medium limit, lattice operators are considered as field operators which are the continuous functions of coordinates [13–16]:

$$a_{j\sigma} \rightarrow a_{\sigma}(\mathbf{r}_j), \dots$$

This makes possible the application of the Taylor series expansion of the right-hand side operators:

$$\begin{aligned} b_{j+\delta, \sigma} \rightarrow b_{\sigma}(\mathbf{r}_j + \delta) &\approx \\ &\approx b_{\sigma}(\mathbf{r}_j) + \delta \cdot \nabla b_{\sigma}(\mathbf{r}_j) + \frac{1}{2} \frac{\partial^2 b_{\sigma}(\mathbf{r}_j)}{\partial x^{\mu} \partial x^{\nu}} \delta^{\mu} \delta^{\nu} + \frac{1}{3!} \frac{\partial^3 b_{\sigma}(\mathbf{r}_j)}{\partial x^{\mu} \partial x^{\nu} \partial x^{\lambda}} \delta^{\mu} \delta^{\nu} \delta^{\lambda} + \dots, \end{aligned} \quad (3)$$

The indices  $\mu$ ,  $\nu$  and  $\lambda$  denote the spatial components of the two-dimensional vectors  $\delta$ . There are sums over these indices. The lattice operators are considered as the finite-difference approximation of the field operators in that approach. The expansion is used to transform the sums of operators at the right hand sides of the equations (2). Finally, one rewrites the model as a system of linear partial differential equations.

When considering a flat layer or averaging over the electron momenta, the gradient terms in the expansion disappear. The final evolution equations include at least the second-order derivatives. E.g., the right-hand side of the first equation in (2) transforms as follows:

$$\begin{aligned} \sum_{\delta} b_{j+\delta, \sigma} &\rightarrow b(\mathbf{r}_j + \delta_1) + b(\mathbf{r}_j + \delta_2) + b(\mathbf{r}_j + \delta_3) = \\ &= 3b + (\delta_{1;x} + \delta_{2;x} + \delta_{3;x}) \frac{\partial b}{\partial x} + (\delta_{1;y} + \delta_{2;y} + \delta_{3;y}) \frac{\partial b}{\partial y} + \\ &+ \frac{1}{2} \left( (\delta_{1;x}^2 + \delta_{2;x}^2 + \delta_{3;x}^2) \frac{\partial^2 b}{\partial x^2} + (\delta_{1;y}^2 + \delta_{2;y}^2 + \delta_{3;y}^2) \frac{\partial^2 b}{\partial y^2} + \right. \\ &\left. + 2(\delta_{1;x} \delta_{1;y} + \delta_{2;x} \delta_{2;y} + \delta_{3;x} \delta_{3;y}) \frac{\partial^2 b}{\partial x \partial y} \right) + \dots \end{aligned}$$

The first-order terms vanish exactly:

$$\delta_{1;x} + \delta_{2;x} + \delta_{3;x} = -1 + \frac{1}{2} + \frac{1}{2} = 0, \quad \delta_{1;y} + \delta_{2;y} + \delta_{3;y} = \frac{\sqrt{3}}{2} - \frac{\sqrt{3}}{2} = 0,$$

while in the second-order term only  $xy$ -derivative vanishes:

$$\begin{aligned} \delta_{1;x}^2 + \delta_{2;x}^2 + \delta_{3;x}^2 &= 1 + \frac{1}{4} + \frac{1}{4} = \frac{3}{2}, & \delta_{1;y}^2 + \delta_{2;y}^2 + \delta_{3;y}^2 &= \frac{3}{4} + \frac{3}{4} = \frac{3}{2}, \\ \delta_{1;x}\delta_{1;y} + \delta_{2;x}\delta_{2;y} + \delta_{3;x}\delta_{3;y} &= 1 \cdot 0 + \frac{1}{2} \cdot \frac{\sqrt{3}}{2} - \frac{1}{2} \cdot \frac{\sqrt{3}}{2} = 0. \end{aligned}$$

The  $xx$ - and  $yy$ -terms produce the two-dimensional Laplace operator. The high-order terms are transformed by the same way.

As a result, in the first non-zero approximation, the model is approximated by the following system:

$$i \frac{da_\sigma}{dt} = -\theta \left( 3 + \frac{3a_0^2}{4} \nabla^2 \right) b_\sigma, \quad i \frac{db_\sigma}{dt} = -\theta \left( 3 + \frac{3a_0^2}{4} \nabla^2 \right) a_\sigma. \quad (4)$$

The description of specific geometric structures requires setting a suitable spatial basis for the wave functions. In particular, the basis of spherical harmonics is used for the shells described in [10–12]. The substitution of the basis reduces the problem to a system of linear ODEs, the eigenfrequencies of the solutions of which determine the energy spectrum of electron in the system.

As expected, substitution of the plane wave solution  $\exp(i\mathbf{q} \cdot \mathbf{r})$  into (4) results in the isotropic energy spectrum:

$$\frac{\omega}{\theta} = \pm \left( 3 - \frac{3}{4} q^2 \right). \quad (5)$$

The particle energy vanishes on the entire circle  $qa_0 = 2$ , which is close to the inner-radius for the Brillouin zone of graphene. The dispersion relation becomes linear near this circle only under the condition  $q_x = q_y$ . Thus, the spectrum obtained in this approximation does not contain the Dirac points, and the applicability of the model to describe flat lattice is limited. However, with a high degree of irregularity due to defects and deviation of the lattice shape from the plane with a change in the angles between the bonds, one should expect better agreement between the proposed model and the characteristics of the material. If one takes into account the highest terms in expansion (3) it is possible to overcome this limitation with using the next order term only.

### 3. Approximate implementation of the Dirac points

If one takes into account the third derivatives in the Taylor series the dispersion relation has the following form

$$\frac{\omega}{\theta} = \pm \left( 3 - \frac{3}{4} q^2 - \frac{iq_x}{8} (q_x^2 - 2q_y^2) \right). \quad (6)$$

That function has six zeros in the points, distributed uniformly over the circle with radius  $2/a_0$  (Fig. 2):

$$\mathbf{Q}_{1,2} = \frac{1}{a_0} (0; \pm 2), \quad \mathbf{Q}_{3,4,5,6} = \frac{1}{a_0} \left( \pm \frac{2}{\sqrt{3}}; \pm \frac{2\sqrt{2}}{\sqrt{3}} \right).$$

The expansion of the dispersion relation near the points  $\mathbf{Q}_j$  confirms the approximate implementation of the deformed Dirac cones. For example, in the neighborhood of  $\mathbf{Q}_1$ , the energy spectrum takes the form of the elliptic cone:

$$\frac{\omega_1}{\theta} \approx 3 \sqrt{\frac{k_x^2}{4} + k_y^2}, \quad (7)$$

where  $\mathbf{k}$  is the deviation of the electron momentum vector from  $\mathbf{Q}$ :  $\mathbf{q} = \mathbf{Q} + \mathbf{k}$ . An increase in the expansion order leads to the consistent refinement of the location of the Dirac points, for which the even derivatives are responsible, and the shape of the cones, determined by the odd terms of the series. It can be seen from Fig. 2 that, within the accuracy of plotting of the graph, their positions in the model and in the exact calculation coincide, and the structure of the energy isolines around the valleys approaches locally isotropic when terms of 6–7th orders and higher are taken into account.

It is expected that when averaging over the directions of wave vectors in a deformed lattice, for example, in a spherical shell, which includes not only hexagonal cells, but also structural elements from a different number of atoms, the contribution of odd orders will decrease down to negligible values.

Of course, there exist a more standard and simple way to introduce the field operators within the flat carbon sheet. It uses the plane electron waves representing the two leading terms of the Fourier series near the Dirac points. It is well-described in literature [2]. That approach is applicable, at first, for flat regular structure.

In the present paper, the main goal of the described method is modeling of the complex shape of the carbon lattice with irregularity which should be strong enough to apply the averaging procedure. Here, the Fourier expansion by plane waves is inapplicable because of possibility of the large lattice curvature. Therefore, the proposed approach allows one to implement a more flexible approximation despite it has lower precision in the case of the flat layer (see [12]). To evaluate the Dirac points here, one should keep the relatively large number of expansion terms. The corresponding high-order equations can be difficult for analysis, but it is possible to use the perturbation theory.

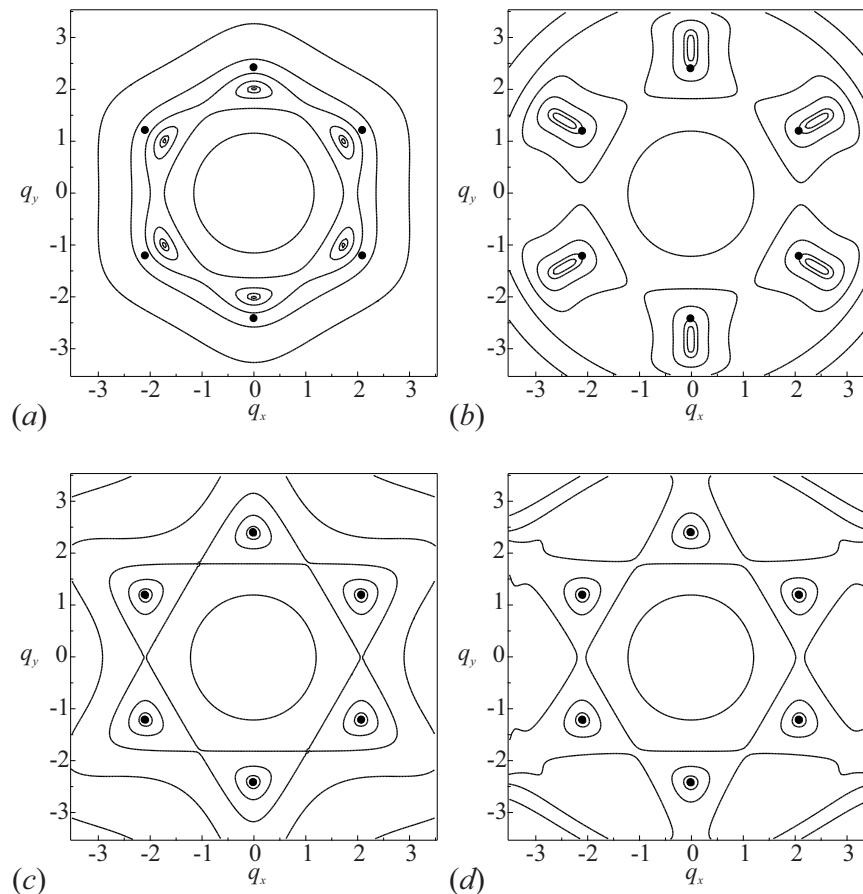


FIG. 2. Contour maps of the energy spectrum calculated within the framework of the continuum model using the expansion to terms of the following orders: (a) – 3rd, (b) – 5th, (c) – 7th, (d) – 9th order. The following energy levels are shown:  $0$ ,  $0.1\theta$ ,  $0.2\theta$ ,  $0.5\theta$ ,  $1.0\theta$ ,  $2.0\theta$  and  $5.0\theta$ . The dots indicate the positions of the Dirac cones of ideal graphene

#### 4. Conclusion

The previously developed approach based on the continuum model produces the approximate energy spectrum of the plane electron waves in the carbon sheet with the approximate implementation of the Dirac cones. This result confirms the applicability of the developed model to the description of various carbon structures and ensures the reliability of the calculations performed for description of the properties of a spherical carbon shell.

It is expected that taking into account higher orders of decomposition makes it possible to refine the quantitative characteristics of the carbon composite based on nanospheres, however, even the first non-vanishing approximation provides reliable information about the features of the observed optical and magnetic properties of the material. In addition, the model, which is actually formulated as a pair of coupled Schrödinger equations for the wave functions of electron related to different carbon sublattices, can be easily adapted to structures of other geometries.

#### References

- [1] Eletsii A. V., Smirnov B. M. Fullerenes and carbon structures. *Physics Uspekhi*, 1995, **38**, P. 935–964.
- [2] Castro Neto A. H., Guinea F., Peres N. M. R., et al. The electronic properties of graphene. *Review of Modern Physics*, 2009, **81**, P. 109–162.
- [3] Esquinazi P. D. *Basic physics of functionalized graphite*, Springer, New-York: 2016, 185 p.
- [4] C. N. R. Rao, R. Seshadri, A. Govindaraj, et al. Fullerenes, nanotubes, onions and related carbon structures. *Material Science and Engineering*, 1995, **15**, P. 209–262.
- [5] Makarova T. L. Magnetic properties of carbon structures. *Semiconductors*, 2004, **38**, P. 615–638.
- [6] Tiwari J. N., Tiwari R. N., Kim K. S. Zero-dimensional, one-dimensional, two-dimensional and three-dimensional nanostructured materials for advanced electrochemical energy devices. *Progress in Material Science*, 2012, **57**, P. 724–803.
- [7] Mironov G. I., Murzashev A. I. Energy spectrum of C60 fullerene. *Physics of Solid State*, 2011, **53**, P. 2393–2397.
- [8] Silantiev A. V. The energy spectrum and optical properties of fullerene C70 within the Hubbard model. *Optics and Spectroscopy*, 2018, **124**, P. 155–162.
- [9] Silantiev A. V. Energy spectrum and optical properties of C24 fullerene within the Hubbard model. *Physics of Metals and Metallography*, 2020, **121**, P. 195–201.
- [10] Rudakov G. A., Tsiberkin K. B., Ponomarev R. S., et al. Magnetic properties of transition metal nanoparticles enclosed in carbon nanocages. *Journal of Magnetism and Magnetic Materials*, 2019, **427**, P. 34–39.

- [11] Sosunov A. V., Ziolkowska D. A., Ponomarev R. S., et al. CFx primary batteries based on fluorinated carbon nanocages. *New Journal of Chemistry*, 2019, **43**, P. 12892–12895.
  - [12] Tsiberkin K. B. Modeling of the energy spectrum of a carbon sphere in the continuous medium limit. *Journal of Theoretical and Experimental Physics*, 2022, **135**, P. 921–926.
  - [13] Herring C., Kittel C. On the theory of spin waves in ferromagnetic media. *Physical Review*, 1951, **81**, P. 869–880.
  - [14] Rabinovich M. I., Trubetskov D. I. *Oscillations and waves in linear and nonlinear systems*, Springer, Amsterdam, 1989, 578 p.
  - [15] Scarpa F., Adhikari S., Gil A. J., Remillat C. The bending of single layer graphene sheets: the lattice versus continuum approach. *Nanotechnology*, 2010, **21**, P. 125702.
  - [16] Popov I. Y., Blinova I. V., Popov A. I. A model of a boundary composed of the Helmholtz resonators. *Complex Variables and Elliptic Equations*, 2021, **66**, P. 1256–1263.
- 

*Submitted 6 September 2023; revised 9 September 2023; accepted 10 September 2023*

*Information about the authors:*

*Kirill B. Tsiberkin* – Perm State University, Bukireva, 15, Perm, 614068, Russia; ORCID 0000-0002-8725-7743; kbtsiberkin@psu.ru

## Magnetic nanoparticles in solid matrices: formation and fixation of structures, induced by magnetic field

Ivan V. Pleshakov<sup>1</sup>, Arseniy A. Alekseev<sup>2</sup>, Efim E. Bibik<sup>3</sup>, Valentin I. Dudkin<sup>4</sup>, Tatiana Yu. Kudryashova<sup>2</sup>, Elina K. Karseeva<sup>2</sup>, Tatiana A. Kostitsyna<sup>2</sup>, Ekaterina A. Medvedeva<sup>2</sup>

<sup>1</sup>Ioffe Institute, St. Petersburg, Russia

<sup>2</sup>Peter the Great St. Petersburg Polytechnic University, St. Petersburg, Russia

<sup>3</sup>Saint Petersburg State Institute of Technology (Technical University), St. Petersburg, Russia

<sup>4</sup>The Bonch-Bruевич Saint Petersburg State University of Telecommunications, St. Petersburg, Russia

<sup>a</sup>ivanple@yandex.ru, <sup>b</sup>arseniy.alekseev98@gmail.com, <sup>c</sup>eefimovich@yandex.ru, <sup>d</sup>vidoodkin@mail.ru,

<sup>e</sup>kudryashova.tyu@spbstu.ru, <sup>f</sup>elina.nep@gmail.com, <sup>g</sup>kostitsyna.ta@edu.spbstu.ru, <sup>h</sup>tato\_ks@mail.ru

Corresponding author: Ivan V. Pleshakov, ivanple@yandex.ru

PACS 75.50.Mm; 75.50.Tt

**ABSTRACT** In this article, the structures formed by the action of the magnetic field to magnetite nanoparticles, embedded into transparent matrices from ferrofluids, were analyzed. As the matrices polyvinyl alcohol and epoxy resin were used, however, the results obtained may be applicable to other media, for example, biological. The data of this work can be useful both for physical investigations of magnetic nanomaterials and for more practical studies, for instance, aimed at solving some environmental problems.

**KEYWORDS** magnetic fluids, ferrofluids, magnetic nanoparticles, transparent matrices, magnetic nanocomposites

**FOR CITATION** Pleshakov I.V., Alekseev A.A., Bibik E.E., Dudkin V.I., Kudryashova T.Yu., Karseeva E.K., Kostitsyna T.A., Medvedeva E.A. Magnetic nanoparticles in solid matrices: formation and fixation of structures, induced by magnetic field. *Nanosystems: Phys. Chem. Math.*, 2023, **14** (5), 544–548.

### 1. Introduction

Magnetic nanoparticles, in particular, those that are component of the so-called ferrofluids or magnetic fluids (MF), are used in a variety of scientific and technological fields [1, 2]. Among the recently proposed areas of applications, biomedicine [3, 4] and optoelectronics [5–7] can be named. Of particular importance and interest are also ideas related to ecology, for example, in [8], an MF-based technique for eliminating oil spills was considered.

MF, further used as starting substances for obtaining samples, are colloidal solutions, the solid phase of which is a magnetic material, and the diverse fluids can act as a carrier liquid, kerosene or water for instance. These materials are stabilized by applying certain surfactants to the surface of nanoparticles or creating electrical charge on it [2].

For most of MF-related utilizations, the important question is how they interact with the external magnetic field  $H$ . It is known that the field forces the colloid nanoparticles to form the extended structures (agglomerates) oriented along the  $H$  direction [9]. The characteristics of these objects vary depending on the type of solvent, particle material, surfactant, as well as the conditions of the experiment. One of the convenient ways to study such clusters is their “freezing” in a congealing environment, which was implemented, for example, in [10]. The purpose of the presented study is further development of this approach and demonstration of the peculiarities of the field induced aggregation process in the viscous media.

### 2. Materials and methods

The samples under consideration were composite materials obtained by infiltration of magnetite ( $\text{Fe}_3\text{O}_4$ ) nanoparticles from MF into a transparent medium which are the polyvinyl alcohol (PVA) or epoxy resin. MF was the same as in a number of previous works [10, 11], being an aqueous colloid of magnetite stabilized by a two-layer surfactant with oleic acid molecules or by a charged layer formed on the surface of particles. The particle size was approximately 10 nm.

In the case of PVA matrix, an initial mixture of two aqueous solutions was prepared, one of them was 5 wt. % solution of PVA powder, and another was MF with oleic stabilization, taken at such a concentration as to provide approximately 0.5 vol. % of the magnetic phase in a solid sample. The mixture was stirred at 90 °C, and then treated with ultrasound for one hour. The resulting liquid was applied to a glass substrate and dried.

Since water cannot be used when working with epoxy resin, when fabricating samples with such matrices, ion-stabilized MF was first dried on glass, and then the obtained paste-like precipitate was diluted in a hardener and sonified

for one hour. After mixing the hardener with the resin, a short-term sonification of the mixture was also carried out and then it was dried on a glass substrate. The magnetite content was such as to be for the solid matrix approximately 0.25 mg per 1 ml.

In all cases, the liquid mixture was applied to the substrate in such quantities as to finally obtain a sample in the form of a film of 40–70  $\mu\text{m}$  thick. Drying was carried out in magnetic fields oriented in the film plane, or without application of the field. The films have always turned out to be quite transparent; if the field was nonzero, a structure of thin extended objects was visually observed in them.

All samples, both based on PVA and epoxy resin, were fabricated in the fields up to 6 kOe, but special attention was paid to the range from 0 to 1000 Oe, since the saturation field  $H_s$  of MF reaches approximately of 1 kOe [9], and the main processes associated with the formation of structures should occur in this interval. This assumption was confirmed experimentally: it was found that the parameters of nanoparticle agglomerates at  $H > 1$  kOe change only slightly.

Using a MICRO 200T-01 PLANAR microscope, micrographs were obtained for films, processed further as follows: for each structural element (spherical at  $H = 0$  and extended at  $H > 0$ ) in the field of the microscope, its dimensions (diameter  $d$  or, respectively, the thickness  $D$  and length  $L$ ) were determined, and then for a given value  $H$ , statistics were being accumulated. The number of analyzed objects,  $N$ , was of an order hundreds, which made it possible to construct histograms of the distribution of the above values.

In addition, a technique for determining  $D$  based on laser probing of the material was used. To do this, a laser beam with a wavelength of  $\lambda = 650$  nm was focused on the film (illuminated from the side of the glass substrate), and by finely moving the latter, such a position was chosen where the light diffracted on a separate aggregate. On a screen at some distance away from the sample, a pattern typical of this was observed, containing maxima and minima of diffracted radiation  $I$ . Assuming that this case is analogous to the slit diffraction and using the well-known expression  $\lambda m = D \sin \theta$ , where  $\theta$  is the angle at the  $I$  minimum with the number  $m$ , it was possible to determine the transverse size of the selected object. (A similar approach was used to study agglomerates in a liquid medium [12]). Since this method is more time-consuming than the analysis of micrographs, the dimensions of a smaller number of aggregates were evaluated by it.

### 3. Experimental results

Figure 1 shows micrographs of PVA-based samples fabricated in fields of less or almost the same magnitude as  $H_s$ . It is clearly seen that at  $H = 0$  inclusions in the polymer matrix are microdroplets whose diameters  $d$  noticeably exceed the characteristic size of the individual nanoparticles (Fig. 1a). A relatively small nonzero field leads to the formation of elongated agglomerates, the length of which,  $L$ , however, can be easily determined (Fig. 2b). With approaching  $H_s$ , the latter, starting from some point, is no longer possible, since the value  $L$  for most of agglomerates becomes comparable with in-plane dimension of the sample (Fig. 1c). It should be noted that for weak fields the diameters of the agglomerates turned out to be approximately the same ( $D \approx 15\text{--}20$   $\mu\text{m}$ ), and, moreover, for  $H > H_s$  they also changed insignificantly.

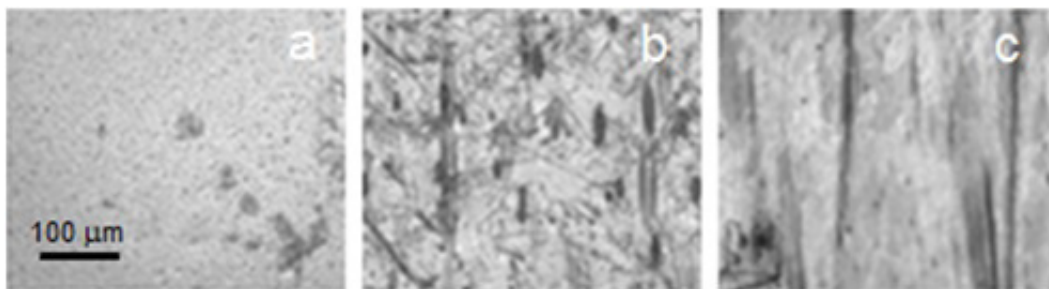


FIG. 1. Micrographs of a sample based on PVA at: a)  $H = 0$ ; b)  $H = 40$  Oe; c)  $H = 1000$  Oe (the scale is the same for all images)

The same regularities are preserved for composites based on epoxy resin matrices; for example, Fig. 2 shows micrographs of these materials for  $H = 0$  and  $H \gg H_s$ . Here we can note the same presence of microdrops in zero field (Fig. 2a), and “infinitely long” agglomerates at fields of a high strength (Figs. 2b and 2c). It should be emphasized that the  $D$  values for different cases may still differ slightly (see Fig. 2c, where the agglomerate with  $D \approx 80$   $\mu\text{m}$  is isolated), however, the characteristic size of the order of several tens of microns is typical for almost all extended structural elements. As an exception, we should mention the existence of a certain number of thin objects at  $H = 4$  kOe and  $H = 6$  kOe (Figs. 2b and 2c).

The statistical properties of the aggregates are illustrated in Fig. 3, which shows examples of histograms of the distribution of  $d$  ( $H = 0$ , Fig. 3a) and  $L$  ( $H = 40$  Oe, Fig. 3a) in PVA-based composites. These data were obtained by analyzing a number of micrographs with, as already was mentioned, a lot of objects  $N$  (in Fig. 3, normalization was performed by the maximum magnitude in the distribution  $N_0$ ). At  $H < H_s$ , there were no qualitative differences in the

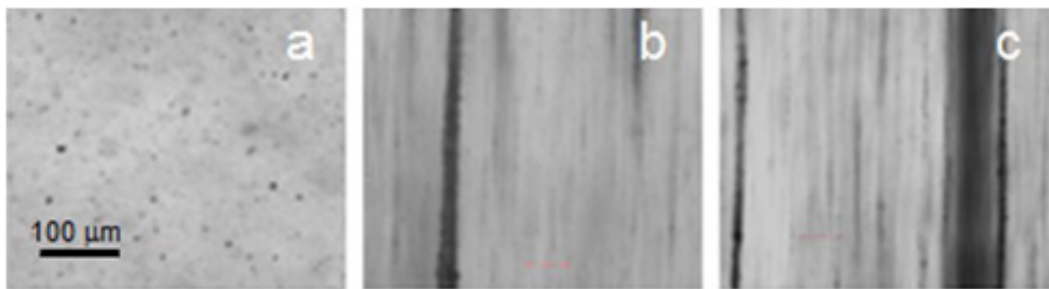


FIG. 2. Micrographs of a sample based on epoxy resin: a)  $H = 0$ ; b)  $H = 4$  kOe; c)  $H = 6$  kOe (the scale is the same for all images)

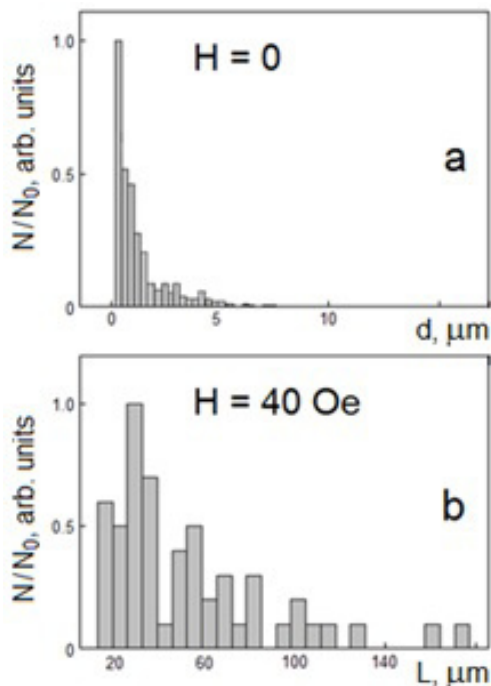


FIG. 3. Histograms of the distribution of the size of agglomerates in a sample with PVA: a) without field; b) in the field  $H = 40$  Oe

behavior of histograms for materials with PVA and epoxy resin: with an increase of the field (where the measurement of length was still possible), their shift towards large values of  $L$  was recorded.

The laser probing method made it possible to obtain verified data on the thickness of the aggregates. Fig. 4 demonstrates the results of one of the diffraction experiments carried out on an epoxy film fabricated at  $H = 4$  kOe. The diffraction pattern, while not ideal, nevertheless allowed us to estimate  $D$ . After digitizing the images of the type presented in Fig. 4a, graphs of the dependence of the normalized light intensity on the distance from the beam center along the  $X$  direction were obtained. Fig. 4b exhibits the distribution of the relative intensity of diffracted light  $I/I_0$  for one of such a section of the pattern. According to these data, and taking into account geometric parameters of the setup, the values of  $D$  were determined. They, slightly differing for different measurements, in order of magnitude amounted to tens of microns in all cases. This gives a useful confirmation of what was obtained earlier, because due to the edge blurring of images, the processing of micrographs is less informative.

#### 4. Discussion

One of the main features of the structures we have considered is that they are formed in a similar way in different environments and under markedly different conditions. Indeed, analyzing the data on the behavior of the magnetic fraction embedded in PVA (Fig. 1) or epoxy resin (Fig. 2), it can be seen that even at very different fields, the thicknesses of agglomerates tend to approximately the same value, and it is observable starting from the smallest  $H$  (Fig. 1b). At  $H \ll H_s$ , large-volume associations of nanoparticles cannot yet occur, and the parameter  $L$ , characterizing the extent of the aggregates, remains small. An increase in the field leads to its significant growth and the appearance of long structural elements, although in the interval roughly limited by  $H_s$  from above, the presence of a certain number of

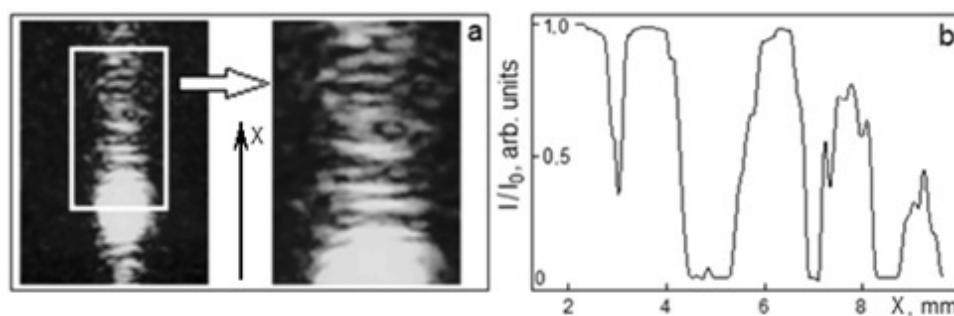


FIG. 4. Diffraction of laser radiation on selected agglomerate (sample based on epoxy resin,  $H = 4$  kOe): a) diffraction pattern at different scales; b) distribution of the relative intensity of diffracted light

”short” aggregates can be noted (Fig. 1c), which reflects the statistical nature of the processes taking place. At  $H > H_s$  most of the particles enter into extended column-like systems (Figs. 2a,b), which, by moving the microscope field, can be traced over a long distance, sometimes comparable to the size of the sample.

The suggested mechanism of formation of the structures in our samples may be as follows. The initial state in the preparing of our samples are emulsions (Fig. 1a, Fig. 2a), which is usual when MF is diluted in viscous media [13]. In our case, the size  $d$  of most of the microdrops can be estimated as  $0.5 \mu\text{m}$  (Fig. 3a), that is, the number of nanoparticles in each of them should be  $\sim 10^4$ – $10^5$ . Thus, when the field inducing the magnetic moment appears, not individual particles, as simple models suggest [9], but large objects begin to interact. Already in very small fields, the drops acquire an ellipsoidal shape [13] and start to attract each other, merging into agglomerates of increasing volume and extent. At higher  $H$ , maintaining approximately the same thickness  $D$  as at the initial stage of growth turns out to be energetically favorable (apparently, from the point of view of minimizing magnetic energy and surface tension energy at the medium-ferrofluid interface). The rate of such a process is determined by the viscosity of the medium and the average size  $d$ , i. e., it is obviously much smaller than for conventional MF. In our case, however, the formation of a system of aggregates accomplished long before the transformation of the liquid into a solid matrix, since their appearance (visually observed) has a characteristic time of the order of minutes, whereas the carrier solidifies for about an hour. Therefore, the structures of magnetic nanoparticles related to a specified field are fixed in the matrix as completed.

The presence of defects in the medium may impose certain features on the formation of aggregates. So, in Fig. 1 imperfections that are not related to magnetite are visible and represent a partially crystallized matrix substance (which is typical for PVA [14]). Of course, there are other possible situations - in Figs. 2b,c can be noticed an aggregates with an included “dot-like” objects. During laser probing of samples, they are recorded as irregularities in the diffraction pattern (Fig. 4a).

The results obtained can be extended, with a degree of conditionality, to other media with similar properties, primarily viscous ones. They include biomaterials containing, for example, some proteins, as well as gel-forming or other similar substances. For ecology, petroleum products are very important, in which the behavior of magnetic nanoparticles may turn out to be similar to what was considered in this paper. Understanding of how the structures are arise in them under the action of a magnetic field and what they are, being necessary for the development of theory, may also have practical significance.

## 5. Conclusion

In this work, a technique for studying agglomerates consisting of magnetic nanoparticles that are fixed in a transparent solidifying medium was considered. It was shown that it allows one to get information about the parameters of these objects, as well as to identify some general patterns of the formation of such structures in a viscous liquid. Statistical properties of agglomerates were obtained, their characteristic sizes were measured, including by laser probing. The possible application of the results was discussed.

## References

- [1] Oehlsen O., Cervantes-Ramírez S.I., Cervantes-Avilís P., Medina-Velo I.A. Approaches on ferrofluid synthesis and applications: current status and future perspectives. *ACS Omega*, 2022, **7**, P. 3134–3150.
- [2] Scherer C., Figueiredo Neto A.M. Ferrofluids: Properties and applications. *Braz. J. Phys.*, 2005, **35**, P. 718–727.
- [3] Socoliuc V., Avdeev M., Kuncser V., Turcu R., Tombácz E., Vekas L. Ferrofluids and bio-ferrofluids: looking back and stepping forward. *Nanoscale*, 2022, **14**, P. 4786–4886.
- [4] Imran M., Alam M.M., Khan A. Advanced biomedical applications of iron oxide nanostructures based ferrofluids. *Nanotechnology*, 2021, **32**, P. 422001.
- [5] Yong Zhao, Yuyan Zhang, Lv R.-Q., Qi Wang. Novel optical devices based on the tunable refractive index of magnetic fluid and their characteristics. *J. Magn. Magn. Mat.*, 2011, **323**, P. 2987–2996.

- [6] Dai Q.-F., Deng H.-D., Zhao W.-R., Liu J., Wu L.-J., Lan S., Gopa A.V. All-optical switching mediated by magnetic nanoparticles. *Opt. Lett.*, 2010, **35**, P. 97–99.
- [7] Taghizadeh M., Bozorgzadeh F., Ghorbani M. Designing magnetic field sensor based on tapered photonic crystal fibre assisted by a ferrofluid. *Scientific Reports*, 2021, **11**, P. 14325.
- [8] Kalaeva S.Z., Morozov N.A., Stradomikiy Yu.I., Makarov V.M., Shipilin A.M., Zakharova I.N. Magnetic fluids for maintaining the cleanliness of surface reservoirs. *ChemChemTech.*, 2006, **49**, P. 91–93 (In Russian).
- [9] Chikazumi S., Taketomi S., Ukita M., Mizukami M., Miyajima H., Setogawa M., Kurihara Y. Physics of magnetic fluids. *J. Magn. Magn. Mat.*, 1987, **65**, P. 245–251.
- [10] Pleshakov I.V., Prokof'ev A.V., Bibik E.E., Kuz'min Yu.I. Investigation of structures formed by magnetic fluid nanoparticles in polymer matrices by static light scattering. *Nanosystems: physics, chemistry, mathematics*, 2022, **13**, P. 285–289.
- [11] Pleshakov I.V., Prokof'ev A.V., Bibik E.E., Nepomnyashchaya E.K., Velichko E.N., Kostitsyna T.A., Seliutin D.M. Spectral characteristics of composite obtained by embedding of magnetic nanoparticles into polymer matrix. *Nanosystems: physics, chemistry, mathematics*, 2021, **12**, P. 279–282.
- [12] Prokof'ev A.V., Pleshakov I.V., Bibik E.E., Kuz'min Yu.I. An optical investigation of the geometric characteristics of aggregates formed by particles of magnetic fluid. *Tech. Phys. Lett.*, 2017, **43**, P. 194–196.
- [13] Zakinyan A.R., Dikansky Yu.I. Effect of microdrops deformation on electrical and rheological properties of magnetic fluid emulsion. *J. Magn. Magn. Mat.*, 2017, **431**, P. 103–106.
- [14] Thomas D., Cebe P. Self-nucleation and crystallization of polyvinyl alcohol. *J. Therm. Anal. Calorim.*, 2017, **127**, P. 885–894.

---

*Submitted 8 September 2023; revised 18 September 2023; accepted 19 September 2023*

*Information about the authors:*

*Ivan V. Pleshakov* – Ioffe Institute, 26 Politechnicheskaya str., St. Petersburg, 194021, Russia; ORCID 0000-0002-6707-6216; ivanple@yandex.ru

*Arseniy A. Alekseev* – Peter the Great St. Petersburg Polytechnic University, 29 Polytechnicheskaya str., St. Petersburg, 195251, Russia; ORCID 0009-0000-5368-6788; arseniy.alekseev98@gmail.com

*Efim E. Bibik* – Saint Petersburg State Institute of Technology (Technical University), 24-26/49 A Moskovskiy ave., 190013, St. Petersburg, Russia; ORCID 0000-0003-4063-2697; eefimovich@yandex.ru

*Valentin I. Dudkin* – The Bonch-Bruевич Saint Petersburg State University of Telecommunications, 22 Bolshevnikov ave., St. Petersburg, 193232, Russia; ORCID 0000-0001-8240-7856; vidoodkin@mail.ru

*Tatiana Yu. Kudryashova* – Peter the Great St. Petersburg Polytechnic University, 29 Polytechnicheskaya str., St. Petersburg, 195251, Russia; ORCID 0000-0002-4498-8204; kudryashova.tyu@spbstu.ru

*Elina K. Karseeva* – Peter the Great St. Petersburg Polytechnic University, 29 Polytechnicheskaya str., St. Petersburg, 195251, Russia; ORCID 0000-0002-4416-9380; elina.nep@gmail.com

*Tatiana A. Kostitsyna* – Peter the Great St. Petersburg Polytechnic University, 29 Polytechnicheskaya str., St. Petersburg, 195251, Russia; ORCID 0009-0003-3170-2507; kostitsyna.ta@edu.spbstu.ru

*Ekaterina A. Medvedeva* – Peter the Great St. Petersburg Polytechnic University, 29 Polytechnicheskaya str., St. Petersburg, 195251, Russia; ORCID 0000-0003-0473-5007; tato.ks@mail.ru

*Conflict of interest:* the authors declare no conflict of interest.

## Nanoparticles in titanite ore

Irina B. Dorosheva<sup>1,a</sup>, Andrey A. Rempel<sup>1,b</sup>, Galina O. Kalashnikova<sup>2,c</sup>, Victor N. Yakovenchuk<sup>2,d</sup>

<sup>1</sup>Institute of Metallurgy of the Ural Branch of the Russian Academy of Sciences, Yekaterinburg, Russia

<sup>2</sup>Nanomaterials Research Centre, Kola Science Centre, Russian Academy of Sciences, Apatity, Russia

<sup>a</sup>[i.b.dorosheva@urfu.ru](mailto:i.b.dorosheva@urfu.ru), <sup>b</sup>[rempe.imet@mail.ru](mailto:rempe.imet@mail.ru), <sup>c</sup>[g.kalashnikova@ksc.ru](mailto:g.kalashnikova@ksc.ru), <sup>d</sup>[yakovenchuk@geoksc.apatity.ru](mailto:yakovenchuk@geoksc.apatity.ru)

Corresponding author: Irina B. Dorosheva, [i.b.dorosheva@urfu.ru](mailto:i.b.dorosheva@urfu.ru)

**ABSTRACT** Nanoparticles in titanite  $\text{CaTiSiO}_5$  were found using transmission electron microscopy. Chemical and XPS analyzes of the nanoparticles were performed. The study showed the content of the elements Si, Ti and Ca to be about 19, 14 and 12 % in the ore, respectively, belonging to the titanite phase. Based on TEM images, it was established that titanite exhibits a disordered lamellar structure with a diameter of 3 to 5 nm and an interplanar distance of about 6.3 Å.

**KEYWORDS** titanite, nanoparticles, transmission electron microscopy (TEM), X-ray photoelectron spectroscopy (XPS)

**ACKNOWLEDGEMENTS** This work was supported by the Russian Science Foundation [grant number 21–73–20039].

**FOR CITATION** Dorosheva I.B., Rempel A.A., Kalashnikova G.O., Yakovenchuk V.N. Nanoparticles in titanite ore. *Nanosystems: Phys. Chem. Math.*, 2023, **14** (5), 549–553.

### 1. Introduction

As for the reserves of titanium raw materials, Russia currently is at the second place in the world. Despite this, its extraction and processing is practically not carried out. Among the most promising and products in demand on the market, we should note weather-resistant and decorative pigments, composite fillers, non-toxic titanium tanning agents, highly effective sorbents for purifying liquid and solid waste from radionuclides and toxic substances [1–3]. The content of the mineral sphene (calcium titanosilicate ( $\text{CaTiSiO}_5$ )) in the ore mass varies widely. Using traditional technology, sphene concentrate is obtained from the foam product of apatite-nepheline ore flotation. This is a fairly complex process in terms of technological flows, so the extraction of sphene does not exceed 10 %. Meanwhile, there are areas, so-called “sphenite lens nests”, in which the concentration of sphene reaches 80 %. An increased content of sphene negatively affects the process of flotation separation of apatite due to the similarity of the properties of calcium-containing minerals. On the other hand, such accumulations of sphene can be quite easily separated from the total mass of ore, and the extraction of sphene can reach 60 – 70 % of the original ore [4]. Up to 1930, it was not known how to process titanite (sphene) in industry. This question arose after the discovery of its industrial reserves in the Khibiny Mountains. Various methods have been proposed for the decomposition of sphene: treatment with bleach; fusion with table salt and exposure of the solution to superheated steam, production of carbides followed by chlorination, decomposition with hydrochloric acid, etc., however, these methods have not found their application in industry due to their complexity [5]. Despite the well developed study of processing sphene concentrate into titanium pigments, which began in 1968, and their subsequent successful testing on a pilot scale, implementation work has been suspended since 2016 due to the optimization of the main production at JSC Apatit, which led to the actual closure of the workshop for the production and processing of sphene concentrate, and therefore the minerals are sent to tailings dumps [6]. A significant part of nepheline, titanomagnetite (16 – 18 %  $\text{TiO}_2$ ), sphene (37 %  $\text{TiO}_2$ ), aegirine annually in the amount of 15 – 20 million tons replenish the dumps of processing factories. More than 500 million tons of waste have already been generated [7]. In this regard, the aim of this work is to study the structure and chemical composition of titanite to develop methods for its subsequent use as highly effective sorbents for purifying liquid media from toxic substances.

### 2. Samples and experiment

The study object is titanite – calcium titanosilicate ( $\text{CaTiSiO}_5$ ). The place of origin of the mineral is the Koashva deposit (Koashva quarry, Murmansk region, personal mineral collection of V.N. Yakovenchuk) [5]. At the first stage, titanite (sphene) wedge-shaped crystals with its matrix (includes apatite  $\text{Ca}_5[\text{PO}_4]_3(\text{Cl}/\text{F}/\text{OH})$ , nepheline  $\text{KNa}_3[\text{AlSiO}_4]_4$  and rock-forming pyroxene group) was crushed using a laboratory jaw crusher, after which a study of the structure, chemical and phase composition, was carried out (Fig. 1).



FIG. 1. Picture of the sphene (original and after grinding)

The quantitative chemical composition was determined by inductively coupled plasma atomic emission spectrometry on a SpectroBlue device (Spectro Analytical Instruments) for all elements except S. The quantitative content of S was determined by the infrared absorption method on a CS-230 automatic analyzer.

The study of the samples surface chemical composition was carried out using a photoelectron spectrometer from SPECS Surface Nano Analysis GmbH (Germany). The spectrometer is equipped with a PHOIBOS-150-MCD-9 hemispherical analyzer, an XR-50 characteristic X-ray source with a double Al/Mg anode. Non-monochromatic Al  $K\alpha$  radiation ( $h\nu = 1486.6$  eV) was used to record the spectra. To consider the effect of charging the samples, we used the spectrum of  $Ti2p_{3/2}$  ( $E_b = 459.0$  eV), corresponding to the  $TiO_2$  carrier. The relative concentrations of elements in the analysis zone are determined based on the integrated intensities of the XPS peaks, considering the photoionization cross section of the corresponding terms. For a detailed analysis, the spectra were decomposed into individual components. Accordingly, after subtracting the background using the Shirley method, the experimental curve was decomposed into several lines corresponding to the photoemission of electrons from atoms in different chemical environments. Data processing was carried out using the CasaXPS software package. The shape of the peaks is approximated by a symmetric function obtained by multiplying the Gaussian and Lorentzian functions.

The structure of the mineral was studied using high-resolution TEM on a JEM-2010 electron microscope (JEOL, Japan) at an accelerating voltage of 200 kV and a resolution of 140 pm. Images were recorded using a CCD Soft Imaging System camera (Germany).

### 3. Results and discussion

Atomic emission spectroscopy with inductively coupled plasma made it possible to determine the quantitative content of chemical elements in the sample (Table 1). The content is more than 10 Wt % of such elements as Si, Ti and Ca, which probably belongs to the Titanite phase; the content is less than 5 Wt % – Al,  $K_2O$ ,  $Na_2O$ , which belongs to the Nepheline and Microcline minerals, and less than 1 Wt % of elements such as Fe, P, Sr, Ba, Zr, Ce, Nb, Mg, Li and S.

TABLE 1. Quantitative chemical analysis

Element	Si	Ti	Ca	Al	$K_2O$	$Na_2O$	Fe	P
Wt, %	18.8	13.6	12.1	4.8	4.3	3.1	0.9	0.8
Element	Sr	Ba	Zr	Ce	Nb	Mg	Li	S
Wt, %	0.6	0.1	0.1	0.1	0.1	0.1	0.02	0.04

The  $Ti2p$  spectra of the studied samples are shown in Fig. 2. It is known that the  $Ti2p$  spectrum due to the spin-orbit interaction is a doublet  $Ti2p_{3/2} - Ti2p_{1/2}$  with a spin-orbit splitting value of 5.7 eV. In the spectrum of the  $Ti2p$  samples, one doublet is observed with a  $Ti2p_{3/2}$  binding energy of 459.0 eV, which corresponds to titanium in the  $Ti^{4+}$  state. No traces of titanium are observed in any other chemical states. In the literature for  $TiO_2$ , the  $Ti2p_{3/2}$  binding energy values are given in the range of 458.7 – 459.2 eV [8–13]. Fig. 2 also shows the  $O1s$  spectra of the studied samples. The spectra are described by several peaks corresponding to oxygen in different environments, so the  $O1s$  peak in the region of 530.3 – 530.6 eV is undoubtedly referred to oxygen in the  $TiO_2$  structure [8–12], the peak in the region of 532.0 – 532.3 eV can

be attributed to surface  $\text{OH}^-$  groups [8–12], the peak in the region of 533.2 – 533.3 – to the adsorbed water and oxygen in the structure of silicon oxide [8–12, 14]. Fig. 3 shows the  $\text{Si}2p$  spectra of the studied samples. The  $\text{Si}2p$  peak in the region of 100.8 eV can be attributed to silicon carbide, the peaks in the region of 101.6 and 102.8 eV are attributed to silicon oxide in different chemical environments [14, 15]. Relative atomic concentrations of elements in the near-surface layer of the studied samples are presented in Table 2.

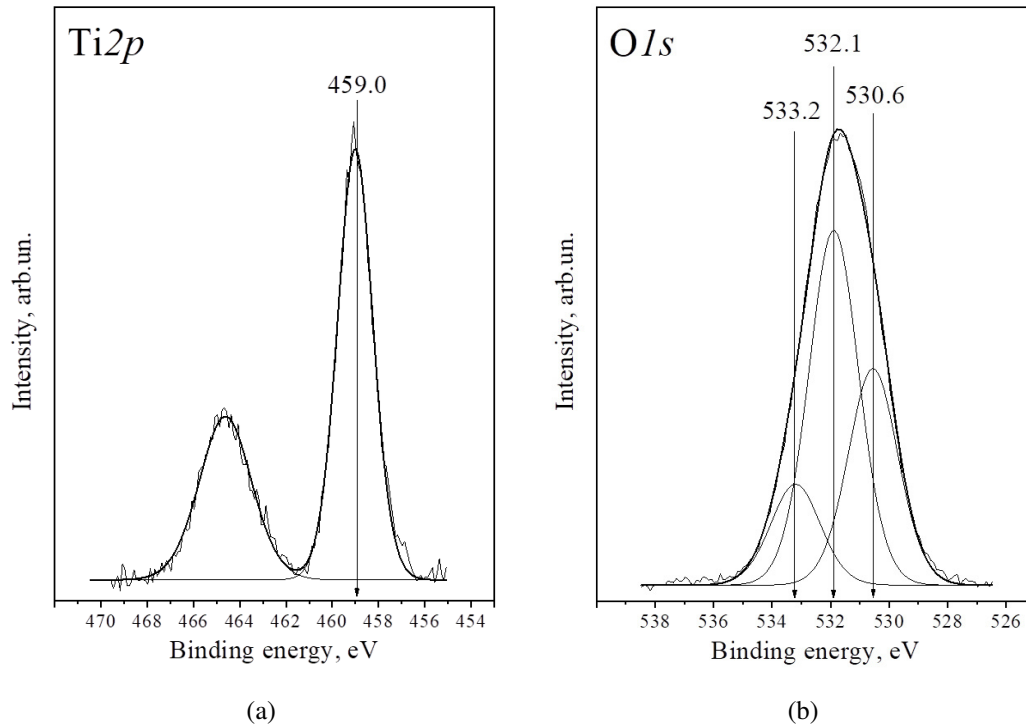


FIG. 2.  $\text{Ti}2p$  and  $\text{O}1s$  spectra of the studied samples. The spectra are normalized to the integrated intensity of the peaks corresponding to the  $\text{C}1s$  spectra

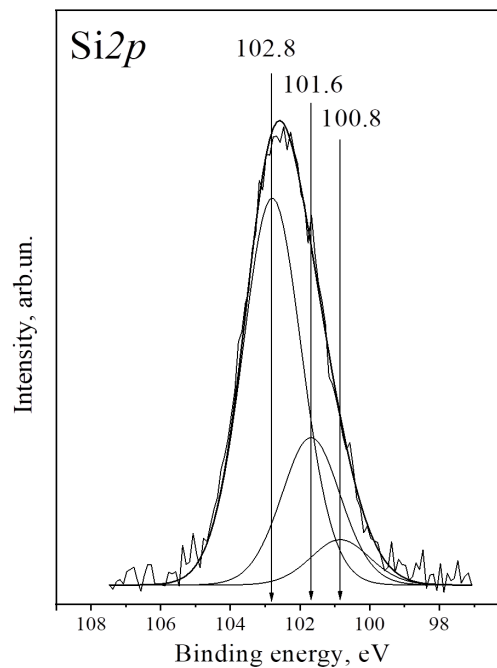


FIG. 3.  $\text{Si}2p$  spectra of the studied samples. The spectra are normalized to the integrated intensity of the peaks corresponding to the  $\text{C}1s$  spectra

TABLE 2. Relative atomic concentrations of elements in the near-surface layer of the studied samples (atomic ratios are normalized to [C])

[O]	[Ti]	[Ca]	[Si]	[K]	[Na]	[Al]	[P]
1.55	0.08	0.14	0.40	0.06	0.10	0.11	0.06

TEM-images (Fig. 4) show the morphology of titanite as a disordered lamellar structure with a diameter size ranging from 3 to 5 nm. Similar picture were obtained for another titanite from Cardiff [16]. A more detailed examination on the left image on Fig. 4 shows an ordered structure with an interplanar distance between atoms of about 0.63 Å, corresponding to titanite (PDF 04-010-2760).

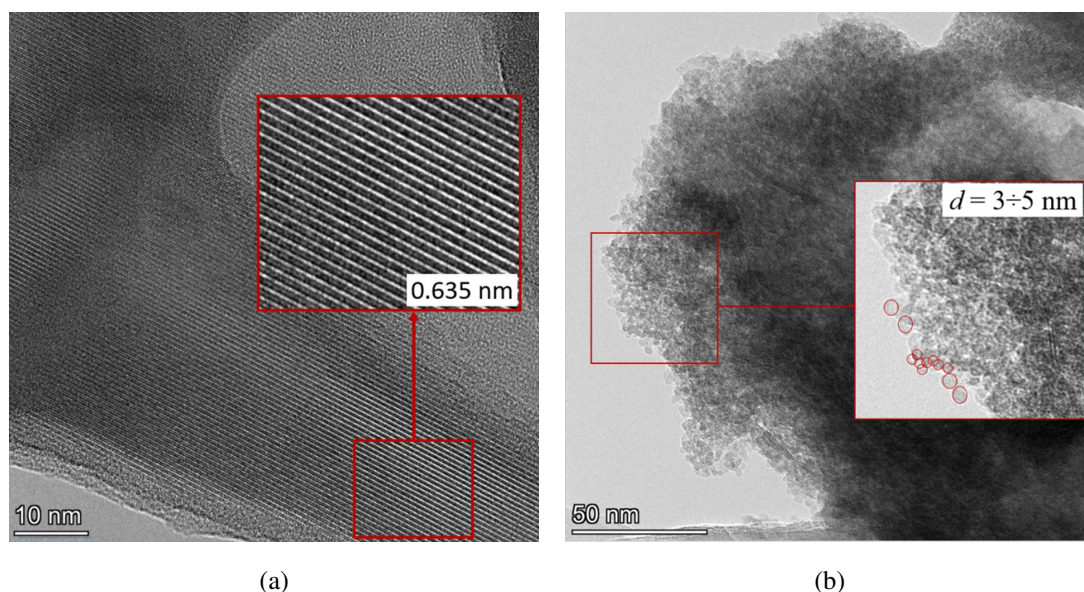


FIG. 4. TEM image of Titanite from the Koashva quarry, Murmansk region

#### 4. Conclusions

In this work, the titanite from the Koashva quarry was studied. Content detected is more than 10 Wt % of such elements as Si, Ti and Ca, which belongs to the Titanite phase; the content is less than 5 Wt % – Al,  $K_2O$ ,  $Na_2O$ , which belongs to the Nepheline and Microcline minerals, and less than 1 Wt % of elements such as Fe, P, Sr, Ba, Zr, Ce, Nb, Mg, Li and S. According to XPS spectra of the  $Ti2p$  samples, one doublet is observed with a  $Ti2p_{3/2}$  binding energy of 459.0 eV, which corresponds to titanium in the  $Ti^{4+}$  state. Spectra of the  $O1s$  are described by several peaks corresponding to oxygen in different environments: in the region of 530.3 – 530.6 eV it is referred to oxygen in the  $TiO_2$  structure, in 532.0 – 532.3 eV it is attributed to surface OH- groups and in 533.2 – 533.3 it belongs to adsorbed water and oxygen in the structure of silicon oxide. Spectra of the  $Si2p$  with peak in the region of 100.8 eV is attributed to silicon carbide, peaks 101.6 and 102.8 eV are attributed to silicon oxide in different chemical environments. This confirms the idea of the phase composition of the studied mineral, which is a promising material for further research targeted on using it as an effective photosorbent for purifying liquid media from toxic substances.

#### References

- [1] Gerasimova L.G., Maslova M.V. *Titanium Hydroxides and Compositions on Their Basis. Production and Application*. Moscow, LKM-press Publ., 2011, 100 p. (In Russian)
- [2] Oleksienko O., Wolkersdorfer C., Sillanpää M. Titanosilicates in Cation Adsorption and Cation Exchange – A Review. *Chemical Engineering J.*, 2017, P. 570–585.
- [3] Milyutin V.V., Nekrasova N.A., Yanicheva N.Y., Kalashnikova G.O., Ganicheva Y.Y. Sorption of Cesium and Strontium Radionuclides onto Crystalline Alkali Metal Titanosilicates. *Radiochemistry*, 2017, **59** (1), P. 65–69.
- [4] Samburov G.O., Kiselev Yu.G. Improving the technology for producing titanium compounds from enriched sphenite ore. *Materials of the Federal Research Centre “KSC” of the RAS*, 2018, **9** (6), P. 51–56 (in Russian).
- [5] Yakovenchuk V.N., Ivanyuk G.Y., Pakhomovsky Y.A., Men’shikov Y.P. *Khibiny, Laplandia Minerals*, Apatity, 2005.
- [6] Nikolaev A.I., Samburov G.O., Kiselev Yu.G., Gerasimova L.G. Sphenite ores – raw materials for the implementation of the titanium compounds technology. *Bulletin of the Academy of Sciences of the U.S.S.R. Physical series*, 2018, P. 83–86 (in Russian).

- [7] Melnikov N.N., Busyrev V.M. The concept of resource-balanced development of the mineral resource base. *Mineral Resources of Russia: Economics and Management*, 2005, **2**, P. 58–64 (in Russian).
- [8] Luan Z., Maes E. M., Van Der Heide P.A.W., Zhao D., Czernuszewicz R.S., Kevan L. Incorporation of Titanium, into Mesoporous Silica Molecular Sieve SBA-15. *Chemistry of Materials*, 1999, **11** (12), P. 3680–3686.
- [9] Hasegawa Y., Ayame A. Investigation of Oxidation States of Titanium in Titanium Silicalite-1 by X-Ray Photoelectron Spectroscopy. *Catalysis Today*, 2001, **71** (1–2), P. 177–187.
- [10] Finetti P., Sedona F., Rizzi G.A., Mick U., Sutara F., Svec M., Matolin V., Schierbaum K., Granozzi G. Core and Valence Band Photoemission Spectroscopy of Well-Ordered Ultrathin  $\text{TiO}_x$  Films on Pt(111). *J. of Physical Chemistry C*, 2007, **111** (2), P. 869–876.
- [11] Kaichev V.V., Popova G.Y., Chesalov Y.A., Saraev A.A., Zemlyanov D.Y., Beloshapkin S.A., Knop-Gericke A., Schlögl R., Andrushkevich T.V., Bukhtiyarov V.I. Selective Oxidation of Methanol to Form Dimethoxymethane and Methyl Formate over a Monolayer  $\text{V}_2\text{O}_5/\text{TiO}_2$  Catalyst. *J. of Catalysis*, 2014, **311**, P. 59–70.
- [12] Kaichev V.V., Chesalov Y.A., Saraev A.A., Klyushin A.Y., Knop-Gericke A., Andrushkevich T.V., Bukhtiyarov V.I. Redox Mechanism for Selective Oxidation of Ethanol over Monolayer  $\text{V}_2\text{O}_5/\text{TiO}_2$  Catalysts. *J. of Catalysis*, 2016, **338**, P. 82–93.
- [13] Mai W., Wen F., Xie D., Leng Y., Mu Z. Structure and Composition Study of Carbon-Doped Titanium Oxide Film Combined with First Principles. *J. of Advanced Ceramics*, 2014, **3** (1), P. 49–55.
- [14] Larina T.V., Dovlitova L.S., Kaichev V.V., Malakhov V.V., Glazneva T.S., Paukshtis E.A., Bal'Zhinimaev B.S. Influence of the Surface Layer of Hydrated Silicon on the Stabilization of  $\text{Co}^{2+}$  Cations in Zr–Si Fiberglass Materials According to XPS, UV-Vis DRS, and Differential Dissolution Phase Analysis. *RSC Advances*, 2015, **5** (97), P. 79898–79905.
- [15] Foucaud Y., Badawi M., Filippov L.O., Barres O., Filippova I.V., Lebègue S. Synergistic Adsorptions of  $\text{Na}_2\text{CO}_3$  and  $\text{Na}_2\text{SiO}_3$  on Calcium Minerals Revealed by Spectroscopic and: Ab Initio Molecular Dynamics Studies. *Chemical Science*, 2019, **10** (43), P. 9928–9940.
- [16] Eby R.K., Ewing R.C. Alpha-Recoil Damage in Titanite ( $\text{CaTiSiO}_5$ ): Direct Observation and Annealing Study Using High Resolution Transmission Electron Microscopy. *J. of Materials Research*, 1991, **6** (3), P. 560–564.

---

*Submitted 11 October 2023; accepted 14 October 2023*

*Information about the authors:*

*Irina B. Dorosheva* – Institute of Metallurgy, Ural Branch of the Russian Academy of Sciences, 620016 Yekaterinburg, Russia; ORCID 0000-0001-9229-6758; dorosheva1993@mail.ru

*Andrey A. Rempel* – Institute of Metallurgy, Ural Branch of the Russian Academy of Sciences, 620016 Yekaterinburg, Russia; ORCID 0000-0002-0543-9982; rempel.imet@mail.ru

*Galina O. Kalashnikova* – Nanomaterials Research Centre, Kola Science Centre, Russian Academy of Sciences, Fersmana str., 14, 184209 Apatity, Russia; ORCID 0000-0002-4857-0884; g.kalashnikova@ksc.ru

*Victor N. Yakovenchuk* – Nanomaterials Research Centre, Kola Science Centre, Russian Academy of Sciences, Fersmana str., 14, 184209 Apatity, Russia; yakovenchuk@geoksc.apatity.ru

*Conflict of interest:* the authors declare no conflict of interest.

## SILD synthesis of porous manganese oxide nanocoatings as electroactive materials for pseudocapacitors

Artem A. Lobinsky, Maria V. Kaneva, Anastasia K. Bachina, Maxim I. Tenevich

Ioffe Institute, St. Petersburg, Russia

Corresponding author: Artem A. Lobinsky, [lobinski.a@mail.ru](mailto:lobinski.a@mail.ru)

PACS 81.07.Bc

**ABSTRACT** In present work the porous nanocoating of manganese oxide were obtained via successive ionic layer deposition from aqueous solutions of potassium permanganate and DMSO. The morphology, phase and chemical composition of the synthesized nanocoatings were characterized by XRD, SEM, EDX and Raman spectroscopy. The possibility of controlled changes in the morphology of the resulting compounds was demonstrated by changing the concentration of reagents and the number of processing cycles in order to obtain optimal electrochemical characteristics. Electrodes based on nickel foam and coated with films of porous manganese oxide showed high specific capacity (1324 and 297 F/g at a current density of 1 A/g in 1 M NaOH and 1 M Na<sub>2</sub>SO<sub>4</sub>, respectively), both in neutral and in aqueous alkaline electrolytes.

**KEYWORDS** manganese oxide, SILD, nanocoatings, electrode materials, pseudocapacitor

**ACKNOWLEDGEMENTS** This research was financial supported by grant of the President of the Russian Federation for state support of young Russian scientists (grant number MK-3864.2022.1.3). The SEM and PXRD study was conducted utilizing equipment at the Engineering Center of the St. Petersburg State Institute of Technology. The authors gratefully acknowledge to the Center for Optical and Laser Materials Research of St. Petersburg State University.

**FOR CITATION** Lobinsky A.A., Kaneva M.V., Bachina A.K., Tenevich M.I. SILD synthesis of porous manganese oxide nanocoatings as electroactive materials for pseudocapacitors. *Nanosystems: Phys. Chem. Math.*, 2023, **14** (5), 554–559.

### 1. Introduction

The increasing demand for more energy every year and the growing environmental problems caused by the burning of limited reserves of fossil fuels encourage the search and use of new, highly efficient and environmentally friendly energy sources [1, 2].

Supercapacitors (SCs) are promising energy storage devices that are characterized by large capacity relative to size, extremely low level of series resistance and high charging speed, which makes them very promising for use in power grids, electric vehicles and portable equipment [3, 4]. Of particular interest are the so-called pseudocapacitors (PSCs), in which energy is stored at the cathode in a double electric layer, and at the anode due to the flow of Faraday processes. Thus, they combine the advantages of electrochemical double-layer (ECDL) supercapacitors (charge rate and cyclic stability) and metal-ion batteries (high energy density), which makes their further application promising [5].

Among the electrode materials for cathodes and anodes of ECDL SCs, carbon materials are most often used, but they have low specific capacity and energy values. The most effective cathode material for PSCs turned out to be ruthenium oxide, since it has high values of theoretical specific capacitance due to the manifestation of the pseudocapacitance, but at the same time such a material is quite expensive, which limits commercial use [6].

Manganese oxides, in particular MnO<sub>2</sub>, are effective electrode materials for chemical current sources because they have a high theoretical specific capacity (1370 F/g) and cycling stability, as well as good stability in various environments [7–9]. However, the obtained specific capacitances of pure MnO<sub>2</sub> are much lower than the theoretical capacity, which is likely due to the low active surface area, poor conductivity, as well as low ion diffusion. Among many ways to increase the capacitive characteristics of the MnO<sub>2</sub> electrode material, increasing its specific surface area by adjusting the pore size and size distribution is considered promising, which can provide better interfacial contact between the electrode and the electrolyte [10]. Thus, the development of methods for the selective synthesis of manganese oxide is a key task for obtaining highly efficient electrode materials.

Currently, several routes are used for the synthesis of manganese oxide nanocoating, namely, hydrothermal route [11], sol-gel route [12], redox reaction [13], thermal decomposition [14], refluxing route [15], co-precipitation [16], etc. However, the presented methods for the synthesis of manganese oxide have a number of limitations related to the duration of the process, the use of devices with high temperature and pressure, higher synthesis temperatures, as well as limiting of the number of possible substrates.

In this research, we propose a novel controllable reduction route synthesis of nanocoatings of manganese oxide on nickel foam via successive ionic layer deposition (SILD) [17, 18] technique from aqueous solutions of manganese permanganate and dimethyl sulfoxide (DMSO) and investigation its application as effective electrode materials for pseudocapacitor in neutral and alkaline electrolytes. The proposed synthesis route is based on the reduction of  $\text{KMnO}_4$  in an aqueous solution of DMSO with different concentrations. The reduction of potassium permanganate by organic compounds is a common method for obtaining manganese oxides [19], however, as far as we know, this route has not been previously used in the SILD method. The production of nanocoats in this way has the advantages of being able to obtain ultrathin oxide films on the surface of various substrates under conditions of “soft chemistry”. Previously, the SILD method has already been successfully used by us to obtain nanocoatings of transition metal oxides and hydroxides [20–22], in particular manganese oxide [23–25].

## 2. Experimental

### 2.1. Fabrication of $\text{MnO}_2$ /nickel foam electrode

Nickel foam (NF) plates (110 PPI, surface area  $1 \text{ cm}^2$ ) were used as substrates. The synthesis of manganese oxide nanocoating was carried out using the SILD method with the occurrence of a reduction reaction on the surface of the nickel foam substrate. As the first reagent for synthesis aqueous solutions of  $\text{KMnO}_4$  (0.01 M) salt were used, and as a second reagent aqueous solution of DMSO (99, 75, 50 and 25 %) is used. The substrates were processed by successive immersion in reagent solutions according to a certain scheme forming one SILD cycle. First, the substrate was immersed in the solution of the first reagent for 30 seconds, then it was washed off the excess reagent in distilled water for 15 seconds. Then the substrate was immersed in a solution of the second reagent and washed again with distilled water for the same time, respectively. As a result of the reduction reaction of  $\text{MnO}_4^{+7}$  to  $\text{Mn}^{+4}$  in DMSO, a layer of sparingly soluble manganese oxide nanocoating on nickel foam surface was formed. After synthesis, the electrodes were dried in air for 24 hours.

The number of SILD cycles was chosen in such a way that it allows on to ensure optimal layer thickness and, at the same time, sufficient mass (1 – 2 mg) required for electrochemical measurements. Concentrations of the DMSO were selected on the basis of preliminary experiments, during which their electrochemical characteristics were analyzed. The 30 SILD cycles and a DMSO concentration of 25 % were chosen as optimal.

### 2.2. Materials characterization

The morphology and chemical composition of synthesized nanocoating were examined by scanning electron microscopy (SEM) (Tescan Vega 3 SBH microscope) and energy-dispersive X-ray spectroscopy (EDX) (Oxford INCA x-act X-ray) technique. Powder X-ray diffraction (PXRD) patterns were acquired using a Rigaku SmartLab 3 X-ray diffractometer, equipped with a Dtex silicon 1-D detector. The X-ray source employed  $\text{Cu K}\alpha$  radiation with a wavelength ( $\lambda$ ) of  $1.540593 \text{ \AA}$ , operating at a voltage of 50 kV and a current of 40 mA. These measurements were carried out utilizing a zero-background silicon holder. The phase identification was accomplished through the utilization of the powder standard database ICSD. Raman spectroscopy measurement was performed with a SENTERRA (Bruker) spectrometer with 633 nm wavelength laser excitation.

### 2.3. Electrochemical measurement

The electrochemical characteristics of synthesized nanolayers as electrode material for pseudocapacitors were studied used cyclic voltammetry (CVA) and galvanostatic charge-discharge (GCD) techniques using Elins P45-X potentiostat/galvanostat. The fabricated working electrodes were measured in a three-electrode electrochemical cell. The  $\text{Ag}/\text{AgCl}$  electrode (neutral media) or  $\text{Hg}/\text{HgO}$  electrode (alkaline media) was used as a reference electrode and the graphite rod was used as a counter electrode. All measurements were carried out at room temperature and atmospheric pressure in aqueous solutions of 1 M  $\text{Na}_2\text{SO}_4$  or 1 M  $\text{NaOH}$ , which were used as an electrolyte.

## 3. Result and discussion

The PXRD pattern obtained for the synthesized sample exhibits diffuse features with broad, low-intensity peaks, as depicted in Fig. 1(a). Phase analysis revealed that the structure of the sample corresponds to the turbostatic birnessite-type. However, differentiating between monoclinic (Space Group:  $\text{C12/m1}$ ) and hexagonal (Space Group:  $\text{P63/mmc}$ ) symmetry is challenging due to the pure crystallinity of the sample. The prominent characteristic reflexes associated with the birnessite structure are highlighted in Fig. 1(b). The shape of the XRD pattern suggests a small crystallite size, imperfections, and the turbostatic nature of the sample. The extinction of some reflexes in the pattern provides evidence for morphological anisotropy observed in such morphological objects like plate-like, lamellar, sheet-like ones.

Birnessite phases are characterized by a layered structure composed of single sheets of  $[\text{MnO}_6]$  octahedrons [26]. In natural birnessite, water molecules and alkaline metal ions are known to occupy the interlayer spaces between the octahedral layers of  $[\text{MnO}_6]$ , typically resulting in a distance between layers of approximately  $7 \text{ \AA}$  [26, 27]. However, in synthetic birnessite, interlayer spaces are predominantly occupied by  $\text{H}_2\text{O}$  molecules, leading to an increased distance

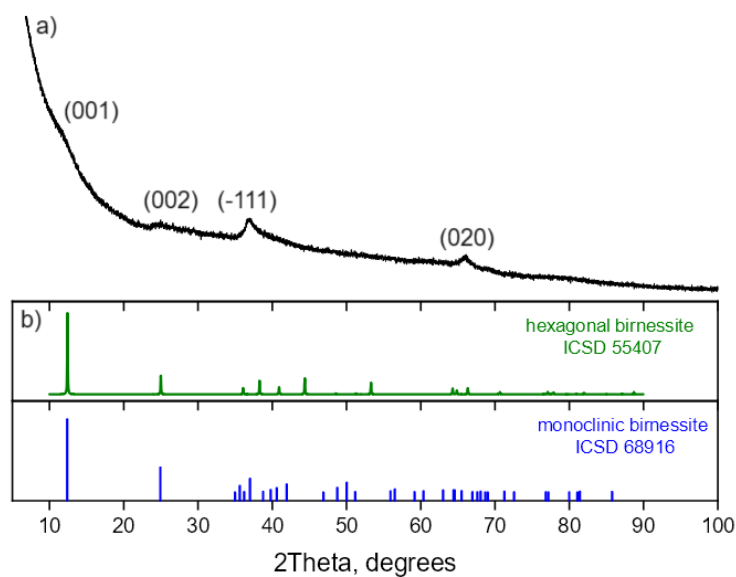


FIG. 1. PXRD pattern of the MnO<sub>2</sub> nanocoatings obtained by SILD method (a) and patterns of the references from ICSD (b)

between successive layers of manganese octahedrons. In turbostratic structures, order within the planes in the *a* and *b* directions is maintained, but there can be a misalignment or complete disorientation within the plane in the *c* direction [28]. The most intense peak at around  $2\theta = 12^\circ$  in the PXRD pattern (Fig. 1(a)) is the indicator of the order in the *c* direction. However, this peak is weak, suggesting a severe misalignment between manganese octahedron layers. The location of this peak corresponds to a d-spacing of  $7.38 [\pm 10] \text{ \AA}$ .

The analysis of SEM data confirms the porous morphology of the synthesized sample. As shown in Fig. 2(a) nanocoating is formed by spherical-like micron-size aggregates of randomly shaped structures. SEM image with higher magnification (Fig. 2(b)), shows that the structure of MnO<sub>2</sub> is porous and built up of set nanosheets with flower-like morphology. EDX results indicate the presence of Mn and O atoms with a small impurity of C, K and S atoms in the nanocoating (no more than 1 %).

The Raman spectrum, presented in Fig. 3, supports the hexagonal birnessite-type structure of the synthesized sample. The relationship between the two highest frequency modes (at around  $570$  and  $680 \text{ cm}^{-1}$ ) is characteristic of the hexagonal birnessite-type structure 4. Moreover, the shift of the high frequency mode at  $680 \text{ cm}^{-1}$  aroused from [MnO<sub>6</sub>] octahedral layer's motions parallel to layer stacking direction is dependent on the interlayer spacing in birnessite-type structures [29, 30]. In work [30], a plot was constructed, depicting the relationship between the Raman shift of the high-frequency mode and the d-spacing, which was subsequently linearly approximated. The determined d-spacing value of  $7.38 [\pm 10] \text{ \AA}$  and the observed shift of the high-frequency mode to  $680 \text{ cm}^{-1}$ , as determined in the present study, closely align with the

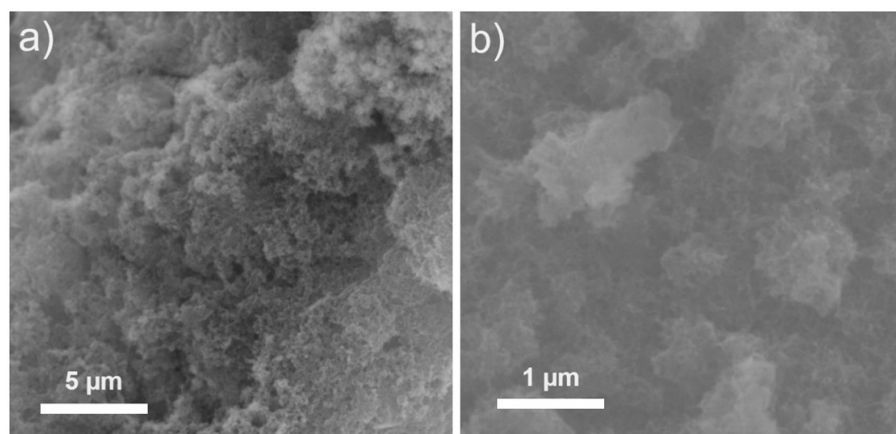


FIG. 2. SEM images of manganese oxide nanocoatings obtained after 30 treatment SILD cycles at lower (a) and at a higher magnification (b)

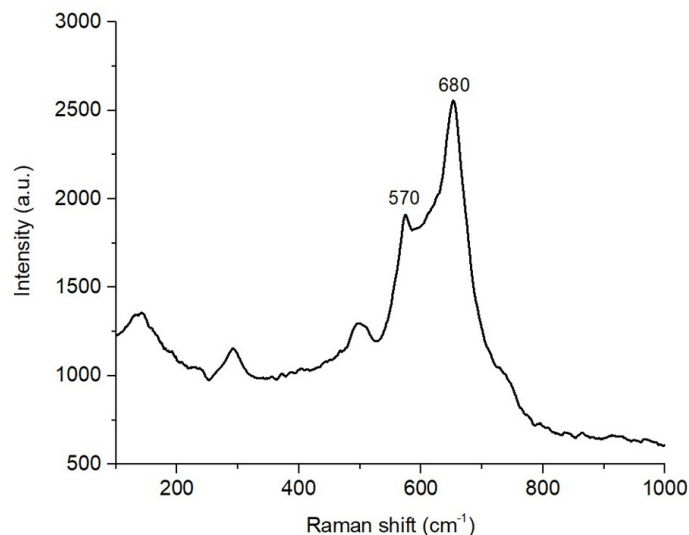


FIG. 3. Raman spectrum of the  $\text{MnO}_2$  nanocoatings obtained by SILD method

results of this approximation. The observed consistency, coupled with an analysis of the intensity distribution of high-frequency modes, serves as additional confirmation of the presence of a hexagonal birnessite-type structure within the obtained sample, characterized by the exclusive intercalation of water molecules between the octahedral layers.

Further, the electrochemical characteristics of the obtained nanocoatings as pseudocapacitor electrodes were evaluated. In an alkaline electrolyte (1 M NaOH) in the electroactive layer of  $\text{MnO}_2$ , the Mn(IV)/Mn(III) redox reaction occurred, which was observed through wide cathode and anode peaks on the CVA curve Fig. 4(a). In a neutral electrolyte (1 M  $\text{Na}_2\text{SO}_4$ ),  $\text{MnO}_2$  electrodes demonstrated pseudocapacitance behavior. The shape of the CVA was close to rectangular with small peaks on the cathode and anode curves Fig. 4(c). The anodic peak is observed at 0.70 V, and the cathodic peak at 0.55 V. This redox process may reflect the redox transitions of the manganese Mn(IV)/Mn(III) or can be related to the cation intercalation/deintercalation.

The specific capacitance was determined from the galvanostatic charge-discharge curves shown in Fig. 4(b,d) for an alkaline and neutral medium, respectively. The measurement was performed at a current density of 1 A/g. The shape of the charge-discharge curves, as well as the CVA, was typical for pseudocapacitors.

Specific capacities for alkaline and neutral media were 1324 and 297 F/g at current density 1 A/g, respectively. The obtained high specific capacitances can be explained by the unique porous thin-film structure of  $\text{MnO}_2$ -based electrodes. The developed morphology and turbostratic structure provides a large number of active sites and a high specific surface area, which ultimately provides excellent capacitive characteristics.

#### 4. Conclusion

For the first time, manganese oxide of the hexagonal turbostratic birnessite-type was successfully synthesized by a direct and simple route based on the reduction of  $\text{KMnO}_4$  by DMSO via SILD method. The characterization of the nanocoating showed that  $\text{MnO}_2$  synthesized in this way has a layered structure with an interlayer space of 7.38 Å and nanoscale crystallites. The morphology obtained by the SEM method, which showed that the nanocoating has a porous structure formed by a set of nanosheets. At the final stage of the study, the electrochemical characteristics of electrodes based on nickel foam with manganese oxide nanocoating were studied. The electrodes demonstrated pseudo-capacitive behaviour and high specific capacitance in both alkaline and neutral electrolytes. Thus, it was shown that the proposed route for the synthesis of  $\text{MnO}_2$  makes it possible to obtain a highly efficient capacitive material in conditions of “soft chemistry” without the use of complex and expensive equipment.

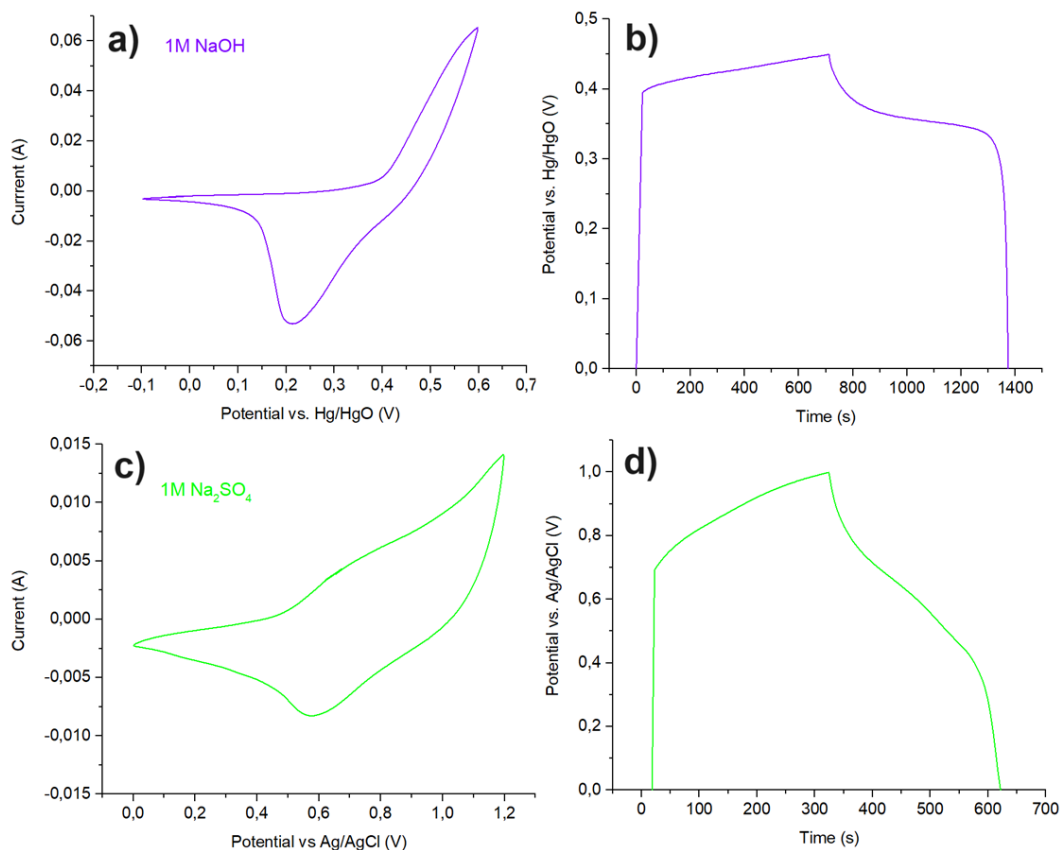


FIG. 4. CVA curves of MnO<sub>2</sub>/NF at scan rate 10 mV/s in 1 M NaOH (a) and 1 M Na<sub>2</sub>SO<sub>4</sub> (c). Galvanostatic charge–discharge curves of MnO<sub>2</sub>/NF at current density 1 A/g in 1 M NaOH (b) and 1 M Na<sub>2</sub>SO<sub>4</sub> (d)

## References

- [1] Liu C., Li F., Ma L.-P., Cheng H.-M. Advanced Materials for Energy Storage. *Adv. Mater.*, 2010, **22**, P. 28–62.
- [2] Zhou G., Li F., Cheng H.-M. Progress in flexible lithium batteries and future prospects. *Energy Environ. Sci.*, 2014, **7**, P. 1307–1338.
- [3] Wang G., Zhang L., Zhang J. A review of electrode materials for electrochemical supercapacitors. *Chem. Soc. Rev.*, 2012, **41**, P. 797–828.
- [4] Zhong C., Deng Y., Hu W., Qiao J., Zhang L., Zhang J. A review of electrolyte materials and compositions for electrochemical supercapacitors. *Chem. Soc. Rev.*, 2015, **44**, P. 7484–7539.
- [5] Bhojane P. Recent advances and fundamentals of Pseudocapacitors: Materials, mechanism, and its understanding. *J. Energy Storage*, 2022, **45**, 103654.
- [6] Sahin M., Blaabjerg F., Sangwongwanich A. A Comprehensive Review on Supercapacitor Applications and Developments. *Energies (Basel)*, 2022, **15** (3), P. 674–699.
- [7] Wei W., Cui X., Chen W., Ivey D.G. Manganese oxide-based materials as electrochemical supercapacitor electrodes. *Chem. Soc. Rev.*, 2011, **40**, P. 1697–1721.
- [8] Simin He, Zunli Mo, Chao Shuai, Wentong Liu, Ruimei Yue, Guigui Liu, Hebing Pei, Ying Chen, Nijuan Liu, Ruibin Guo. Pre-intercalation  $\delta$ -MnO<sub>2</sub> zinc-ion hybrid supercapacitor with high energy storage and ultra-long cycle life. *Applied Surface Science*, 2022, **577**, 151904.
- [9] Gao Y.N., Yang H.Y., Bai Y., Wu C. Mn-based oxides for aqueous rechargeable metal ion batteries. *J. Mater. Chem. A*, 2021, **9**, P.11472–11500.
- [10] Julien C., Mauger A. Nanostructured MnO<sub>2</sub> as electrode materials for energy storage. *Nanomaterials*, 2017, **7**, 396.
- [11] Subramanian V., Zhu H., Vajtai R., Ajayan P.M., Wei B. Hydrothermal synthesis and pseudocapacitance properties of MnO<sub>2</sub> nanostructures. *J. Phys. Chem. B*, 2005, **109**, P. 20207–20214.
- [12] Hashem A.M., Abdel-Ghany A.E., El-Tawil R., Bhaskar A., Hunzinger B., Ehrenberg H., Mauger A., Julien C.M. Urchin-like  $\alpha$ -MnO<sub>2</sub> formed of nano-needles for high-performance lithium batteries. *Ionics*, 2016, **22**, P. 2263–2271.
- [13] Yin B., Zhang S., Jiang H., Qu F., Wu X. Phase-controlled synthesis of polymorphic MnO<sub>2</sub> structures for electrochemical energy storage. *J. Mater. Chem.*, 2015, **3**, P. 5722–5729.
- [14] Alfaruqi M.H., Gim J., Kim S., Song J., Kim J. A layered  $\delta$ -MnO<sub>2</sub> nanoflake cathode with high zinc-storage capacities for eco-friendly battery applications. *Electrochem. Commun.*, 2015, **60**, P. 121–125.
- [15] Cui H.J., Huang H.Z., Fu M.L., Yuan B.L., Pearl W. Facile synthesis and catalytic properties of single crystalline  $\beta$ -MnO<sub>2</sub> nanorods. *Catal. Commun.*, 2011, **12**, P. 1339–1343.
- [16] Kumar H., Sangwan M., Sangwan P. Synthesis and characterization of MnO<sub>2</sub> nanoparticles using co-precipitation technique. *Int. J. Chem. Chem. Eng.*, 2013, **3**, P. 155–160.
- [17] Samantha Prabath Ratnayake, Jiawen Ren, Elena Colusso, Massimo Guglielmi, Alessandro Martucci, Enrico Della Gaspera. SILAR deposition of metal oxide nanostructured films. *Small*, 2021, 2101666.
- [18] Tolstoy V.P. Successive ionic layer deposition. The use in nanotechnology *Russ. Chem. Rev.*, 2006, **75**, P. 161.

- [19] Ragupathy P., Vasan H.N., Munichandraiah N. Synthesis and characterization of nano-MnO<sub>2</sub> for electrochemical supercapacitor studies. *J. Electrochem. Soc.*, 2008, **155**, P. 34–40.
- [20] Kodintsev I.A., Martinson K.D., Lobinsky A.A., Popkov V.I. SILD synthesis of the efficient and stable electrocatalyst based on CoO-NiO solid solution toward hydrogen production. *Nanosystems: Physics, Chemistry, Mathematics*, 2019, **10** (6), P. 681–685.
- [21] Kodintsev I.A., Martinson K.D., Lobinsky A.A., Popkov V.I. Successive ionic layer deposition of co-doped Cu(OH)<sub>2</sub> nanorods as electrode material for electrocatalytic reforming of ethanol. *Nanosystems: Physics, Chemistry, Mathematics*, 2019, **10** (5), P. 573–578.
- [22] Lobinsky A.A., Kaneva M.V. Synthesis Ni-doped CuO nanorods via successive ionic layer deposition method and their capacitive performance. *Nanosystems: Physics, Chemistry, Mathematics*, 2020, **11** (5), P. 573–578.
- [23] Lobinsky A.A., Kaneva M.V. Layer-by-layer synthesis of Zn-doped MnO<sub>2</sub> nanocrystals as cathode materials for aqueous zinc-ion battery. *Nanosystems: Physics, Chemistry, Mathematics*, 2021, **12** (2), P. 182–187.
- [24] Lobinsky A.A., Tenevich M.I. Synthesis 2D nanocrystals of Co-doped manganese oxide as cathode materials of zinc-ion hybrid supercapacitor. *Nanosystems: Physics, Chemistry, Mathematics*, 2022, **13** (5), P. 525–529.
- [25] Lobinsky A.A., Kodintsev I.A., Tenevich M.I., Popkov V.I. A novel oxidation–reduction route for the morphology-controlled synthesis of manganese oxide nanocoating as highly effective material for pseudocapacitors. *Coatings*, 2023, **13** (2), 361.
- [26] Post J.E., Veblen D.R. Crystal structure determinations of synthetic sodium, magnesium, and potassium birnessite using TEM and the Rietveld method. *American Mineralogist*, 1990, **75**.
- [27] Min S., Kim Y. Physicochemical characteristics of the birnessite and todorokite synthesized using various methods. *Minerals*, 2020, **10**, P. 1–17.
- [28] Sabri M., King H.J., Gummow R.J., Malherbe F., Hocking R.K. The Oxidation of Peroxide by Disordered Metal Oxides: A Measurement of Thermodynamic Stability “By Proxy”. *Chempluschem*, 2018, **83**, P. 620–629.
- [29] Post J.E., McKeown D.A., Heaney P.J. Raman spectroscopy study of manganese oxides: Layer structures. *American Mineralogist*, 2021, **106**, P. 351–366.
- [30] Julien C., et al. Raman spectra of birnessite manganese dioxides. *Solid State Ion*, 2003, **159**, P. 345–356.

---

*Submitted 5 September 2023; accepted 10 October 2023*

*Information about the authors:*

*Artem A. Lobinsky* – Ioffe Institute, Saint Petersburg, 194021, Russia; ORCID 0000-0001-5930-2087; lobinsky.a@gmail.com

*Maria V. Kaneva* – Ioffe Institute, Saint Petersburg, 194021, Russia; ORCID 0000-0003-2816-7059; skt94@bk.ru

*Anastasia K. Bachina* – Ioffe Institute, Saint Petersburg, 194021, Russia; ORCID 0000-0001-7015-1435; a.k.bachina@yandex.ru

*Maxim I. Tenevich* – Ioffe Institute, Saint Petersburg, 194021, Russia; ORCID 0000-0003-2003-0672; mtenevich@gmail.com

*Conflict of interest:* the authors declare no conflict of interest.

## Cerium oxide@silica core-shell nanocomposite as multimodal platforms for drug release and synergistic anticancer effects

Elizaveta A. Zamyatina<sup>1,a</sup>, Sergey Yu. Kottsov<sup>2,b</sup>, Viktoriia A. Anikina<sup>1,c</sup>, Anton L. Popov<sup>1,d</sup>, Marina P. Shevelyova<sup>3,e</sup>, Nelli R. Popova<sup>1,f</sup>

<sup>1</sup>Institute of Theoretical and Experimental Biophysics of the Russian Academy of Sciences, Pushchino, Russia

<sup>2</sup>Kurnakov Institute of General and Inorganic Chemistry of the Russian Academy of Sciences, Moscow, Russia

<sup>3</sup>Institute for Biological Instrumentation of the Russian Academy of Sciences, Pushchino, Russia

<sup>a</sup>sonyoru162@gmail.com, <sup>b</sup>sergey12-17@yandex.ru, <sup>c</sup>viktoriya.anikina@list.ru,

<sup>d</sup>antonpopovleonid@gmail.com, <sup>e</sup>marina.shevelyova@gmail.com, <sup>f</sup>nellipopovaran@gmail.com

Corresponding author: Nelli R. Popova, nellipopovaran@gmail.com

**ABSTRACT** Cerium oxide nanoparticles (CeNPs) are among the most promising materials with pH-sensitive redox-activity for biomedical nanotechnologies. CeNPs are known to reduce the toxicity of the chemotherapeutic drug doxorubicin (DOX) for normal cells. Here we have proposed and analyzed a new hybrid cerium/silica containing SiNPs@DOX@CeNPs nanocomposite. We showed that the average size of the nanocomposite is 190 nm and it has a spherical shape. The SiNPs@DOX@CeNPs nanocomposite provides effective synergistic anticancer activity of CeNPs with doxorubicin (DOX), as well as selective toxicity against human osteosarcoma (MNNG/HOS) cells *in vitro*. The SiNPs@DOX@CeNPs nanocomposite may be a good candidate to increase the effectiveness of cancer doxorubicin chemotherapy.

**KEYWORDS** nanocomposites, silica nanoparticles, cerium oxide nanoparticles, biomedical application, characterization, drug delivery

**ACKNOWLEDGEMENTS** This research was funded by the Russian Science Foundation, grant number 22-63-00082 and performed using the equipment of the Joint Research Centre for Physical Methods of Research at Kurnakov Institute of General and Inorganic Chemistry of the Russian Academy of Sciences (JRC PMR IGIC RAS).

**FOR CITATION** Zamyatina E.A., Kottsov S.Yu., Anikina V.A., Popov A.L., Shevelyova M.P., Popova N.R. Cerium oxide@silica core-shell nanocomposite as multimodal platforms for drug release and synergistic anticancer effects. *Nanosystems: Phys. Chem. Math.*, 2023, **14** (5), 560–570.

### 1. Introduction

Currently, nanomaterials are being widely studied as potential means of increasing the bioavailability of drugs and the effectiveness of therapy for socially significant diseases [1–4]. Cerium oxide nanoparticles (CeNPs) hold a special place among engineered nanomaterials due to the wide range of their enzyme-like activities and bioavailability. They possess superoxide dismutase-, catalase- and peroxidase-like properties, as well as recently discovered phosphatase-, photolyase-, phospholipase-, nuclease-, lipo- and phospholipoperoxidase-like properties [5]. This makes CeNPs a unique multifunctional nanozyme and expands the scope of its future biomedical applications [6–8]. Moreover, it is known that CeNPs increases the bioavailability of a number of biologically active compounds, for example, curcumin [9], and also provides selective redox activity of widely used therapeutic agents for example, doxorubicin (DOX) [10, 11].

DOX has been widely acknowledged as the most commonly used anticancer drug for several decades [12]. However, DOX administration is related to some side effects including the toxicity to multiple organs as well as resistance development towards DOX of cancer cells [13–15]. The use of nanoscale carriers, silica nanoparticles (SiNPs) belong to, is considered as potential solution to increase the performance on tumor cells and reduce the adverse effects on normal cells of DOX due to their ability to access efficaciously into tumor cells [16]. Interestingly, CeNPs with their concomitant administration with DOX managed to mitigate doxorubicin-induced hepatic insult on both histological and biochemical aspects in rats. Recently, an inspiring *in vitro* study [17] has reported that the co-administration of CeNPs with DOX could boost its anti-neoplastic activity in melanoma cells without hampering the viability of normal stromal cells [10]. Moreover, cerium-based nanomaterials were found to enhance the chemosensitization of cancer cells rather than normal cells [11].

Moreover, it has been revealed that the biomimetic enzyme activity of the CeNPs was positively correlated with its surface area-to-volume ratio [18]. It is nanocrystalline cerium oxide of 2 – 10 nm size that most clearly manifests its biological activity, which was shown *in vitro* and *in vivo* [19, 20]. However, due to the ultrasmall size of CeO<sub>2</sub> particles,

short circulation half-time and interparticle agglomeration are anticipated, which compromises the bioavailability and enzyme-like activity of the CeNPs in the targeted site.

SiNPs can be used to accommodate ultrasmall CeNPs to solve this problem. SiNPs have been widely studied as effective systems for the delivery of therapeutic and diagnostic agents to combat various types of diseases, including diabetes, oncological diseases, and diseases accompanied by inflammatory processes [21–25]. It has been shown that, when ingested, SiNPs are rapidly degraded in the excretory organs to orthosilicic acid and excreted in the urine [26–28]. In addition, this approach will also make it possible to combine a model therapeutic agent (DOX) in one nanocomposite. There are several studies showing the possibility of using SiNPs to deliver DOX and CeNPs separately [18, 29]. We found only one paper where the responsive system was designed based on CeNPs coated DOX and photosensitizer hematoporphyrin dual-loaded mesoporous SiNPs for synergetic chemotherapy and photodynamic therapy [30].

Thus, the aim of the present study is to combine CeNPs and DOX in a single nanocomposite using simple SiNPs synthesis technique as a basis in order to analyze their properties and selective toxicity *in vitro*. The results obtained are of special importance for advancing the pharmacotherapeutic applications of CeNPs for the treatment of socially significant diseases and development of synergetic chemotherapy.

## 2. Materials and methods

### 2.1. Materials

Tetraethoxysilane (TEOS) (purity  $\geq 99.0\%$ ) was obtained from Sigma-Aldrich (USA), aqueous ammonia (25 %) was purchased from Dia-M (Russia), ethanol (purity 94 – 96 %, ACS) was obtained from Alfa Aesar (USA), anhydrous copper (II) sulfate (purity  $\geq 99.0\%$ ) was purchased from Acros Organics (Belgium). CeNPs were obtained from Kurnakov Institute of General and Inorganic Chemistry of the Russian Academy of Sciences. DOX was obtained from Teva Pharmaceutical Industries (Israel).

### 2.2. SiNPs synthesis

The synthesis procedure was carried out using the Stöber method [31]. Ethanol was preliminarily dried to reduce the amount of H<sub>2</sub>O entering the system. To do this, anhydrous copper (II) sulfate was added to 94 – 96 % ethanol, kept for 24 h, and then the resulting ethanol was filtered off. The process of ethyl alcohol drying was carried out for 14 days. Then, 0.2 M ammonia was added to 50 ml of anhydrous ethanol, then the beaker was placed on a magnetic stirrer and the solution was stirred (500 rpm) at room temperature for 10 minutes. Then 0.1 M TEOS was added dropwise, the resulting solution was stirred for 1 hour. Mixture solutions were centrifuged at 6000 rpm for 20 minutes, then washed with anhydrous ethanol and deionized water. The washing cycle was repeated until the required pH was reached. After each step of the synthesis, the pH of the solutions was measured to control the rate of reactions under alkaline conditions (pH > 10). The resulting SiNPs sol in water after completion of all stages was stored at a temperature of 4 °C. Then, other types of SiNPs were synthesized with a change in one of the synthesis parameters in the established range (Table 1), while the remaining characteristics corresponded to the standard protocol presented above.

### 2.3. CeNPs synthesis

The aqueous sol of CeNPs stabilized by citrate ions was prepared according to the procedure below: 0.24 g of citric acid was dissolved in 25 ml of 0.05 M aqueous solution of cerium (III) nitrate. This solution was rapidly added to 100 ml of 3 M ammonia solution under stirring and kept for 2 h. A stable sol of CeNPs is thus obtained [32].

TABLE 1. SiNPs samples obtained by variations in synthesis characteristics (ammonia, ethanol, TEOS) using the Stöber method

Sample name	Ammonia concentration, M	Ethanol volume, ml	TEOS concentration, M
A	0.2	50	0.1
B	0.5	50	0.1
C	0.6	50	0.1
D	1.2	50	0.1
E	0.2	25	0.1
F	0.2	75	0.1
G	0.2	50	0.04
H	0.2	50	0.2

#### 2.4. SiNPs@DOX@CeNPs synthesis

The following was done for the modification of nanoparticles with DOX: 900  $\mu\text{l}$  of water was added to 100  $\mu\text{l}$  of SiNPs particles. Then DOX was added to SiNPs at concentrations of 0.5, 1, 2.5, 5 mg/ml. The resulting solutions were mixed on a rotary mixer for 24 h in the dark. Then the pH of the solutions was adjusted to 7.8 with 0.1 M  $\text{Na}_2\text{HPO}_4$ . The resulting nanoparticles were collected by centrifugation (9000 rpm, 10 min) and washed with deionized water three times. The amount of loaded DOX was analyzed by spectrophotometry as detailed below in 2.5. Then the ratio of SiNPs and CeNPs was 1:1.43 to modify the nanoparticles. CeNPs were added in concentration 200 mg/ml to SiNPs solution, then the solution was placed in the ultrasonic bath for 1 minute, after which the nanoparticles were left to mix on a rotary mixer for 15 h [33]. The nanoparticles were collected by centrifugation (9000 rpm, 20 min) and washed 3 times with deionized water.

#### 2.5. DOX loading

The amount of loaded DOX was measured by spectrophotometry using a microplate spectrophotometer Multiscan FC (Thermo Fisher, USA) with a detection wavelength of 480 nm. The encapsulation efficiency (EE) was calculated as amount of DOX loaded in SiNPs/amount of drug added  $\times 100\%$ ; loading capacity (LC) was calculated as amount of DOX in SiNPs/amount of SiNPs  $\times 100\%$  [29].

$$EE (\%) = \left[ \left( \frac{\text{Amount of DOX loaded into SiNP}}{\text{Initial amount of DOX}} \right) \right] \times 100,$$

$$LC (\%) = \left[ \left( \frac{\text{Initial amount of DOX} - \text{amount of DOX supernatant}}{\text{Amount of MSN} + \text{amount of DOX}} \right) \right] \times 100.$$

#### 2.6. Nanoparticles size, shape, $\zeta$ -potential and EDX analysis

Size of nanoparticles was measured by scanning electron microscopy (SEM) using an NVision 40 microscope (Carl Zeiss, Germany) at an accelerating voltage of 3 kV. The shape of the nanoparticles was analyzed by transmission electron microscopy (TEM) using a JEM-1011 electron microscope (JEOL, Japan). The chemical composition analysis (energy dispersive X-ray analysis, EDX) of the samples was performed using a Carl Zeiss NVision 40 field emission scanning electron microscope equipped with an Oxford Instruments Oxford Instruments INCA (80 mm<sup>2</sup>) detector, at an accelerating voltage of 20 kV. The hydrodynamic diameter and  $\zeta$ -potential of the resulting nanoparticles were measured using dynamic light scattering (DLS) and electrophoretic light scattering (ELS) with a Zetasizer Nano ZS nanoparticle characterization system (Malvern Panalytical, UK). The measurements were carried out at 25 °C. Each measurement represented an average of 15 runs (the number of runs was determined automatically by the instrument). The signals were analyzed using a single-plate multichannel correlator coupled to computer equipped with the Zetasizer Software package for estimating the diameters by the distribution analysis model. All the samples were measured at least 5 times; the average measurement error was about 5 %.

#### 2.7. BET surface area analysis

SiNPs specific surface area (SBET) was determined using a low-temperature nitrogen adsorption device Sorbtometer-M (Katakon, Russia) using the Brunauer–Emmett–Teller (BET) model based on experimental data in  $P/P_0$  range of 0.05 – 0.25. Before the measurements, the samples were outgassed for 1 h at 200 °C under a nitrogen flow.

#### 2.8. FTIR-spectroscopy

The Fourier-transform infrared (FTIR) spectra of the samples were obtained using a Spectrum 65 FT-IR spectrometer (Perkin Elmer, USA) with a Quest ATR attenuated total reflection (ATR) accessory (Specac, UK) in the wavenumber range of 400 – 4000  $\text{cm}^{-1}$ .

#### 2.9. Raman spectroscopy

Raman spectra were obtained using a Confotec NR500 Raman microscope (Sol Instruments, Belarus) at 633 nm excitation laser wavelength operating at  $\sim 3$  mW power using  $\times 40$  magnification lens (NA = 0.75).

#### 2.10. Cell culture

Human Mesenchymal Stem cells (hMSc) were isolated from the tooth pulp of a healthy donor, according to orthodontic prescription and with the informed consent of the patient. All procedures were carried out in accordance with the approved clinical rules for biomaterial sampling. Human Bone Osteosarcoma (MNNG/HOS) cell culture was obtained from the Cryobank of the Institute of Cell Biophysics of the Russian Academy of Science (Russia). hMSc and MNNG/HOS were cultured in Dulbecco's Modified Eagle's Medium (DMEM)/F12 (1:1) with the addition of 10 % fetal bovine serum and 100 U/ml penicillin/streptomycin under 5 %  $\text{CO}_2$  at 37 °C.

### 2.11. MTT assay

The determination of mitochondrial and cytoplasmic dehydrogenases activity in living cells was carried out using a MTT assay based on the reduction of the colorless tetrazolium salt (3-[4,5-dimethylthiazol-2-yl]-2,5-diphenyltetrazolium bromide, MTT, Sigma-Aldrich, USA). Briefly, SiNPs, SiNPs@CeNPs, SiNPs@DOX@CeNPs, DOX and CeNP were added to cells growing in 96-well plates (for 24, 48 and 72 h at 37 °C in humid air (98 %) containing 5 % CO<sub>2</sub>). 3 h prior to the end of the exposure period, the supernatant was removed, and MTT solution in phosphate-buffered saline (0.5 mg/mL, 100  $\mu$ L/well) was added to the cells for 10 min. Upon the completion of the exposure period, the supernatant was removed, and a lysis solution containing 0.1 % sodium dodecyl sulfate (Sigma-Aldrich, USA) solution in dimethyl sulfoxide was added. Plates were shaken for 10 min, placed on a microplate spectrophotometer Multiskan FC (Thermo Fisher, USA), and the absorbance was read colorimetrically at 570 nm. Each experiment was repeated three times, with five replications.

### 2.12. Live/dead assay

Cell viability after exposure to nanoparticles was assessed using a Carl Zeiss Axiovert 200 microscope. Cells were seeded into 96-well plates and stained with Hoechst 33342 fluorescent dye (absorption – 350 nm, emission – 461 nm) and a propidium iodide dye (absorption – 493 nm, emission – 636 nm). The dyes were added to the DMEM/F12 without serum (1  $\mu$ g/ml) and the plate was placed in a CO<sub>2</sub> incubator for 15 min. Microphotographs were taken after washing the cells with a phosphate-buffered saline. For each cell group, four fields in each well were examined. The number of cells (total cells/dead cells) was calculated using the ImageJ software.

## 3. Results and discussion

### 3.1. Synthesis, properties and characterization of nanoparticles

*3.1.1. Synthesis, properties and morphology of SiNPs.* To obtain SiNPs, the Stöber method is widely used [31], being one of the most widespread and easy-to-control methods for obtaining nanoparticles of controlled size, shape, and morphology [34]. For the biomedical applications the preferred nanoparticles size is to be in the range of 10 – 150 nm. This is due to the fact that nanoparticles smaller than 10 nm are rapidly excreted by the renal system. On the other hand, too large nanoparticles (more than 200 nm) do not pass through endothelial pores. Optimizations of the synthesis conditions are required to achieve the optimal SiNPs size. The influence of the concentrations of TEOS/ethanol/ammonia on the size and morphology of the synthesized SiNPs was studied (Table 1). The particle size and other structural characteristics the concentrations of the precursors of each sample are shown in Table 2.

TABLE 2. Main characteristics of SiNPs

Sample name	Particle diameter (SEM), nm	Hydrodynamic diameter in deionized water, nm	$\zeta$ -potential in deionized water, mV	PDI
A	70 $\pm$ 6	140 $\pm$ 12	-53.6 $\pm$ 1.8	0.14 $\pm$ 0.02
B	77 $\pm$ 13	285 $\pm$ 23	-54.5 $\pm$ 2.5	0.19 $\pm$ 0.01
C	110 $\pm$ 17	253 $\pm$ 21	-30.1 $\pm$ 1.4	0.15 $\pm$ 0.01
D	682 $\pm$ 28	755 $\pm$ 17	-10.2 $\pm$ 1.5	0.73 $\pm$ 0.02
E	77 $\pm$ 9	126 $\pm$ 16	-53.5 $\pm$ 0.9	0.16 $\pm$ 0.01
F	282 $\pm$ 10	403 $\pm$ 26	-45.8 $\pm$ 1.7	0.51 $\pm$ 0.02
G	94 $\pm$ 11	104 $\pm$ 15	-46.2 $\pm$ 1.4	0.28 $\pm$ 0.01
H	342 $\pm$ 15	363 $\pm$ 19	-59.4 $\pm$ 2.3	0.24 $\pm$ 0.01

The size of the nanoparticles was investigated using DLS and SEM (Table 2, Fig. 1) methods. TEOS acts as a silica precursor for the synthesis of SiNPs, and its concentration affects the rate of seed growth and nucleation [32]. An increase in TEOS concentration raises the number of hydrolyzed silicic acid monomers and ultimately the size of SiNPs. For the 0.1 M TEOS, the nanoparticles have optimal size for biological applications (hydrodynamic diameter is 140  $\pm$  12 nm ( $\zeta$ -potential of -53.6  $\pm$  1.8 mV) with low PDI values of 0.14  $\pm$  0.02). The PDI values confirm high homogeneity of the samples. Ammonia used during Stöber synthesis acts as a catalyst for the hydrolysis of TEOS (silica precursor), i.e., partially to fully hydrolyzed silanol monomers are produced with increasing ammonia concentration. It enhances the degree of polymerization/condensation and hence leads to the larger SiNPs. Less hydrolyzed monomers are produced at lower ammonia concentration resulting in the small-sized SiNPs. With an increase of ammonia concentration from 0.2 to 1.2 M, the particle size increased from 70 to 680 nm. It is known that there is a correlation between the ammonia

concentration and the size of silica spheres, which is associated with the processes of increasing polymerization [31, 35]. Smaller size of spherical SiNPs was obtained using a lower concentration of ethanol. This may indicate that the solvent interacts with silanol groups (Si–O–H) in the formation of SiNPs. The particle size increases with the length of the alcohol chain [36].

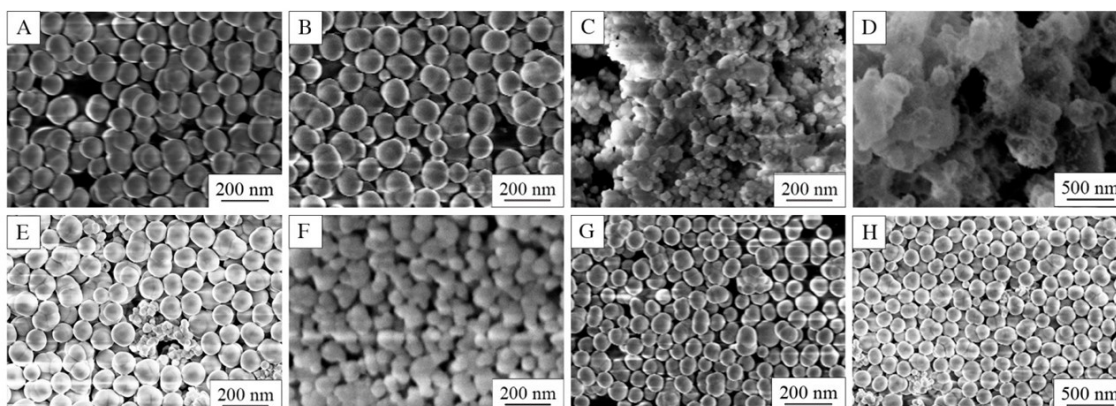


FIG. 1. SEM images of SiNPs obtained by varying concentrations of ammonia: 0.2 M (A); 0.5 M (B); 0.6 M (C) and 1.2 M (D); by varying the volume of ethanol: 25 ml (E) and 75 ml (F); by varying the concentration of TEOS 0.04 M (G), 0.2 M (H)

The morphology of SiNPs was observed using SEM images (Fig. 1). SiNPs showed uniform particle distribution with a diameter of 70 to 670 nm. All synthesized SiNPs have spherical shape. Spherical nanoparticles with hydrodynamic diameter of  $140 \pm 12$  nm were chosen for the further modification in this study.

SiNPs specific surface area was measured to be  $S_{BET} = 19 \text{ m}^2/\text{g}$  (Sample A, Tables 1, 2). That value corresponds to smooth spherical SiNPs ( $\rho = 2.1 \text{ g/cm}^3$ ) of about 150 nm in diameter  $d [\text{nm}] = \frac{6 \cdot 10^3}{\rho \cdot S_{BET}}$ , which is significantly higher than the particle size estimated from SEM ( $70 \pm 6$  nm). Thus, the obtained surface area value is probably underestimated due to BET method experimental error [37] and SiNPs aggregation during the sample degassing stage.

**3.1.2. SiNPs@DOX, SiNPs@CeNPs, SiNPs@DOX and SiNPs@DOX@CeNPs synthesis and properties.** SiNPs were synthesized by the method described above. At the next stage, DOX was conjugated to the SiNPs surface. In order to confirm the adsorption of DOX on SiNPs surface and the absence of the chemical interaction between them, an FTIR and Raman spectroscopy study was carried out (Fig. 2).

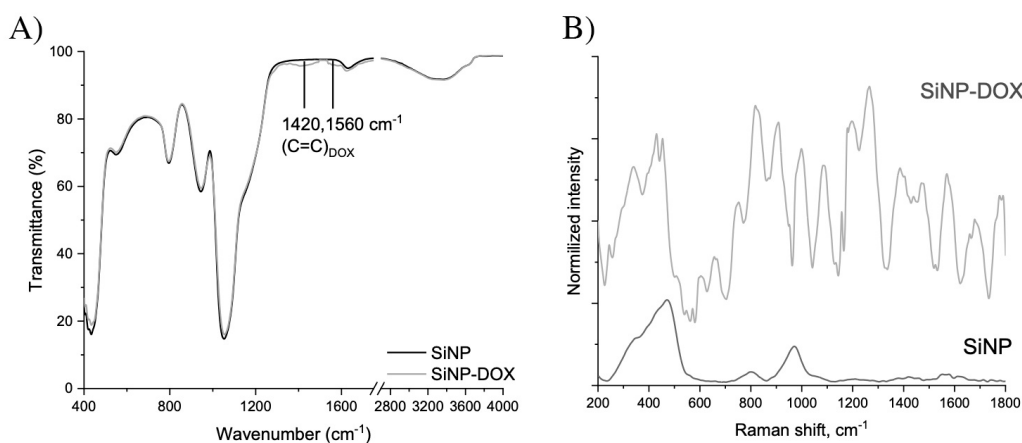


FIG. 2. (a) FTIR and (b) Raman spectra of SiNPs loaded with DOX

FTIR spectrum of SiNPs is typical for sol-gel silica nanoparticles with, all major silica bands vibrations present: bending O–Si–O ( $434 \text{ cm}^{-1}$ ), breathing  $(\text{Si–O})_3$  cycle vibrations ( $548 \text{ cm}^{-1}$ ) and Si–O–Si stretching vibrations ( $796$ ,  $1054$  and  $1200$  (shoulder)  $\text{cm}^{-1}$ ) [38]. The peak at  $946 \text{ cm}^{-1}$  is attributed to Si–OH stretching vibrations at nanoparticles surface; the presence of OH-groups is also confirmed by the negative  $\delta$ -potential of SiNPs (Table 2). The bands of bending ( $1630 \text{ cm}^{-1}$ ) and stretching ( $\sim 3300 \text{ cm}^{-1}$ ) vibrations of residual water in SiNPs are also present [39]. The

FTIR spectrum of the nanoparticles barely changed after the DOX loading. The only new vibration bands appeared at 1420 and 1560  $\text{cm}^{-1}$  which can be attributed to C=C bond vibrations in the aromatic structure of DOX [38–40].

To reliably confirm DOX loading at SiNPs, Raman spectroscopy was used due to its better sensitivity to nonpolar, but polarizable moieties [41], such as aromatic system of DOX molecule. Spectrum of bare SiNPs was also typical for SiNPs: bands at 354 (O–Si–O deformation), 469 (HO–SiO<sub>3</sub> breathing mode), 801 (Si–O–Si stretching) and 972  $\text{cm}^{-1}$  (Si–OH asymmetric stretching) were observed [38, 42]. After DOX incorporation in SiNPs many new vibration bands were registered in Raman spectrum indicating the successful DOX adsorption, with the main characteristic DOX bands at 454 and 1082  $\text{cm}^{-1}$  (deformation C–O vibrations), 996  $\text{cm}^{-1}$  (C–C ring breathing vibration), 1201 and 1265  $\text{cm}^{-1}$  (combinational modes of ring breathing vibrations and OH band deformation), and 1571  $\text{cm}^{-1}$  (non-aromatic ring stretching) [38, 42–44]. No noticeable band wavelength shift was registered for SiNPs@DOX composite compared to pure DOX indicating the lack of chemical interaction between silica and DOX.

DOX loading was studied using different concentrations of DOX, the evaluation of the SiNPs modification efficiency was carried out by calculating the EE and LC parameters. EE and LC values of DOX in SiNPs are shown in Table 3. With an increase in the concentration of loaded DOX from 0.5 to 5 mg/ml, the EE of the drug increased from 90.69 to 98.99 %. Also, the drug loading capacity increased from 75.57 to 97.04 %. Thus, in the further study, the DOX concentration of 5 mg/ml was selected for the fabrication of SiNPs@DOX. SiNPs are effectively loaded with DOX mainly due to the physical adsorption.

TABLE 3. Encapsulation efficiency (EE) and loading capacity (LC) of DOX in SiNPs

Amount of loaded DOX, mg/ml	EE, %	LC, %
0.5	90.69	75.57
1	95.34	86.68
2.5	98.13	94.36
5	98.99	97.04

At the second stage, SiNPs@DOX were conjugated with CeNPs. In this study, we used a simple procedure for the synthesis of stable aqueous cerium oxide sols and studied the effect of the concentration and molar ratio of the initial reagents on the size of CeNPs [32]. The average size of CeNPs was about 5 nm by TEM (Fig. 3A), while an average hydrodynamic diameter of CeNPs was  $16 \pm 4$  nm (Table 4). The average hydrodynamic diameter of SiNPs without DOX and CeNPs was  $140 \pm 12$  nm. The size of the SiNPs modified with CeNPs was  $123 \pm 3$  nm. Adsorption of DOX to the SiNPs led to increasing nanoparticles' hydrodynamic diameter to  $150 \pm 17$  nm ( $\zeta$ -potential of  $-23.7 \pm 2.0$  mV). Adsorption of CeNPs on the SiNPs@DOX led to increasing the nanocomposite hydrodynamic size to  $198 \pm 13$  nm. This increase indicates that CeNPs were adsorbed on the surface. Measurements of the SiNPs@DOX@CeNPs diameter were also carried out using the SEM method (Fig. 4), which confirmed an average size of about 190 nm. SiNPs@DOX@CeNPs nanocomposite has a spherical shape which was confirmed by TEM (Fig. 3B).

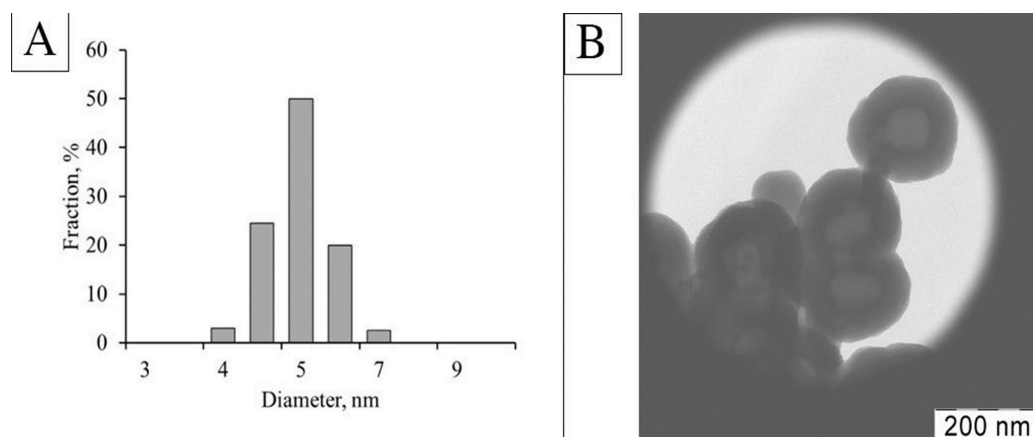


FIG. 3. Size distribution of CeNPs (A), TEM high magnification image of SiNPs modified by DOX and CeNPs (SiNPs@DOX@CeNPs) (B)

The chemical composition of SiNPs@DOX@CeNPs nanoparticles was confirmed with EDX analysis (Fig. 5). As expected, only Si, Ce, O and C elements were found. The Si:Ce (SiO<sub>2</sub>:CeO<sub>2</sub>) ratio in the sample was 9:1, and the difference in SiO<sub>2</sub>:CeO<sub>2</sub> ratios measured in ten different locations did not exceed 1 %.

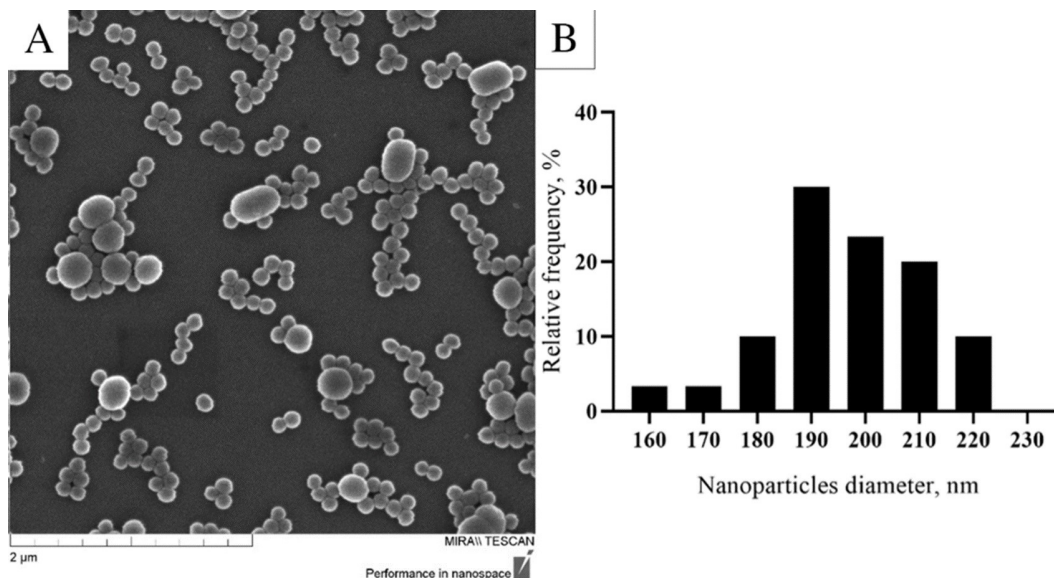


FIG. 4. SEM image of SiNPs modified by DOX and CeNPs (SiNPs@DOX@CeNPs) (A); size distribution of SiNPs@DOX@CeNPs (B)

TABLE 4. Physical characteristics of the core-shell nanocomposite and its individual components

Samples	Hydrodynamic diameter, nm	$\zeta$ -potential, mV
SiNPs	$140 \pm 12$	$-53.6 \pm 1.8$
CeNPs	$16 \pm 4$	$-41.7 \pm 1.2$
SiNPs@CeNPs	$123 \pm 3$	$-31.2 \pm 2.1$
SiNPs@DOX	$150 \pm 17$	$-19.4 \pm 2.4$
SiNPs@DOX@CeNPs	$198 \pm 13$	$-23.7 \pm 2.0$

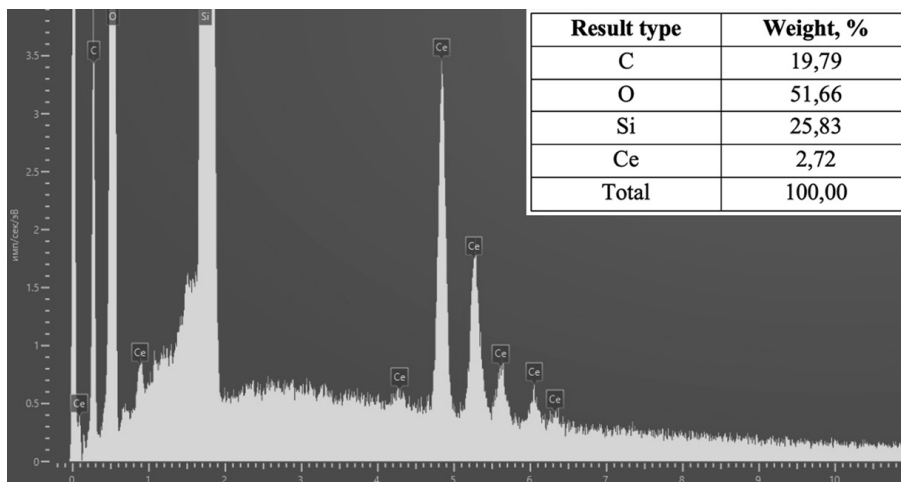


FIG. 5. EDX spectrum of SiNPs@DOX@CeNPs

### 3.2. Cytotoxicity study of SiNPs@DOX@CeNPs

The cytotoxicity of the SiNPs, free DOX, CeNPs, SiNPs@CeNPs, SiNPs@DOX@CeNPs was assessed using MTT method and Live/Dead assay (cell viability analysis by fluorescent dye staining). Human mesenchymal stem cells (hMSc) and human bone osteosarcoma cells (MNNG/HOS) were separately incubated with SiNPs, free DOX, CeNPs, SiNPs@CeNPs, SiNPs@DOX@CeNPs ( $70 \mu\text{M}$ ) for 24, 48 and 72 h. The concentration of  $70 \mu\text{M}$  was chosen as the optimal for detecting biological effects, while being non-toxic. The cell cultures were chosen because DOX [45–47] is often used for osteosarcoma chemotherapy, and so it is of primary importance to establish how new nanocomposite could affect cancer cells. Mesenchymal stem cells were used to study the effect of the nanocomposite on normal cells. As it is shown in Fig. 6 the dehydrogenase activity of hMSc was not decreased upon incubation with all tested the types of nanoparticles for three days. On the contrary, DOX provided a decrease in activity up to 50 % by 72 h of incubation. The results of cell viability analysis by fluorescent staining showed that the nanoparticles upon incubation during 24, 48 and 72 h with hMSc did not have a cytotoxic effect in the concentration (Fig. 7).  $\text{IC}_{20}$  and  $\text{IC}_{50}$  for SiNPs, CeNPs, SiNPs@CeNPs, SiNPs@DOX@CeNPs were not detected. The ratio of dead cells to total cells increased by 30 – 50 % compared to the intact control in experiments with hMSc incubation with DOX.

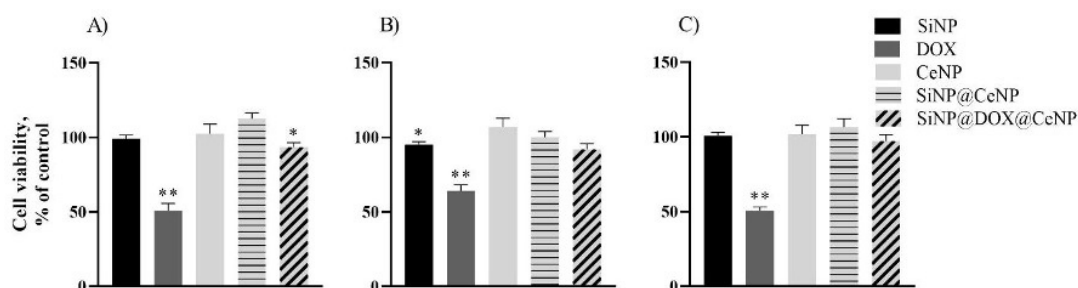


FIG. 6. MTT assay results obtained on human mesenchymal stem cells (hMSc) *in vitro*. The test was carried out after 24 (A), 48 (B), and 72 (C) h. Results are represented as a mean  $\pm$  SD. The values of the metabolic activity of cells are shown as a percentage of the control. Statistical significance was assumed for  $P$ -values  $< 0.05$ : (\* $P < 0.05$ , \*\* $P < 0.01$ )

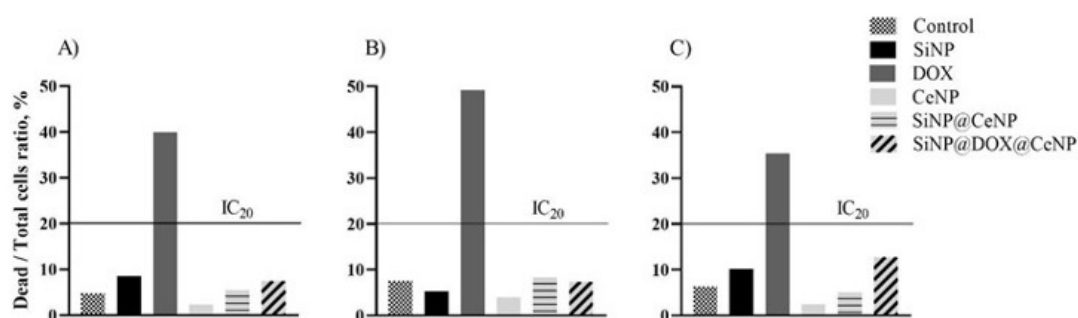


FIG. 7. Live/dead test results obtained on human mesenchymal stem cells (hMSc) *in vitro*. The test was carried out after 24 (A), 48 (B), and 72 (C) h of cell incubation with tested samples at a concentration of  $70 \mu\text{M}$ . The values are indicated as a percentage of the number of dead cells to their total number

24 h after incubation of MNNG/HOS with free DOX, the dehydrogenase activity of cells (Fig. 8) was comparable to control values, and no decrease in dehydrogenase activity was observed in the case of incubation with SiNPs@DOX@CeNPs. Therefore, during incubation for 48 h with free DOX, no significant differences were observed with the control. During the incubation of MNNG/HOS with SiNPs@DOX@CeNPs, dehydrogenase activity decreased by 45 % compared to the intact control. When the MNNG/HOS is incubated for 72 h with free DOX, 25 % decrease in the dehydrogenase activity of the cells is observed compared to the control. In the case of MNNG/HOS incubation with SiNPs@DOX@CeNPs, the dehydrogenase activity of cells decreased by 65 % compared to the control. Thus, the MNNG/HOS cell culture, despite the initial decrease in dehydrogenase activity, showed resistance to free doxorubicin over time. On the contrary, DOX incorporated SiNPs@CeNPs had an inhibitory effect on the viability of MNNG/HOS after three days of incubation with SiNPs@DOX@CeNPs. Live/dead test results show (Fig. 9) an increase in the number of dead cells up to almost 80 %

with SiNPs@DOX@CeNPs incubation. The effect shown on cell cultures may be due to the fact that CeNPs possess self-regenerative, redox-responsive dual-catalytic activities, thus attracting interest as an innovative means to treating cancer [48–50]. Depending on surface characteristics and environment, CeNPs exerts either anti- or pro-oxidative effects which regulate reactive oxygen species (ROS) levels in biological systems. CeNPs mimics ROS-related enzymes that protect normal cells at physiological pH range from oxidative stress and induce ROS production in the slightly acidic tumor microenvironment to trigger cancer cell death [51, 52].

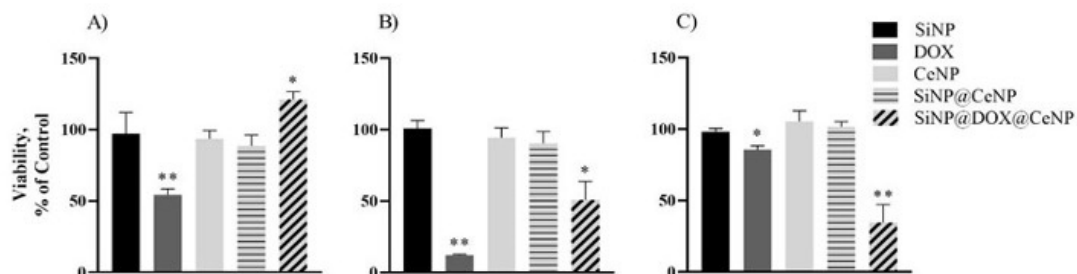


FIG. 8. MTT assay results obtained on human bone osteosarcoma cells (MNNG/HOS) *in vitro*. The test was carried out after 24 (A), 48 (B), and 72 (C) h of cell incubation with tested samples at a concentration of 70 μM. Results are shown as a mean ± SD. The values of the metabolic activity of cells are indicated as a percentage of the control. Statistical significance was assumed for *P*-values < 0.05: (\**P* < 0.05, \*\**P* < 0.01

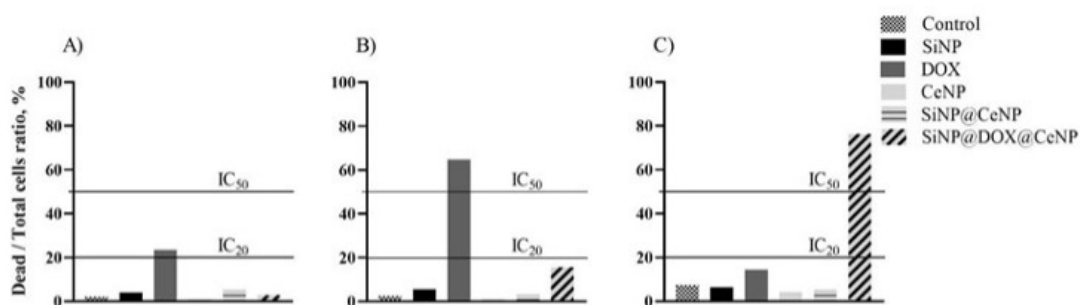


FIG. 9. Live/dead test results obtained on human bone osteosarcoma cells (MNNG/HOS) *in vitro*. The test was carried out after 24 (A), 48 (B), and 72 (C) h of cell incubation with tested samples at a concentration of 70 μM. The values are shown as a percentage of the number of dead cells to their total number

The results obtained, indicated that SiNPs@DOX@CeNPs provided high cytotoxicity to cancer cells while having protective effect on normal cells.

#### 4. Conclusions

Herein, a new hybrid nanocomposite SiNPs@DOX@CeNPs based on silica nanoparticles (SiNPs), doxorubicin (DOX) and cerium oxide nanoparticles (CeNPs) were proposed as multimodal platform having selective cytotoxicity to cancer cells. The synthesized nanocomposite was characterized by SEM, TEM, FTIR, DLS and Raman spectroscopy. The average size of the nanoparticles is 190 nm. The proposed drug loading method provides a high doxorubicin capacity (over 90 %). SiNPs@DOX@CeNPs demonstrated low toxicity to the human mesenchymal stem cell line, while exhibited high toxicity to osteosarcoma cells reducing their viability by up to 30 % compared to untreated control. CeNPs enhance the cytotoxic effect of doxorubicin when introduced in the nanocomposite. The SiNPs@DOX@CeNPs has a great potential for effective drug delivery aimed at increasing the efficiency of cancer treatment.

## References

- [1] Sozarukova M.M., Ivanov V.K., Shestakova M.A., et al. Quantification of free radical scavenging properties and SOD-like activity of cerium dioxide nanoparticles in biochemical models. *Russ. J. Inorg. Chem.*, 2020, **65**, P. 597–605.
- [2] Kozlova T.O., Popov A.L., Romanov M.V., et al. Ceric phosphates and nanocrystalline ceria: selective toxicity to melanoma cells. *Nanosystems: Phys. Chem. Math.*, 2023, **14**, P. 223–230.
- [3] Zhu W., Wei Z., Han C., Weng X. Nanomaterials as Promising Theranostic Tools in Nanomedicine and Their Applications in Clinical Disease Diagnosis and Treatment. *Nanomaterials*, 2021, **11**, 3346.
- [4] Yusuf A., Almotairy A.R.Z., Henidi H., Alshehri O.Y., Aldughaim M.S. Nanoparticles as Drug Delivery Systems: A Review of the Implication of Nanoparticles' Physicochemical Properties on Responses in Biological Systems. *Polymers*, 2023, **15**, 1596.
- [5] Sozarukova M.M., Proskurnina E.V., Popov A.L., Kalinkin A.L., Ivanov V.K. New Facets of Nanozyme Activity of Ceria: Lipo- and Phospholipoperoxidase-like Behaviour of CeO<sub>2</sub> Nanoparticles. *RSC Adv.*, 2021, **11**, P. 35351–35360.
- [6] Rajeshkumar S., Naik P. Synthesis and Biomedical Applications of Cerium Oxide Nanoparticles – A Review. *Biotechnol. Rep. Amst. Neth.*, 2018, **17**, P. 1–5.
- [7] Dhall A., Self W. Cerium Oxide Nanoparticles: A Brief Review of Their Synthesis Methods and Biomedical Applications. *Antioxid. Basel Switz.*, 2018, **7**, 97.
- [8] Shcherbakov A.B., Reukov V.V., Yakimansky A.V., Krasnopeeva E.L., Ivanova O.S., Popov, A.L., Ivanov V.K. CeO<sub>2</sub> Nanoparticle-Containing Polymers for Biomedical Applications: A Review. *Polymers*, 2021, **13**, 924.
- [9] Shirokikh A.D., Anikina V.A., Zamyatina E.A., Mishchenko E.V., Koroleva M.Y., Ivanov V.K., Popova N.R. Bioavailability of Nanoemulsions Modified with Curcumin and Cerium Dioxide Nanoparticles. *Nanosyst. Phys. Chem. Math.*, 2023, **14**, P. 89–97.
- [10] Ibrahim H.G., Attia N., Hashem F.E.Z.A., El Heneidy M.A.R. Cerium Oxide Nanoparticles: In Pursuit of Liver Protection against Doxorubicin-Induced Injury in Rats. *Biomed. Pharmacother. Biomedecine Pharmacother.*, 2018, **103**, P. 773–781.
- [11] Wu G., Zhang Z., Chen X., Yu Q., Ma X., Liu L. Chemosensitization Effect of Cerium Oxide Nanosheets by Suppressing Drug Detoxification and Efflux. *Ecotoxicol. Environ. Saf.*, 2019, **167**, P. 301–308.
- [12] Bahrami Z., Badiei A., Atyabi F. Surface Functionalization of SBA-15 Nanorods for Anticancer Drug Delivery. *Chem. Eng. Res. Des.*, 2014, **92**, P. 1296–1303.
- [13] Yu F., Tang X., Pei M. Facile Synthesis of PDMAEMA-Coated Hollow Mesoporous Silica Nanoparticles and Their PH-Responsive Controlled Release. *Microporous Mesoporous Mater.*, 2013, **173**, P. 64–69.
- [14] Rehman F., Ahmed K., Airoldi C., Gaisford S., Buanz A., Rahim A., Muhammad N., Volpe P.L.O. Amine Bridges Grafted Mesoporous Silica, as a Prolonged/Controlled Drug Release System for the Enhanced Therapeutic Effect of Short Life Drugs. *Mater. Sci. Eng. C*, 2017, **72**, P. 34–41.
- [15] Lee S., Kwon J.A., Park K.H., Jin C.M., Joo J.B., Choi I. Controlled Drug Release with Surface-Capped Mesoporous Silica Nanoparticles and Its Label-Free in Situ Raman Monitoring. *Eur. J. Pharm. Biopharm.*, 2018, **131**, P. 232–239.
- [16] Nguyen T.N.T., Le N.T.T., Nguyen N.H., Ly B.T.K., Nguyen T.D., Nguyen D.H. Aminated Hollow Mesoporous Silica Nanoparticles as an Enhanced Loading and Sustained Releasing Carrier for Doxorubicin Delivery. *Microporous Mesoporous Mater.*, 2020, **309**, 110543.
- [17] Yu J., Wang C., Kong Q., Wu X., Lu J.-J., Chen X. Recent Progress in Doxorubicin-Induced Cardiotoxicity and Protective Potential of Natural Products. *Phytomedicine Int. J. Phytother. Phytopharm.*, 2018, **40**, P. 125–139.
- [18] Liu H., Wang J., Wang M., Wang Y., Shi S., Hu X., Zhang Q., Fan D., Xu P. Biomimetic Nanomedicine Coupled with Neoadjuvant Chemotherapy to Suppress Breast Cancer Metastasis via Tumor Microenvironment Remodeling. *Adv. Funct. Mater.*, 2021, **31**, 2100262.
- [19] Popov A.L., Popova N.R., Selezneva I.I., Akkizov A.Y., Ivanov V.K. Cerium Oxide Nanoparticles Stimulate Proliferation of Primary Mouse Embryonic Fibroblasts in Vitro. *Mater. Sci. Eng. C Mater. Biol. Appl.*, 2016, **68**, P. 406–413.
- [20] Popov A.L., Shcherbakov A.B., Zholobak N.M., Baranchikov A.E., Ivanov V.K. Cerium Dioxide Nanoparticles as Third-Generation Enzymes (Nanozymes). *Nanosyst.: Phys. Chem. Math.*, 2017, P. 760–781.
- [21] Fitzmaurice S.D., Sivamani R.K., Isseroff R.R. Antioxidant Therapies for Wound Healing: A Clinical Guide to Currently Commercially Available Products. *Skin Pharmacol. Physiol.*, 2011, **24**, P. 113–126.
- [22] Ahsan H., Hadi S.M. Strand Scission in DNA Induced by Curcumin in the Presence of Cu (II). *Cancer Lett.*, 1998, **124**, P. 23–30.
- [23] Thomas L., Zakir F., Mirza M.A., Anwer M.K., Ahmad F.J., Iqbal Z. Development of Curcumin Loaded Chitosan Polymer Based Nanoemulsion Gel: In Vitro, Ex Vivo Evaluation and in Vivo Wound Healing Studies. *Int. J. Biol. Macromol.*, 2017, **101**, P. 569–579.
- [24] Ahmad N., Ahmad R., Al-Qudaihi A., Alaseel S.E., Fita I.Z., Khalid M.S., Pottoo F.H. Preparation of a Novel Curcumin Nanoemulsion by Ultrasonication and Its Comparative Effects in Wound Healing and the Treatment of Inflammation. *RSC Adv.*, 2019, P. 20192–20206.
- [25] Legonkova O.A., Korotaeva A.I., Terekhova R.P., Asanova L.Yu., Shcherbakov A.B., Zholobak N.M., Baranchikov A.E., Krasnova E.V., Shekunova T.O., Ivanov V.K. Method for producing a biologically active composite based on nanocrystalline cerium dioxide and curcumin. Patent RU 2665378 C1, filed October 3, 2017, issued August 29 2018.
- [26] Xue Y., Luan Q., Yang D., Yao X., Zhou K. Direct Evidence for Hydroxyl Radical Scavenging Activity of Cerium Oxide Nanoparticles. *J. Phys. Chem. C*, 2011, **115**, P. 4433–4438.
- [27] Plakhova T.V., Romanchuk A.Y., Butorin S.M., Konyukhova A.D., Egorov A.V., Shiryayev A.A., Baranchikov A.E., Dorovatovskii P.V., Huthwelker T., Gerber E., et al. Towards the Surface Hydroxyl Species in CeO<sub>2</sub> Nanoparticles. *Nanoscale*, 2019, **11**, P. 18142–18149.
- [28] Popova N.R., Shekunova T.O., Popov A.L., Selezneva I.I., Ivanov V.K. Cerium Oxide Nanoparticles Provide Radioprotective Effects upon X-Ray Irradiation by Modulation of Gene Expression. *Nanosystems: Phys. Chem. Math.*, 2019, **10**, P. 564–572.
- [29] Kim M.-K., Ki D.-H., Na Y.-G., Lee H.-S., Baek J.-S., Lee J.-Y., Lee H.-K., Cho C.-W. Optimization of Mesoporous Silica Nanoparticles through Statistical Design of Experiment and the Application for the Anticancer Drug. *Pharmaceutics*, 2021, **13**, 184.
- [30] Wen J., Yang K., Xu Y., Li H., Liu F., Sun S. Construction of A Triple-Stimuli-Responsive System Based on Cerium Oxide Coated Mesoporous Silica Nanoparticles. *Sci. Rep.*, 2016, **6**, 38931.
- [31] Ghimire P.P., Jaroniec M. Renaissance of Stöber Method for Synthesis of Colloidal Particles: New Developments and Opportunities. *J. Colloid Interface Sci.*, 2021, **584**, P. 838–865.
- [32] Ivanova O.S., Shekunova T.O., Ivanov V.K., Shcherbakov A.B., Popov A.L., Davydova G.A., Selezneva I.I., Kopitsa G.P., Tret'yakov Yu.D. One-Stage Synthesis of Ceria Colloid Solutions for Biomedical Use. *Dokl. Chem.*, 2011, **437**, P. 103–106.
- [33] Shcherbakov A.B., Ivanov V.K. *Practical Manual on Nanomaterials and Nanotechnologies*, Second edition. 2022, 382 p.
- [34] Chang H., Kim J., Rho W.-Y., Pham X.-H., Lee J.H., Lee S.H., Jeong D.H., Jun B.-H. Silica Nanoparticles. *Adv. Exp. Med. Biol.*, 2021, **1309**, P. 41–65.
- [35] Zeng D., Zhang H., Wang B., Sang K., Yang J. Effect of Ammonia Concentration on Silica Spheres Morphology and Solution Hydroxyl Concentration in Stober Process. *J. Nanosci. Nanotechnol.*, 2015, **15**, P. 7407–7411.

- [36] Zainal N.A., Shukor S.R.A., Razak K.A. Study on the effect of synthesis parameters of silica nanoparticles entrapped with rifampicin. *Chem. Eng.*, 2013, **32** (7), P. 432–434.
- [37] Thommes M., Kaneko K., Neimark A.V., Olivier J.P., Rodriguez-Reinoso F., Rouquerol J., Sing K.S.W. Physisorption of Gases, with Special Reference to the Evaluation of Surface Area and Pore Size Distribution (IUPAC Technical Report). *Pure Appl. Chem.*, 2015, **87**, P. 1051–1069.
- [38] Capozzi C.A., Pye L.D., Condrate R.A. Vibrational Spectral/Structural Changes from the Hydrolysis/Polycondensation of Methyl-Modified Silicates. I. Comparisons for Single Monomer Condensates. *Mater. Lett.*, 1992, **15**, P. 130–136.
- [39] Socrates G. *Infrared and Raman Characteristic Group Frequencies: Tables and Charts*, Wiley, 2004.
- [40] Bansal R., Singh R., Kaur K. Quantitative Analysis of Doxorubicin Hydrochloride and Arterolane Maleate by Mid IR Spectroscopy Using Transmission and Reflectance Modes. *BMC Chem.*, 2021, **15**, 27.
- [41] Smith E., Dent G. *Modern Raman Spectroscopy: A Practical Approach*, John Wiley and Sons, 2005.
- [42] Yuan P., He H.P., Wu D.Q., Wang D.Q., Chen L.J. Characterization of Diatomaceous Silica by Raman Spectroscopy. *Spectrochim. Acta. A. Mol. Biomol. Spectrosc.*, 2004, **60**, P. 2941–2945.
- [43] Zhang R., Zhu J., Sun D., Li J., Yao L., Meng S., Li Y., Dang Y., Wang K. The Mechanism of Dynamic Interaction between Doxorubicin and Calf Thymus DNA at the Single-Molecule Level Based on Confocal Raman Spectroscopy. *Micromachines*, 2022, **13**, 940.
- [44] Gautier J., Munnier E., Douziech-Eyrolles L., et al. SERS spectroscopic approach to study doxorubicin complexes with Fe<sup>2+</sup> ions and drug release from SPION-based nanocarriers. *Analyst*, 2013, **24**, P. 7354–7361.
- [45] Zheng Y., Wang G., Chen R., Hua Y., Cai Z. Mesenchymal stem cells in the osteosarcoma microenvironment: their biological properties, influence on tumor growth, and therapeutic implications. *Stem Cell Research & Therapy*, 2018, **9**, 22.
- [46] Wei H., Chen J., Wang S., Fu F., Zhu X., Wu C., Liu Z., Zhong G., Lin J. A Nanodrug Consisting Of Doxorubicin And Exosome Derived From Mesenchymal Stem Cells For Osteosarcoma Treatment In Vitro. *Int. J. Nanomedicine*, 2019, **14**, P. 8603–8610.
- [47] Smrke A., Anderson P.M., Gulia A., Gennatas S., Huang P.M., Jones R.L. Future Directions in the Treatment of Osteosarcoma. *Cells*, 2021, **10** (1), 172.
- [48] Niu J., Wang K., Kolattukudy P.E. Cerium Oxide Nanoparticles Inhibits Oxidative Stress and Nuclear Factor-KB Activation in H9c2 Cardiomyocytes Exposed to Cigarette Smoke Extract. *J. Pharmacol. Exp. Ther.*, 2011, **338**, P. 53–61.
- [49] Ramachandran M., Subadevi R., Sivakumar M. Role of PH on Synthesis and Characterization of Cerium Oxide (CeO<sub>2</sub>) Nano Particles by Modified Co-Precipitation Method. *Vacuum*, 2019, **161**, P. 220–224.
- [50] Seminko V., Maksimchuk P., Grygorova G., Okrushko E., Avrunin O., Semenets V., Malyukin Y. Mechanism and Dynamics of Fast Redox Cycling in Cerium Oxide Nanoparticles at High Oxidant Concentration. *J. Phys. Chem. C*, 2021, **125**, P. 4743–4749.
- [51] Shi X., Tian Y., Zhai S., Liu Y., Chu S., Xiong Z. The Progress of Research on the Application of Redox Nanomaterials in Disease Therapy. *Front. Chem.*, 2023, **11**.
- [52] Popov A.L., Kolmanovich D.D., Popova N.R., Sorokina S.S., Ivanova O.S., Chukavin N.N., Shcherbakov A.B., Kozlova T.O., Kalashnikova S.A., Ivanov V.K. Synthesis and Biocompatibility Study of Ceria-Mildronate Nanocomposite in Vitro. *Nanosyst.: Phys. Chem. Math.*, 2022, **13**, P. 96–103.

---

Submitted 6 September 2023; accepted 11 September 2023

*Information about the authors:*

*Elizaveta A. Zamyatina* – Institute of Theoretical and Experimental Biophysics of the Russian Academy of Sciences, Institutskaya str., 3, Pushchino, 142290, Russia; ORCID 0000-0002-1275-565X; sonyoru162@gmail.com

*Sergey Yu. Kottsov* – Kurnakov Institute of General and Inorganic Chemistry of the Russian Academy of Sciences, Leninskiy prosp., 31, Moscow, 119991, Russia; ORCID 0000-0001-8263-889X; sergey12-17@yandex.ru

*Viktoria A. Anikina* – Institute of Theoretical and Experimental Biophysics of the Russian Academy of Sciences, Institutskaya str., 3, Pushchino, 142290, Russia; ORCID 0000-0002-5028-2064; viktoria.anikina@list.ru

*Anton L. Popov* – Institute of Theoretical and Experimental Biophysics of the Russian Academy of Sciences, Institutskaya str., 3, Pushchino, 142290, Russia; ORCID 0000-0003-2643-4846; antonpopovleonid@gmail.com

*Marina P. Shevelyova* – Institute for Biological Instrumentation of the Russian Academy of Sciences, Institutskaya str., 7, Pushchino, 142290, Russia; ORCID 0009-0004-7638-5143; marina.shevelyova@gmail.com

*Nelli R. Popova* – Institute of Theoretical and Experimental Biophysics of the Russian Academy of Sciences, Institutskaya str., 3, Pushchino, 142290, Russia; ORCID 0000-0002-0982-6349; nellipopovaran@gmail.com

*Conflict of interest:* the authors declare no conflict of interest.

## Synthesis of lanthanum manganite powders via combustion reactions: some aspects of the influence of magnetic field and charge generation in precursors on the formation of properties

Alexander A. Ostroushko, Iliya D. Gagarin, Egor V. Kudyukov, Tatiana Yu. Zhulanova, Anastasya E. Permyakova, Olga V. Russkikh

Ural Federal University Scientific Research Institute of Physics and Applied Mathematics, Ekaterinburg, Russia

Corresponding author: Alexander A. Ostroushko, [alexander.ostroushko@urfu.ru](mailto:alexander.ostroushko@urfu.ru)

**ABSTRACT** The mutual influence of the process of electric charge generation in nitrate organic precursors and a constant external magnetic field on the magnetic properties formation was considered for lanthanum strontium manganite  $\text{La}_{0.7}\text{Sr}_{0.3}\text{MnO}_{3\pm y}$  powders obtained via combustion reactions. The investigated properties of the obtained samples include hysteresis, magnetocaloric and magnetoresistive effects. The correlation between formation process of extended ensembles of nanoparticles and the functional properties of complex oxide materials was also discussed. The manifestation of a strong magneto-gas-selective effect has been observed during the combustion of precursors in a constant magnetic field, which affects the charge generation process.

**KEYWORDS** complex oxides, lanthanum manganite, synthesis, combustion reactions, nitrate-organic systems, nanoparticles, charges generation, magnetic properties, magneto-gas selective effect

**ACKNOWLEDGEMENTS** The research was financially supported by a grant from the Russian Science Foundation (Project No. 22-23-00718). The research was carried out using the equipment of the Ural Center for Collective Use “Modern Nanotechnologies”.

**FOR CITATION** Ostroushko A.A., Gagarin I.D., Kudyukov E.V., Zhulanova T.Yu., Permyakova A.E., Russkikh O.V. Synthesis of lanthanum manganite powders via combustion reactions: some aspects of the influence of magnetic field and charge generation in precursors on the formation of properties. *Nanosystems: Phys. Chem. Math.*, 2023, **14** (5), 571–583.

### 1. Introduction

Complex oxides based on lanthanum manganite with a perovskite-like structure are widely used as multifunctional materials, for example, in various sensor devices, energy converters and other due to their unique properties. They include magneto-optical properties [1], the presence of colossal magnetoresistance effects [2–5] and magnetocaloric properties [6–12] that are acceptable for practical, including biomedical, applications. In particular, the colossal magnetoresistance is due to the presence of manganese ions with oxidation states of +3 and +4 in the perovskite structure, leading to the emergence of kinetic ferromagnetic electron exchange and ferromagnetic ordering in doped manganites containing ions with mixed valences, which is achieved, for example, by introducing heterovalent substituents into the lanthanum sublattice. One of the most important aspects of the use of lanthanum manganite materials is their high catalytic properties [13–16]. Due to these properties, the aforementioned perovskites are used in solid oxide fuel cells and thermocatalytic devices for environmental protection. The functional properties of these materials are influenced by synthesis characteristics, particle size and morphology. In some cases, complex oxide materials consisting of nanoscale particles and their ensembles exhibit the most favorable properties. Methods based on the use of appropriate salts (often nitrates) as starting forms have significant advantages in the synthesis of such materials. Among the above-mentioned methods, Solution Combustion Synthesis (SCS) occupies one of the most important positions due to its simplicity of implementation, the possibility of varying the conditions for obtaining the materials, which makes it possible to control their properties. In particular, Solution Combustion Synthesis allows one to obtain highly efficient nanostructured complex oxide catalysts, including deposited ones [14, 17–19]. In addition, it is advisable to pay attention to the formation of magnetic properties of the materials during synthesis.

In addition to the target electromagnetic properties of lanthanum manganite-based perovskites, it is also important to consider the potential influence of the magnetic properties of catalytic materials on heterogeneous catalytic reactions [20–24], such as the combustion of toxic substances. The phenomenon of the so-called magnetogas-selective effect, which is based on the determinative flow of paramagnetic oxygen molecules from the air onto the catalyst surface and the expulsion of diamagnetic molecules of catalytic oxidation products and nitrogen, helps to increase the efficiency of thermocatalytic devices. At the same time, simultaneous reduction of nitrogen oxides occurs. Similar effects have been observed in liquid

reaction media. The magnetogas-selective effect could be used in various reactions to control their kinetics. On the surface of lanthanum manganite-based catalysts, heterogeneous redox reactions occur even at temperatures below 100 °C [14], where the catalytic material is able to exhibit ferromagnetic properties. Therefore, the possibility of the above effect should be considered.

The properties of complex oxide materials obtained via combustion reactions are influenced by such conditions as process temperature, composition and concentration of the gases formed. One of the important phenomena accompanying the synthesis processes of complex oxides by combustion of nitrate-organic precursors [5, 16, 19, 25–56] is the generation of high-density electric charges in the precursors and nanoparticles [45, 56–63]. The possibility of charge formation is associated with the release of ionized molecular groups into the gaseous environment and also with the lability of the oxidation state of transition metal ions which are the part of the precursors and the resulting material. The density of such charges correlates with the potential difference between the precursor and the earth, which can be conveniently measured [45], and its value reaches hundreds of volts. The potential differences detected on different sides of the combustion front during the implementation of the self-propagating high-temperature synthesis method do not exceed tenths or units of volts [64–71], and ionization of the gaseous environment is also possible when using this method. In many cases, the presence of charges during SCS determines the morphology of the synthesized complex oxides and has a significant impact on powder sintering processes. The temperature interval of intense sintering can be reduced by hundreds of degrees in the presence of high charges [57, 59]. The presence of high charges leads to mutual repulsion of nanoparticles, formation of small contact area between them, which significantly increases the reserve of excess surface energy of particles.

It should be noted that there is information in the literature on the influence of external magnetic fields on the formation of electromagnetic properties of complex oxides [72]. It seems interesting and useful to study how the combination of two factors – the presence of charges in the precursors and the influence of an external field – affects such properties. Previously [57], on the example of the lanthanum-strontium manganite  $\text{La}_{0.7}\text{Sr}_{0.3}\text{MnO}_{3\pm y}$ , it was found that the application of an external alternating electromagnetic field leads to a decrease in saturation magnetization and coercive force of the obtained materials, due to the disordering effect of the aforementioned field. The presence of medium intensity charge generation generally has a favorable effect on the hysteresis properties. The investigations in the above work [57] were carried out on samples with identical crystallographic structures and oxygen non-stoichiometry, which allows one to compare the results correctly. In this work we have investigated the influence of a constant magnetic field applied during synthesis on the magnetic properties of lanthanum-strontium manganites.

## 2. Experimental part

The synthesis of lanthanum manganite powders  $\text{LaMnO}_{3\pm\delta}$ , including doped  $\text{La}_{0.7}\text{Sr}_{0.3}\text{MnO}_{3\pm\delta}$ , was carried out by combustion of nitrate-organic precursors obtained by mixing two separately prepared solutions. The first one contained the respective metal nitrates dissolved in distilled water, the second one contained the organic component. Mixing the solutions resulted in the formation of precursors. The ratio of the organic part to the nitrates was stoichiometric ( $\varphi = 1$ ) according to the combustion reaction [59] with the formation of water, carbon dioxide and nitrogen as the main gaseous products, or exceeded it ( $\varphi > 1$ ). The following starting reagents (analytical grade) were used: lanthanum (III) nitrate hexahydrate  $\text{La}(\text{NO}_3)_3 \cdot 6\text{H}_2\text{O}$ , strontium nitrate  $\text{Sr}(\text{NO}_3)_2$ , manganese (II) nitrate tetrahydrate  $\text{Mn}(\text{NO}_3)_2 \cdot 4\text{H}_2\text{O}$ , glycine (Gly)  $\text{NH}_2\text{CH}_2\text{COOH}$ , polyvinyl alcohol (PVA)  $(\text{C}_2\text{H}_4\text{O})_n$  (viscosity of 4 % aqueous solution at room temperature 11 cP, content of residual acetate groups not exceeding 2 %) and polyvinyl pyrrolidone (PVP)  $(\text{C}_6\text{H}_9\text{NO})_n$  (molecular weight 40000, Sigma-Aldrich, PVP40).

For the preparation of precursors, two solutions were prepared separately in distilled water containing nitrates of the corresponding metals and an organic component. Solutions of polymer components (concentration of PVA or PVP – 5 or 10 wt.%, respectively) were prepared by heating in a water bath. When mixing the two solutions, the quantitative proportions were set in accordance with the stoichiometry of the nitrate combustion reaction with the formation of nitrogen, carbon dioxide and water as gaseous products [56]. The resulting solution was poured onto inert substrates, further evaporation of water (drying) took place at room temperature, this process took up to 7 days, as a result of which precursors in the form of films containing a stoichiometric amount of an organic component ( $\varphi = 1$ ) or its double excess ( $\varphi = 2$ ) were obtained. Combustion of precursors was carried out in porcelain cups using an alcohol lamp to initiate the combustion process. The combustion was carried out in the absence or under the influence of a constant magnetic field. The composition of gaseous combustion products (in particular, the concentration of nitrogen oxide NO, carbon monoxide CO) was determined using a Testo 350 XL gas analyzer (Testo, Germany). The final heat treatment was carried out at a temperature of 650 °C in the absence or under the influence of a constant magnetic field.

The synthesis was carried out after drying the precursor in air by placing it in a quartz tube reactor with an air flow of 2 l/min and heating it with an alcohol burner. The level of charge generation was determined as the potential difference between the precursor and the ground using an IPEP-1 electrostatic field meter (MNIPI, Republic of Belarus) with a special metal screen made of an inert material as the measuring lead. The device was calibrated by applying a potential of a given value to the screen using a B5-46 DC source (Priborelectro, Russian Federation). Similarly, to the method described above, synthesis was carried out by placing the reactor in a constant magnetic field created in the gap

between the electromagnet poles. Phase composition was determined by diffractometer D8 Advance (Bruker, Germany) in CuK $\alpha$  radiation ( $\lambda = 1.5418 \text{ \AA}$ ). X-ray images were taken in the range of  $20^\circ \leq 2\theta \leq 80^\circ$  with a step of 0.04 and a shutter speed of 1 second at the point. Phase identification was carried out using the Fpeak and MATCH! software packages. Alternatively, the pre-synthesized samples were annealed in a magnetic field. SEM was carried out by means of AURIGA CrossBeam scanning electron microscope (Carl Zeiss NTS, Germany); the data were controlled, monitored and analyzed using the Analysis Station software package, AURIGA series, version 3.7. The granulometric composition of the obtained powders was determined by laser diffraction on a SALD-7101 dispersion analyzer (Shimadzu, Japan). The hysteresis characteristics and magnetoresistance effect of the samples were measured using a LakeShore VSM 7407 (Lake Shore Cryotronics, USA) vibrating-sample magnetometer with the option of measuring magnetoresistance using compacted pressed samples. The magnetocaloric effect was measured by the direct method – the adiabatic temperature change was recorded when the magnetic field was switched on. The magnetic field was applied using a Halbach magnetic system; the field strength was up to 17 kOe. The system used allowed the field strength to change abruptly from 0 to maximum.

### 3. Results and discussion

Complex oxide samples  $\text{LaMnO}_{3\pm\delta}$  and  $\text{La}_{0.7}\text{Sr}_{0.3}\text{MnO}_{3\pm\delta}$  were synthesized by combustion of nitrate-organic precursors differing in organic component and its quantity. The combustion was carried out in the absence or under the influence of a constant magnetic field. Phase composition was controlled after the heat treatment at  $650^\circ\text{C}$ . The XRD analysis showed that samples were single phase independently from the precursors' content and the conditions of both combustion and annealing. Lanthanum manganite  $\text{LaMnO}_{3\pm\delta}$  and solid solutions on its base with R-3c spatial group were formed. The example of XRD patterns is shown in Fig. 1.

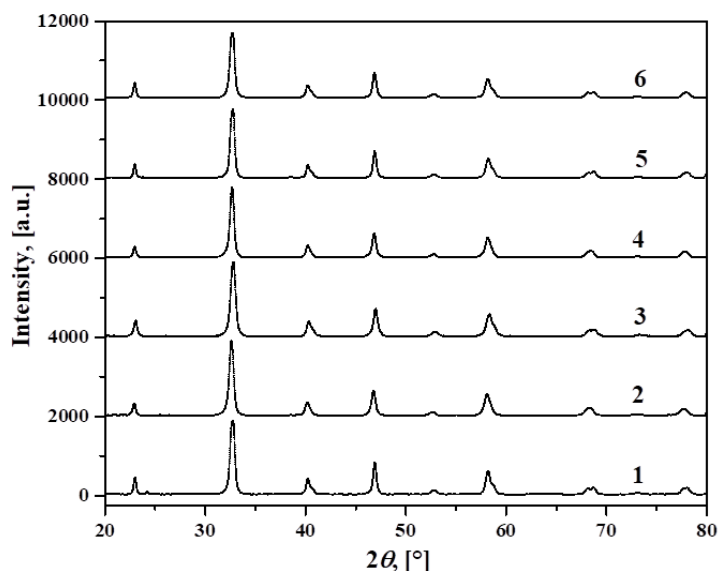


FIG. 1. XRD of  $\text{La}_{0.7}\text{Sr}_{0.3}\text{MnO}_{3\pm\delta}$  samples synthesized from different precursors without impact of external magnetic field: 1 – PVP,  $\varphi = 1$ ; 2 – PVP,  $\varphi = 2$ ; 3 – PVA,  $\varphi = 1$ ; 4 – PVA,  $\varphi = 2$ ; 5 – Gly,  $\varphi = 1$ ; 6 – Gly,  $\varphi = 2$

Magnetic (hysteresis) characteristics of lanthanum strontium manganite samples synthesized under the influence of a constant magnetic field in the absence of a significant external electric field have been obtained (Fig. 2). An example of the experimental curves used to calculate the magnetic parameters is shown in Fig. 3. Experimental data (after two hours of annealing at  $650^\circ\text{C}$ ) revealed certain regularities in the formation of the magnetic properties of the samples, which can be roughly divided into three groups according to the intensity of the charge generation during the synthesis. The first group consists of samples whose synthesis was accompanied by high charge generation (potential difference ground – precursor was up to and above 100 V), the second one – samples with low intensity of charge generation (potential difference close to zero) and the last – samples in the average range for this parameter. The first group included materials synthesized from precursors containing PVA, the second – PVP and the third one – Gly. The first group of samples was characterized by the tendency to an increase of magnetic properties when a constant magnetic field was applied during the combustion of precursors. While for the samples from the second and third group the measured parameters decreased (coercive force, Curie temperature) or had a maximum at the average field strength (saturation magnetization) as the field strength applied during combustion increased.

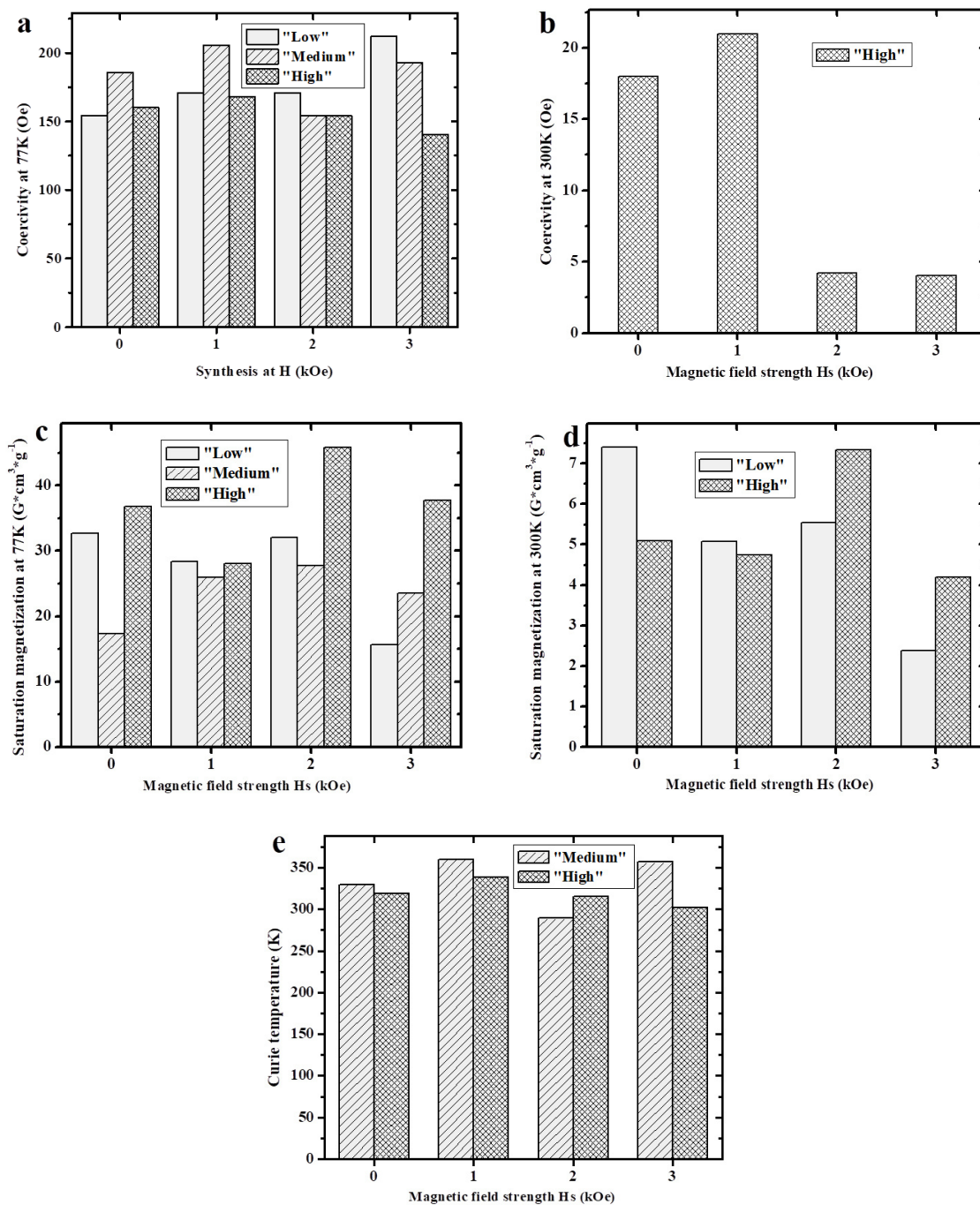


FIG. 2. Characteristics of the obtained samples.  $H_s$  is the strength of the magnetic field, which was applied during the synthesis

Analysis of the trends obtained from the experimental data shows that the saturation magnetization value also showed a maximum as a function of field strength (at 2 kOe) for the samples that had intermediate charges during synthesis. In contrast, the coercivity of the samples and the Curie temperature showed a minimum. Samples with low charges showed an increase in coercivity and Curie temperature with increasing field and the dependence with a maximum for magnetization. It should be noted that in this case the values of the magnetic parameters (saturation magnetization, Curie temperature) were higher for the samples obtained in the absence of an external field.

The maximum influence of the value of the external magnetic field strength applied during the synthesis on saturation magnetization value was observed for the samples with high generated charges, while the coercive force was more dependent on the change of the magnetic field for the samples with low values of generated charges. The maximum saturation magnetization values achieved in the described series of experiments had samples from the range of high generated charges, the coercive force values were higher for samples with medium and low charges. Correspondingly, the Curie

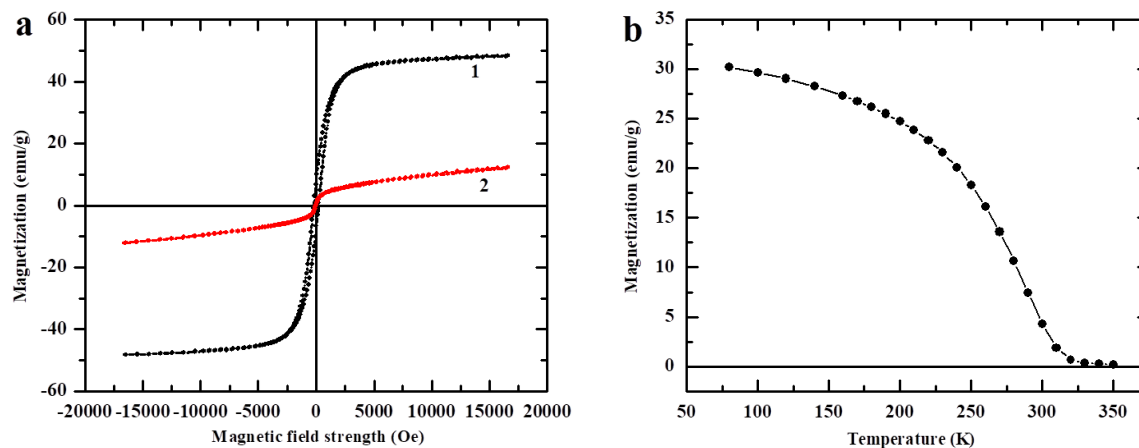


FIG. 3. Example of experimental magnetization dependence on (a) field strength for LSM sample (synthesized from PVA-containing precursor ( $\varphi = 2$ ), combustion under the impact of external magnetic field 20e, annealed at 650 °C during 2 hours without impact of external magnetic field during thermal treatment): (1) black curve at 77 K; (2) red curve at 300 K; (b) temperature for LSM, obtained from PVA-containing precursor ( $\varphi = 2$ ) annealed at 650 °C during 2 hours without impact of external magnetic field during combustion of precursor and thermal treatment

temperature was higher for samples with low charges. Based on the results obtained, it can be assumed that the presence of a magnetic field generally positively influences the formation of the magnetic structure of individual perovskite particles, which is most pronounced in the case of high charge generation in precursors during synthesis. However, the presence of high charges, as mentioned above, leads to strong mutual repulsion of nanoparticles and apparently prevents their specific aggregation into extended ensembles, which provides the increase of the coercive force, the Curie temperature. The dependence of the properties, e.g. the Curie temperature, on the effective size of the formations obtained in powders has already been noted [5, 73] for doped lanthanum manganites. There are also data on rather complicated correlations between the magnetic properties [5, 73] (magnetization) and the size and shape of manganite particles of different composition or their aggregates, which in turn may be related in particular to the magnetic moment of the manganese ions, the bonding angle of the Mn-O-Mn clusters in the nanoparticle structure, on their surface and at the interparticle boundaries. These aspects can also be influenced by synthesis conditions via combustion reactions (magnetic field effect, etc.), particle shape, packing density, etc.

Magnetocaloric and magnetoresistive effects were investigated for samples obtained under and without a magnetic field influence (for samples with different intensities of charge generation during the synthesis). Fig. 4 shows an example of the temperature dependence of the electrical resistivity measured in the absence of a magnetic field and in a constant magnetic field of 17 kOe or a compact sample of lanthanum strontium manganate in the form of a flat parallelepiped. The sample was obtained from a precursor containing a stoichiometric (for the combustion reaction) amount of glycine in a 3 kOe field. The coercive force was also higher for these samples (relatively low charges) (Fig. 2). The higher values compared to samples obtained from precursors with high charges may also indirectly indicate the positive effect of extended particle aggregation, which is not prevented by mutual repulsion of nanoparticles. Fig. 5 shows an example of the measurement of the magnetocaloric effect on a sample of doped lanthanum manganate characterized by the effect value of about 0.4 K in the temperature range  $\sim 200 - 300$  K. The sample was obtained from a precursor with intensive charge generation in the absence of an external field. For comparison, the result for the sample with bulk composition  $\text{La}_{0.7}\text{Ag}_{0.3}\text{MnO}_{3\pm y}$  (synthesis in field 3 kOe, PVA  $\varphi = 2$ , low charges) is given. The indicated effects for the samples synthesized in combustion reactions have an acceptable value, which indicates the possibility of further studies to establish the influence of external electromagnetic fields during synthesis on the mentioned target parameters.

Regarding the formation of the morphology of the obtained samples, it could be noted that the possibility of obtaining a material containing extended ensembles of particles is associated with the superposition of at least two opposite factors. On the one hand, there is electrostatic repulsion between nanoparticles [74] due to charge generation, and on the other hand, magnetic interaction between particles is possible [75]. It can be assumed that an additional factor contributing to the minimization of particle contact is the presence of gases emitted during the combustion process. Considering the relatively low Curie temperature of the resulting samples, slightly above 100 °C, magnetic attraction with the emergence of the corresponding mutual spatial orientation is mainly possible below this temperature. In the absence of an external magnetic field, the residual (spontaneous) magnetization is the determining factor, while in the presence of a magnetic field it is induced by the field. In this case, we can assume that the formation of extended ensembles can occur mainly when the material cools down after the combustion of the precursor. In the literature, there are examples of modeling the

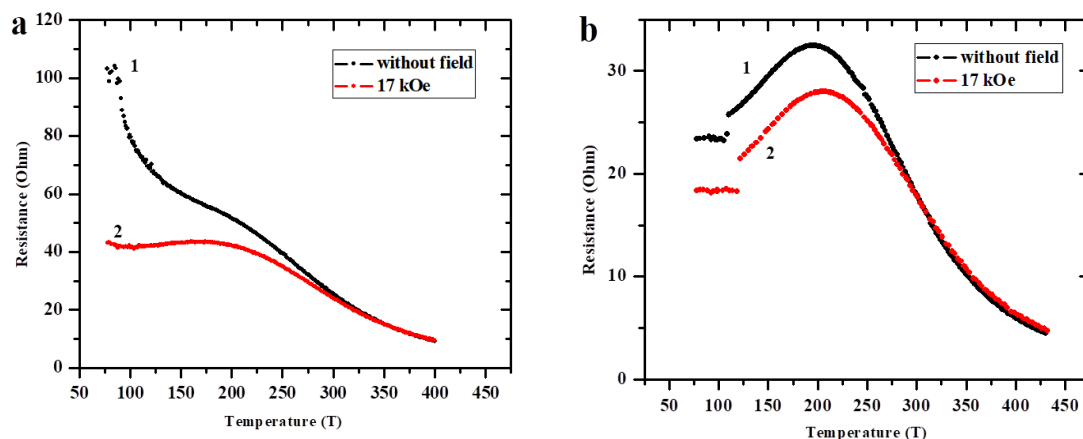


FIG. 4. Example of determining the magnetoresistance effect value: a – with a maximum value of 150 % at 77 K; 10 % at 0 °C and about 5 % at room temperature for lanthanum strontium manganese sample, synthesized from glycine containing precursor ( $\varphi = 1$ ) in a field of 3 kOe; b – lanthanum strontium manganese sample, synthesized from glycine containing precursor ( $\varphi = 2$ ) in a field of 3 kOe

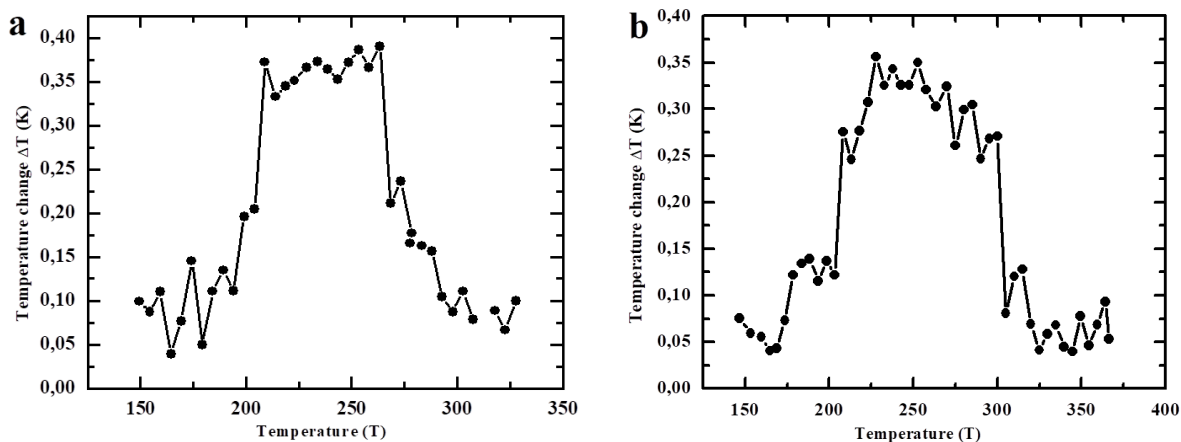


FIG. 5. Examples of magnetocaloric effect measurements for samples: a –  $\text{La}_{0.7}\text{Sr}_{0.3}\text{MnO}_{3\pm y}$ ; b –  $\text{La}_{0.7}\text{Ag}_{0.3}\text{MnO}_{3\pm y}$

superposition of attraction and repulsion forces [76] (the interaction potential  $V$ ), in particular, during the formation of extended structures of ferrogels in a liquid medium [74, 77–79], using the corresponding equations. When considering the interaction potential  $V$  of the particles formed in combustion reactions, in principle, the closely acting van der Waals forces [80] can also be taken into account. However, these forces do not contribute significantly (Fig. 6). In contrast to the particles of gels, steric repulsion, which is typical for colloidal systems, is not taken into account [81]. The relatively low permittivity of the gas medium compared to aqueous solutions, where ferrogels and similar formations are formed, should be considered. This will weaken the electrostatic repulsion.

An approximate scheme of the interaction potential  $V$  of manganite particles may look as follows (Fig. 6). Such a consideration approximates the interaction of at least two complex oxide particles at the initial stage of their chain formation. In this case, the real sizes of the particles and the effective distances between them in the  $\text{La}_{0.7}\text{Sr}_{0.3}\text{MnO}_{3\pm y}$  sample can be used to estimate the above potentials (Fig. 7). If the average size of a “cell” occupied by each particle is assumed to be 100 nm, then according to [61], where the charge density on the precursor surface is given as  $\sim 2 \cdot 10^{-6} \text{ C/cm}^2$  or  $10^{13}$  elementary charges per  $1 \text{ cm}^2$ , we can estimate the charge of each of the  $10^{10}$  particles to be of the order of  $2 \cdot 10^{-16} \text{ C}$ . This corresponds to the order of  $10^3$  excess charges per particle or evaluated by 1 excess elementary charge per  $3.5 \cdot 10^5$  crystallographic cells of lanthanum-strontium-manganite. The potential of electrostatic repulsion between particles by means of Coulomb’s law in such a case is evaluated as 18 V, which corresponds to rather typical measured potential difference ground – precursor in the process of synthesis of complex oxides. This value increases with higher charge densities and correspondingly higher precursor-ground potential difference  $U$ .

Consideration of the estimated resultant curve for electrostatic repulsion and magnetic interaction of particles (Fig. 6) at different precursor charges indicates the possibility of self-organization and formation of extended magnetic formations in the region of intermediate charges. Despite the approximate nature of the estimation, a correlation with the actually

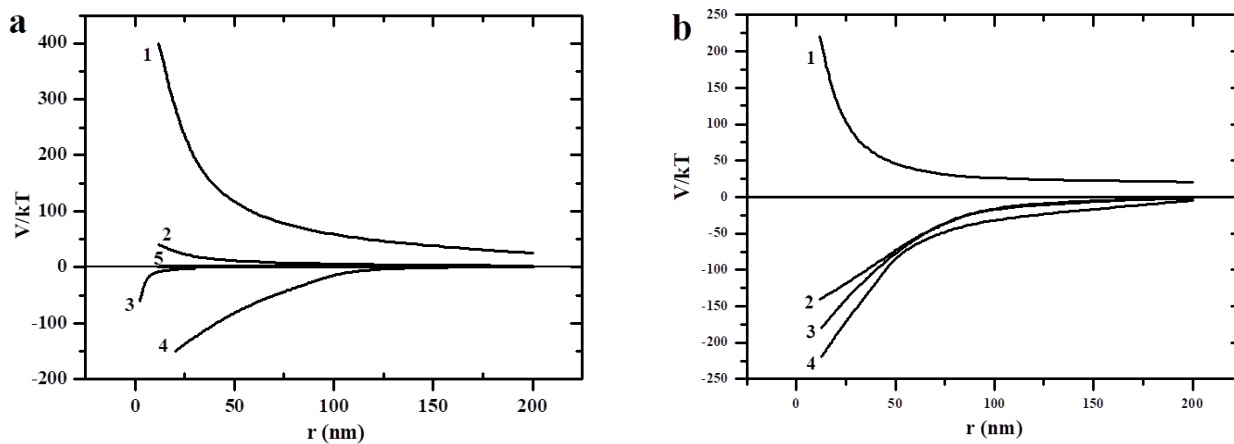


FIG. 6. The dependence of interaction potential of particles  $V/kT$  from the distance between particles: a – electrostatic repulsion at a potential difference ground – precursor 1, 10, 100 V (bottom-up), van der Waals force and magnetic interaction; b – resultant curves for the same potential difference ground – precursor

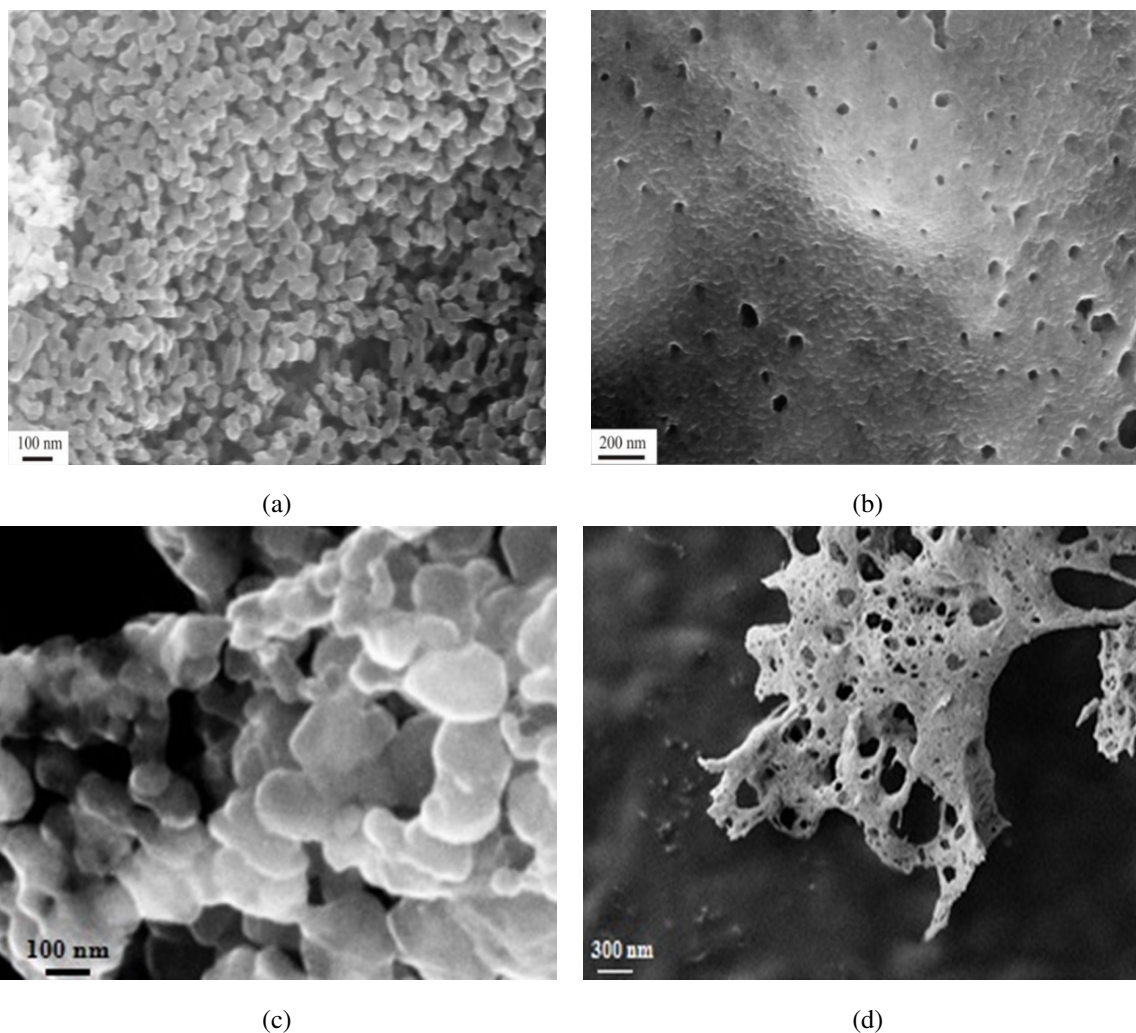


FIG. 7. SEM of  $\text{La}_{0.7}\text{Sr}_{0.3}\text{MnO}_{3\pm y}$  samples, obtained by combustion of PVA containing precursors with different  $\varphi$  value: a – potential difference ground – precursor fixed during synthesis about 200 V (weak particle contact); b – potential difference ground – precursor fixed during synthesis about 10 – 20 V (dense contact); c – beginning of chain aggregates formation; d – fractal (branched structures). SEM images were obtained without changing the integrity of the fragments of materials synthesized via combustion reactions

observed interparticle interactions can be seen. Thus, the generation of high charges leads to the predominance of repulsive forces, while relatively low charges or their practical absence lead to denser contacts between particles (Fig. 7). It is noteworthy that the particles themselves are close in size, which is apparently determined by physicochemical features of the oxide material synthesis processes under combustion reaction conditions [82, 83]. Resulting particles with a size of 50 – 350 nm form submicron and micron aggregates up to 20  $\mu\text{m}$  (Fig. 7). Certain regularity can be observed in the spatial arrangement of the particles. The difference in powders obtained from precursors with different charge generation intensities is clearly seen when comparing their intense sintering temperature [57, 59]. This difference is also clearly seen in the dependence of the specific surface area on the value of the generated potential difference ground – precursor (Fig. 8). It is very interesting that for deterministic [82, 83] particle sizes of complex oxides of different compositions, the dependence of the specific surface area of powders on the above potential difference is practically the same. This can be seen, for example, for doped lanthanum manganite and cerium iron oxide (Fig. 9).

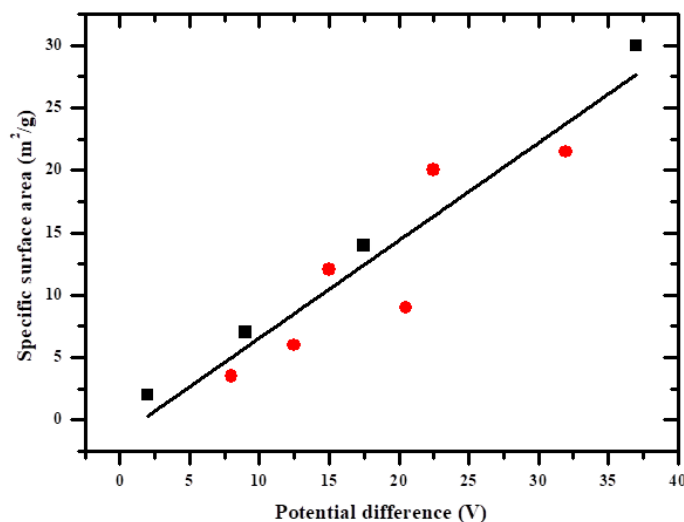


FIG. 8. The dependence of the specific surface area ( $\text{m}^2/\text{g}$ ) on the maximum potential difference ( $V$ ) of the precursor-ground during synthesis from organic nitrate compositions of complex oxides  $\text{Ce}_{0.9}\text{Fe}_{0.1}\text{O}_2$  [65] (circles) and lanthanum manganites (squares)

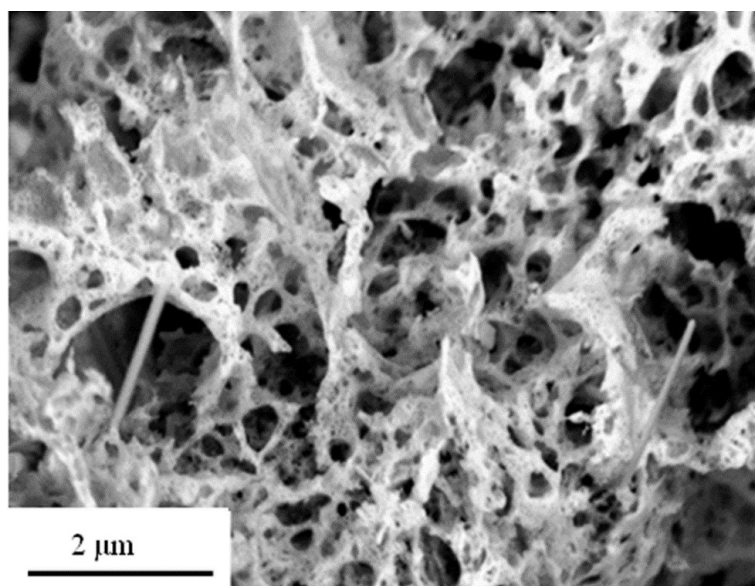


FIG. 9. SEM of  $\text{Ce}_{0.9}\text{Cu}_{0.1}\text{O}_2$  sample synthesized from PVA containing precursor ( $\varphi = 1$ )

Apparently, the chains of nanoparticles are not limited to their ability to associate by magnetic interaction. If such particles have more than two active interaction centers, the chains can branch into Y and X (Fig. 7) and more complex chains with the formation of dendritic (fractal) structures, the mechanism of whose formation is described in the literature,

at least for such objects as magnetic fluids [84]. It can be assumed that in the future it would be productive to use a mathematical technique similar to the models of such media as magnetic fluids and ferrogels to describe and predict the behavior of systems in which the synthesis of magnetic nanoparticles takes place. It is clear that our approach to estimating the possibility of forming extended ensembles of nanoparticles is quite suitable for the systems in which complex oxides exhibit ferromagnetic properties at much higher temperatures than lanthanum manganites. In the first place it concerns hexaferrites Sr, Ba with magnetoplumbite-type structure, since the Curie temperature of such complex oxides is equal to their synthesis temperature in combustion reactions. It should also be assumed that the resulting curve of interaction potentials between particles  $V$  for complex oxides, including lanthanum manganite, under the influence of magnetic field, at the same intensity of charge generation  $U$ , will be located below the curve obtained in the absence of external field (Fig. 6). It is clear that exposure to an external magnetic field, other conditions being equal, increases the tendency to form nanoparticle chain associations by increasing the magnetization of the material. At the same time, dendritic associates similar to those observed for manganites (Fig. 7) can also be found in other systems whose morphology formation is not related to magnetic interaction. A sample based on cerium dioxide (Fig. 9) can serve as an example. It can be assumed that one of the conditions determining the formation of dendritic structures is usually an intensive volumetric combustion of the precursor. On the other hand, proper chain ensembles are most likely to be formed under smoldering combustion or close to the SHS regime.

Some additional assumptions about the processes of synthesis of complex oxide materials via combustion of organic nitrate precursors could be proposed. Some peculiarities of obtaining the double perovskite  $\text{Sr}_2\text{Ni}_{0.7}\text{Mg}_{0.3}\text{MoO}_{6-d}$  [60] as a potential anode material for solid oxide fuel cells have already been considered. This and similar materials exhibit ferromagnetic properties only at rather low temperatures due to the low Curie temperature [83, 85]. However, the formation of the target product occurs through the appearance of intermediate oxide products containing either molybdenum or nickel. At the same time, the formation of nano-sized molybdenum oxide particles with an intermediate degree of oxidation, which can form in the presence of organic compounds, nickel oxide and other phases, which may also have magnetic properties and give rise to extended ensembles, as observed in electron micrographs of samples [60], cannot be excluded. The presence of such chains may also contribute to the high electrical conductivity of the material [60], obtained from a precursor with sufficiently intense charge generation. Another important point is the possibility of generating charges of different sign on the particles of the intermediate phases, which differ in the presence of transition metal ions (Ni, Mo). The sign of the charge, among other conditions, is related to the tendency of such ions to change the direction of the degree of oxidation [57]. In case of formation of charges of different signs, such nanoparticles will experience a sufficiently strong mutual attraction, judging by the value of the electrostatic interaction potentials discussed above. This point will probably contribute to a good contacting of the intermediate phase particles and facilitate the synthesis of the final product, as observed in [60].

Further research can include aspects such as the formation of extended structures in complex oxide materials during their synthesis when coatings are deposited on substrates using combustion reactions. In such a case, the texturing factors are the electrostatic repulsion of the particles and the topological orientation effect of the substrate. An example is the textured coating of  $\text{YBa}_2\text{Cu}_3\text{O}_{7-\delta}$  on an oxide support (Fig. 10); in precursors based on the respective metal nitrates and polyvinyl alcohol, the appearance of charges of negative sign was recorded [61].

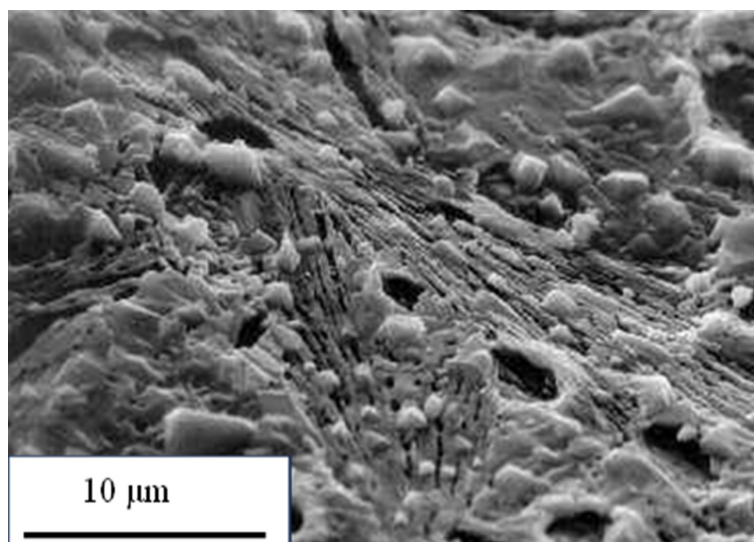


FIG. 10. SEM of  $\text{YBa}_2\text{Cu}_3\text{O}_{7-\delta}$  coating on an  $\text{Al}_2\text{O}_3$  carrier with a zirconium dioxide sublayer obtained by pyrolysis of nitrate-polyvinyl alcohol compositions [86]

Another important point concerning the synthesis processes discovered during the study should be noted. A fairly strong manifestation of the magnetic-gas-selective effect during the combustion of organo-nitrate compositions was established. This effect was discussed above [20–24]. In this case, during the precursor (PVA,  $\varphi = 1$ ) combustion in a magnetic field ( $H = 3$  kOe), the potential difference  $U$  of the order of  $+60$  V was determined while this value was about  $-8$  V when the combustion of the same precursor occurred in the absence of a magnetic field. It should be noted that the value of  $U$  reached  $+100$  V and even more when the combustion occurs under the influence of an electromagnetic field [59]. Consequently, a constant magnetic field prevented the removal of negatively charged paramagnetic molecular groups like  $\text{H}_2\text{O}^-$ ,  $\text{CO}_3^-$  during combustion, whereas the application of an alternating electromagnetic field, on the contrary, promoted it [50, 59]. The pattern established initially allows us to control the process of charge generation and influence the formation of the morphology of the samples; it requires further study. On the other hand, this point makes more understandable the results of formation of magnetic properties of samples (Fig. 2), where non-monotone dependence on the external field strength is observed, because the intensity of manifestation of the magnetic-gas-selective effect may be related to the field strength.

#### 4. Conclusion

In conclusion, it should be noted that the influence of the magnetic field on the results of synthesis of lanthanum manganites appears in a rather complex superposition with such a factor as the presence and intensity of generation of electric charges, determined by synthesis conditions, in particular, the composition of precursors. Nevertheless, it is possible to trace the regularity of such mutual influence. When considering the effect of magnetic field, it is reasonable to divide the studied systems into groups according to the intensity of charge generation: high, medium and low. An external magnetic field had a predominantly positive influence on the lanthanum-strontium-manganite samples, in which high intensity of charge generation was observed in terms of their magnetization enhancement, apparently due to obtaining a more perfect magnetic structure of crystallites. Under conditions of medium and low intensity of charge generation, when the electrostatic repulsive forces are lower, but still strong enough to minimize contacts between nanoparticles, conditions are created for the formation of chain-like ensembles as well as dendritic forms. At the same time, the application of a magnetic field has a positive effect on the value of the coercive force of the samples, and increase of the Curie temperature. The use of the detected trends allows one to purposefully optimize the conditions of manganite production, including the choice of the conditions for obtaining materials with such properties as magnetocaloric and magnetoresistance effects, on the basis of the available data on the intensity of charge generation in a given system of starting reagents. A magneto-gas-selective effect was found to occur during the combustion of nitrate organic precursors, leading to a decrease in the resulting potential difference between the ground and the precursor. This phenomenon requires further detailed investigation.

#### References

- [1] Sukhorukov Yu. P., Gan'shina E.A., Loshkareva N.N., Kaul A.R., Gorbenko O.Yu., Telegin A.V., et al. Evolution of magneto-optical and transport properties of  $\text{La}_{1-x}\text{Ag}_x\text{MnO}_3$  films depending on silver concentration. *J. Exp. Theor. Phys.*, 2007, **104** (4), P. 569–576.
- [2] Vasil'ev A.V., Vizgalov V.A., Trusov L.A., Kazin P.E., Tretyakov Yu.D., Jansen M. Magnetoresistive composites  $\text{La}_{0.7}\text{Sr}_{0.3}\text{MnO}_{3-\delta}$  – PMMA. *Dokl. Chem.*, 2012, **445** (1), P. 137–139.
- [3] Kaul A.R., Gorbenko O.Y., Kamenev A.A. The role of heteroepitaxy in the development of new thin-film oxide-based functional materials. *Russ. Chem. Rev.*, 2004, **73** (9), P. 861–880.
- [4] Gamzatov A.G., Batdalov A.B., Melnikov O.V., Gorbenko O.Yu. Spin-polarized transport in the manganite  $\text{La}_{0.85}\text{Ag}_{0.15}\text{MnO}_3$ . *Low Temp. Phys.*, 2009, **35** (3), P. 219–222.
- [5] Teplykh A.E., Bogdanov S.G., Valiev É.Z., Pirogov A.N., Dorofeev Yu.A., Ostroushko A.A., et al. Size effect in nanocrystalline manganites  $\text{La}_{1-x}\text{A}_x\text{MnO}_3$  (A=Ag, Sr). *Phys. Solid State*, 2003, **45** (12), P. 2328–2333.
- [6] Bubnovskaya L., Belous A., Solopan S., Kovelskaya A., Bovkun L., Podoltsev A., et al. Magnetic Fluid Hyperthermia of Rodent Tumors Using Manganese Perovskite Nanoparticles. *J. of Nanoparticles*, 2014, **2014**, P. 1–9.
- [7] Zheng L., Chen Y., Wang Y., Wang P., Wang T. Effect of Bi Ions on the Hyperthermia Properties of Hyaluronic Acid-Coated  $\text{La}_{1-x}\text{Sr}_x\text{MnO}_3$  Nanoparticles. *NANO*, 2020, **15** (01), 2050015.
- [8] Wu S., Wang Y., Shi D. Positively Charged Magnetic Nanoparticles for Capture of Circulating Tumor Cells from Clinical Blood Samples. *Nano LIFE*, 2020, **10** (03), 1971001.
- [9] Estemirova S.K., Mitrofanov V.Y., Uporov S.A., Kozhina G.A. Magnetocaloric properties of Fe-substituted La–Sr-manganites. *Solid State Sciences*, 2022, **124**, 106806.
- [10] Szewczyk A., Gutowska M., Piotrowski K., Dabrowski B. Direct and specific heat study of magnetocaloric effect in  $\text{La}_{0.845}\text{Sr}_{0.155}\text{MnO}_3$ . *J. Appl. Phys.*, 2003, **94** (3), P. 1873–1876.
- [11] Gamzatov A.G., Aliev A.M., Batdalov A.B., Abdulvagidov Sh.B., Melnikov O.V., Gorbenko O.Yu. Magnetocaloric effect in silver-doped lanthanum manganites. *Tech. Phys. Lett.*, 2006, **32** (6), P. 471–473.
- [12] Gamzatov A.G., Khizriev K.Sh., Batdalov A.B., Abdulvagidov Sh.B., Aliev A.M., Melnikov O.V., et al. Critical behavior of the specific heat of manganites  $\text{La}_{1-x}\text{Ag}_x\text{MnO}_3$  ( $x = 0.1, 0.15, 0.2$ ) near the Curie point. *Low Temp. Phys.*, 2009, **35** (3), P. 214–218.
- [13] Ifrah S., Kaddouri A., Gelin P., Leonard D. Conventional hydrothermal process versus microwave-assisted hydrothermal synthesis of  $\text{La}_{1-x}\text{Ag}_x\text{MnO}_{3+\delta}$  ( $x = 0, 0.2$ ) perovskites used in methane combustion. *Comptes Rendus Chimie*, 2007, **10** (12), P. 1216–1226.
- [14] Ostroushko A.A., Shubert E., Makarov A.M., Minyaev V.I., Udilov A.E., Elokhina L.V., et al. Catalytic Activity of Complex-Oxide Perovskite-containing Compositions in Reactions of Oxidation of CO and Organic Compounds. *Russ. J. Appl. Chem.*, 2003, **76** (8), P. 1253–1259.
- [15] Kalinina E.G., Pikalova E.Yu. New trends in the development of electrophoretic deposition method in the solid oxide fuel cell technology: theoretical approaches, experimental solutions and development prospects. *Russ. Chem. Rev.*, 2019, **88** (12), P. 1179–1219.

- [16] Russkikh O.V., Ivanov D.V., Isupova L.A., Chezganov D.S., Ostroushko A.A. Synthesis, morphology, and activity of  $\text{La}_{1-x}\text{Ag}_x\text{MnO}_{3\pm y}$  catalysts. *Kinet. Catal.*, 2016, **57** (5), P. 712–721.
- [17] Ostroushko A.A., Russkikh O.V., Kormil'tzev I.I., Kolosov V.Yu., Tsvetkov D.S., Vylkov A.I. Study of nanostructured catalysts on the basis of complex oxides deposited on a carrier. *J. Synch. Investig.*, 2011, **5** (4), P. 677–682.
- [18] Ostroushko A.A., Russkikh O.V. Catalytic properties of complex oxide coatings on foamed nickel. *Russ. J. Appl. Chem.*, 2015, **88** (10), P. 1582–1588.
- [19] Ostroushko A.A., Russkikh O.V., Chezganov D.S. Formation and morphology of nickel foam–complex oxide coatings with the perovskite structure. *J. Synch. Investig.*, 2015, **9** (6), P. 1237–1242.
- [20] Yao G., Wang F., Wang X., Gui K. Magnetic field effects on selective catalytic reduction of NO by  $\text{NH}_3$  over  $\text{Fe}_2\text{O}_3$  catalyst in a magnetically fluidized bed. *Energy*, 2010, **35** (5), P. 2295–2300.
- [21] Wang D., Pan J., Zhu D., Guo Z., Yang C., Duan X. Enhanced adsorption of NO onto activated carbon by gas pre-magnetization. *Sci. Total Environ.*, 2022, **830**, 154712.
- [22] Xie Y., Wang M., Wang X., Wang L., Ning P., Ma Y., et al. Magnetic-field-assisted catalytic oxidation of arsine over Fe/HZSM-5 catalyst: Synergistic effect of Fe species and activated surface oxygen. *J. Clean. Prod.*, 2022, **337**, 130549.
- [23] Nikitin V.A. *Lekzii po teplotekhnike*. Orenburg State University, Orenburg, 2011, 532 p.
- [24] Cai Y., Zou H., Qu G., Li J., Che L., Hu Y., et al. The mechanism of catalytic oxidation phosphine in liquid phase by transition metal magnetic catalyst in external magnetic field. *Environ. Technol. Innov.*, 2022, **28**, 102958.
- [25] Xu C., Manukyan K.V., Adams R.A., Pol V.G., Chen P., Varma A. One-step solution combustion synthesis of  $\text{CuO/Cu}_2\text{O/C}$  anode for long cycle life Li-ion batteries. *Carbon*, 2019, **142**, P. 51–59.
- [26] Pikalova E., Kolchugin A., Zakharchuk K., Boiba D., Tsvinkinberg V., Filonova E., et al. Mixed ionic-electronic conductivity, phase stability and electrochemical activity of Gd-substituted  $\text{La}_2\text{NiO}_{4+\delta}$  as oxygen electrode material for solid oxide fuel/electrolysis cells. *Int. J. Hydrog.*, 2021, **46** (32), P. 16932–16946.
- [27] Khaliullin Sh.M., Koshkina A.A. Influence of fuel on phase formation, morphology, electric and dielectric properties of iron oxides obtained by SCS method. *Ceram. Int.*, 2021, **47** (9), P. 11942–11950.
- [28] Popkov V.I., Almjasheva O.V., Nevedomskiy V.N., Panchuk V.V., Semenov V.G., Gusarov V.V. Effect of spatial constraints on the phase evolution of  $\text{YFeO}_3$ -based nanopowders under heat treatment of glycine-nitrate combustion products. *Ceram. Int.*, 2018, **44** (17), P. 20906–20912.
- [29] Tugova E., Yastrebov S., Karpov O., Smith R.  $\text{NdFeO}_3$  nanocrystals under glycine nitrate combustion formation. *J. Cryst. Growth*, 2017, **467**, P. 88–92.
- [30] Wang X., Qin M., Fang F., Jia B., Wu H., Qu X., et al. Effect of glycine on one-step solution combustion synthesis of magnetite nanoparticles. *J. Alloys Compd.*, 2017, **719**, P. 288–295.
- [31] Lomanova N.A., Tomkovich M.V., Osipov A.V., Ugolkov V.L., Danilovich D.P., Panchuk V.V., et al. Formation of  $\text{Bi}_{1-x}\text{Ca}_x\text{FeO}_{3-\delta}$  Nanocrystals via Glycine-Nitrate Combustion. *Russ. J. Gen. Chem.*, 2019, **89** (9), P. 1843–1850.
- [32] Popkov V.I., Almjasheva O.V., Semenova A.S., Kellerman D.G., Nevedomskiy V.N., Gusarov V.V. Magnetic properties of  $\text{YFeO}_3$  nanocrystals obtained by different soft-chemical methods. *J. Mater. Sci. Mater. Electron.*, 2017, **28** (10), P. 7163–7170.
- [33] Lomanova N.A., Tomkovich M.V., Sokolov V.V., Gusarov V.V. Special features of formation of nanocrystalline  $\text{BiFeO}_3$  via the glycine-nitrate combustion method. *Russ. J. Gen. Chem.*, 2016, **86** (10), P. 2256–2262.
- [34] Popkov V.I., Almjasheva O.V. Yttrium orthoferrite  $\text{YFeO}_3$  nanopowders formation under glycine-nitrate combustion conditions. *Russ. J. Appl. Chem.*, 2014, **87** (2), P. 167–171.
- [35] Lomanova N.A., Tomkovich M.V., Sokolov V.V., Ugolkov V.L., Panchuk V.V., Semenov V.G., et al. Thermal and magnetic behavior of  $\text{BiFeO}_3$  nanoparticles prepared by glycine-nitrate combustion. *J. Nanopart. Res.*, 2018, **20** (2), 17.
- [36] Ostroushko A.A., Shubert E., Zhuravleva L.I. Synthesis and physicochemical and catalytic properties of perovskites  $\text{ABO}_{3\pm y}$  (A = La, Sr, Ag; B = Mn, Co, Fe, Cu, Ti, Mo, V). *Russ. J. Appl. Chem.*, 2000, **73** (8), 1311.
- [37] Zaboeva E.A., Izotova S.G., Popkov V.I. Glycine-nitrate combustion synthesis of  $\text{CeFeO}_3$ -based nanocrystalline powders. *Russ. J. Appl. Chem.*, 2016, **89** (8), P. 1228–1236.
- [38] Farhadi S., Zaidi M. Bismuth ferrite ( $\text{BiFeO}_3$ ) nanopowder prepared by sucrose-assisted combustion method: A novel and reusable heterogeneous catalyst for acetylation of amines, alcohols and phenols under solvent-free conditions. *J. Mol. Catal. A: Chem.*, 2009, **299** (1–2), P. 18–25.
- [39] Farbun I.A., Romanova I.V., Khainakov S.A., Kirillov S.A. Properties of nanosized materials on the base of manganese and cerium oxides obtained from the citric solutions. *Surface*, 2010, **2** (17), 197.
- [40] Delimaris D., Ioannides T. VOC oxidation over  $\text{MnO}_x\text{-CeO}_2$  catalysts prepared by a combustion method. *Appl. Catal. B*, 2008, **84** (1–2), P. 303–312.
- [41] Delimaris D., Ioannides T. VOC oxidation over  $\text{CuO-CeO}_2$  catalysts prepared by a combustion method. *Appl. Catal. B*, 2009, **89** (1–2), P. 295–302.
- [42] Rao G.R., Sahu H.R., Mishra B.G. Surface and catalytic properties of  $\text{Cu-Ce-O}$  composite oxides prepared by combustion method. *Colloids Surf. A Physicochem. Eng. Asp.*, 2003, **220** (1–3), P. 261–269.
- [43] Mahour L.N., Choudhary H.K., Kumar R., Anupama A.V., Sahoo B. Structural, optical and Mössbauer spectroscopic investigations on the environment of Fe in Fe-doped  $\text{ZnO}$  ( $\text{Zn}_{1-x}\text{Fe}_x\text{O}$ ) ceramics synthesized by solution combustion method. *Ceram. Int.*, 2019, **45** (18), P. 24625–24634.
- [44] Komlev A.A., Gusarov V.V. Glycine-nitrate combustion synthesis of nonstoichiometric  $\text{Mg-Fe}$  spinel nanopowders. *Inorg. Mater.*, 2014, **50** (12), P. 1247–1251.
- [45] Ostroushko A.A., Russkikh O.V., Gagarin I.D., Filonova E.A. Study of the charge generation in the synthesis of nanosized complex oxides in the combustion reactions of organo-inorganic precursors. *Phys. Chem. Aspect. Stud. Clust. Nanostr. Nanomater.*, 2019, **11**, 215.
- [46] Chick L.A., Pederson L.R., Maupin G.D., Bates J.L., Thomas L.E., Exarhos G.J. Glycine-nitrate combustion synthesis of oxide ceramic powders. *Mater. Lett.*, 1990, **10** (1–2), P. 6–12.
- [47] Popkov V.I., Almjasheva O.V., Nevedomskiy V.N., Sokolov V.V., Gusarov V.V. Crystallization behavior and morphological features of  $\text{YFeO}_3$  nanocrystallites obtained by glycine-nitrate combustion. *Nanosystems: Phys. Chem. Math.*, 2015, **6** (6), P. 866–874.
- [48] Chiu T.-W., Yu B.-S., Wang Y.-R., Chen K.-T., Lin Y.-T. Synthesis of nanosized  $\text{CuCrO}_2$  porous powders via a self-combustion glycine nitrate process. *J. Alloys Compd.*, 2011, **509** (6), P. 2933–2935.
- [49] Enikeeva M.O., Kenges K.M., Proskurina O.V., Danilovich D.P., Gusarov V.V. Influence of Hydrothermal Treatment Conditions on the Formation of Lanthanum Orthophosphate Nanoparticles of Monazite Structure. *Russ. J. Appl. Chem.*, 2020, **93** (4), P. 540–548.
- [50] Khaliullin Sh.M., Bamburov V.G., Russkikh O.V., Ostroushko A.A., Zhuravlev V.D.  $\text{CaZrO}_3$  synthesis in combustion reactions with glycine. *Dokl. Chem.*, 2015, **461** (2), P. 93–95.
- [51] Smirnova M.N., Goeva L.V., Simonenko N.P., Beresnev E.N., Kop'eva M.A., Ketsko V.A. Gel formation specifics in the synthesis of  $\text{Mg}(\text{Fe}_{0.8}\text{Ga}_{0.2})_2\text{O}_4$  by the glycine-nitrate method. *Russ. J. Inorg. Chem.*, 2016, **61** (10), P. 1301–1306.

- [52] Zhuravlev V.D., Bamburov V.G., Beketov A.R., Perelyaeva L.A., Baklanova I.V., Sivtsova O.V., et al. Solution combustion synthesis of  $\alpha$ -Al<sub>2</sub>O<sub>3</sub> using urea. *Ceram. Int.*, 2013, **39** (2), P. 1379–1384.
- [53] Khaliullin Sh.M., Zhuravlev V.D., Bamburov V.G. Solution-combustion synthesis of oxide nanoparticles from nitrate solutions containing glycine and urea: Thermodynamic aspects. *Int. J. Self-Propag. High-Temp. Synth.*, 2016, **25** (3), P. 139–148.
- [54] Ostroushko A.A., Mogil'nikov Y.V., Ostroushko I.P. Synthesis of Molybdenum-and Vanadium-Containing Mixed Oxides in Polymer-Salt Systems. *Inorg. Mater.*, 2000, **36** (12), P. 1256–1263.
- [55] Popkov V.I., Almjashaeva O.V., Schmidt M.P., Izotova S.G., Gusarov V.V. Features of nanosized YFeO<sub>3</sub> formation under heat treatment of glycine-nitrate combustion products. *Russ. J. Inorg. Chem.*, 2015, **60** (10), P. 1193–1198.
- [56] Ostroushko A.A., Russkikh O.V. Oxide material synthesis by combustion of organic-inorganic compositions. *Nanosystems: Phys. Chem. Math.*, 2017, **8** (4), P. 476–502.
- [57] Ostroushko A.A., Maksimchuk T.Yu., Permyakova A.E., Russkikh O.V. Determinative Factors for the Thermochemical Generation of Electric Charges upon Combustion of Nitrate–Organic Precursors for Materials Based on Lanthanum Manganite and Cerium Dioxide. *Russ. J. Inorg. Chem.*, 2022, **67** (6), P. 799–809.
- [58] Ostroushko A.A., Zhulanova T.Yu., Kudukov E.V., Gagarin I.D., Russkikh O.V. Lanthanum manganite nanopowders synthesis via combustion reactions under the influence of electromagnetic field. *Phys. Chem. Aspect. Stud. Clust. Nanostr. Nanomater.*, 2022, (14), P. 820–828.
- [59] Ostroushko A.A., Russkikh O.V., Maksimchuk T.Yu. Charge generation during the synthesis of doped lanthanum manganites via combustion of organo-inorganic precursors. *Ceram. Int.*, 2021, **47** (15), P. 21905–21914.
- [60] Filonova E.A., Russkikh O.V., Skutina L.S., Vylkov A.I., Maksimchuk T.Yu., Ostroushko A.A. Sr<sub>2</sub>Ni<sub>0.7</sub>Mg<sub>0.3</sub>MoO<sub>6- $\delta$</sub> : Correlation between synthesis conditions and functional properties as anode material for intermediate-temperature SOFCs. *Int. J. Hydrog.*, 2021, **46** (72), P. 35910–35922.
- [61] Ostroushko A.A., Sennikov M.Yu. Thermochemical charge generation in polymer-salt films. *Russ. J. Inorg. Chem.*, 2005, **50** (6), P. 933–936.
- [62] Ostroushko A.A., Sennikov M.Yu. Thermochemical charge generation in polymer-salt films as a function of temperature. *Russ. J. Inorg. Chem.*, 2008, **53** (8), P. 1172–1175.
- [63] Filonova E.A., Russkikh O.V., Skutina L.S., Kochetova N.A., Korona D.V., Ostroushko A.A. Influence of synthesis conditions on phase formation and functional properties of prospective anode material Sr<sub>2</sub>Ni<sub>0.75</sub>Mg<sub>0.25</sub>MoO<sub>6- $\delta$</sub> . *J. Alloys Compd.*, 2018, **748**, P. 671–678.
- [64] Martirosyan K.S., Filimonov I.A., Luss D. Electric-field generation by gas-solid combustion. *AIChE J.*, 2004, **50** (1), P. 241–248.
- [65] Markov A.A., Filimonov I.A., Poletaev A.V., Vadchenko S.G., Martirosyan K.S. Generation of charge carriers during combustion synthesis of sulfides. *Int. J. Self-Propag. High-Temp. Synth.*, 2013, **22** (2), P. 69–76.
- [66] Martirosyan K.S., Setoodeh M., Luss D. Electric-field generated by the combustion of titanium in nitrogen. *J. Appl. Phys.*, 2005, **98** (5), 054901.
- [67] Setoodeh M., Martirosyan K.S., Luss D. Electrical pulse formation during high temperature reaction between Ni and Al. *J. Appl. Phys.*, 2006, **99** (8), 084901.
- [68] Filimonov I., Luss D. Formation of electric potential during the oxidation of a metal particle. *AIChE J.*, 2004, **50** (9), P. 2287–2296.
- [69] Filimonov I., Kidin N. Formation of charged defects during the nitridation of a metal particle. *Proc. Combust. Inst.*, 2007, **31** (2), P. 1991–1999.
- [70] Kuznetsov M.V., Belousova O.V., Morozov Yu.G., Schipakin S.Yu. Electromotive force of combustion in the periodical table. *ISJAE*, 2014, **20** (160), 38.
- [71] Martirosyan K.S., Filimonov I.A., Nersisyan M.D., Luss D. Electric Field Formation during Combustion of Single Metal Particles. *J. Electrochem. Soc.*, 2003, **150** (5), P. 9–16.
- [72] Gubin S.P., Koksharov Y.A., Khomutov G.B., Yurkov G.Y. Magnetic nanoparticles: preparation, structure and properties. *Russ. Chem. Rev.*, 2005, **74** (6), P. 489–520.
- [73] Zhang N., Yang W., Ding W., Xing D., Du Y. Grain size-dependent magnetism in fine particle perovskite, La<sub>1-x</sub>Sr<sub>x</sub>MnO<sub>z</sub>. *Solid State Communications*, 1999, **109** (8), P. 537–542.
- [74] Walker D.A., Kowalczyk B., De La Cruz M.O., Grzybowski B.A. Electrostatics at the nanoscale. *Nanoscale*, 2011, **3** (4), P. 1316–1344.
- [75] Genz U., Aguanno B.D., Mewis J. Structure of Sterically Stabilized Colloids. *Langmuir*, 1994, **10**, P. 2206–2212.
- [76] Shankar A., Safronov A.P., Mikhnevich E.A., Beketov I.V., Kurlyandskaya G.V. Ferrogels based on entrapped metallic iron nanoparticles in a polyacrylamide network: extended Derjaguin–Landau–Verwey–Overbeek consideration, interfacial interactions and magnetodeformation. *Soft Matter*, 2017, **13** (18), P. 3359–3372.
- [77] Skomski R. Nanomagnetism. *J. Phys.: Condens. Matter*, 2003, **15** (20), R841–R896.
- [78] Ivanov A.O., Zubarev A. Chain Formation and Phase Separation in Ferrofluids: The Influence on Viscous Properties. *Materials*, 2020, **13** (18), 3956.
- [79] Mikhnevich E.A., Chebotkova P.D., Safronov A.P. Synthesis and Study of Mechanical Properties of Polyelectrolyte Ferrogels Based on Strontium Ferrite Particles. *Inorg. Mater. Appl. Res.*, 2020, **11** (4), P. 855–860.
- [80] Sanchez-Dominguez Ed. M., Rodriguez-Abreu C. *Nanocolloids: a meeting point for scientists and technologists*. Elsevier, Amsterdam, 2016, 514 p.
- [81] Lim J.K., Majetich S.A., Tilton R.D. Stabilization of Superparamagnetic Iron Oxide Core-Gold Shell Nanoparticles in High Ionic Strength Media. *Langmuir*, 2009, **25** (23), P. 13384–13393.
- [82] Almjashaeva O.V., Popkov V.I., Proskurina O.V., Gusarov V.V. Phase formation under conditions of self-organization of particle growth restrictions in the reaction system. *Nanosystems: Phys. Chem. Math.*, 2022, **13** (2), P. 164–180.
- [83] Almjashaeva O.V., Lomanova N.A., Popkov V.I., Proskurina O.V., Tugova E.A., Gusarov V.V. The minimum size of oxide nanocrystals: phenomenological thermodynamic vs crystal-chemical approaches. *Nanosystems: Phys. Chem. Math.*, 2019, **10** (4), P. 428–437.
- [84] Kantorovich S.S., Ivanov A.O., Rovigatti L., Tavares J.M., Sciortino F. Temperature-induced structural transitions in self-assembling magnetic nanocolloids. *Phys. Chem. Chem. Phys.*, 2015, **17** (25), P. 16601–16608.
- [85] Urusova N., Kumar M.R., Semkin M., Filonova E., Kratochvilova M., Neznakhin D., et al. Crystal structure and magnetic properties of Sr<sub>2</sub>Ni<sub>1-x</sub>Mg<sub>x</sub>MoO<sub>6</sub> (x = 0, 0.25, 0.5, and 0.75) polycrystals. *Solid State Sci.*, 2020, **99**, 106008.
- [86] Ostroushko A.A. *Physico-chemical bases of obtaining solid-phase materials for electronic engineering and catalysis: students guide*. UrFU, Ekaterinburg, 2011, 160 p. (in Russian).

*Information about the authors:*

*Alexander A. Ostroushko* – Ural Federal University Scientific Research Institute of Physics and Applied Mathematics, Ekaterinburg 620002, Russia; ORCID 0000-0003-0206-5513; alexander.ostroushko@urfu.ru

*Iliya D. Gagarin* – Ural Federal University Scientific Research Institute of Physics and Applied Mathematics, Ekaterinburg 620002, Russia; ORCID 0000-0002-8545-927X; ilya.gagarin@urfu.ru

*Egor V. Kudyukov* – Ural Federal University Scientific Research Institute of Physics and Applied Mathematics, Ekaterinburg 620002, Russia; ORCID 0000-0002-4382-7695; e.v.kudyukov@urfu.ru

*Tatiana Yu. Zhulanova* – Ural Federal University Scientific Research Institute of Physics and Applied Mathematics, Ekaterinburg 620002, Russia; ORCID 0000-0002-8009-4398; tatiana.maksimchuk@urfu.ru

*Anastasya E. Permyakova* – Ural Federal University Scientific Research Institute of Physics and Applied Mathematics, Ekaterinburg 620002, Russia; ORCID 0009-0004-3194-4626; nastia2605permiakova@yandex.ru

*Olga V. Russkikh* – Ural Federal University Scientific Research Institute of Physics and Applied Mathematics, Ekaterinburg 620002, Russia; ORCID 0000-0001-5923-095X; o.v.russkikh@urfu.ru

*Conflict of interest:* the authors declare no conflict of interest.

## Planar perovskite solar cells with La<sub>2</sub>NiMnO<sub>6</sub> buffer layer

Sergey S. Kozlov<sup>1</sup>, Anna B. Nikolskaia<sup>1</sup>, Olga K. Karyagina<sup>1</sup>, Ekaterina K. Kosareva<sup>2</sup>,  
Olga V. Alexeeva<sup>1</sup>, Vasilisa I. Petrova<sup>1</sup>, Oksana V. Almjasheva<sup>3,4</sup>, Oleg I. Shevaleevskiy<sup>1</sup>

<sup>1</sup>Emanuel Institute of Biochemical Physics, Russian Academy of Sciences, Moscow, Russia

<sup>2</sup>N. N. Semenov Federal Research Center for Chemical Physics, Russian Academy of Science, Moscow, Russia

<sup>3</sup>St. Petersburg State Electrotechnical University “LETI”, St. Petersburg, Russia

<sup>4</sup>Ioffe Physical-Technical Institute, Russian Academy of Sciences, St. Petersburg, Russia

Corresponding author: Anna B. Nikolskaia, [anickolskaya@mail.ru](mailto:anickolskaya@mail.ru)

PACS 84.60.Jt

**ABSTRACT** Thin films of La<sub>2</sub>NiMnO<sub>6</sub> (LNMO) double perovskite oxide were first used as buffer layers in planar perovskite solar cells (PSCs) with the architecture of glass/FTO/LNMO/CH<sub>3</sub>NH<sub>3</sub>PbI<sub>3</sub>/Spiro-MeOTAD/Au. All PSCs were fabricated under ambient conditions and their photovoltaic parameters were measured under standard illumination (AM1.5G, 1000 W/m<sup>2</sup>). Power conversion efficiency (PCE) values (10 – 11 %) for the PSCs developed were comparable with those obtained for conventional PSCs with compact TiO<sub>2</sub> (cTiO<sub>2</sub>) layer, but the stability of PSCs with LNMO buffer layer was significantly higher than for cTiO<sub>2</sub>-based PSCs.

**KEYWORDS** nanostructures, double perovskite oxides, perovskite solar cells, solar photovoltaics

**ACKNOWLEDGEMENTS** This work was supported by the Russian Science Foundation under grant No. 20-69-47124.

**FOR CITATION** Kozlov S.S., Nikolskaia A.B., Karyagina O.K., Kosareva E.K., Alexeeva O.V., Petrova V.I., Almjasheva O.V., Shevaleevskiy O.I. Planar perovskite solar cells with La<sub>2</sub>NiMnO<sub>6</sub> buffer layer. *Nanosystems: Phys. Chem. Math.*, 2023, **14** (5), 584–589.

### 1. Introduction

The search and development of new types of solar cells with high efficiency and stability is one of the most urgent tasks of the modern photovoltaics [1,2]. In the last decade, the great interest has been focused on the studies of perovskite solar cells (PSCs), in which hybrid organic-inorganic materials, such as CH<sub>3</sub>NH<sub>3</sub>PbX<sub>3</sub> (X = Cl<sup>-</sup>, Br<sup>-</sup> or I<sup>-</sup>), are used as photosensitive layers. Improvement of the PSC fabrication technology allowed one to achieve high values of power conversion efficiency (PCE), which nowadays exceeds 25 % [3–5]. Low cost and simple manufacturing methods make PSCs a promising alternative to traditional silicon-based solar cells. However, perovskite materials used in PSCs are characterized by low stability and degrade under ambient conditions or under continuous illumination. As a result, PCE of PSCs is significantly decreased over time, which limits the application prospects [6, 7].

Previously, it was shown that the highest PCE values can be achieved using PSCs with a planar structure [8, 9]. The architecture of the state-of-the-art planar PSC sample is glass/FTO/cTiO<sub>2</sub>/CH<sub>3</sub>NH<sub>3</sub>PbI<sub>3</sub>/SpiroMeOTAD/Au, where FTO is a fluorine-doped tin oxide conductive coating (F:SnO<sub>2</sub>), cTiO<sub>2</sub> is a compact layer of TiO<sub>2</sub> nanoparticles with the thickness ~ 50 nm. The functions of cTiO<sub>2</sub> layer include blocking hole transfer from the perovskite material to the FTO coating and preventing direct contact between CH<sub>3</sub>NH<sub>3</sub>PbI<sub>3</sub> layer and the FTO surface [10, 11]. However, PSCs with planar structure were found to be the most sensitive to external factors such as humidity, temperature, and illumination. The latter is due to both the degradation of the perovskite material itself and the instability of the TiO<sub>2</sub> layer when exposed to ultraviolet radiation. Long-term illumination causes desorption of oxygen molecules inside the TiO<sub>2</sub> material, which initiate the degradation of the perovskite layer [12–14]. In addition, FTO layer is characterized by relatively rough and non-uniform surface, which may lead to non-uniform deposition of cTiO<sub>2</sub> layer on FTO substrate. The latter causes the appearance of morphological defects in the perovskite layer deposited on top of FTO/cTiO<sub>2</sub> substrate, which also initiates rapid degradation of PSCs [12, 13]. In the literature, attempts to reduce the degradation effects in PSCs by applying CH<sub>3</sub>NH<sub>3</sub>PbI<sub>3</sub> layer directly to the FTO coating were described, but this led to the decrease in PCE values [15, 16]. Thus, nowadays an important task for PSC improvement is to find new materials suitable for use in planar PSC as a buffer layer that do not contribute to the degradation of perovskite material.

In this work, a highly stable inorganic material such as double perovskite oxide La<sub>2</sub>NiMnO<sub>6</sub> (LNMO) was first used as a buffer layer in planar PSCs. The LNMO thin films on glass substrates were obtained by spin coating and were

investigated using optical spectroscopy and X-ray diffraction techniques, as well as atomic force microscopy (AFM). Planar PSCs with the architecture of glass/FTO/LNMO/ $\text{CH}_3\text{NH}_3\text{PbI}_3$ /Spiro-MeOTAD/Au were fabricated under ambient conditions at high humidity level ( $\sim 50\%$ ) and their photovoltaic (PV) parameters were measured. The data obtained demonstrate a new approach to PSCs optimization for long-term operation in outdoor conditions.

## 2. Experimental

### 2.1. Buffer layer preparation

The appropriate amounts of  $\text{La}(\text{NO}_3)_3 \cdot 6\text{H}_2\text{O}$ ,  $\text{Ni}(\text{NO}_3)_2 \cdot 6\text{H}_2\text{O}$  and  $\text{Mn}(\text{NO}_3)_2 \cdot 6\text{H}_2\text{O}$  powders were dissolved in a mixture of 2-ethoxyethanol and acetic acid (4:1 v/v) to obtain 0.3 M stock solution. The LNMO thin films were obtained by spin coating of the stock solution on the surface of non-conductive glass substrates (3000 rpm, 30 s), followed by annealing at 550 – 650 °C during 2 hrs in the muffle furnace. The obtained LNMO thin films were used for XRD, AFM and optical measurements. LNMO-based buffer layers were deposited on the FTO-glass substrates following the same spin coating and annealing protocols using the 5-fold diluted stock solution and were used further for PSCs fabrication. FTO glass substrates coated by  $\text{cTiO}_2$  layer were obtained following the technique described in [17].

### 2.2. Device fabrication

Planar PSCs were fabricated under ambient conditions at relatively high humidity level ( $\sim 50 - 60\%$ ) according to the procedure described in [18]. Perovskite ( $\text{CH}_3\text{NH}_3\text{PbI}_3$ ) layer was formed on the surface of LNMO layer using a conventional one-step deposition method [19]. A layer of Spiro-MeOTAD hole transport material was spin-coated onto the surface of the perovskite layer (3000 rpm, 20 s). The final stage of PSC fabrication was the deposition of  $\sim 50$ -nm thick Au contacts by vacuum thermal evaporation using the VUP-4 vacuum post. Schematic representation of the PSC architecture is illustrated in Fig. 1. The state-of-the-art planar PSCs were fabricated using FTO glass substrates coated by  $\text{cTiO}_2$  layer via the same technique as described above [18].

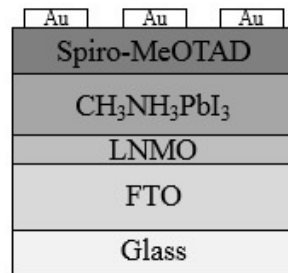


FIG. 1. Schematic representation of the planar PSC architecture

## 3. Characterization studies

The X-ray diffraction (XRD) measurements of LNMO thin films were provided using DRON-3M X-ray diffractometer with  $\text{Cu K}\alpha$  radiation ( $\lambda = 1.5405 \text{ \AA}$ ) as the X-ray source. Atomic force microscope (AFM) NTEGRA Prima (NT-MDT) with HA\_NC probes (TipsNano, resonant frequency 140 kHz, stiffness constant 3.5 N/m) was used to investigate the surface morphology and to evaluate average particle size in LNMO thin films. The optoelectronic properties of the LNMO layers were studied using UV-Vis spectrophotometer (Shimadzu UV-3600, Japan) with an ISR-3100 integrating sphere in the wavelength range of 300 – 1400 nm.

Photovoltaic (PV) characteristics of the developed PSCs were measured under standard illumination conditions ( $\text{AM1.5G}$ ,  $1000 \text{ W/m}^2$ ) by recording the current density-voltage (J–V) characteristics using Keithley 4200-SCS Semiconductor Characterization System (Keithley, USA) and Abet Technologies 10500 solar simulator with Xenon lamp (Abet, USA) as the light source. The PCE ( $\eta$ ) values of the PSCs were calculated from the J–V data using the known formula [20]:

$$\eta = \frac{J_{SC} \cdot V_{OC} \cdot FF}{P_{IN}} \cdot 100\%, \quad (1)$$

where  $J_{SC}$  – short-circuit current density,  $V_{OC}$  – open-circuit voltage,  $FF$  – fill factor and  $P_{IN}$  – incoming light intensity.

#### 4. Results and discussion

XRD patterns of the LNMO thin films deposited on non-conductive glass substrates and annealed at different temperatures (550 – 650 °C) are shown in Fig. 2(a). LNMO films obtained at 575 – 650 °C showed XRD reflexes corresponding to monoclinic, rhombohedral and orthorhombic phases of LNMO, confirming the triple phase structure of  $\text{La}_2\text{NiMnO}_6$  double perovskite oxides [21]. The absence of additional XRD peaks indicates the purity of the samples. In contrast, LNMO film obtained at 550 °C was found to possess amorphous structure.

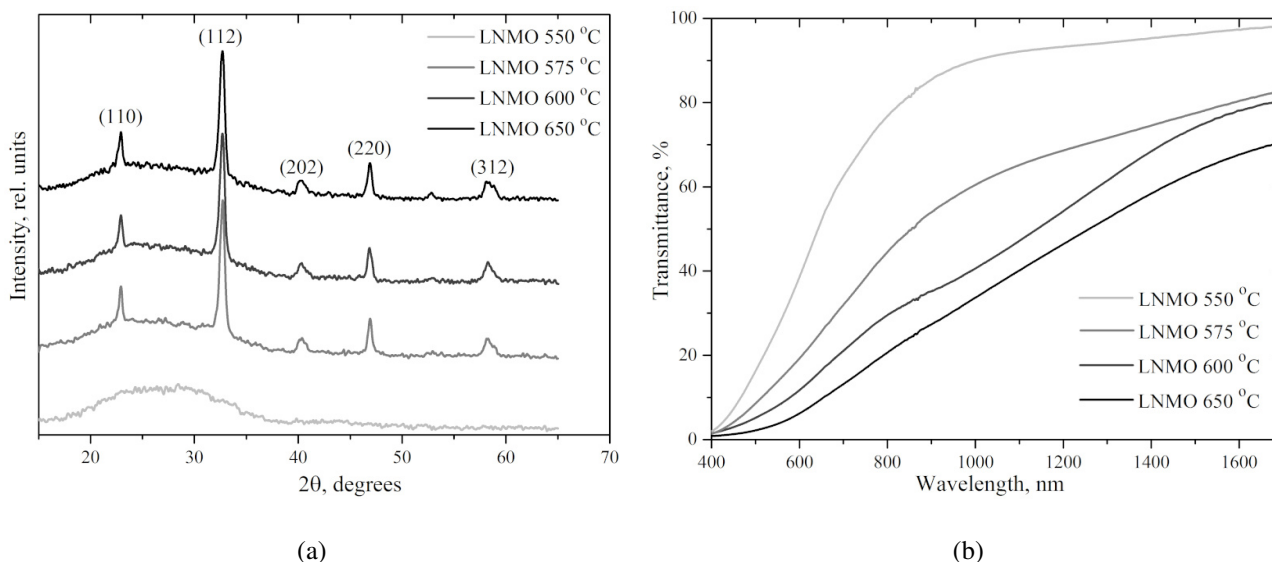


FIG. 2. XRD patterns (a) and transmittance spectra (b) of LNMO thin films, obtained at different annealing temperatures

Transmittance spectra for LNMO thin films deposited on the surface of non-conductive glass substrates is shown on Fig. 2(b). Using these data and Tauc equation for direct transitions, the energy bandgap ( $E_g$ ) values were obtained (Table 1) [22]. It can be seen that an increase in annealing temperature leads to a decrease in the  $E_g$  value for the studied LNMO layers from 1.75 to 1.04 eV. As a result, all LNMO samples possess semiconductor properties.

TABLE 1. The energy bandgap ( $E_g$ ) values calculated for LNMO thin films, obtained at different annealing temperatures ( $T$ )

$T$ , °C	550	575	600	650
$E_g$ , eV	1.75	1.50	1.05	1.04

AFM images of LNMO thin layers deposited on FTO glass substrates show that regardless of annealing temperature, fabricated layers are characterized by homogeneous structure with uniform particle distribution (Fig. 3). The average particle size determined using AFM was found to be around 60 – 70 nm. A comparison of the particle size (Fig. 3) and the crystallite size determined from data about the broadening of X-ray diffraction lines indicates that the particles are polycrystalline, consisting of crystallites  $15 \pm 2$  nm in size.

The LNMO thin films fabricated on the surface of FTO conductive glasses were used for fabrication of planar PSCs with the architecture of FTO/LNMO/ $\text{CH}_3\text{NH}_3\text{PbI}_3$ /Spiro-OMeTAD/Au under ambient conditions. State-of-the-art planar PSC with  $\text{cTiO}_2$  layer was constructed for providing comparative analysis. J–V curves recorded under standard illumination ( $1000 \text{ W/m}^2$ , AM1.5G) for PSCs with LNMO and  $\text{cTiO}_2$  layers are shown in Fig. 4(a). The PV parameters for all PSCs are listed in Table 2. It can be seen that the PSCs with LNMO layers demonstrated PCE values (10 – 11 %) comparable to the efficiency obtained for conventional  $\text{TiO}_2$ -based PSCs (Table 2). The highest PCE was observed for the PSC samples with LNMO thin films prepared at annealing temperature 600 °C. The results confirm that LNMO materials can be successfully used as buffer layers in planar PSCs.

PV parameters of planar PSCs with LNMO and  $\text{cTiO}_2$  layers were investigated during long-term storage under ambient conditions. The data obtained (Fig. 4(b)) revealed that PSCs with LNMO-based buffer layer demonstrate more stable behavior than PSCs with  $\text{cTiO}_2$  layer. Thus when PSCs were exposed under ambient conditions for 35 days, PCE for PSC with LNMO thin film was almost unchanged, while PCE for  $\text{cTiO}_2$ -PSC decreased more than 60 %.

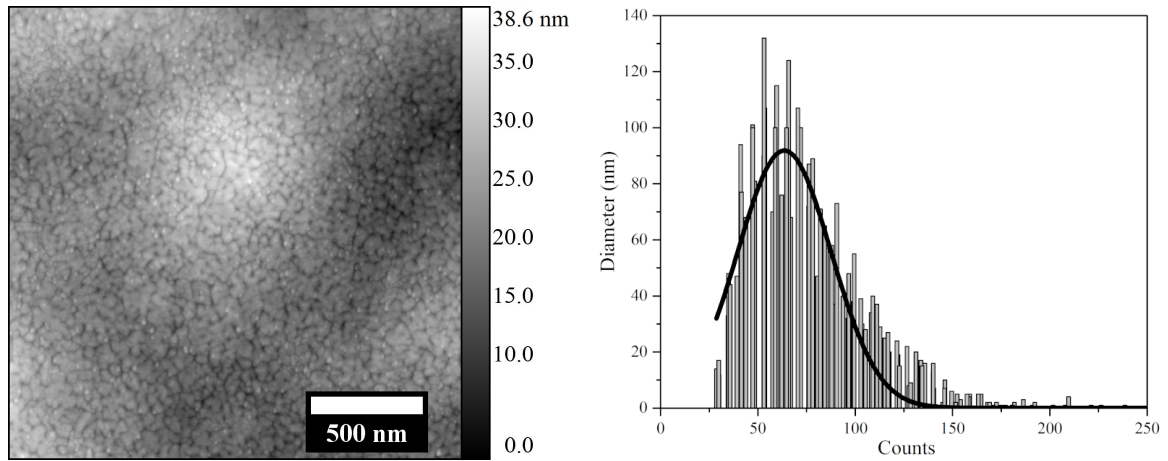


FIG. 3. AFM surface image (left) and particle size distribution (right) for LNMO thin layer obtained at 600 °C

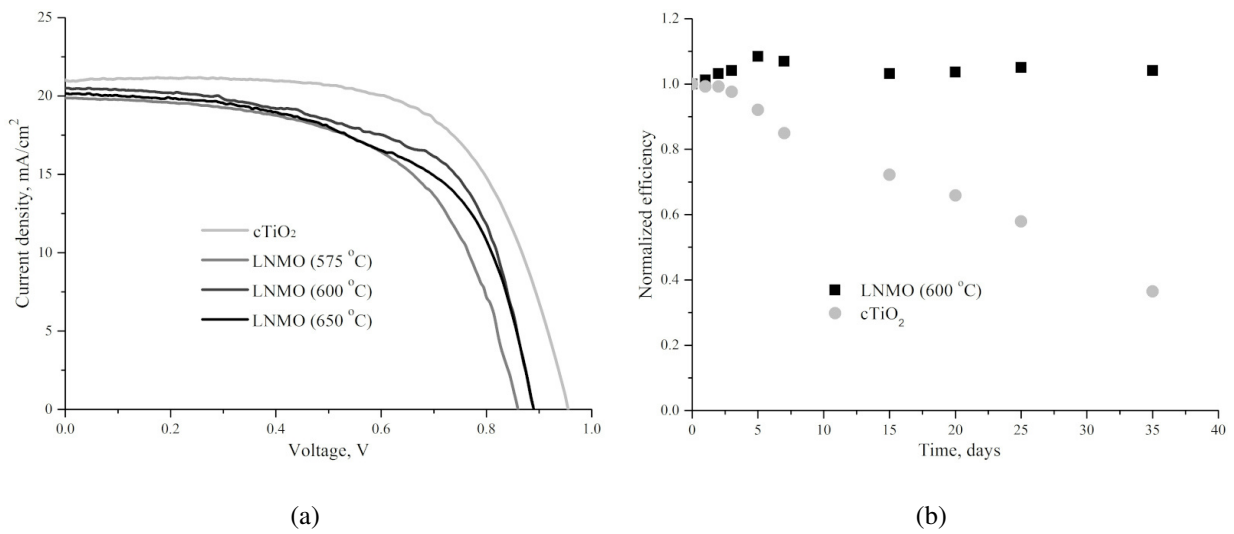


FIG. 4. J–V curves (a) and stability test (b) for PSCs under standard illumination ( $1000 \text{ W/m}^2$ , AM1.5G)

TABLE 2. The PV parameters for PSCs under standard illumination ( $1000 \text{ W/m}^2$ , AM1.5G)

Sample	$J_{SC}$ , $\text{mA/cm}^2$	$V_{OC}$ , V	$FF$ , a.u.	$\eta$ , %
PSC with $\text{cTiO}_2$	21.0	0.96	0.65	12.6
PSC with LNMO 575 °C	19.3	0.86	0.58	10.0
PSC with LNMO 600 °C	20.5	0.89	0.62	11.4
PSC with LNMO 650 °C	20.2	0.89	0.58	10.5

Summing up, it was shown that  $\text{La}_2\text{NiMnO}_6$  (LNMO) double perovskite oxide thin films demonstrate semiconductor properties and their optoelectronic characteristics including bandgap values could be easily tuned by changing the synthesis conditions, namely, the annealing temperature.  $\text{La}_2\text{NiMnO}_6$ -based thin films were successfully used as buffer layers in planar PSCs, showing PCE values comparable with those obtained for conventional  $\text{TiO}_2$ -based PSCs. Due to the high stability of LNMO double perovskite oxides towards moisture and oxygen, incorporation of LNMO buffer layer in PSCs architecture allowed to significantly increase the stability of planar PSCs under ambient conditions as compared to  $\text{TiO}_2$ -based PSCs behavior.

## 5. Conclusions

Thin films of  $\text{La}_2\text{NiMnO}_6$  (LNMO) double perovskite oxide were synthesized on the glass substrates via spin coating and were first used as buffer layers in planar PSCs. LNMO thin films revealed higher homogeneity and stability in comparison with the state-of-the-art  $\text{cTiO}_2$  layers. The optical and photoelectrical properties of LNMO layers can be tuned by changing the annealing temperature. Planar PSCs with the architecture of FTO/LNMO/ $\text{CH}_3\text{NH}_3\text{PbI}_3$ /Spiro-OMeTAD/Au were fabricated under ambient conditions. The maximum PCE value of 11.4 % under standard illumination conditions ( $\text{AM1.5G}$ ,  $1000 \text{ W/m}^2$ ) was obtained for PCE with LNMO buffer layer annealed at  $600^\circ\text{C}$  and was comparable to the PCE for PSCs with  $\text{cTiO}_2$  layer. The stability of PSCs based on LNMO buffer layer was significantly higher than the stability of PSCs with  $\text{cTiO}_2$  layer. The data obtained demonstrate a novel approach for optimization of PSCs designed for long-term operation in outdoor conditions.

## References

- [1] Kumar N.S., Naidu K.C.B. A review on perovskite solar cells (PSCs), materials and applications. *J. Materiomics*, 2021, **7**, P. 940–956.
- [2] Miah M.H., Rahman M.B., Nur-E-Alam M., Das N., Soin N.B., Hatta S.F.W.M., Islam M.A. Understanding the degradation factors, mechanism and initiatives for highly efficient perovskite solar cells. *Chem. Nano Mat.*, 2023, **9**, e202200471.
- [3] Green M.A., Dunlop E.D., Yoshita M., Kopidakis N., Bothe K., Siefert G., Hao X. Solar cell efficiency tables (version 62). *Prog. Photovolt. Res. Appl.*, 2023, **31**, P. 651–663.
- [4] Roy P., Kumar Sinha N., Tiwari S., Khare A. A review on perovskite solar cells: evolution of architecture, fabrication techniques, commercialization issues and status. *Sol. Energy*, 2020, **198**, P. 665–688.
- [5] Shao J.Y., Li D., Shi J., Ma C., Wang Y., Liu X., Jiang X., Hao M., Zhang L., Liu C., Jiang Y., Wang Z., Zhong Y.W., Liu S.F., Mai Y., Liu Y., Zhao Y., Ning Z., Wang L., Xu B., Meng L., Bian Z., Ge Z., Zhan X., You J., Li Y., Meng Q. Recent progress in perovskite solar cells: material science. *Sci. China Chem.*, 2023, **66**, P. 10–64.
- [6] Ahmed S.F., Islam N., Kumar P.S., Hoang A.T., Mofijur M., Inayat A., Shafiqullah G.M., Vo D.N., Badruddin I.A., Kamangar S. Perovskite solar cells: thermal and chemical stability improvement, and economic analysis. *Mater. Today Chem.*, 2023, **27**, 101284.
- [7] Zhuang J., Wang J., Yan F. Review on chemical stability of lead halide perovskite solar cells. *Nano-Micro Lett.*, 2023, **15**, 84.
- [8] Noh M.F.M., Teh C.H., Daik R., Lim E.L., Yap C.C., Ibrahim M.A., Ludin N.A., Yusoff Abd.R.M., Jange J., Teridi M.A.M. The architecture of the electron transport layer for a perovskite solar cell. *J. Mater. Chem. C*, 2018, **6**, P. 682–712.
- [9] Wang K., Olthof S., Subhani W. S., Jiang X., Cao Y., Duan L., Wang H., Du M., Liu S. F. Novel inorganic electron transport layers for planar perovskite solar cells: progress and prospective. *Nano Energy*, 2020, **68**, 104289.
- [10] Chowdhury T.A., Zafar M.A.B., Islam M.S., Shahinuzzaman M., Islam M.A., Khandaker M.U. Stability of perovskite solar cells: issues and prospects. *RSC Adv.*, 2023, **13**, P. 1787–1810.
- [11] Yang G., Tao H., Qin P., Ke W., Fang G. Recent progress in electron transport layers for efficient perovskite solar cells. *J. Mater. Chem. A*, 2016, **4**, P. 3970–3990.
- [12] Dipta S.S., Uddin A. Stability Issues of perovskite solar cells: a critical review. *Energy Technol.*, 2021, **9**, 2100560.
- [13] Zhao P., Han M., Yin W., Zhao X., Kim S.G., Yan Y., Kim M., Song Y. J., Park N.G., Jung H.S. Insulated interlayer for efficient and photostable electron-transport-layer-free perovskite solar cells. *ACS Appl. Mater. Interfaces*, 2018, **10**, P. 10132–10140.
- [14] Kozlova E.A., Valeeva A.A., Sushnikova A.A., Zhurenok A.V., Rempel A.A. Photocatalytic activity of titanium dioxide produced by high-energy milling. *Nanosystems: Phys. Chem. Math.*, 2022, **13**, P. 632–639.
- [15] Huang C., Lin P., Fu N., Liu C., Xu B., Sun K., Wang D., Zenga X., Ke S. Facile fabrication of highly efficient ETL-free perovskite solar cells with 20 % efficiency by defect passivation and interface engineering. *Chem. Commun.*, 2019, **55**, P. 2777–2788.
- [16] Isikgor F.H., Zhumagal S., Merino L.V.T., De Bastiani M., McCulloch I., De Wolf S. Molecular engineering of contact interfaces for high-performance perovskite solar cells. *Nat. Rev. Mater.*, 2023, **8**, P. 89–108.
- [17] Kozlov S.S., Alexeeva O.V., Nikolskaia A.B., Shevaleevskiy O.I., Averkiev D.D., Kozhuhovskaya P.V., Almjashaeva O.V., Larina L.L. Double perovskite oxides  $\text{La}_2\text{NiMnO}_6$  and  $\text{La}_2\text{Ni}_{0.8}\text{Fe}_{0.2}\text{MnO}_6$  for inorganic perovskite solar cells. *Nanosystems: Phys. Chem. Math.*, 2022, **13**, P. 314–319.
- [18] Nikolskaia A.B., Vildanova M.F., Kozlov S.S., Shevaleevskiy O.I. Physicochemical approaches for optimization of perovskite solar cell performance. *Russ. Chem. Bull.*, 2023, **69**, P. 1245–1252.
- [19] Nikolskaia A.B., Kozlov S.S., Karyagina O.K., Alexeeva O.V., Almjashaeva O.V., Averkiev D.D., Kozhuhovskaya P.V., Shevaleevskiy O.I. Cation doping of  $\text{La}_2\text{NiMnO}_6$  complex oxide with the double perovskite structure for photovoltaic applications. *Russ. J. Inorg. Chem.*, 2022, **67**, P. 921–925.
- [20] Han G., Zhang S., Boix P.P., Wong L.H., Sun L., Lien S.-Y. Towards high efficiency thin film solar cells. *Progr. Mater. Sci.*, 2017, **87**, P. 246–291.
- [21] Sheikh M.S., Sakhya A.P., Dutta A., Sinha T.P. Light induced charge transport in  $\text{La}_2\text{NiMnO}_6$  based Schottky diode. *J. Alloy. Comp.*, 2017, **727**, P. 238–245.
- [22] Tauc J., Grigorovici R., Vancu A. Optical properties and electronic structure of amorphous germanium. *Phys. Status Solidi*, 1966, **15**, P. 627–637.

*Information about the authors:*

*Sergey S. Kozlov* – Emanuel Institute of Biochemical Physics, Russian Academy of Sciences, Kosygin St., 4, Moscow, 119334, Russia; ORCID 0000-0002-8660-5646; sergeykozlov1@gmail.com

*Anna B. Nikolskaia* – Emanuel Institute of Biochemical Physics, Russian Academy of Sciences, Kosygin St., 4, Moscow, 119334, Russia; ORCID 0000-0002-7430-4133; anickolskaya@mail.ru

*Olga K. Karyagina* – Emanuel Institute of Biochemical Physics, Russian Academy of Sciences, Kosygin St., 4, Moscow, 119334, Russia; ORCID 0000-0002-6702-5195; olgakar07@mail.ru

*Ekaterina K. Kosareva* – N. N. Semenov Federal Research Center for Chemical Physics, Russian Academy of Science, Kosygin St., 4, Moscow, 119991, Russia; ORCID 0000-0001-8090-2052; catherine.kos@yandex.ru

*Olga V. Alexeeva* – Emanuel Institute of Biochemical Physics, Russian Academy of Sciences, Kosygin St., 4, Moscow, 119334, Russia; ORCID 0000-0001-8982-3959; alexol@yandex.ru

*Vasilisa I. Petrova* – Emanuel Institute of Biochemical Physics, Russian Academy of Sciences, Kosygin St., 4, Moscow, 119334, Russia; ORCID 0009-0001-6357-2052; balagur.sh@yandex.ru

*Oksana V. Almjashaeva* – St. Petersburg State Electrotechnical University “LETI”, Professora Popova St., 5, St. Petersburg, 197376, Russia; Ioffe Physical-Technical Institute, Russian Academy of Sciences, Politekhnikeskaya St., 26, St. Petersburg, 194021, Russia; ORCID 0000-0002-6132-4178; almjashaeva@mail.ru

*Oleg I. Shevaleevskiy* – Emanuel Institute of Biochemical Physics, Russian Academy of Sciences, Kosygin St., 4, Moscow, 119334, Russia; ORCID 0000-0002-8593-3023; shevale2006@yahoo.com

*Conflict of interest:* the authors declare no conflict of interest.

## Evaluation of the electrochemical active surface area for carbon felt and nanostructured Ni coatings as electrocatalysts for hydrogen evolution reaction

Dmitry S. Dmitriev, Maksim I. Tenevich

Ioffe Institute, St. Petersburg, Russia

Corresponding author: Dmitry S. Dmitriev, [elchemorg@gmail.com](mailto:elchemorg@gmail.com)

PACS 82.45.Rr

**ABSTRACT** This study is devoted to the evaluation of electrochemical active surface area (ECSA) for carbon felt used in various fields of electrochemical technology. For the evaluation, we used techniques based on Faraday's law, the Randles–Sevcik equation and the calculation of the electric double layer capacitance in the electrolyte with different pH value. The measurement results are consistent with each other and for neutral, acidic and alkaline medium, the ECSA value are 20 – 30, 30 – 40 and 50 – 90 cm<sup>2</sup> per 1 cm<sup>2</sup> of geometric surface, respectively. Based on the results, the synthesis of nanostructured nickel coatings on carbon felt with prior electrochemical activation was performed. The pre-treatment in 1M KOH vs 1 M Na<sub>2</sub>SO<sub>4</sub> reduces the crystallite size from 26 to 15 nm and increases the ECSA from 133 to 700 cm<sup>2</sup> per 1 cm<sup>2</sup> of geometric surface. These changes cause an improvement in other electrocatalytic features for hydrogen evolution reaction.

**KEYWORDS** carbon felt, electrochemical surface area, electrodeposition, voltammetry, double layer capacitance, Randles–Sevcik equation, nickel coating, hydrogen evolution reaction

**ACKNOWLEDGEMENTS** The authors express their gratitude to the Engineering Center of the St. Petersburg State Institute of Technology for the prompt possibility of performing studies on a scanning electron microscope

**FOR CITATION** Dmitriev D.S., Tenevich M.I. Evaluation of the electrochemical active surface area for carbon felt and nanostructured Ni coatings as electrocatalysts for hydrogen evolution reaction. *Nanosystems: Phys. Chem. Math.*, 2023, **14** (5), 590–600.

### 1. Introduction

The development of new electrode materials is carried out in all fields of electrochemical technology from electrocatalysts of water splitting reactions to chemical current sources and supercapacitors. Currently, the use of porous carbon materials (fibers, felt) as a substrate is popular. Carbon felt is a polyacrylonitrile (PAN) or viscose fiber that has been needle-punched to form a structure and carbonized at 1200 – 1600 °C or graphitized at 2000 – 2600 °C [1]. Carbon felt is widely used in redox-flow batteries [2–7], lithium-, sodium- and zinc-ion batteries [8–15], as well as in supercapacitors [16–21] and alternative energy storage and generation technologies [22–25]. Mingxing Wu et al. have shown that the inclusion of cobalt particles in carbon fibers [13] increases the efficiency of the zinc-air battery, and boron doping [16] improves their capacitive properties when used as supercapacitor electrodes. In addition, carbon fibers are used in the synthesis of electrocatalysts for the reaction of hydrogen, oxygen production and the Fenton process [26–34]. Paper [30] reports on the synthesis of rhenium disulfide nanosheets on the carbon fiber surface as an effective electrocatalyst of the hydrogen evolution reaction (HER) with overpotential values of 69 mV@ 10 mA·cm<sup>-2</sup> and Tafel slope of 90 mV·dec<sup>-1</sup>.

Unlike a metal substrate, carbon materials are economically and environmentally beneficial, more resource-intensive and can be removed thermally in the next, i.e. they are able to perform the role of templates [35–39]. This makes it possible to significantly increase the electrochemically active surface area of electrode materials, which has a positive effect on their functional features. Paweł Jakobczyk et al. [38] have shown that thermal and chemical modification of the carbon felt surface improves its catalytic properties in the acetaminophen degradation reaction. The authors of [26] declare the successful use of modified carbon felt as a cathode in the Fenton process for the removal of tetracycline. Modification was carried out together by chemical and thermal methods. This allowed one to reduce the relative concentration of tetracycline during the Fenton process by two times. In paper [36], we previously showed that the use of carbon felt as a template makes it possible to obtain copper microtubes with a lower overpotential of HER.

However, the authors using carbon felt in their research are often limited to their geometric (visible) surface area ( $S_{geo}$ , cm<sup>2</sup>) or report the surface area of the final material after activation or modification of the fiber. In the datasheet of carbon felt from various manufacturers, approximate values of the surface area are given, usually estimated by the method of low-temperature adsorption calculated using the Brunauer–Emmett–Teller (BET) method [40–48]. These values do not always correspond to the electrochemical active surface area obtained by electrochemical methods [1, 49–51]. The value of the specific surface area ( $A_m$ , m<sup>2</sup>g<sup>-1</sup>) obtained by the BET method varies from 0.12 to 8 m<sup>2</sup>g<sup>-1</sup>. The most commonly mentioned value is 1.1 – 1.3 m<sup>2</sup>g<sup>-1</sup>. The results of ECSA obtained by electrochemical methods (from the

Randles–Sevcik and Cottrell equations) are also different and are given by the authors without taking into account mass, geometric surface or volume. On average, for a sample with a visible surface of  $10 \text{ cm}^2$ , the ECSA value is  $40 - 50 \text{ cm}^2$ .

In this paper, we have tried to evaluate the ECSA by three different electrochemical techniques: 1) on the basis of Faraday's law, measuring the thickness of nickel coatings obtained during coulostatic and galvanostatic modes of electroplating; 2) from calculating the value of electric double layer capacitance (EDLC), as the most common method due to its simplicity and clarity of the values obtained; and 3) from the Randles–Sevcik equation for single-electron redox process involving potassium ferrocyanide.

Based on the results, the synthesis of nanostructured nickel coatings on carbon felt with electrochemical surface pre-treatment in a neutral and alkaline medium was carried out. The electrocatalytic activity of these coatings was evaluated and the ECSA value was measured.

## 2. Experimental detail

### 2.1. Materials

The following materials and reagents were used in the study:

Carbon Felt (CF) (Beijing Great Wall Co., Ltd.), Nickel sulfate ( $\text{NiSO}_4 \times 7\text{H}_2\text{O}$ ), Sodium sulfate ( $\text{Na}_2\text{SO}_4 \times 10\text{H}_2\text{O}$ ), Boric acid ( $\text{H}_3\text{BO}_3$ ), Potassium chloride (KCl), Sulfuric acid ( $\text{H}_2\text{SO}_4$ ), Potassium hydroxide (KOH), Potassium ferrocyanide ( $\text{K}_4\text{Fe}(\text{CN})_6 \times 3\text{H}_2\text{O}$ ) from Nevareaktiv.

Platinum foil (Pt, 99.999 %), Copper wire (Cu, 99.999 %), Nickel plates (Ni, 99.99 %), Distilled water ( $\Omega = 18 \text{ MOhm}\cdot\text{cm}$ ) were also used in this work.

### 2.2. Experimental and measurement conditions

**2.2.1. Nickel electroplating.** Carbon felt ( $1.25 \times 0.5 \times 0.5 \text{ cm}$ ) with copper wire ( $d = 0.4 \text{ mm}$ ) as a collector was used for nickel electroplating. The geometric surface area was  $S_{geo} = 3 \text{ cm}^2$ . Electroplating was carried out in Watts electrolyte (Table 1) at the room temperature with a magnetic stirrer. Nickel plates with a working surface area of  $S_a = 10 \text{ cm}^2$  were used as anodes. The experiment was carried out in two series: with a fixed current value (30 mA) and with a constant amount of electricity (30 mA·h). In the both series, the process was performed for 0.5, 1, 2 hours.

TABLE 1. Electrolyte composition and nickel electroplating mode

Component	Concentration g/L
$\text{NiSO}_4 \times 7\text{H}_2\text{O}$	75
$\text{Na}_2\text{SO}_4 \times 10\text{H}_2\text{O}$	50
$\text{H}_3\text{BO}_3$	25
KCl	10
pH = $5.6 \pm 0.1$ ; $T = 25 \text{ }^\circ\text{C}$ ;	
1st series: $I = 30 \text{ mA}=\text{const}$ ; $t = 0.5, 1, 2 \text{ h}$ ;	
2nd series: $Q = It = 30 \text{ mA}\cdot\text{h}$ (15 mA·2 h, 30 mA·1 h, 60 mA·0.5 h)	

Before electrolysis, carbon felt was treated with ultrasound in ethanol for 10 minutes to degreasing, degassing and improving the wettability of surface. After electroplating, the samples were rinsed in warm ( $60 \text{ }^\circ\text{C}$ ) and room ( $25 \text{ }^\circ\text{C}$ ) distillate and dried at  $100 \text{ }^\circ\text{C}$  for 1 hour.

Weighing of samples (carbon felt + copper wire) for gravimetric analysis was performed before ultrasonic treatment ( $m_0$ ) and after drying ( $m_1$ ). The thickness of the synthesized coatings was measured using a scanning electron microscope TESCAN SEM with the VEGA 3 SBH microanalyzer.

In the second part of the study, nickel electrodeposition was performed with electrochemical pre-treatment of carbon felt in solutions of 1M  $\text{Na}_2\text{SO}_4$  and 1 M KOH for 10 min at a current density of  $10 \text{ mA}\cdot\text{cm}^{-2}$ . Next, the samples were rinsed in distillate and nickel electrodeposition was performed at a current density of  $10 \text{ mA}\cdot\text{cm}^{-2}$  for 1 hour. After that, the samples were rinsed in warm and room distillate and dried for 1 hour at  $100 \text{ }^\circ\text{C}$ . The synthesized coatings were labeled Ni@CF- $\text{Na}_2\text{SO}_4$  and Ni@CF-KOH, respectively.

**2.2.2. Voltammetric techniques.** Cyclic voltammetry (CVA) was executed in a three-electrode cell using a potentiostat-galvanostat ELINS P-45X equipped with a frequency response analyzer module FRA-24M. During the measurements, carbon felt samples with dimensions of  $2.75 \times 0.5 \times 0.5 \text{ (cm)}$  ( $S_{geo} = 6 \text{ cm}^2$ ) were used, mounted on a JJ110 sample holder with a platinum plate as a collector. The platinum plate ( $S = 1 \text{ cm}^2$ ) and Ag/AgCl ( $E_{\text{Ag}/\text{AgCl}}^0 = 0.194 \text{ V}$ , 3 M KCl) were counter and reference electrodes, respectively. The obtained polarization curves were converted to the scale of the normal hydrogen electrode (NHE):

$$E_{NHE} = E_{Ag/AgCl} + E_{Ag/AgCl}^0 \quad (1)$$

When measuring the capacitance of electric double layer, solutions of  $H_2SO_4$ ,  $Na_2SO_4$  and  $KOH$  with a concentration of 1 M were used as electrolytes. The mass of the sample was  $m = 70$  mg. Previously, the sample was treated with ultrasound in ethanol for 10 minutes to degreasing, degassing and improving the wettability of surface. The solution was stirred using a magnetic stirrer. Measurements were performed from the open circuit potential (OCP) to the potential corresponding to overpotential of HER  $dE_{HER} = -400$  mV. Scanning rates ( $v$ ) were 10, 20, 40, 60, 80, 100  $mV \cdot s^{-1}$ .

To study the redox reaction



a solution of 0.005 M  $K_4Fe(CN)_6$  + 0.1 M  $KCl$  was used as the electrolyte. The mass of the sample in this test was  $m = 78$  mg. Measurements were carried out starting from the OCP to the anode side. The range of scanning potentials was from  $-200$  to  $800$  mV vs  $Ag/AgCl$ . Scanning rates ( $v$ ) were 10, 20, 40, 60, 80, 100  $mV \cdot s^{-1}$ .

**2.2.3. Characterization of pre-treated nickel coatings.** The structure and morphology of the synthesized samples were studied using a scanning electron microscope TESCAN SEM with the VEGA 3 SBH microanalyzer (EDX-mapping). XRD analysis was performed on a Rigaku SmartLab III diffractometer (CuK $\alpha$  radiation,  $\lambda = 0.15405$  nm).

The electrocatalytic properties of  $Ni@CF-Na_2SO_4$  and  $Ni@CF-KOH$  were evaluated by the CVA with the determination of Tafel slope, ECSA and the turnover frequency (TOF). The methodology and equipment used are similar to paragraph 2.2.2.

### 2.3. Calculation methods

**2.3.1. The ECSA from Faraday's Law ( $A_{ED}$ ).** The calculation of the ECSA value from the thickness of electrodeposited nickel was carried out in two steps. Initially, a selection of values was collected from the coating thicknesses in the SEM images (Fig. A1, Appendix). The average number of values in the selection for each sample was 35. Further, the values were statistically processed to determine the absolute and relative ( $\varepsilon$ ) errors (probability  $P = 0.99$ ). At the second step, the values obtained for the samples synthesized in the coulostatic mode were compared with each other, and for the samples electrodeposited in the galvanostatic mode, a graphical dependence of the coating thickness on the electrolysis time was constructed.

According to Faraday's law

$$m = q_{Ni} \cdot Q \cdot FE, \quad (2)$$

$$\rho A_w H = q_{Ni} \cdot It \cdot FE, \quad (3)$$

$$H(t) = \frac{q_{Ni} \cdot I \cdot FE}{\rho A_w} \cdot t, \quad (4)$$

$$H(t) = n \cdot t; \quad n = \frac{q_{Ni} \cdot I \cdot FE}{\rho A_w}, \quad (5)$$

where  $m$  is the mass of deposited nickel (g),  $q_{Ni}$  is the electrochemical equivalent of the nickel plating process ( $gA^{-1}h^{-1}$ ),  $Q$  is the amount of electricity (C),  $FE$  is the Faraday efficiency,  $\rho_{Ni}$  is the nickel density ( $gcm^{-3}$ ),  $A_w$  is the working surface area ( $cm^2$ ),  $H$  is the coating thickness (cm),  $I$  is the current (A),  $t$  is the electrolysis time (h). Hence the working surface  $A_w$  is as follows

$$A_w = \frac{q \cdot I \cdot FE}{\rho \cdot n}, \quad (6)$$

and the specific value of ECSA:

$$A_{ED} = \frac{A_w}{S_{geo}}. \quad (7)$$

**2.3.2. The ECSA from EDLC value ( $A_{DL}$ ).** To calculate the EDLC, a graph was plotted in the coordinates  $\Delta_j = f(v)$ , where

$$\Delta_j = \frac{|j_a + j_c|}{2}, \quad (8)$$

$\Delta_j$  is the arithmetic mean of the anode ( $j_a$ ) and cathode ( $j_c$ ) current densities ( $mA \cdot cm^{-2}$ ).

The EDLC ( $C_{dl}$ ) was obtained from the slope of the approximation line. Further, the specific value of ECSA was calculated according to the expression

$$A_{DL} = \frac{C_{dl}}{C^*}, \quad (9)$$

where  $C^* = 0.08$   $mF \cdot cm^{-2}$  is the specific value of the capacitance on a porous, highly active and inhomogeneous surface.

2.3.3. *The ECSA from Randles–Sevcik equation ( $A_{RS}$ ).* To determine the specific value of ECSA during CVA in a solution of 0.005 M  $K_4Fe(CN)_6$  + 0.1 M KCl, a graphical dependence  $j_{pa,geo} - (v)^{0.5}$  was constructed, according to the Randles–Sevcik equation

$$j_{pa,geo} = 2.69 \times 10^5 A_{RS} C_{ox} n^{1.5} D^{0.5} v^{0.5}, \quad (10)$$

$$j_{pa,geo} = k \cdot v^{0.5}; \quad k = 2.69 \times 10^5 A_{RS} C_{ox} n^{1.5} D^{0.5}, \quad (11)$$

where  $j_{pa,geo}$  is anodic peak current density (per geometric surface) ( $A \cdot cm^{-2}$ ),  $2.69 \cdot 10^5$  is the constant of the Randles–Sevcik equation ( $C \cdot mole^{-1} \cdot V^{-0.5}$ ),  $A_{RS}$  is the electrochemical active surface area ( $cm^2$  per  $1 cm^2$  geometric),  $C_{ox}$  is the concentration of the oxidized form ( $mole \cdot cm^{-3}$ ),  $n$  is the number of electrons involved in the reaction,  $D$  is the diffusion coefficient ( $cm^2 s^{-1}$ ),  $v$  is the scanning rate ( $V \cdot s^{-1}$ ).

From the slope value ( $k$ ) of the linear approximation, the specific value of ECSA was calculated by the following expression

$$A_{RS} = \frac{k}{2.69 \cdot 10^5 \cdot C_{ox} \cdot n^{1.5} \cdot D^{0.5}}. \quad (12)$$

### 3. Results and discussion

#### 3.1. Evaluation of the ECSA from coating thickness by Faraday's law

Table 2 presents the results of gravimetric analysis for carbon felt samples and the average Faraday efficiency ( $\overline{FE}$ ) for the nickel electrodeposition process.

TABLE 2. Results of nickel electroplating

Sample	Current, mA	Time, h	$m_0$ , mg	$m_1$ , mg	$\Delta m$ , mg	$\Delta m_{teo}$ , mg	FE
Ni-30-0.5	30	0.5	106.3	121.8	15.5	16.4	0.94
Ni-30-1	30	1	104.4	134.5	30.1	32.9	0.92
Ni-30-2	30	2	108.0	172.0	64.0	65.7	0.97 $\overline{FE} = 0.95$
Ni-15-2	15	2	106.6	137.6	31.0	32.9	0.94
Ni-60-0.5	60	0.5	102.7	134.8	32.1	32.9	0.98

It can be noted that the process proceeds with high efficiency (95 %), the remaining 5 % of electricity is spent to the hydrogen evolution reaction on the forming coating surface. Fig. 1 shows the results of measuring the thickness of the coating during coulometric and galvanostatic electrodeposition of nickel on carbon felt.

In coulometric electrolysis, the thickness of the nickel coating is  $H_1 = 0.57 \pm 0.02$  microns ( $\varepsilon = 3.5\%$ ). When passing the same amount of electricity in galvanostatic mode, the nickel coating has a thickness of  $H_2 = 0.54 \pm 0.02$  microns ( $\varepsilon = 2.9\%$ ). The working surface areas, in this case, are equal

$$A_{w1} = \frac{q \cdot Q \cdot \overline{FE}}{\rho_{Ni} \cdot H_1} = \frac{1.095 \cdot 0.03 \cdot 0.95}{8.9 \cdot 0.57 \cdot 10^{-4}} = 62.2 \text{ cm}^2, \quad \Delta A_1 = \pm(62.2 \cdot 0.035) = \pm 2.2 \text{ cm}^2,$$

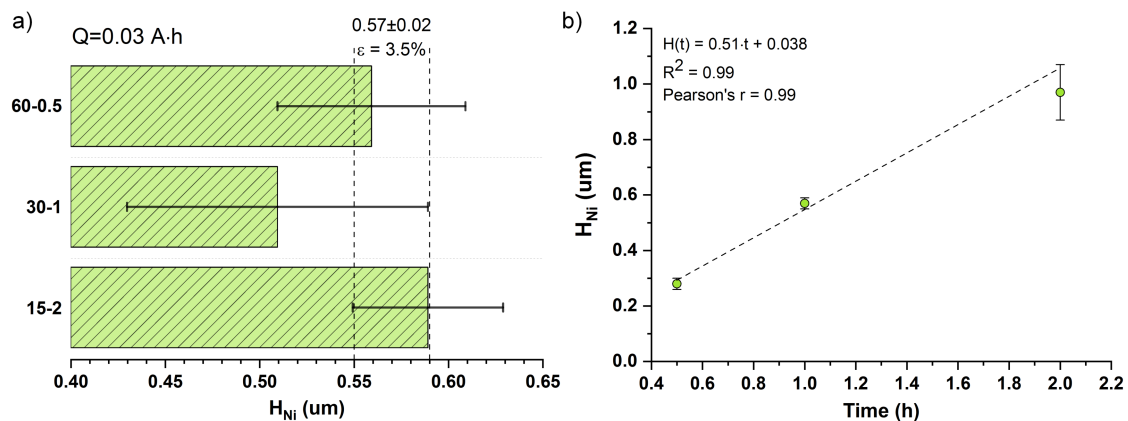


FIG. 1. Results of electroplating nickel in coulometric (a) and galvanostatic (b) modes

$$A_{w2} = \frac{q \cdot Q \cdot \overline{FE}}{\rho_{Ni} \cdot H_2} = \frac{1.095 \cdot 0.03 \cdot 0.95}{8.9 \cdot 0.54 \cdot 10^{-4}} = 65.6 \text{ cm}^2, \quad \Delta A_2 = \pm(65.6 \cdot 0.029) = \pm 1.9 \text{ cm}^2.$$

These values are overlapped in the region  $A_w = (64.05 \pm 0.35) \text{ cm}^2$ , and the specific ECSA value of the carbon felt during electrodeposition is

$$A_{ED} = \frac{A_w}{S_{geo}} = \frac{64.05}{3} = 21.35 \text{ cm}^2 \text{ per } 1 \text{ cm}^2 \text{ geometric.}$$

### 3.2. Evaluation of the ECSA from double layer capacitance

Determination of the ECSA from the value of EDL capacitance is one of classical methods. Fig. 2(a) shows the linear approximations in the coordinates  $\Delta j - v$ . The slope coefficient of these lines is numerically equal to the capacitance of double layer. Using expression (9), ECSA values for carbon felt in acidic, neutral and alkaline environments were calculated. From the presented histograms (Fig. 2(b)), we can conclude about the advantage of alkaline solutions when using carbon felt as an electrode material. The ECSA value in alkaline, acidic and neutral media is 95, 34.3 and 26.8  $\text{cm}^2$  per 1  $\text{cm}^2$  geometric. Presumably, this result is caused by the greater lyophilicity of the carbon filament in an alkaline medium compared to acidic and neutral media.

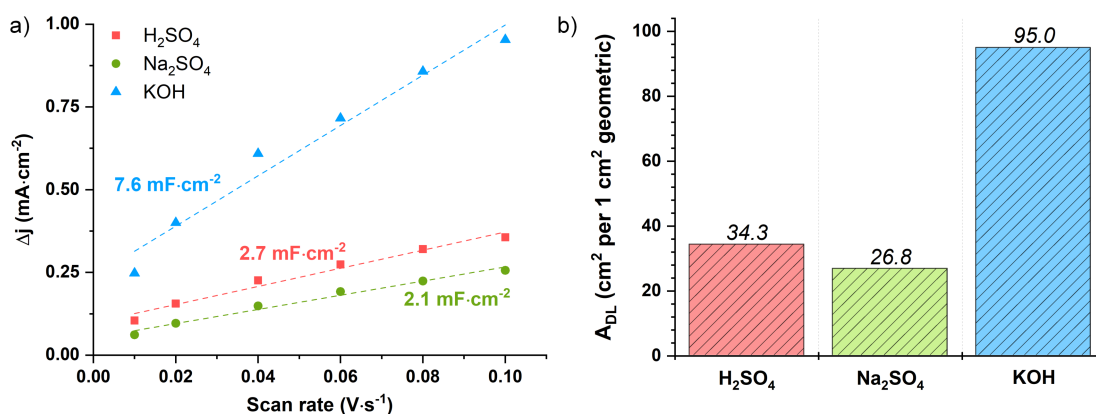


FIG. 2. Capacitance plot (a) and values of ECSA (b) for carbon felt in different electrolyte

It is worth noting that when using an acid solution as an electrolyte on the CVA curves (Fig. A2, Appendix), an anode peak is observed at a potential of  $E = 0.23 \text{ V}$  vs NHE, which corresponds to the oxidation of ethanol used in pre-preparation.

### 3.3. Evaluation of the ECSA from Randles–Sevcik equation

The results of processing CVA curves are shown in Fig. 3.

It can be seen from Fig. 3(a) that with increasing scanning rate, the process taking place on the electrode under study becomes less reversible or quasi-reversible. The probable cause may be diffusion control due to the porosity of the electrode, which makes it difficult for natural convection and the movement of reagents from the reaction zone into the bulk of the solution. This is confirmed by the slope of the linear approximation in  $\log(j_{geo}) - \log(v)$  coordinates

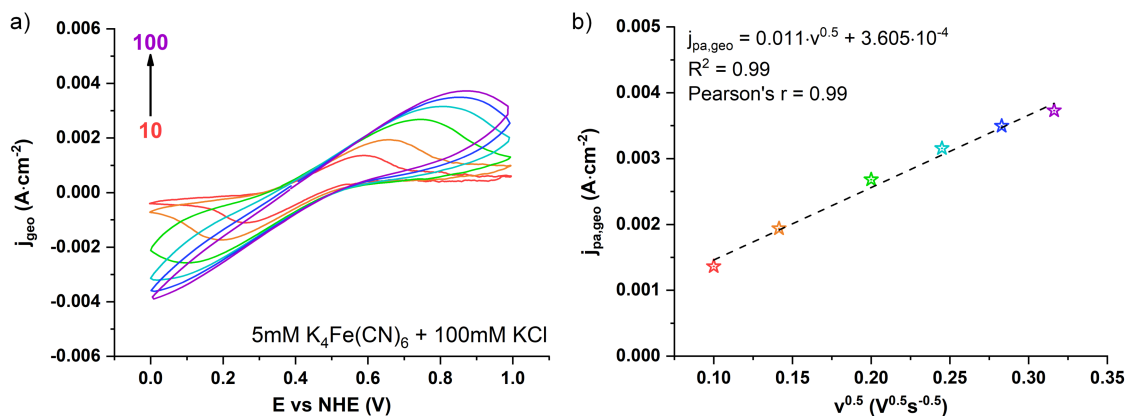


FIG. 3. CVA curves of  $[\text{Fe}(\text{CN})_6]^{4-}/[\text{Fe}(\text{CN})_6]^{3-}$  process (a) and the Randles–Sevcik plot (b)

(Fig. A3(a), Appendix) equal to  $m = 0.44$ . For reactions with diffusion limitations, it is as follows:  $m = 0.4 \pm 0.1$ . From the linear approximation in the coordinates  $j_{pa,geo} - v^{0.5}$ , the slope was determined for further calculation of the surface area (Fig. 3(b)). The ECSA value from the Randles–Sevcik equation is equal to

$$A_{RS} = \frac{0.011}{2.69 \cdot 10^5 \cdot 3.1 \cdot 10^{-7} \cdot 1^{1.5} \cdot (6.5 \cdot 10^{-6})^{0.5}} = 51.6 \text{ cm}^2 \text{ per } 1 \text{ cm}^2 \text{ geometric.}$$

The calculation used the effective concentration of the oxidized form obtained by integrating the polarization curve at the lowest scanning rate in I–t coordinates (Fig. A3(b), Appendix). As a result of diffusion limitations, the pH of the near-electrode region shifts to a slightly-alkaline range, which gives a higher ECSA value. This value is consistent with the one previously obtained in work [1].

### 3.4. Comparison of the evaluation results and the ECSA value for carbon felt

Table 3 summarizes the evaluation of ECSA values obtained by various electrochemical techniques.

TABLE 3. The ECSA values of carbon felt by various electrochemical techniques

Technique	ECSA, cm <sup>2</sup> per 1 cm <sup>2</sup> geometric
Faraday's law	21.4
	34.3 (pH < 7)
Double layer capacitance	26.8 (pH ≈ 7)
	95.0 (pH > 7)
Randles–Sevcik equation	51.6

As can be seen, the specific value of ECSA for carbon felt lies in the range from 20 to 100 cm<sup>2</sup> per 1 cm<sup>2</sup> geometric surface. The ECSA significantly depends on the pH electrolyte used, and for acidic and neutral media, its range of values is 20 – 40 cm<sup>2</sup> per 1 cm<sup>2</sup> geometric surface. In an alkaline media, activation of the surface is observed [32], as a result of which the area increases at least 8 – 10 times. Comparing the results of ECSA with the average values of the specific surface area for carbon felt measured by the BET method, it can be determined that the ECSA in acidic and neutral media is 0.1 – 0.3 m<sup>2</sup>g<sup>-1</sup>, and in alkaline it is 0.4 – 0.8 m<sup>2</sup>g<sup>-1</sup>. This is 1.5 – 4 times lower than the average value  $S_{BET} = 1.2 \text{ m}^2\text{g}^{-1}$ . This difference is, among other things, due to the low lyophilicity of carbon materials in aqueous electrolytes, as a result of which it is recommended to use surfactants, or to activate the surface by chemical and thermal methods.

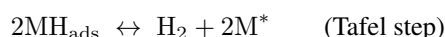
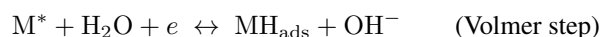
### 3.5. Effect of carbon felt pre-treatment on electrocatalytic features of nanostructured nickel coatings

Figure 4(a,b) shows the SEM results with mapping. It can be seen from the SEM images that the morphology of coating with pre-treatment in an alkaline solution differs significantly from a similar process in a neutral medium. The Ni@CF-KOH coating is not smooth, unlike Ni@CF-Na<sub>2</sub>SO<sub>4</sub>, has a distinct defect in the form of dendrites on surface.

The results of XRD analysis (Fig. 4(c)) demonstrate the presence of a carbon felt phase at 20 – 30 degrees and peaks corresponding to ICSD card No. 426960, which describes the cubic modification of nickel. According to calculations, the observed broadening for the characteristic nickel peaks (Fig. 4(d)) indicates a decrease in the crystallite sizes from 26.5 to 15.1 nm.

The results of electrocatalytic measurements for synthesized coatings are shown in Fig. 5. When using as an electrolyte for the pre-treatment of 1 M KOH instead 1 M Na<sub>2</sub>SO<sub>4</sub>, an improvement in the main electrocatalytic features of HER is observed.

Figure 5(a,b) demonstrates that the overpotential value shifts from –210 to –120 mV. At the same time, the absolute value of Tafel slope decreases. The value greater than 120 mVdec<sup>-1</sup> indicates a reaction mechanism with the presence of diffusion limitations, which corresponds to the Volmer–Tafel model:



The ECSA measurement shows a sharp increase in both the EDLC and the surface area value (Figs. 5(c) and A4). For Ni@CF-Na<sub>2</sub>SO<sub>4</sub> and Ni@CF-KOH, the ECSA value is 133 and 700 cm<sup>2</sup> per 1 cm<sup>2</sup> geometric surface, respectively. There was also an improvement in the coating efficiency from the results of TOF-test (Fig. 5(d)).

It can be seen that the electrochemical activation of carbon felt in an alkaline solution allows obtaining a more catalytically active surface both in terms of the value of surface area and improving kinetic parameters. All this results in a synergistic effect expressed by an increase in the total number of molecules transformations per unit surface per unit time.

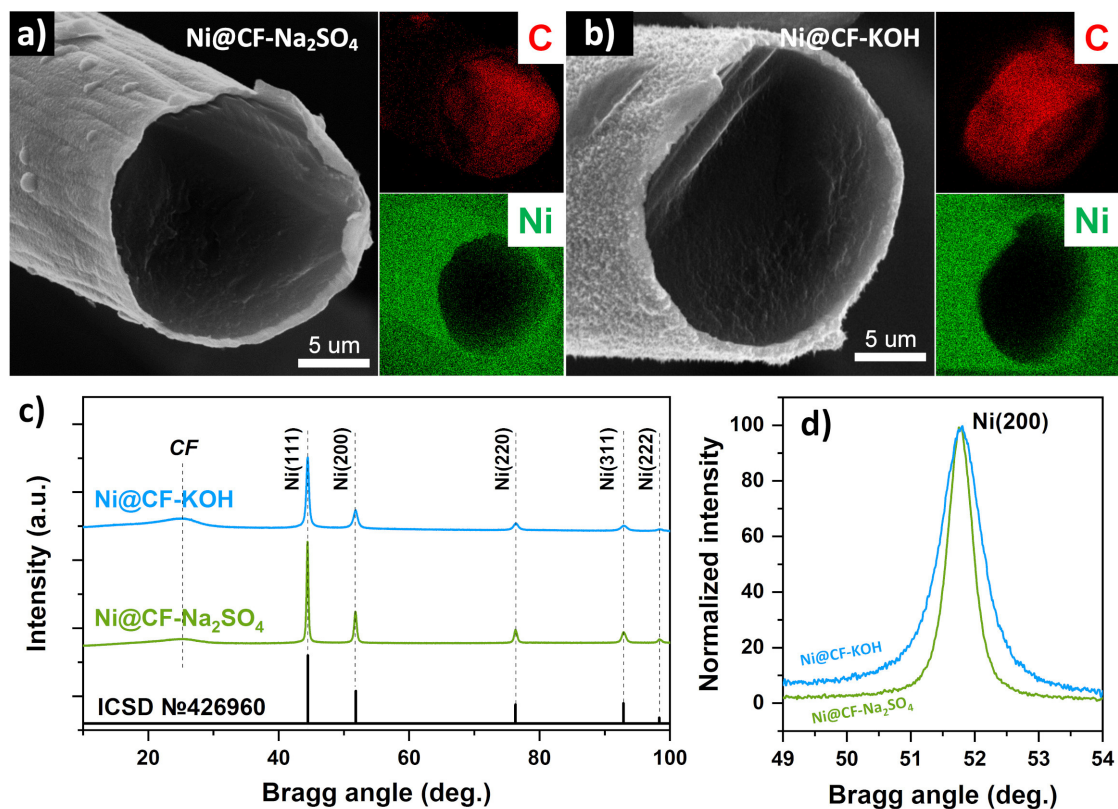


FIG. 4. SEM images (a, b) and XRD patterns (c, d) for synthesized samples

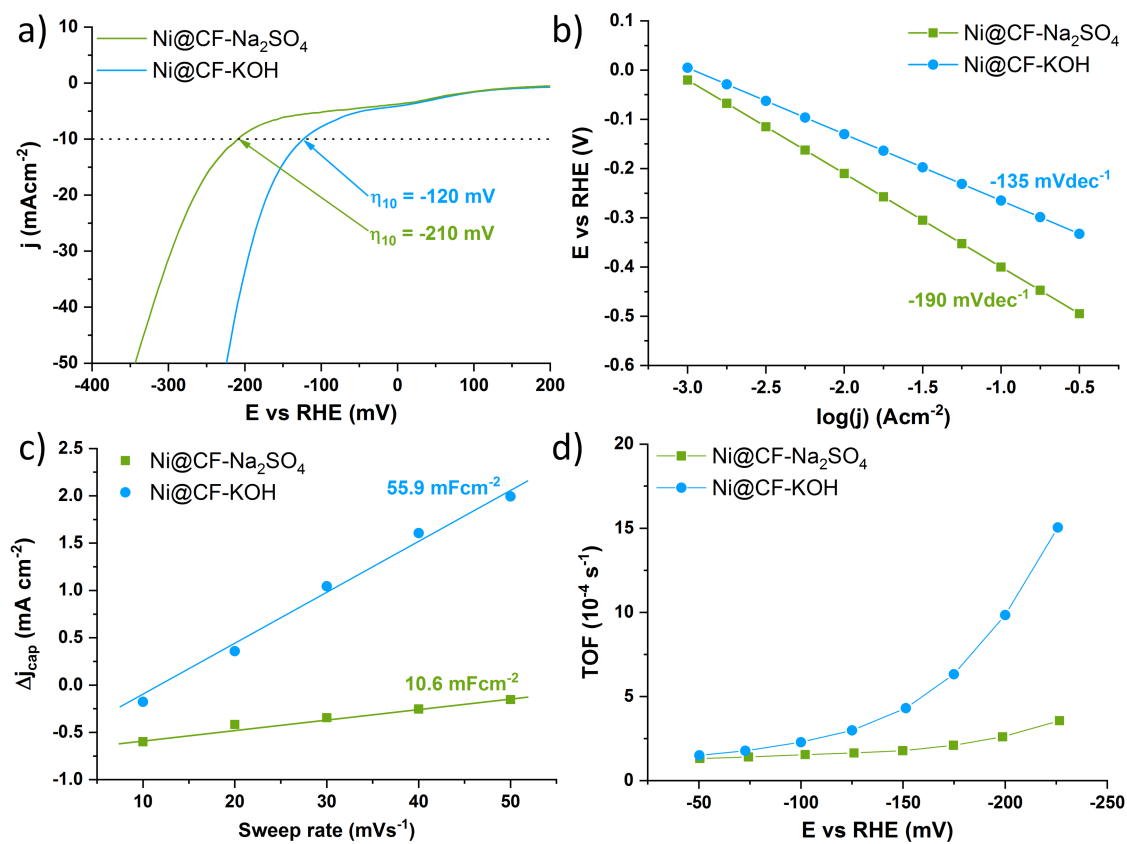


FIG. 5. LSV curves (a), Tafel plot (b), capacitance plot (c) and TOF result (d) for Ni@CF-Na<sub>2</sub>SO<sub>4</sub> and Ni@CF-KOH

#### 4. Conclusion

Based on the study results, it can be concluded that

- (i) The evaluation of ECSA by various techniques gives convergent results within 1 order of magnitude when using electrolytes with the same pH value.
- (ii) For a neutral medium, the ECSA of carbon felt can be assumed to be 20 – 30 cm<sup>2</sup> per 1 cm<sup>2</sup> geometric surface. For acidic and alkaline media, the ECSA value is 30 – 40 cm<sup>2</sup> and 50 – 100 cm<sup>2</sup> per 1 cm<sup>2</sup> geometric surface, respectively.
- (iii) When estimating the ECSA from the Randles–Sevcik equation, diffusion limitations are observed in the redox process. This shifts the pH of near-electrode layer to a slightly-alkaline range and overestimates the ECSA value of carbon felt.
- (iv) It is shown that the electrochemical activation of carbon felt in neutral and alkaline solutions allows the synthesis of nanostructured nickel coatings with a crystallite size of 26 and 15 nm, respectively.
- (v) Electrochemical pre-treatment of carbon substrate in 1 M KOH decreases the overpotential of HER and the Tafel slope for nickel coating to –120 mV and –135 mV·dec<sup>-1</sup>.

#### Appendix

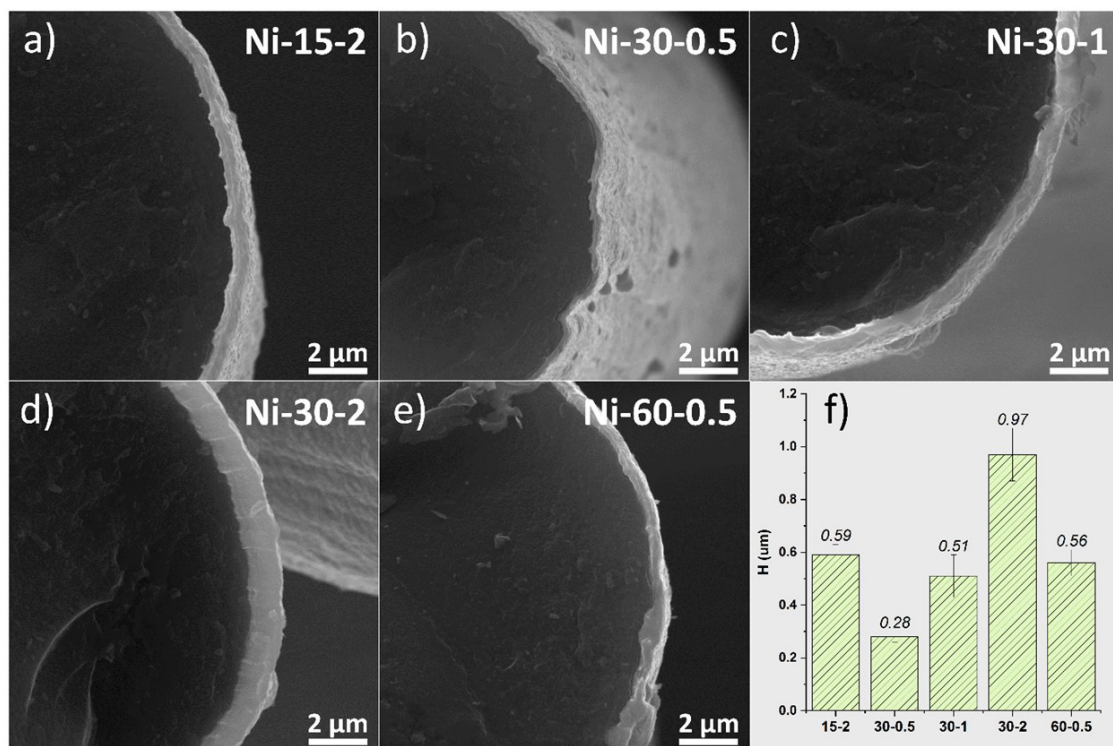


FIG. A1. SEM images of samples (a-e) and average coating thicknesses (e)

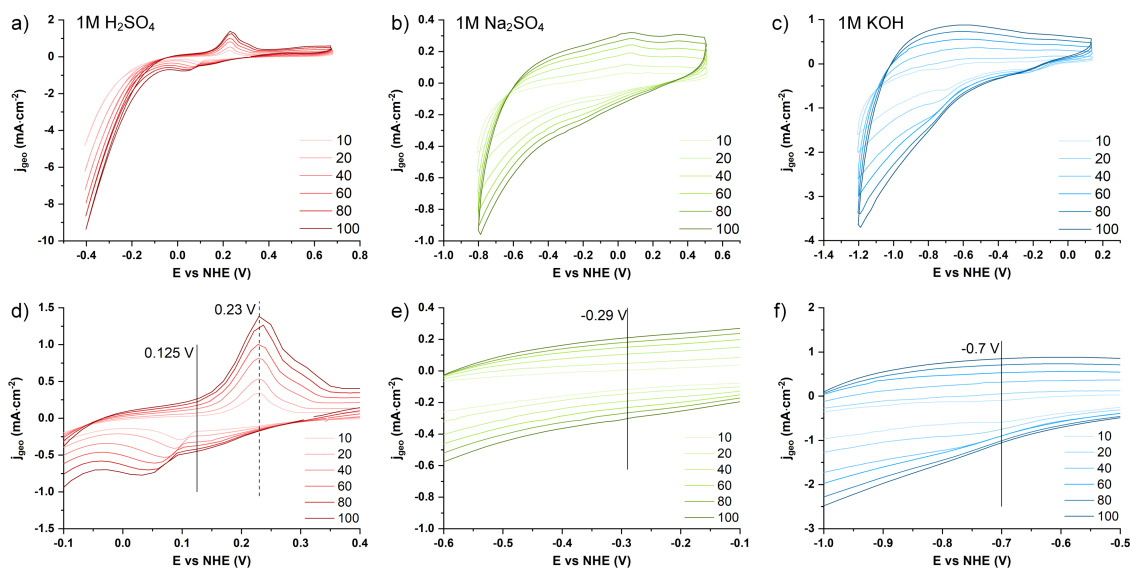


FIG. A2. CVA curves of carbon felt in 1 M H<sub>2</sub>SO<sub>4</sub> (a,d), 1 M Na<sub>2</sub>SO<sub>4</sub> (b,e), 1 M KOH (c,f)

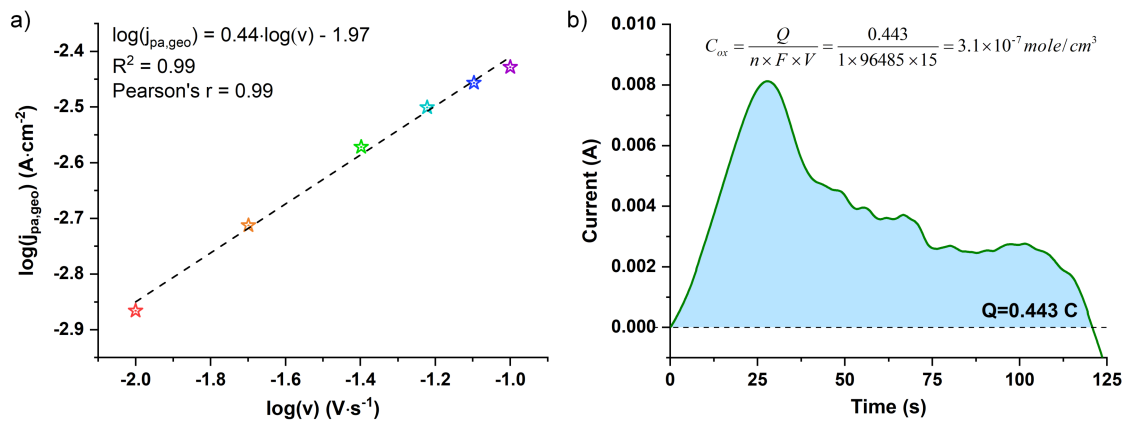


FIG. A3. Logarithmic plot (a) and  $I-t$  graph of  $[\text{Fe}(\text{CN})_6]^{4-}/[\text{Fe}(\text{CN})_6]^{3-}$  process ( $v = 10 \text{ mVs}^{-1}$ )

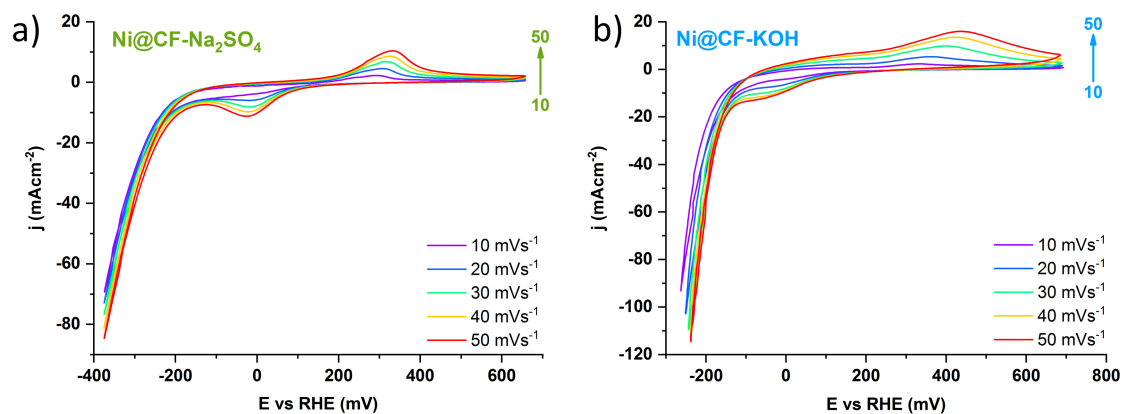


FIG. A4. CVA curves of Ni@CF-Na<sub>2</sub>SO<sub>4</sub> (a) and Ni@CF-KOH (b)

## References

- [1] Huong Le T.X., Bechelany M., Cretin M. Carbon felt based-electrodes for energy and environmental applications: A review. *Carbon N. Y.*, 2017, **122**, P. 564–591.
- [2] Uan J.Y., Chen Y.J., Hsu Y.H., Arpornwichanop A., Chen Y.S. Deposition of Li/Al layered double hydroxides on the graphite felts for the performance improvement of an all-vanadium redox flow battery. *Mater. Today Commun.*, 2021, **27**, 102280.
- [3] Kim M., Park J., Yeo G., Ko M., Jang H. Designing CNT-implanted graphite felt as a sustainable electron network for long-cycling of vanadium redox flow batteries. *Carbon N. Y.*, 2023, **206**, P. 1–6.
- [4] Abbas S., Lee H., Hwang J., Mehmood A., Shin H.-J., Mehboob S., Lee J.Y., Ha H.Y. A novel approach for forming carbon nanorods on the surface of carbon felt electrode by catalytic etching for high-performance vanadium redox flow battery. *Carbon N. Y.*, 2018, **128**, P. 31–37.
- [5] Moghim M.H., Eqra R., Babaiee M., Zarei-Jelyani M., Loghavi M.M. Role of reduced graphene oxide as nano-electrocatalyst in carbon felt electrode of vanadium redox flow battery. *J. Electroanal. Chem.*, 2017, **789**, P. 67–75.
- [6] Anarghya D., Anantha M.S., Venkatesh K., Santosh M.S., Priya M.G., Muralidhara H.B. Bermuda grass derived nitrogen-doped carbon as electrocatalyst in graphite felt electrode to increase the efficiency of all-iron redox flow batteries. *J. Electroanal. Chem.*, 2020, **878**, 114577.
- [7] León M.I., Arenas L.F., Walsh F.C., Nava J.L. Simulation of a vanadium-cerium redox flow battery incorporating graphite felt electrodes. *J. Electroanal. Chem.*, 2021, **903**, 115847.
- [8] Jin C.-B., Shi P., Zhang X.-Q., Huang J.Q. Advances in carbon materials for stable lithium metal batteries. *New Carbon Mater.*, 2022, **37**, P. 1–24.
- [9] Wang Y., Zhu M., Liu H., Zhang Y., Wu K., Wang G., Wu C. Carbon-based current collector materials for sodium metal anodes. *New Carbon Mater.*, 2022, **37**, P. 93–108.
- [10] Zhang J., Wang W., Shi R., Wang W., Wang S., Kang F., Li B. Three-dimensional carbon felt host for stable sodium metal anode. *Carbon N. Y.*, 2019, **155**, P. 50–55.
- [11] Watson V.G., Haynes Z.D., Telama W., Yeboah Y.D., Weatherspoon M.H., Zheng J.P., Kalu E.E. Electrochemical performance of heat treated SnO<sub>2</sub>-SnCu@C-Felt anode materials for lithium ion batteries. *Surfaces and Interfaces*, 2018, **13**, P. 224–232.
- [12] Gong Y., Xue Y. Carbon nanomaterials for stabilizing zinc anodes in zinc-ion batteries. *New Carbon Mater.*, 2023, **38**, P. 438–454.
- [13] Wu M., Tian X., Yang W., Guo B., Guo J. Co nanoparticles embedded in wheat-like porous carbon nanofibers as bifunctional electrocatalysts for rechargeable zinc-air batteries. *Electrochim. Acta*, 2022, **411**, 140090.
- [14] Chen W., Liu X., Wu J., Wang Q., Zhang Y., Yan S., Hou P., Luo S. Electrospun Fe<sub>1-x</sub>S@ nitrogen-doped carbon fibers as anode material for sodium-ion batteries. *J. Electroanal. Chem.*, 2023, **929**, 117095.
- [15] Peng J., Luo J., Li W., Zeng P., Wu Z., Wang Y., Li J., Shu H., Wang X. Insight into the performance of the mesoporous structure SiO<sub>x</sub> nanoparticles anchored on carbon fibers as anode material of lithium-ion batteries. *J. Electroanal. Chem.*, 2021, **880**, 114798.
- [16] Wu M., Zhao X., Gao J., Guo J., Xiao J., Chen R. Multifunctional boron-doped carbon fiber electrodes synthesized by electrospinning for supercapacitors, dye-sensitized solar cells, and photocapacitors. *Surfaces and Interfaces*, 2022, **31**, 101983.
- [17] Sawadsitang S., Duangchuen T., Karaphun A., Putjuso T., Kumnorkaew P., Swatsitang E. Synthesis, characterization and electrochemical properties of activated coconut fiber carbon (ACFC) and CuO/ACFC nanocomposites for applying as electrodes of supercapacitor devices. *Surfaces and Interfaces*, 2021, **25**, 101174.
- [18] Ye D., Yu Y., Tang J., Liu L., Wu Y. Electrochemical activation of carbon cloth in aqueous inorganic salt solution for superior capacitive performance. *Nanoscale*, 2016, **8**, P. 10406–10414.
- [19] Rodrigues A.C., da Silva E.L., Oliveira A.P.S., Matsushima J.T., Cuiña A., Marcuzzo J.S., Gonçalves E.S., Baldan M.R. High-performance supercapacitor electrode based on activated carbon fiber felt/iron oxides. *Mater. Today Commun.*, 2019, **21**, 100553.
- [20] Wang S., Liu Y., Wang Q., Liu P., Li L., Wang T. Fabrication of self-doped aramid-based porous carbon fibers for the high-performance supercapacitors. *J. Electroanal. Chem.*, 2022, **923**, P. 116829.
- [21] Zhang L., Yu X., Zhu P., Sun R., Wong C. Surface functional treatment of carbon fiber with ultra wide potential range in neutral electrolyte for high performance supercapacitor. *J. Electroanal. Chem.*, 2020, **876**, 114478.
- [22] Toyoda M., Inagaki M. Carbon materials for solar steam-generation. *Carbon N. Y.*, 2023, **214**, 118373.
- [23] Hidalgo D., Tommasi T., Bocchini S., Chiolerio A., Chiodoni A., Mazzarino I., Ruggeri B. Surface modification of commercial carbon felt used as anode for Microbial Fuel Cells. *Energy*, 2016, **99**, P. 193–201.
- [24] Zhuang H., Yang F. Vanadium metal-organic framework derived 2D hierarchical VO<sub>2</sub> nanosheets grown on carbon cloth for advanced flexible energy storage devices. *Surfaces and Interfaces*, 2021, **25**, 101232.
- [25] Xu H., Zhang M., Ma Z., Zhao N., Zhang K., Song H., Li X. Improving electron transport efficiency and power density by continuous carbon fibers as anode in the microbial fuel cell. *J. Electroanal. Chem.*, 2020, **857**, 113743.
- [26] Chen S., Tang L., Feng H., Zhou Y., Zeng G., Lu Y., Yu J., Ren X., Peng B., Liu X. Carbon felt cathodes for electro-Fenton process to remove tetracycline via synergistic adsorption and degradation. *Sci. Total Environ.*, 2019, **670**, P. 921–931.
- [27] Koca M.B., Gümüşgöz Çelik G., Kardeş G., Yazıcı B. NiGa modified carbon-felt cathode for hydrogen production. *Int. J. Hydrogen Energy*, 2019, **44**, P. 14157–14163.
- [28] Fan X., Ma Y., Sun A., Zhang X., Tang L., Guo J. Engineering heterogeneous nickel-iron oxide/iron phosphate on P, N co-doped carbon fibers for efficient oxygen evolution reaction in neutral and alkaline solutions. *Surfaces and Interfaces*, 2021, **25**, 101193.
- [29] Jin Y., Zhang T., Pan N., Wang S., Zhang B., Zhu X., Hao Y., Wang X., Song L., Zhang M. Surface functionalization of carbon cloth with conductive Ni/Fe-MOFs for highly efficient oxygen evolution. *Surfaces and Interfaces*, 2022, **33**, 102294.
- [30] Lee D.J., Kumar G.M., Sekar S., Ganesh V., Jeon H.C., Kim D.Y., Kang T.W., Ilanchezhiyan P. Re<sub>1-x</sub>Ni<sub>x</sub>S<sub>2</sub> nanosheets for high efficient electrocatalytic hydrogen evolution functions. *Surfaces and Interfaces*, 2023, **40**, 103014.
- [31] Dmitriev D.S., Tenevich M.I. Electrocatalytic performance of nickel coating on carbon felt with silver particles inclusions. *J. Taiwan Inst. Chem. Eng.*, 2022, **141**, 104591.
- [32] Ifires M., Addad A., Barras A., Hadjersi T., Chegroune R., Szunerits S., Boukherroub R., Amin M.A. Cathodic pre-polarization studies on the carbon felt/KOH interface: An efficient metal-free electrocatalyst for hydrogen generation. *Electrochim. Acta*, 2021, **375**, 137981.
- [33] García-Rodríguez O., Banuelos J.A., El-Ghenymy A., Godínez L.A., Brillas E., Rodríguez-Valadez F.J. Use of a carbon felt–iron oxide air-diffusion cathode for the mineralization of Malachite Green dye by heterogeneous electro-Fenton and UVA photoelectro-Fenton processes. *J. Electroanal. Chem.*, 2016, **767**, P. 40–48.
- [34] Liu L., Zhang D., Duan D., Li Y., Yuan Q., Chen L., Liu S. In situ fabrication of 3D self-supporting cobalt phosphate-modified graphite felt electrocatalysts for oxygen evolution reaction in neutral solution. *J. Electroanal. Chem.*, 2020, **862**, 114031.
- [35] Zhang G., Yu J., Su C., Di C., Ci S., Mou Y., Fu Y., Qiao K. The effect of annealing on the properties of copper-coated carbon fiber. *Surfaces and Interfaces*, 2023, **37**, 102630.

- [36] Dmitriev D.S., Martinson K.D., Popkov V.I. Electrochemical template synthesis of copper hollow microtubes with dendritic surface and advanced HER performance. *Mater. Lett.*, 2021, **305**, 130808.
- [37] Zhou Q., Li G., Qu Y., Zhou S., Xu W., Gao X., Yang F., Li R. Preparation and antioxidation of Cu–Sn composite coating on the surface of Cu-coated carbon fibers. *Surfaces and Interfaces*, 2022, **31**, 102016.
- [38] Jakóbczyk P., Skowierzak G., Kaczmarzyk I., Nadolska M., Wcislo A., Lota K., Bogdanowicz R., Ossowski T., Rostkowski P., Lota G., Ryl J. Electrocatalytic performance of oxygen-activated carbon fibre felt anodes mediating degradation mechanism of acetaminophen in aqueous environments. *Chemosphere*, 2022, **304**, 135381.
- [39] Dmitriev D.S., Tenevich M.I., Lobinsky A.A., Popkov V.I. Coaxial structures based on NiO/Ni@Carbon felt: Synthesis features, electrochemical behavior and application perspectives. *J. Electroanal. Chem.*, 2022, **911**, 116216.
- [40] Zhou H., Zhang H., Zhao P., Yi B. A comparative study of carbon felt and activated carbon based electrodes for sodium polysulfide/bromine redox flow battery. *Electrochim. Acta*, 2006, **51**, P. 6304–6312.
- [41] Jing M., Xu Z., Fang D., Fan X., Liu J., Yan C. Improvement of the Battery Performance of Vanadium Flow Battery by Enhancing the Specific Surface Area of the Carbon Felt Electrodes: II. Digging Effect. *J. Electrochem. Soc.*, 2021, **168**, 030539.
- [42] Su Y., Chen N., Ren H., Guo L., Li Z., Wang X. Preparation and Properties of Indium Ion Modified Graphite Felt Composite Electrode. *Front. Chem.*, 2022, **10**, P. 1–7.
- [43] Popat Y., Trudgeon D., Zhang C., Walsh F.C., Connor P., Li X. Carbon Materials as Positive Electrodes in Bromine-Based Flow Batteries. *Chempluschem*, 2022, **87**.
- [44] Jiang H.R., Shyy W., Wu M.C., Zhang R.H., Zhao T.S. A bi-porous graphite felt electrode with enhanced surface area and catalytic activity for vanadium redox flow batteries. *Appl. Energy*, 2019, **233–234**, P. 105–113.
- [45] Gautam R.K., Kapoor M., Verma A. Tactical Surface Modification of a 3D Graphite Felt as an Electrode of Vanadium Redox Flow Batteries with Enhanced Electrolyte Utilization and Fast Reaction Kinetics. *Energy & Fuels*, 2020, **34**, P. 5060–5071.
- [46] Noh T.H., Kim M.Y., Kim D.H., Yang S.H., Lee J.H., Park H.S., Noh H.S., Lee M.S., Kim H.S. Electrochemical studies of carbon felt electrode modified under airless conditions for redox flow batteries. *J. Electrochem. Sci. Technol.*, 2017, **8**, P. 155–161.
- [47] Zhou X., Zhang X., Lv Y., Lin L., Wu Q. Nano-catalytic layer engraved carbon felt via copper oxide etching for vanadium redox flow batteries. *Carbon N. Y.*, 2019, **153**, P. 674–681.
- [48] González-García J., Bonete P., Expósito E., Montiel V., Aldaz A., Torregrosa-Maciá R. Characterization of a carbon felt electrode: structural and physical properties. *J. Mater. Chem.*, 1999, **9**, P. 419–426.
- [49] Wang Y., Lin B. Enhancement of performance for graphite felt modified with carbon nanotubes activated by KOH as Cathode in electro-fenton systems. *J. Appl. Biomater. Funct. Mater.*, 2021, **19**, 228080002110053.
- [50] Rabbow T.J., Whitehead A.H. Deconvolution of electrochemical double layer capacitance between fractions of active and total surface area of graphite felts. *Carbon N. Y.*, 2017, **111**, P. 782–788.
- [51] Kato K., Kano K., Ikeda T. Electrochemical Characterization of Carbon Felt Electrodes for Bulk Electrolysis and for Biocatalyst-Assisted Electrolysis. *J. Electrochem. Soc.*, 2000, **147**, 1449.

---

*Submitted 7 September 2023; revised 5 October 2023; accepted 7 October 2023*

*Information about the authors:*

*Dmitry S. Dmitriev* – Ioffe Institute, 194021 Saint Petersburg, 26 Polytechnicheskaya street, Russian Federation; ORCID 0000-0002-7261-6694; elchemorg@gmail.com

*Maksim I. Tenevich* – Ioffe Institute, 194021 Saint Petersburg, 26 Polytechnicheskaya street, Russian Federation; ORCID 0000-0003-2003-0672; chwm420@gmail.com

*Conflict of interest:* the authors declare no conflict of interest.

## Growth of nanotextured thin films of GaInAsP and GaInAsSbBi solid solutions on GaP substrates by pulsed laser deposition

Alexander S. Pashchenko<sup>1,2,a,b</sup> Oleg V. Devitsky<sup>1,2,c</sup> Leonid S. Lunin<sup>1,2</sup>, Marina L. Lunina<sup>1</sup>, Olga S. Pashchenko<sup>1</sup>, Eleonora M. Danilina<sup>1</sup>

<sup>1</sup>Federal Research Center Southern Scientific Center of the Russian Academy of Sciences, Rostov-on-Don, Russia

<sup>2</sup>North Caucasian Federal University, Stavropol, Russia

<sup>a</sup>semicondlab@ya.ru, <sup>b</sup>as.pashchenko@gmail.com, <sup>c</sup>v2517@rambler.ru

Corresponding author: Alexander S. Pashchenko, [semicondlab@ya.ru](mailto:semicondlab@ya.ru), [as.pashchenko@gmail.com](mailto:as.pashchenko@gmail.com)

PACS 68.35.Ct, 68.55.Jk, 81.15.-z, 81.15.Cd

**ABSTRACT** GaInAsP and GaInAsSbBi solid solutions were grown on GaP (111) substrates by pulsed laser deposition using a laser fluence of 2.3 J/cm<sup>2</sup>. Energy Dispersive X-ray microanalysis, atomic force microscopy, and Raman spectroscopy were used for analysis of the elemental composition and study of the surface morphology and chemical bonds of the obtained solid solutions. It was found that at constant growth temperature and the fluence of 2.3 J/cm<sup>2</sup>, the elemental composition of the film has a significant effect on the growth kinetics. Surface-active elements (Sb and Bi) in the composition of the solid solution lead to a change in the surface diffusion of In and Ga, which is accompanied by a decrease in roughness. It was established that the films growth in the Volmer–Weber mode. The grown films are nanotextured with a predominant orientation in the direction of growth (111).

**KEYWORDS** pulsed laser deposition, solid solutions, GaP, semiconductors, III–V compounds

**ACKNOWLEDGEMENTS** This work was funded as part of a state order to the Southern Scientific Centre of the Russian Academy of Sciences, projects No. 122020100254-3 (studies of chemical composition and morphology) and No. 122020100326-7 (Raman studies). The growth of experimental samples was carried out using the resources of Center for Collective Use of North Caucasus Federal University and with the financial support of the Ministry of Education and Science of Russia, the unique identifier of the project is RF-2296.61321X0029 (agreement No. 075-15-2021-687).

The authors express their gratitude to the North Caucasian Federal University for their assistance in the framework of the competition for supporting projects of scientific groups and individual scientists of the university.

**FOR CITATION** Pashchenko A.S., Devitsky O.V., Lunin L.S., Lunina M.L., Pashchenko O.S., Danilina E.M. Growth of nanotextured thin films of GaInAsP and GaInAsSbBi solid solutions on GaP substrates by pulsed laser deposition. *Nanosystems: Phys. Chem. Math.*, 2023, **14** (5), 601–605.

### 1. Introduction

Pulsed laser deposition (PLD) is a promising and rapidly developing method for obtaining multicomponent compounds [1–3]. The advantages of PLD over other methods of physical deposition are the possibility of controlling the film stoichiometry, lowering the substrate temperature for growing thin III–V films, and the discrete flow of a substance from the target to the substrate in the time intervals between laser pulses. The advantage of the method is its relative simplicity of equipment, high purity of the deposited layers, and preservation of the stoichiometry of the chemical composition of a layer and a sputtered target [3, 4]. During PLD at the laser fluence of less than 2 J/cm<sup>2</sup>, an erosion-plasma plume forms a spot beam, due to which the expansion diagram of some target components, especially volatile ones, for example, As, P, Sb. In PLD at the laser fluence of more than 2 J/cm<sup>2</sup>, the uniformity of the expansion of the target components increases, but the growth kinetics and properties of the grown films change simultaneously [4]. As applied to III–V and CIGS semiconductor solid solutions, if the target contains more than one group III metal, then droplets can be formed on the surface [5, 6], the morphology deteriorates, and the layer stoichiometry is violated [7]. To understand these processes under PLD conditions, in this work, we study the properties of films grown with the laser fluence of 2.3 J/cm<sup>2</sup>.

The objects of study were Ga<sub>x</sub>In<sub>1-x</sub>As<sub>y</sub>P<sub>1-y</sub> and Ga<sub>x</sub>In<sub>1-x</sub>As<sub>1-y-z</sub>Sb<sub>y</sub>Bi<sub>z</sub> solid solutions deposited on GaP substrates. The solid solutions consisting of two group III metals and three highly volatile group V metalloids were selected based on the indicated difficulties in PLD, as well as on the relevance of their practical use for growing optoelectronic heterostructures in the visible [8] and infrared [9] ranges. The study of solid solutions with Bi and Sb is topical due to the discovery of the effect of valence band anticrossing [10], which significantly affects the optoelectronic properties of dilute

semiconductors. The object of this work is to grow  $\text{Ga}_x\text{In}_{1-x}\text{As}_y\text{P}_{1-y}$  and  $\text{Ga}_x\text{In}_{1-x}\text{As}_{1-y-z}\text{Sb}_y\text{Bi}_z$  solid solutions on GaP (111) substrates by PLD at the laser fluence of  $2.3 \text{ J/cm}^2$  and study the morphology, chemical composition, and chemical bonds in them.

## 2. Methods and experiments

PLD of  $\text{Ga}_x\text{In}_{1-x}\text{As}_y\text{P}_{1-y}$  and  $\text{Ga}_x\text{In}_{1-x}\text{As}_{1-y-z}\text{Sb}_y\text{Bi}_z$  solid solutions was carried out using an AYG:Nd<sup>3+</sup> laser (LS-2134Y) with a wavelength of 532 nm (second harmonic). For sputtering, we used targets with the calculated composition  $\text{Ga}_{0.84}\text{In}_{0.16}\text{As}_{0.68}\text{P}_{0.32}$  and  $\text{Ga}_{0.85}\text{In}_{0.15}\text{Sb}_{0.1}\text{As}_{0.8}\text{Bi}_{0.1}$ . The deposition was carried out on n-GaP (111) substrates. The choice of the substrate with the (111) orientation is due to the specifics of growth due to the polarity of Group III–V solid solutions, as well as the closeness of the lattice parameters of GaP and Si. We used the classical PLD method. The deposition time for all samples was 60 min, and the background pressure in the chamber was  $10^{-4}$  Pa. The distance from the target to the substrate was 70 mm. Growth was carried out at a temperature of 450 °C, a laser fluence  $F = 2.3 \text{ J/cm}^2$ , pulse duration time 10 ns, pulse-recurrence frequency 15 Hz.

The chemical composition was determined by Energy Dispersive X-ray microanalysis (EDX) using an INCAx-sight attachment (Oxford Instruments, UK) on a Carl Zeiss Evo 40 microscope with a beam energy of 8 keV to reduce the signal from the substrate. The film thickness was determined from the cleavages of the structures on a Carl Zeiss Evo 40 microscope. The study of the morphology and root-mean-square (RMS) roughness of the films was carried out on an atomic force microscope (AFM) “NTEGRA Academia” (NT-MDT SI, Russia). Scanning was carried out in a tapping mode. An NS15 silicon cantilever with a resonant frequency of 373.35 kHz and a curvature radius of 10 nm was used as a probe. The scanning speed varied in the range of 0.6 – 1 Hz depending on the surface topography. Line-scan direction is forward. The scanning area is  $1 \times 1 \mu\text{m}^2$ . AFM images were processed using the Gwyddion program [11]. The filtering included standard operations of subtracting the surface of the 3rd order, removing steps in the X direction, and removing scratches. The root-mean-square roughness parameter  $S_q$  was estimated for the entire scan area as an estimated value of the surface roughness. The study of chemical bonds in the obtained films was carried out by Raman spectroscopy on an inVia Raman Microscope spectrometer (Renishaw, UK) with an excitation wavelength of 514 nm at room temperature.

## 3. Results and discussions

At the first stage, the elemental analysis was carried out by the EDS (Fig. 1). In the spectra in Fig. 1, all the chemical elements of  $\text{Ga}_x\text{In}_{1-x}\text{As}_y\text{P}_{1-y}$  (Fig. 1a) and  $\text{Ga}_x\text{In}_{1-x}\text{As}_{1-y-z}\text{Sb}_y\text{Bi}_z$  (Fig. 1b) solid solutions were presented. The features of the measured EDX spectra are the high intensity of the Ga and P peaks and the low intensities of the Bi, Sb, and As peaks.

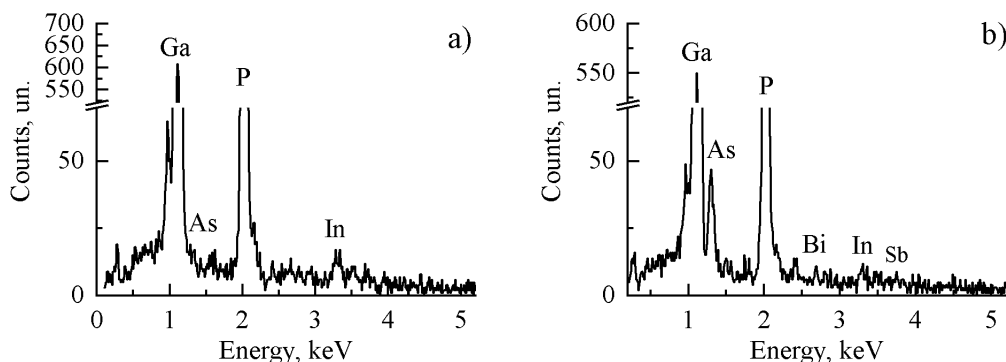


FIG. 1. EDX spectra of elemental analysis of solid solutions on n-GaP (111) substrates: a) GaInAsP; b) GaInAsSbBi

Estimation of the atomic concentration of the solid solution elements gave one the following results: for  $\text{Ga}_x\text{In}_{1-x}\text{As}_y\text{P}_{1-y}$ : Ga – 46.32 at.%; In – 2.66 at.%; As – 0.56 at.%, P – 50.45 at.%; for  $\text{Ga}_x\text{In}_{1-x}\text{As}_{1-y-z}\text{Sb}_y\text{Bi}_z$ : Ga – 47.26 at.%; In – 1.93 at.%; As – 21.31 at.%, Sb – 1.32 at.%; Bi – 0.89 at.%; P – 29.46 at.%. The phosphorus in the EDX spectrum (Fig. 1b) is due to its presence in the substrate and the small film thickness. This factor also introduces an error in determining the concentration of elements of group V. Nevertheless, for qualitative elemental analysis, the EDX method gives reliable results. The thickness of the grown films was determined from the cleavages of the heterostructure: GaInAsP – 223 nm; GaInAsSbBi – 152 nm. It can be seen that the growth film kinetics increases significantly.

Figure 2a shows the results of study of the morphology of the grown films by the AFM. In the case of the  $\text{Ga}_x\text{In}_{1-x}\text{As}_y\text{P}_{1-y}$  solid solution (Fig. 2a), the developed relief pattern is on the film surface. The height difference is 43 nm, and the RMS roughness  $S_q = 5.2$  nm. In the case of the GaInAsSbBi solid solution (Fig. 2b), the maximum height difference reaches 23 nm with the RMS roughness  $S_q = 2.8$  nm. A distinctive feature of the  $\text{Ga}_x\text{In}_{1-x}\text{As}_{1-y-z}\text{Sb}_y\text{Bi}_z$

film is the larger grain size with a smoother surface than in the case of the GaInAsP film with a highly developed surface relief pattern. In Fig. 2a the surface topography is due to chaotic grain boundaries, which are antiphase boundaries. Only some grains have plateaus on the surface oriented in the (111) plane. At the same time, the grain boundaries in the  $\text{Ga}_x\text{In}_{1-x}\text{As}_{1-y-z}\text{Sb}_y\text{Bi}_z$  film (Fig. 2b) appear as dislocations along certain directions, and to a greater extent have lateral faceting along the (110) planes, while plateaus in the growth direction are predominantly orientation in the (111) plane, i.e. the  $\text{Ga}_x\text{In}_{1-x}\text{As}_{1-y-z}\text{Sb}_y\text{Bi}_z$  film is nanotextured. It can be seen that in the case of the film in Fig. 2b, a large surface area is represented by hillocks with a plateau at the top, rather than pits, which also reveals itself in a lower RMS roughness  $S_q$ .

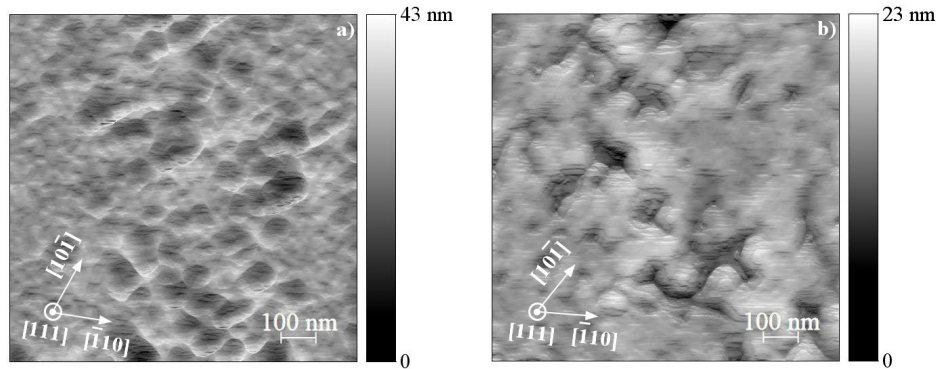


FIG. 2. AFM images ( $1 \times 1 \mu\text{m}$ ) of solid solution morphology on n-GaP (111) substrates: a) GaInAsP; b) GaInAsSbBi

The AFM analysis shows that the selected solid solutions grow at different rates due to different surface diffusion at the same growth temperature of  $450^\circ\text{C}$  and laser fluence  $F = 2.3 \text{ J/cm}^2$ . Therefore, under PLD conditions, the growth kinetics is significantly affected by the elemental composition of the film. The larger grain size in the  $\text{Ga}_x\text{In}_{1-x}\text{As}_{1-y-z}\text{Sb}_y\text{Bi}_z$  film is explained by the presence of Bi in its composition. It is known that Bi has a high surface diffusion and exhibits a strong surfactant effect [12], due to which it leads to a significant change in the diffusion of indium. These factors explain the larger grain size in Fig. 2b. Based on the AFM results, it can be concluded that the growth of thin films occurs through the nucleation of 3D islands, and then their coalescence occurs; the mode of epitaxial growth according to Volmer–Weber is implemented. Note that outside researchers also observed a similar growth when growing strongly mismatched group III–V heterostructures using other methods [13–15].

Raman spectra were measured to study the chemical bonds between the elements of the solid solution (Fig. 3). Table 1 summarizes the results of the measured frequencies of the phonon optical modes of the components of solid solutions and their values published in the literature references.

From the features of the measured spectra (Fig. 3), one can distinguish the dominance of the GaP LO ( $404.46 \text{ cm}^{-1}$ ) and TO ( $364 \text{ cm}^{-1}$ ) modes for both solid solutions, due to the small thickness of the films and the penetration of laser radiation into the substrate GaP, as well as the mode shift of GaAs, GaSb, InAs, and InSb in the region ( $200 - 300 \text{ cm}^{-1}$ ), compared with the literature data (Table 1). In the case of the  $\text{Ga}_x\text{In}_{1-x}\text{As}_y\text{P}_{1-y}$  solid solution (Fig. 3a), the peaks of InP LO ( $339.1 \text{ cm}^{-1}$ ) and TO ( $313.16 \text{ cm}^{-1}$ ) have weak intensities, which is due to its low concentration in the layer and the predominance of indirect-gap optical transitions [13].

Another feature of the Raman spectrum in Fig. 3a is the predominance of GaAs TO modes over GaAs LO in intensity, as well as their low intensity compared to those in  $\text{Ga}_x\text{In}_{1-x}\text{As}_{1-y-z}\text{Sb}_y\text{Bi}_z$  solid solution. In the  $\text{Ga}_x\text{In}_{1-x}\text{As}_{1-y-z}\text{Sb}_y\text{Bi}_z$  solid solution (Fig. 3b), the GaAs LO mode dominates over the GaAs TO mode in intensity with their simultaneous shift to lower wavenumbers (Table 1). This effect is explained by higher As concentration in the  $\text{Ga}_x\text{In}_{1-x}\text{As}_{1-y-z}\text{Sb}_y\text{Bi}_z$  film compared to  $\text{Ga}_x\text{In}_{1-x}\text{As}_y\text{P}_{1-y}$  (Fig. 1). The shift of these modes is due to the relaxation mechanisms in the film and the presence of dislocations (Fig. 2b). We associate the broad peak at  $208.66 \text{ cm}^{-1}$  with the GaBi LO mode, whose position is close to the theoretical  $205 \text{ cm}^{-1}$  [16]. The mode shift of InAs, InSb, GaSb, GaBi, and InBi is explained by the difference in the concentrations of Sb, Bi, As and the shift of electron densities during the formation of chemical bonds In–As, In–Sb, In–Bi, Ga–Sb, Ga–Bi. These factors indicate a violation of the selection rule for the zinc blende lattice, which is expressed in the mixing of phonon modes (InBi + InSb) in the range of  $150 - 200 \text{ cm}^{-1}$  due to disordering of the elements (disturbance of long-range order) of the solid solution.

#### 4. Conclusion

In conclusion, we note that nanotextured  $\text{Ga}_x\text{In}_{1-x}\text{As}_y\text{P}_{1-y}$  and  $\text{Ga}_x\text{In}_{1-x}\text{As}_{1-y-z}\text{Sb}_y\text{Bi}_z$  solid solutions with a laser fluence of  $2.3 \text{ J/cm}^2$  were grown by PLD. It is shown that in the case of PLD with a high fluence, the stoichiometry of the composition of solid solutions is disturbed. It is established that at constant growth temperature and the fluence

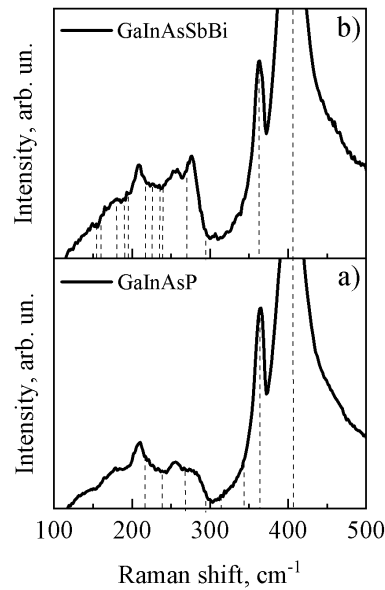


FIG. 3. Raman shift spectra of solid solutions on n-GaP (111) substrates: a) GaInAsP; b) GaInAsSbBi. Dashed lines indicate the frequencies of phonon modes from the literature (Table 1)

TABLE 1. Phonon frequencies of group III–V binary components constituting GaInAsP and GaInAsSbBi alloys

Binary component of a solid solution	Known phonon mode frequencies		Measured frequencies of phonon modes in the GaInAsP solid solution		Measured frequencies of phonon modes in the GaInAsSbBi solid solution	
	LO, cm <sup>-1</sup>	TO, cm <sup>-1</sup>	LO, cm <sup>-1</sup>	TO, cm <sup>-1</sup>	LO, cm <sup>-1</sup>	TO, cm <sup>-1</sup>
GaP	402 [16]	363 [16]	404.46	364.95	—	—
GaAs	292 [17]	268 [11]	281.93	255.84	276.73	257.58
InP	344 [18]	312 [18]	339.1	313.16	—	—
InAs	238.8 [19]	217.3 [19]	233.15	210.42	252.35	220.92
GaSb	236 [17]	226 [17]	—	—	234.90	226.16
InSb	190.8 [19]	179.8 [19]	—	—	192.88	180.59
InBi	161 [20]	155 [20]	—	—	161.24	154.19
GaBi	205 [21]	189 [20]	—	—	208.66	189.37

under PLD conditions, the elemental composition of the film has a significant effect on the growth kinetics. The surface-active elements (Sb and Bi) in the composition of the solid solution lead to a change in the surface diffusion of In and Ga. It is established that the growth of films occurs according to the Volmer–Weber mode. The AFM results show that the relaxation of stresses caused by the mismatch of the crystal lattices of  $\text{Ga}_x\text{In}_{1-x}\text{As}_y\text{P}_{1-y}$  and  $\text{Ga}_x\text{In}_{1-x}\text{As}_{1-y-z}\text{Sb}_y\text{Bi}_z$  and the GaP substrate occurs through plastic mechanisms and a change in roughness, which manifests itself in the formation of grains in the texture of the grown thin films. To improve the structural properties of the films, we plan to use GaAs buffer layers for the growth of  $\text{Ga}_x\text{In}_{1-x}\text{As}_y\text{P}_{1-y}$  and  $\text{Ga}_x\text{In}_{1-x}\text{As}_{1-y-z}\text{Sb}_y\text{Bi}_z$  solid solutions.

## References

- [1] Ogugua S.N., Ntwaeaborwa O.M., Swart H.C. Latest Development on Pulsed Laser Deposited Thin Films for Advanced Luminescence Applications. *Coatings*, 2020, **10** (11), 1078.
- [2] Li G., Wang W., Yang W., Wang H. Epitaxial growth of group III-nitride films by pulsed laser deposition and their use in the development of LED devices. *Surface Science Reports*, 2015, **70** (3), P. 380–423.
- [3] Vanalakar S.A., Agawane G.L., Shin S.W., Suryawanshi M.P., Gurav K.V., Jeon K.S., Patil P.S., Jeong C.W., Kim J.Y., Kim J.H. A review on pulsed laser deposited CZTS thin films for solar cell applications. *J. of Alloys and Compounds*, 2015, **619**, P. 109–121.

- [4] Ettlinger R.B., Cazzaniga A., Canulescu S., Pryds N., Schou J. Pulsed laser deposition from ZnS and Cu<sub>2</sub>SnS<sub>3</sub> multicomponent targets. *Applied Surface Science*, 2015, **336**, P. 385–390.
- [5] Pashchenko A.S., Devitsky O.V., Lunin L.S., Kasyanov I.V., Pashchenko O.S., Nikulin D.A. Structure and morphology of GaInAsP solid solutions on GaAs substrates grown by pulsed laser deposition. *Thin Solid Films*, 2022, **743**, 139064.
- [6] Chen S.C., Hsieh D.H., Jiang H., Liao Y.K., Lai F.I., Chen C.H., Luo C.W., Juang J.Y., Chueh Y.L., Wu K.H., Kuo H.C. Growth and characterization of Cu(In,Ga)Se<sub>2</sub> thin films by nanosecond and femtosecond pulsed laser deposition. *Nanoscale Research Letters*, 2014, **9**, 280.
- [7] Pashchenko A.S., Devitsky O.V., Lunin L.S., Lunina M.L., Pashchenko O.S. Structural properties of GaInAsSbBi solid solutions grown on GaSb substrates. *Technical Physics Letters*, 2022, **48** (5), P. 52–55.
- [8] Oshima R., France R.M., Geisz J.F., Norman A.G., Steiner M.A. Growth of lattice-matched GaInAsP grown on vicinal GaAs(001) substrates within the miscibility gap for solar cells. *J. of Crystal Growth*, 2017, **458**, P. 1–7.
- [9] Carrasco R.A., Morath C.P., Logan J.V., Woller K.B., Grant P.C., Orozco H., Milosavljevic M.S., Johnson S.R., Balakrishnan G., Webster P.T. Photoluminescence and minority carrier lifetime of quinary GaInAsSbBi grown on GaSb by molecular beam epitaxy. *Applied Physics Letters*, 2022, **120** (3), 031102.
- [10] Alberi K., Wu J., Walukiewicz W., Yu K.M., Dubon O.D., Watkins S.P., Wang C.X., Liu X., Cho Y.-J., Furdyna J. Valence-band anticrossing in mismatched III–V semiconductor alloys. *Physical Review B*, 2007, **75**, 045203.
- [11] Nečas D., Klapetek P. Gwyddion: an open-source software for SPM data analysis. *Open Physics*, 2012, **10** (1), P. 181–188.
- [12] Zvonkov B.N., Karpovich I.A., Baidus N.V., Filatov D.O., Morozov S.V., Gushina Yu.Yu. Surfactant effect of bismuth in the MOVPE growth of the InAs quantum dots on GaAs. *Nanotechnology*, 2000, **11** (4), P. 221–226.
- [13] Devenyi G.A., Woo S.Y., Ghanad-Tavakoli S., Hughes R.A., Kleiman R.N., Botton G.A., Preston J.S. The role of vicinal silicon surfaces in the formation of epitaxial twins during the growth of III–V thin films. *J. of Applied Physics*, 2011, **110** (12), 124316.
- [14] Fang S.F., Adomi K., Iyer S., Morkoç H., Zabel H., Choi C., Otsuka N. Gallium arsenide and other compound semiconductors on silicon. *J. of Applied Physics*, 1990, **68** (7), R31–R58.
- [15] Kim Y.H., Noh Y.K., Kim M.D., Oh J.E., Chung K.S. Transmission electron microscopy study of the initial growth stage of GaSb grown on Si (001) substrate by molecular beam epitaxy method. *Thin Solid Films*, 2010, **518** (8), P. 2280–2284.
- [16] Gudovskikh A.S., Uvarov A.V., Morozov I.A., Baranov A.I., Kudryashov D.A., Zelentsov K.S., Bukatin A.S., Kotlyar K.P. Low temperature plasma enhanced deposition approach for fabrication of microcrystalline GaP/Si superlattice. *J. of Vacuum Science & Technology A*, 2018, **36** (2), 02D408.
- [17] Vorlíček V., Moiseev K.D., Mikhailova M.P., Yakovlev Yu.P., Hulicius E., Šimeček T. Raman Scattering Study of Type II GaInAsSb/InAs Heterostructures. *Crystal Research & Technology*, 2002, **37** (2–3), P. 259–267.
- [18] Bedel E., Landa G., Carles R., Redoules J.P., Renucci J.B. Raman investigation of the InP lattice dynamics. *J. of Physics C: Solid State Physics*, 1986, **19**, 1471.
- [19] Frost F., Lippold G., Schindler A., Bigl F. Ion beam etching induced structural and electronic modification of InAs and InSb surfaces studied by Raman spectroscopy. *J. of Applied Physics*, 1999, **85** (12), P. 8378–8385.
- [20] Verma P., Oe K., Yamada M., Harima H., Herms M., Irmer G. Raman studies on GaAs<sub>1-x</sub>Bi<sub>x</sub> and InAs<sub>1-x</sub>Bi<sub>x</sub>. *J. of Applied Physics*, 2001, **89** (3), P. 1657–1663.
- [21] Yue L., Wang P., Wang K., Wu X., Pan W., Li Y., Song Y., Gu Y., Gong Q., Wang Sh., Ning J., Xu Sh. Novel InGaPBi single crystal grown by molecular beam epitaxy. *Applied Physics Express*, 2015, **8** (4), 041201.

---

*Submitted 3 July 2023; revised 9 August 2023; accepted 20 August 2023*

#### *Information about the authors:*

*Alexander S. Pashchenko* – Federal Research Center Southern Scientific Center of the Russian Academy of Sciences, Chekhov Ave., 41, Rostov-on-Don, 344006, Russia; North Caucasian Federal University, Pushkina st., 1, Stavropol, 355017, Russia; ORCID 0000-0002-7976-9597; semicondlab@ya.ru, as.pashchenko@gmail.com

*Oleg V. Devitsky* – Federal Research Center Southern Scientific Center of the Russian Academy of Sciences, Chekhov Ave., 41, Rostov-on-Don, 344006, Russia; North Caucasian Federal University, Pushkina st., 1, Stavropol, 355017, Russia; ORCID 0000-0003-3153-696X; v2517@rambler.ru

*Leonid S. Lunin* – Federal Research Center Southern Scientific Center of the Russian Academy of Sciences, Chekhov Ave., 41, Rostov-on-Don, 344006, Russia; North Caucasian Federal University, Pushkina st., 1, Stavropol, 355017, Russia; ORCID 0000-0002-5534-9694; lunin\_LS@mail.ru

*Marina L. Lunina* – Federal Research Center Southern Scientific Center of the Russian Academy of Sciences, Chekhov Ave., 41, Rostov-on-Don, 344006, Russia; ORCID 0009-0004-5761-3999; MarinaSchaz@rambler.ru

*Olga S. Pashchenko* – Federal Research Center Southern Scientific Center of the Russian Academy of Sciences, Chekhov Ave., 41, Rostov-on-Don, 344006, Russia; ORCID 0000-0003-3698-1835; paschenko.o.s@mail.ru

*Eleonora M. Danilina* – Federal Research Center Southern Scientific Center of the Russian Academy of Sciences, Chekhov Ave., 41, Rostov-on-Don, 344006, Russia; ORCID 0000-0001-6232-3217; el.m.danilina@gmail.com

*Conflict of interest:* the authors declare no conflict of interest.



# NANOSYSTEMS:

**PHYSICS, CHEMISTRY, MATHEMATICS**

## INFORMATION FOR AUTHORS

The journal publishes research articles and reviews, and also short scientific papers (letters) which are unpublished and have not been accepted for publication in other magazines. Articles should be submitted in English. All articles are reviewed, then if necessary come back to the author to completion.

The journal is indexed in Web of Science Core Collection (Emerging Sources Citation Index), Chemical Abstract Service of the American Chemical Society, Zentralblatt MATH and in Russian Scientific Citation Index.

### Author should submit the following materials:

1. Article file in English, containing article title, the initials and the surname of the authors, Institute (University), postal address, the electronic address, the summary, keywords, MSC or PACS index, article text, the list of references.
2. Files with illustrations, files with tables.
3. The covering letter in English containing the article information (article name, MSC or PACS index, keywords, the summary, the literature) and about all authors (the surname, names, the full name of places of work, the mailing address with the postal code, contact phone number with a city code, the electronic address).
4. The expert judgement on possibility of publication of the article in open press (for authors from Russia).

Authors can submit a paper and the corresponding files to the following addresses: nanojournal.ifmo@gmail.com, popov1955@gmail.com.

### Text requirements

Articles should be prepared with using of text editors MS Word or LaTeX (preferable). It is necessary to submit source file (LaTeX) and a pdf copy. In the name of files the English alphabet is used. The recommended size of short communications (letters) is 4-6 pages, research articles– 6-15 pages, reviews – 30 pages.

#### Recommendations for text in MS Word:

Formulas should be written using Math Type. Figures and tables with captions should be inserted in the text. Additionally, authors present separate files for all figures and Word files of tables.

**Recommendations for text in LaTeX:**

Please, use standard LaTeX without macros and additional style files. The list of references should be included in the main LaTeX file. Source LaTeX file of the paper with the corresponding pdf file and files of figures should be submitted.

References in the article text are given in square brackets. The list of references should be prepared in accordance with the following samples:

- [1] Surname N. *Book Title*. Nauka Publishing House, Saint Petersburg, 2000, 281 pp.
- [2] Surname N., Surname N. Paper title. *Journal Name*, 2010, **1** (5), P. 17-23.
- [3] Surname N., Surname N. Lecture title. In: Abstracts/Proceedings of the Conference, Place and Date, 2000, P. 17-23.
- [4] Surname N., Surname N. Paper title, 2000, URL: <http://books.ifmo.ru/ntv>.
- [5] Surname N., Surname N. Patent Name. Patent No. 11111, 2010, Bul. No. 33, 5 pp.
- [6] Surname N., Surname N. Thesis Title. Thesis for full doctor degree in math. and physics, Saint Petersburg, 2000, 105 pp.

**Requirements to illustrations**

Illustrations should be submitted as separate black-and-white files. Formats of files – jpeg, eps, tiff.



# ***NANOSYSTEMS:***

***PHYSICS, CHEMISTRY, MATHEMATICS***

**Журнал зарегистрирован**

Федеральной службой по надзору в сфере связи, информационных технологий и массовых коммуникаций

(свидетельство ПИ № ФС 77 - 49048 от 22.03.2012 г.)

ISSN 2220-8054

**Учредитель:** федеральное государственное автономное образовательное учреждение высшего образования

«Национальный исследовательский университет ИТМО»

**Издатель:** федеральное государственное автономное образовательное учреждение высшего образования

«Национальный исследовательский университет ИТМО»

**Отпечатано** в Учреждении «Университетские телекоммуникации»

Адрес: 197101, Санкт-Петербург, Кронверкский пр., 49

**Подписка на журнал НФХМ**

На первое полугодие 2024 года подписка осуществляется через

ОАО «АРЗИ», подписной индекс Э57385